MICROCOPY RESOLUTION TEST CHART
NATIONAL BUREAU OF STANDARDS-1963-A

STUDY OF UNSTEADY
TURBULENT BOUNDARY LAYERS

Interim Technical Report

by

A. N. Menendez and B. R. Ramaprian

IIHR Report No. 270

Iowa Institute of Hydraulic Research
The University of Iowa
Iowa City, Iowa 52242

December 1983

DTIC
SELECTE
FEB 21 1984

D

84 02 16 088

STUDY OF UNSTEADY
TURBULENT BOUNDARY LAYERS

Interim Technical Report

by

A. N. Menendez and B. R. Ramaprian

IIHR Report No. 270

Iowa Institute of Hydraulic Research
The University of Iowa
Iowa City, Iowa 52242

December 1983

Qualified requestors may obtain additional
copies from the Defense Technical Information
Service

Conditions of Reproduction

STUDY OF UNSTEADY
TURBULENT BOUNDARY LAYERS

Interim Technical Report

by

A.N. Menendez and B.R. Ramaprian

Sponsored by

IIHR Report No. 270

Iowa Institute of Hydraulic Research
The University of Iowa
Iowa City, Iowa 52242

December 1983

REPORT DOCUMENTATION PAGE	READ INSTRUCTIONS BEFORE COMPLETING FORM

1. REPORT NUMBER	2. GOVT ACCESSION NO.	3. RECIPIENT'S CATALOG NUMBER
	AD-A138156	

4. TITLE (and Subtitle)	5. TYPE OF REPORT & PERIOD COVERED
Study of Unsteady Turbulent Boundary Layers	Interim Technical Sept 1, 1980 to Oct 31, 1983
	6. PERFORMING ORG. REPORT NUMBER
	IIHR Report 270

7. AUTHOR(s)	8. CONTRACT OR GRANT NUMBER(s)
A.N. Menendez B.R. Ramaprian	DAAG29-79-G-0017

9. PERFORMING ORGANIZATION NAME AND ADDRESS	10. PROGRAM ELEMENT, PROJECT, TASK AREA & WORK UNIT NUMBERS
Iowa Institute of Hydraulic Research The University of Iowa Iowa City, Iowa 52242	

11. CONTROLLING OFFICE NAME AND ADDRESS	12. REPORT DATE
U. S. Army Research Office Post Office Box 12211 Research Triangle Park, NC 27709	31 December 1983
	13. NUMBER OF PAGES

14. MONITORING AGENCY NAME & ADDRESS(if different from Controlling Office)	15. SECURITY CLASS. (of this report)
	Unclassified
	15a. DECLASSIFICATION/DOWNGRADING SCHEDULE

16. DISTRIBUTION STATEMENT (of this Report)

Approved for public release; distribution unlimited.

17. DISTRIBUTION STATEMENT (of the abstract entered in Block 20, if different from Report)

NA

18. SUPPLEMENTARY NOTES

The view, opinions, and/or findings contained in this report are those of the author(s) and should not be construed as an official Department of the Army position, policy, or decision, unless so designated by other documentation.

19. KEY WORDS (Continue on reverse side if necessary and identify by block number)

Unsteady Flows   Oscillatory Boundary Layers
Turbulent Flows
Boundary Layers
Periodic Flows

20. ABSTRACT (Continue on reverse side if necessary and identify by block number)

A turbulent boundary layer, subjected to a free-stream velocity which changes sinusoidally in time under a zero time-mean pressure gradient, is studied both experimentally and analytically. Using a two-component Laser Doppler Anemometer and a Heat Flux Gage, detailed and high quality information is obtained on the instantaneous velocity distribution and wall shear stress, respectively, at various stations. An asymptotic theory, for

20. ABSTRACT CONTINUED

large Reynolds numbers, is developed for the oscillatory motion.
It is valid for both boundary layers at arbitrary time-mean pressure
gradients and fully developed pipe and channel flow, and is success-
fully applied to the present and previous available experimental
information. The theory identifies two frequency parameters, in
terms of which four different frequency regimes are defined. Simi-
larity laws are identified for each one of these frequency regimes.
All the experimental data have been archived on magnetic tape.

Accession For	
NTIS GRA&I	☒
DTIC TAB	☐
Unannounced	☐
Justification	
By	
Distribution/	
Availability Codes	
Dist	Avail and/or Special
A|	

ACKNOWLEDGMENTS

TABLE OF CONTENTS

LIST OF TABLES

LIST OF FIGURES

LIST OF SYMBOLS

C_f $2\tau_w/\rho\overline{U}_e^2$ = skin friction coefficient

E $u_*/\overline{U}_e$

f frequency of oscillation

f_b bursting turbulent frequency

H δ_*/θ = shape factor

k von Karman constant (= .418)

L θ/E^2 = length scale in the longitudinal direction

p pressure

Re_θ $\overline{U}_e\overline{\theta}/\nu$ = momentum thickness Reynolds number

Re_x $\overline{U}_e x/\nu$ = longitudinal Reynolds number

R_* $t_0/t_i = u_*\Delta/\nu$ = 'asymptotic' Reynolds number

t time coordinates

t_0 Δ/u_* = outer time scale

t_i ν/u_*^2 = inner time scale

u turbulent fluctuation of U

u_* $(\tau_w/\rho)^{1/2}$ = shear velocity

U x-component of the velocity

U_0 $\overline{U}_e$ for zero time-mean pressure gradient flow

v turbulent fluctuation of V

V y-component of the velocity

x streamwise coordinate

y cross-stream coordinate normal to the test plate

z	cross-stream coordinates parallel to the test plate
α	$u_*^2/\omega\nu$ = frequency parameter for the inner flow
δ	boundary layer thickness
δ_*	displacement thickness
Δ	θ/E = length scale for the boundary layer thickness
ε	relative amplitude of oscillation of the free-stream velocity
η	y/Δ = dimensionless outer cross-stream coordinates
θ	momentum thickness
θ_p	phase position along the oscillation cycle
ν	kinematic viscosity of the fluid
ν_t	eddy viscosity
ξ	$\int_0^x dx/L$ = dimensionless streamwise coordinate
Π	Coles wake parameter
ρ	density of the fluid
τ	$-uv$
τ_w	wall shear stress
ω	$2\pi f$ = angular frequency of oscillation
$\tilde{\omega}$	$\omega\Delta/u_*$ = frequency parameter for the outer flow
$\langle\ (\ )\ \rangle$	ensemble-averaged value
$[()]$	amplitude of oscillation
$\overline{(\ )}$	time-averaged value
$\tilde{(\ )}$	dimensionless outer variable
$(\ )^+$	dimensionless inner variable
$(\ )$	dimensionless variable in unsteady layer coordinates

Subscripts

e	conditions at the edge of the boundary layer
p	periodic (or oscillatory) component
1	complex amplitude
11	in-phase component
12	out-of-phase component

CHAPTER 1

INTRODUCTION

1.1. Problem Introduced

There has been increasing interest in recent times in the study of unsteady viscous flows. This is not surprising since, to a certain degree, unsteady viscous effects are present in the majority of practical flow situations. Viscous effects play either the leading or a secondary role in such varied fields as biofluid flows, turbomachinery flows, aircraft flutter, helicopter rotor-blade flows, etc.

The particular case of a boundary layer subjected to a free-stream velocity which is forced to change sinusoidally with time around a nonzero mean is of primary theoretical and practical importance. Its study received pioneering contributions from Lighthill (1954) and Karlsson (1959). The former introduced an analysis and the first (asymptotic) solutions for laminar flow, which set the basis for future theoretical investigations on the subject. Karlsson, in turn, performed the first series of experiments in the turbulent regime, covering a wide range of cases (varying the frequency and amplitude of the imposed free-stream oscillation) which have not been matched by any other study, either in number or in the range of experimental conditions.

Since then, broadly three different lines of approach have been taken to study the phenomenon of oscillatory boundary layers. One is the theoretical analysis, which has been mainly confined to laminar-flow situations. In the restricted cases it can deal with, it provides an understanding of the interplay among the different physical mechanisms and the resulting effects. The works of Ackerberg and Phillips (1972) and Pedley (1972) belong to this category. In turbulent flow, however, the theoretical analysis is difficult because of the well-known closure problem.

Another line of approach is the numerical solution of the differential equations. In laminar flow, this allows one to extend the analytical solutions beyond their range of validity, sometimes bridging the gaps between asymptotic solutions. Reference can be made to the works of Tsahalis and Telionis (1974) and McCroskey and Phillipe (1975) in this connection. When dealing with turbulent flows, the use of a turbulence model is necessary in order to close the system of equations. This limits considerably the generality of the solution. In addition, in unsteady flow, the turbulence models used so far are unmodified versions of those developed for steady flow. Therefore, the predictions are expected to fail for relatively large frequencies of oscillation. Work in this area has been done by, among others, Nash and Patel (1975), Cousteix et al. (1977), Orlandi (1981) and Menendez and Ramaprian (1982, 1983a, 1983b). Integral methods have also been developed to obtain approximate solutions [Cousteix et al. (1977), Lyrio and Ferziger (1983)].

The third line of approach to the study of unsteady boundary layers is through experiments. With regard to laminar flows they have served primarily to corroborate the theoretical results. Hill and Stenning (1960) have provided some of the few known experimental data. In the case of turbulent flows, on the contrary, much of the current understanding of the phenomenon comes from the experimental studies. These include the works of Patel (1977), Schachenmann and Rockwell (1976), Cousteix et al. (1977, 1981), Jarayaman et al. (1982), and Simpson et al. (1983a, 1983b). Related investigations on duct (pipe or channel) flows have been performed by Binder and Kueny (1981), Kobashi and Hayakawa (1981) and Tu and Ramaprian (1983a, 1983b). In a recent book, Telionis (1981) summarizes much of the current knowledge about unsteady boundary layers.

1.2. State of the Art in Unsteady
Turbulent Boundary Layers

From the available experimental information, the following picture of the phenomenon of oscillatory turbulent boundary layers can be constructed:

(i)   The time-mean velocity distribution is practically coincident with that in steady-flow at the time-mean free-stream velocity [Karlsson (1959), Cousteix et al. (1977), Jarayaman et al. (1982)]. Small deviations from this behavior were observed by Ramaprian and Tu (1982) in pipe flow.

(ii) The oscillatory velocity component depends strongly on the forcing frequency. For low frequencies, the unsteady effects spread

over the outer part of the boundary layer. For larger frequencies, the outer part is subjected to rigid-body oscillations, and the unsteady viscous effects are concentrated in regions increasingly closer to the wall [Karlsson (1959), Jarayaman et al. (1982)]. However, unsteady viscous effects in turbulent flow extend over a much wider region than in a hypothetical laminar flow with the same boundary-layer thickness and at the same frequency of oscillation. Using eddy-viscosity arguments, Ramaprian and Tu (1982) identified the frequency parameter $\omega\delta/u_*$ as the one characterizing the extent of unsteady viscous effects in the outer layer. They also used this parameter to define five different frequency regimes. However, their analysis is not rigorous but heuristic. Furthermore, it does not properly account for the viscous effects very near the wall and hence is unable to characterize the flow completely, especially at high frequencies.

(iii) The amplitude of the oscillatory velocity shows an overshoot, which is especially large for adverse time-mean pressure-gradient flows at low frequencies [Cousteix et al. (1981), Jarayaman et al. (1982)]. For high frequencies, this overshoot is small irrespective of the free-stream conditions. Close to the wall and, at least, for relatively large frequencies, the oscillatory velocity leads the free-stream velocity [Karlsson (1959)]. At high frequencies, the oscillatory motion seems to approach the laminar (Stokes) solution given by Lighthill (1954) [Binder and Kueny (1981), Jarayaman et al. (1982)].

(iv)   The turbulence properties are modulated with the forcing frequency.   Some of the existing data suggest that their time-mean distributions coincide with the steady-flow distributions at the time-mean free-stream velocity [Cousteix et al. (1977), Jarayaman et al. (1982)].   Others [Ramaprian and Tu (1982)] do not seem to suggest this trend.

(v)   The oscillatory component of the turbulence properties has a strong dependence on the forcing frequency.   For low frequencies, significant amplitude and phase variations occur all across the boundary layer.   For higher frequencies, these variations are confined to the near-wall region, and the turbulence oscillations are practically supressed in the outer layer [Jarayaman et al. (1982)].

(vi)   There is controversy about the interaction between the forced oscillation and the turbulent fluctuations.   It still remains to be answered if there is any interaction; and, if so, at what frequency and what its nature is.

(vii)   No direct wall-shear-stress measurements have been performed.   Cousteix et al. (1981) utilized the conventional procedure developed for steady flow to obtain the wall shear stress distribution in a cycle.   This consists of assuming the validity of the "logarithmic law" for the ensemble-averaged velocity profile and using the "Clauser plots".   However, it is not clear whether this procedure is correct.   Moreover, for high frequencies the logarithmic region may disappear for part of the cycle [Jarayaman et al. (1982)].   Ramaprian and Tu (1982) performed direct wall-shear-stress measurements in pipe flow.   They found that the time-mean value was

slightly larger than the steady value at the time-mean free-stream velocity.

In an admirable effort, Carr (1981b) is compiling all the available experimental data on unsteady turbulent boundary layers. This has provided him with the opportunity of establishing some correlations among the different experimental conditions, which may bring more order into the ongoing research. Figures 1.1 and 1.2, taken from Carr (1981a), show two different ways of correlating experiments with zero (ZPG) and adverse (APG) time-mean pressure-gradient boundary layers and with pipe flows. Both are in terms of the frequency and amplitude of oscillation and the extent of unsteady viscous effects. In Fig. 1.1, the frequency is presented in terms of a Strouhal number based on the local time-mean boundary layer thickness and free-stream velocity. In Fig. 1.2 f is normalized by a critical value associated with the local turbulent burst frequency. These figures suggest that there is still a need for experiments on boundary layers at zero time-mean pressure gradient, especially at high frequencies and large amplitudes of oscillation.

1.3. Objectives of the Present Research

The objectives of the present work were twofold. First, detailed and high quality experimental information was sought for a turbulent boundary layer in a zero time-mean pressure gradient with a relatively large amplitude of oscillation. Two frequencies were studied; for the lower one, the unsteady viscous effects extend over the outer layer, while they are confined in the near-wall region for

the higher frequency. The higher frequency is comparable to the turbulent bursting frequency in the boundary layer. One can, therefore, expect the imposed oscillation to interact with the turbulent motions. The experiments are represented in Figs. 1.1 and 1.2 by means of lines, which cover the conditions from the first to the last measuring station along the tunnel employed. The main differences with the similar experiments performed by Karlsson (1959) and Cousteix et al. (1977) are:

(i) Water was used instead of air as the working fluid. Hence, the amplitude modulation imposed by acoustic effects was avoided and a long test section could be used. This allowed study of spatial history effects as the boundary layer evolves through transition and develops into a fully turbulent boundary layer.

(ii) The high frequency utilized, when properly normalized, was much larger than those used by Cousteix et al. (see Figs. 1.1 and 1.2). Though some of Karlsson's frequencies are comparable to the present ones (or even much larger than the present ones, as in an experiment not represented in the foregoing figures), he was not able to isolate properly the turbulence properties due to limitations in his data processing system.

(iii) Laser Doppler Anemometry, capable of nonintrusive measurements, was used in the present studies. Also, wall-shear-stress measurements were made using a surface-mounted probe rather than inferring it indirectly from a 'law of the wall' of unestablished validity.

Some similarities between the present experiments and those by Jarayaman et al. (1982) are evident. However, the latter correspond to an adverse time-mean pressure-gradient flow. In addition, in the present experiments, two velocity components were measured instead of one.

The second objective of the present research was to provide, following an analytical approach, a theoretical framework to classify and characterize different unsteady turbulent-flow regimes for nonseparating boundary layers in an arbitrary (time-mean) pressure gradient, as well as for fully developed pipe/channel flows. A singular perturbation technique was used, and led to asymptotic similarity laws for the different frequency regimes. These laws can be considered as extensions to unsteady flows of the classical steady-flow laws, such as the "law-of-the-wall" for the inner layer, the "velocity-defect law" for the outer layer, and the "logarithmic law" for the overlap region.

1.4. Layout of the Report

The experimental apparatus and procedures are described in Chapter 2. The results of the experiments are presented and discussed in Chapter 3. The asymptotic analysis of unsteady turbulent boundary layers and pipe/channel flows is developed in Chapter 4. Chapter 5 presents an examination of the present as well as earlier experimental data in the light of this analysis. The major conclusions of the present work are summarized in Chapter 6. The detailed experimental data are too voluminous to be presented in

a report. They are, however, archived on digital tape and will be sent to the AGARD Data Bank [Carr (1981b)], from which they will be available on request.
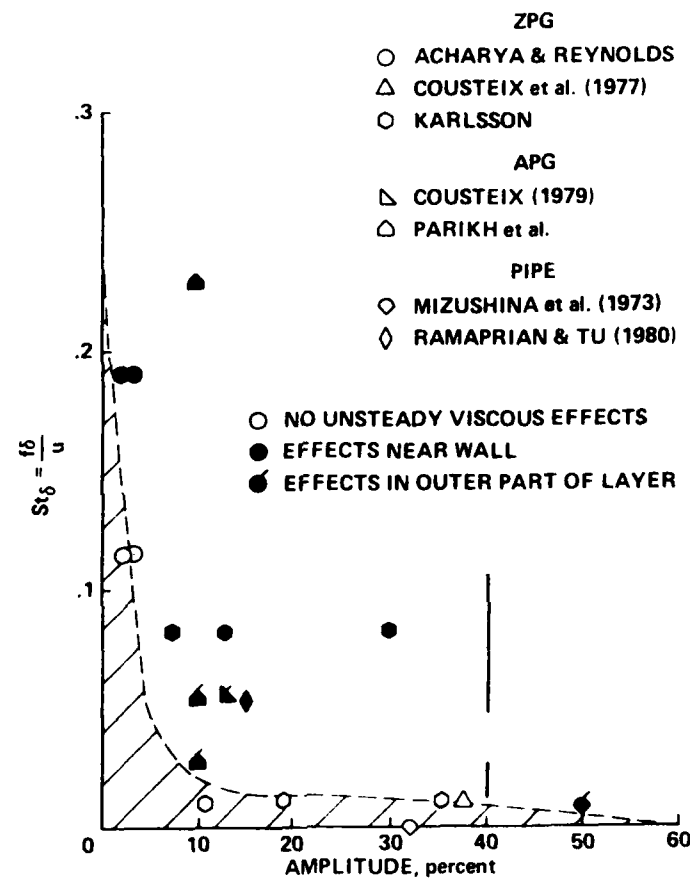
Figure 1.1. Correlation between amplitude and Strouhal
number [Carr (1981a)]. ——, present experi-
ments.
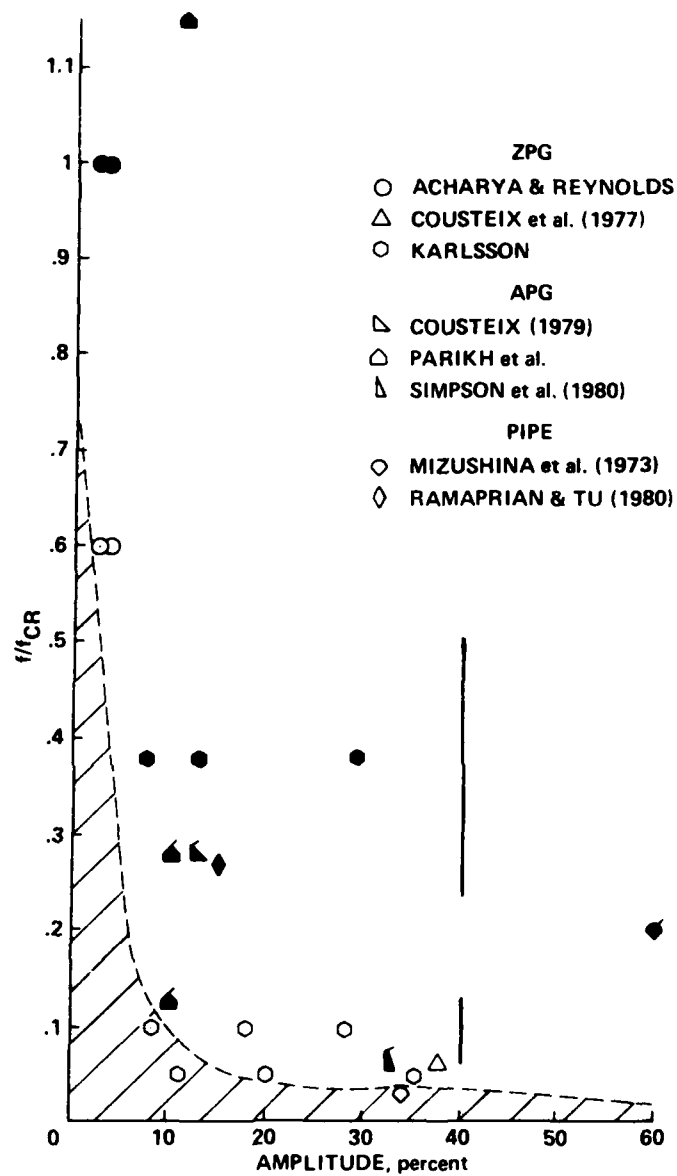
Figure 1.2. Correlation between amplitude and relative frequency [Carr (1981a)]. ——, present experiments.

CHAPTER 2

EXPERIMENTAL DETAILS

2.1. General

The object of the experimental investigation was to generate and study a zero time-mean pressure gradient boundary-layer flow, with a free-stream velocity given by

$$\langle U_e \rangle = U_0 \ (1 + \epsilon \sin \omega t) \tag{2.1}$$

where U_0, ϵ and $\omega = 2\pi f$ are constant. A large water tunnel was built for this purpose. The use of water as the working fluid has the following advantages:

(i)   It is possible to study oscillation frequencies that approach the turbulent frequencies.

(ii)   There is a significant separation between the oscillation and turbulent frequencies on one hand, and the acoustic frequencies on the other.

(iii)   No seeding is necessary for use of Laser Doppler Anemometer.

In addition, there exists a good deal of experience at IIHR in building such facilities for steady flow.

The main instrumentation consisted of a Laser Doppler Anemometer (LDA) to measure the velocity, and a heat-flux gage (HFG) operated by constant-temperature hot-wire anemometer to determine the skin friction. The data were digitally acquired and processed on an HP/1000 minicomputer. More details are presented below.

2.2. Apparatus

A unique water tunnel was built especially for this study. Fig. 2.1 shows a layout of the apparatus. It works under a constant head of about 8 m. The test section is 2.4 m long, with a rectangular cross-section 50 cm in width and 22.5 cm in height. Its bottom, used as the test surface for the boundary layer studies, is a smooth brass plate. Transition was promoted by means of a strip of 14-mesh brass screen (15 cm in width) glued to the test surface at a distance (x) of about 22.5 cm from the end of the contraction. The side walls of the tunnel are 9.5 mm thick steel plates, with five windows located at, approximately, x = 48, 69, 90, 142 and 203 cm. The windows are made of Plexiglas. Originally, the side walls were tempered glass, but it was found that they depolarized the laser beams, so they had to be removed. The top wall of the test section is a Plexiglas sheet 37.5 mm thick. In addition, a 6.4 mm thick flexible Plexiglas sheet was used as a 'false' wall. By adjusting its position to correct for the displacement thickness of the boundary layers along the walls a nearly zero (time-mean) longitudinal pressure gradient was obtained

in the test section. For the 0.5-Hz experiments (see below), the false wall was reinforced with transverse strips 6.4 to 9.5 mm thick, spaced approximately 23 cm apart. Other details of the tunnel can be seen in Fig. 4.1. Note, in particular, that no screens were used in the tunnel. This was to avoid clogging problems, likely to arise from the use of unfiltered recirculated water. The tunnel ends in a steel cylinder (40 cm diameter x 60 cm long) whose downstream end is closed. The cylinder has two longitudinal rectangular slots, 61 x 2.54 cm, located 180 degrees apart, from which the water exits. The area of opening of the slots is varied by a rotating profiled sleeve driven by a 3 H.P. geared D.C. motor whose speed can be regulated to within 1/4 percent. Each complete rotation of the sleeve corresponds to two oscillation cycles. The sleeve profile was contoured to produce a sinusoidally varying free-stream velocity in the test section at the desired frequency. The details of the design are given by Ramaprian and Tu (1982). Note that a different profile should be used, in principle, for each desired frequency (and amplitude) of oscillation. However, it was found that, with a given profile, the frequency can be changed appreciably from the design value without producing a large change in the amplitude or any significant distortion in the velocity wave form.

2.3. Instrumentation

Two types of instruments were used; a two-component LDA, and a flush-mounted HFG. The first measures the longitudinal and vertical velocity components. The HFG measures the shear stress at the

wall.   Each of these is described in some detail in the following subsections.

2.3.1. Laser Doppler Anemometer

The principle of operation of the LDA is well known.   Two laser beams intersect each other producing an interference fringe pattern in the small intersecting region ("measuring volume").   When particles suspended in the fluid cross the measuring volume, they scatter light with a frequency proportional to the particle velocity, assumed to be the same as the fluid velocity.   The detector of the frequency-shift provides a signal linearly related to the velocity. For more details see, for example, Drain (1980).

In the present experiments, a two-component LDA was used.   This system works with three laser beams which, when properly polarized, produce two sets of interference fringes, allowing the simultaneous measurement of two velocity components.   The system consists of a SPECTRAPHYSICS 5 mW He-Ne Laser, TSI (Thermo System Inc.) optics, an acousto-optic Bragg cell for frequency shifting (which allows directionality distinction), a pair of photodetectors (one for each signal) and a pair of TSI Model 1090 frequency trackers, which process the photodetector signals.   The output-voltage signal on each channel is then low-pass filtered by an active filter (Rockland, Model 852) with a sharp cut off (36 db/octave), and sampled simultaneously by the computer.   A sketch of the optical arrangement is shown in Fig. 2.2.   For more details, see Ramaprian and Chandrasekhara (1983).   The LDA was operated in the forward scatter

mode. A beam expander was used to reduce the size of the focal volume to 1.8 mm x 0.1 mm. The transmitting and receiving optics were both mounted on a traverse, which could be moved in three spatial directions.

The calibration of the LDA depends on the frequency of the laser beams (fixed) and their geometrical configuration. Once the latter is set, the calibration constant is fixed, known, and independent of the experimental conditions. To determine the distance of the measuring volume from the wall, it is necessary to establish the position of the wall ("zero"). This is done with an estimated error of the order of the laser beam thickness at the focal plane of the optical system, namely 0.1 mm.

2.3.2. Heat-Flux Gage

The use of the flush-mounted HFG in steady laminar or turbulent flow is based on the analogy between heat transfer from the heated element to the fluid and the local wall shear stress. The proposed relation is the following:

$$\tau_w^{1/3} = AE^2 + B \qquad (2.2)$$

where the voltage E, read from the anemometer, is related to the wall heat transfer, and the constants A and B are obtained by calibration [see Bellhouse and Schultz (1966)]. As part of the present work, considerable effort was directed to determine the extent to which this technique is applicable to unsteady flow situations. As a

result, a more general relationship between the two quantities, τ_w and E, has been developed, namely [Menendez and Ramaprian (1983c)]

$$\tau_w = (AE^2 + B)^3 + \frac{c_1}{(AE^2+B)} \frac{dU_e}{dt} + c_2 A \frac{dE^2}{dt} \qquad (2.3)$$

where the constants c_1 and c_2 depend on the fluid properties and the effective dimensions of the heated element. Fig. 2.3, taken from the above reference, shows typically the improvement in results for phase and amplitude of $\langle \tau_w \rangle$ obtained by the use of Eq. (2.3) instead of Eq. (2.2), under different operating conditions. The results are compared in each case with theoretical results obtained from a numerical solution of the unsteady boundary layer equations. Eq. (2.3) reduces practically to Eq. (2.2) when the frequency of oscillation is small enough to satisfy the conditions

$$\omega \ll \frac{|\tau_w|^{4/3}}{c_1[U_e]} \qquad (2.4)$$

$$\omega \ll \frac{|\tau_w|}{c_2[\tau_w^{1/3}]} \qquad (2.5)$$

[For details, see Menendez and Ramaprian (1983c)]. These conditions were satisfied in the present experiments. Hence, Eq. (2.2) was used for the determination of τ_w.

A TSI quartz-coated film probe was used, and operated by a DISA constant-temperature hot-wire anemometer. A sketch of the probe, mounted on the wall, is shown in Fig. 2.4. An overheat ratio of

about 1.1 was used. Measurements were performed at four stations; x
= 48 cm, x = 80 cm, x = 142 cm and x = 203 cm. The signal was low-
pass filtered before being sampled by the computer. Simultaneously,
an LDA signal corresponding to the longitudinal velocity was also
sampled as a reference. The probe was mounted just before each
experimental run, and removed and cleaned after the run. The
calibration was performed in steady turbulent flow, for which the
wall shear stress is known from a Coles' fit to the velocity profile
(see section 2.6.3). The calibration depends critically on both the
film and water temperatures, and thus could change considerably
during an experiment. Hence, two calibration curves were obtained
for each experiment, one immediately before and one immediately after
the unsteady run, and an average of the two was taken as the final
curve. For more experimental details, reference may be made to
Ramaprian and Tu (1982).

2.4. Acquisition and Processing of the Information

An HP/1000 data acquisition system with a PRESTON Analog-to
Digital Converter was used for both data acquisition and
processing. A triggering mechanism synchronized with the sleeve
rotation provides the sampling pulses at fixed phase positions. This
is described in detail in Ramaprian and Tu (1982). An improvement
over the previous way of operation is that the starting, stopping,
and eventual repetition (in case of missed pulses) of the sampling
was done automatically by the computer. The triggering mechanism
gives 200 pulses for each complete revolution of the sleeve, which

corresponds to 100 pulses per oscillation cycle. For the steady-flow experiments, the pulses were provided by a square-wave generator. For each pulse, the computer sampled simultaneously the two signals (either two LDA signals or one HFG and one LDA signal) received from the two channels. This information was temporarily stored in disk file and later processed. Both the raw and processed data were permanently stored on digital tape. The latter type of files are in the format appropriate for the AGARD Data Bank of L.W. Carr (1981b).

The software for data acquisition and processing of single periodic unsteady signals, previously developed at IIHR, has been extended to deal with two simultaneous signals. It has also been enhanced with new features which allow the automatic recognition of spurious signals and the consequent discarding of the corresponding cycle during the processing. Spurious signals may appear due to LDA drop-outs [see Drain (1980)] or the temporary locking of the tracker to a secondary signal (for example, the signal corresponding to the other channel).

The signals are processed according to the concept of the "triple deck decomposition" [Hussain and Reynolds (1970)]. This means that any instantaneous quantity Φ is expressed as

$$\Phi = \overline{\Phi}(x,y) + \Phi_p(x,y,\theta_p) + \phi(x,y,t) \tag{2.6}$$

where $\overline{\Phi}$ is the time-mean value, Φ_p the periodic deterministic component, ϕ the turbulent fluctuation and θ_p the phase position within a cycle. The first step, in practice, is to obtain the

ensemble-averaged value $\langle\phi\rangle(x,y,\theta_p)$ by averaging the instantaneous values at identical θ_p positions over a large number of cycles. The time-mean value $\overline{\phi}$ is then obtained by averaging $\langle\phi\rangle$ over the complete cycle $(0 \leq \theta_p < 2\pi)$. The periodic component Φ_p is the difference $\langle\phi\rangle - \overline{\phi}$. Finally, the turbulent fluctuation ϕ is simply $\phi - \langle\phi\rangle$. This is a statistical quantity, for which the phase-averaged and time-averaged mean squared values, $\langle\phi^2\rangle$ and $\overline{\phi^2}$, respectively, are also calculated using the above procedure. For more details of the whole procedure, see Ramaprian and Tu (1982).

2.5. Experimental Conditions

The nominal free-stream conditions are expressed by Eq. (2.1), with U_0 = 90 cm/sec and ϵ = 0.40, and two different frequencies, f = 0.5 Hz and f = 2 Hz. They were attainable within $\pm$ 0.5 cm/s for the velocity, $\pm$ 0.0015 for the relative amplitude, and $\pm$ 0.005 Hz for the frequency.

The turbulent bursting frequency f_b in the boundary layer, which can be regarded as a characteristic frequency of turbulence, was estimated, from the criterion of Rao et al. (1971) [see Eq. (4.9)] to vary from about 13 to 4.5 Hz from the first to the last measuring station. It is seen that the higher of the two oscillation frequencies is comparable to the bursting frequency, at least for the downstream stations. The fundamental resonant acoustic frequency of the tunnel is estimated to be about 40 Hz. The turbulent energy spectrum was found to contain only a very small amount of the energy beyond 40 Hz. Hence, no significant acoustic interaction with the turbulence is expected.

The number of sampled cycles was chosen equal to 1000 for the 2-Hz experiment. In order to keep the experimental time within reasonable limits, this was reduced to 250 for the 0.5-Hz experiment. However, to obtain statistically stable averages for the turbulent quantities, the results for each four consecutive phase-positions in a cycle were averaged, assigning the result to the intermediate value of the phase. This brought the effective number of samples again to 1000.

Estimations of the (random) measurement errors are presented in Table 2.1. They were obtained from the scatter in the data from repeated trials. Systematic errors may also occur. In the LDA measurements, the main source of systematic error is the determination of the distance between laser beams as they exit from the transmitting optics. This quantity is used in determining the calibration constant, and may produce a deviation of the order of 3%. In the HFG measurements systematic errors are considered to be negligible in comparison to random ones. The estimated error in the distance of the measuring volume from the wall is 0.4 mm in the outer region ($y > 1$ cm) and 0.12 mm in the inner one (1 mm $\lesssim y \leq 1$ cm). The (x) location of the measurement station along the tunnel, is specified with a tolerance of 1 cm.

2.6. Flow Quality

To assess the quality of the flow in the test section, the following tests were performed:

(i) Check for uniformity and two-dimensionality: this amounts to verifying the absence of organized structures (such as vortices) in the core of the flow and determining the range of influence of the side walls.

(ii) Check for design conditions: this included verification of Eq. (2.1), i.e. establishing the variation of the time-mean free-stream velocity and the amplitude and phase of its oscillatory component along the test section.

(iii) Check for performance of the tunnel as a steady flow facility: this required comparison of the boundary-layer structure to standard data available in the literature.

The results of each of these tests are presented and discussed in the three following subsections.

2.6.1. Uniformity and Two-Dimensionality

The uniformity of the flow in the core region (beyond the boundary layers on the walls) was verified in the steady flow at extreme upstream and downstream stations, $x = 45$ and 190 cm, respectively. The results for the latter station are presented in Fig. 2.5, and are seen to be very satisfactory. In fact, the standard deviation of the velocity is only 0.61% of the mean velocity at this station, and 0.64% at $x = 45$ cm.

To check the two-dimensionality of the flow in the core region, similar measurements were made, except that they were spaced much closer together. The results for the station $x = 190$ cm are shown in Fig. 2.6. It is observed that the flow is free from any kind of organized structure.

Two-dimensionality checks were also performed in the boundary layer. This time, however, complete sets of velocity profiles were measured at eight spanwise locations in the unsteady flow at the higher frequency (2 Hz) at the most downstream station ($x = 203$ cm). The results for the time-mean value of the longitudinal velocity are presented in Figs. 2.7 and 2.8 for the "left" ($z < 25$ cm) and "right" side of the test section ($z > 25$ cm) respectively, when facing the flow. In these figures, the parameter Re stands for $y\overline{U}_e/\nu$. The bottommost distribution in both figures corresponds to the plane $z = 18.9$ cm where all the subsequent detailed studies were performed. It is superimposed as a line on the other distributions so as to assess the extent of two-dimensionality. It is observed that the agreement is good, at least in the range 13.6 cm $< z < 29.6$ cm. It is necessary to mention that the measurements at the far-right locations (largest z values) are of lower quality due to optical constraints imposed by the larger distance from the transmitting optics and of the LDA. Furthermore, a misalignment of the right wall was discovered and corrected after these measurements had been completed. Hence, an improvement in the performance of the flow on the right side may be expected, producing a more symmetrical behavior. Similar results were obtained for the amplitude and phase of the first harmonic of the longitudinal velocity, as shown in Figs. 2.9 to 2.12. Results for the time-mean value and amplitude of oscillation of the turbulent quantities $\langle u^2 \rangle$ and $- \langle uv \rangle$ are presented in Figs. 2.13 to 2.20. Again, the same conclusions hold. The flow in the boundary layer can, therefore, be considered to be two-dimensional at least over the central 30% of the span.

2.6.2. Design Conditions

The design conditions were checked in both the steady and unsteady regimes. Figure 2.21 presents the longitudinal variation of the time-mean velocity, relative to its value at the first measured station, denoted by the subscript '0'. Some of these measurements were made before the glass side walls were removed (see section 2.2). Two sets of data points are shown for the steady-flow case, corresponding to experiments conducted on two different days. They agree well with each other. It is observed that the longitudinal variation of $\overline{U}$ is within about $\pm$ 3.5% relative to the mean, which is acceptable. The "peak" at $x \simeq 90$ cm seems to be associated with some waviness in the upper wall. In turn, it is seen that the time-mean velocity for the unsteady flow at 2 Hz agrees very well with the steady flow data. Some deviation from the steady-flow results is observed in the case of the 0.5-Hz experiment. This is due to the readjustment made in the false-wall position after its reinforcement (see section 2.2). The maximum variation in $\overline{U}$ is now about ± 1.5%.

The longitudinal distribution of the relative amplitude of oscillation for the unsteady runs is shown in Fig. 2.22. The variation is of the same order as for the time-mean velocity. Figure 2.23 presents the relative phase, which shows a maximum difference of only about 4 and 1.20 degrees for the 2 and 0.5-Hz experiments, respectively.

The higher harmonic content of the free-stream oscillation was found to be of the order of 0.3% relative to the time-mean value, and thus negligible.

2.6.3. Steady Boundary Layer

Measurements of the velocity profile in steady flow were made at various free-stream velocities and at the five measuring stations, namely x = 48 cm (station 1), x = 69 cm (2), x = 90 cm (3), x = 142 cm (4) and x = 203 cm (5). From the time-mean velocity profiles the integral parameters, namely the displacement thickness, δ_*, the momentum thickness, θ, and the shape parameter, $H = \delta_*/\theta$, were calculated. In addition, the data were fitted by Coles' "log + wake" law,

$$\frac{\overline{U}}{u_*} = [5.5 \log (\frac{yu_*}{\nu}) + 5] + \frac{\Pi}{k} W (\frac{y}{\delta}) \qquad \text{for } \frac{y}{\delta} \leq 1$$
$$\frac{\overline{U}}{u_*} = \frac{U_0}{u_*} \qquad\qquad\qquad\qquad \text{for } \frac{y}{\delta} > 1$$

(2.7)

where the function $W(\eta)$, which characterizes the 'wake component', is taken as

$$W(\eta) = 2 (3\eta^2 - 2\eta^3) \qquad\qquad (2.8)$$

The fitting was performed by matching δ_* and θ, and using the logarithmic friction law [Eq. (4.23)], from which the shear velocity, u_*, the boundary layer thickness, δ, and the wake strength parameter, Π, are calculated. Figure 2.24 shows the velocity profiles in the inner or wall coordinates at station 5 and the corresponding fit to the Coles-profile, Eq. (2.7). It is observed that the profiles do, in fact, follow very closely Coles' law at all

the free-stream velocities. Very similar results were obtained for the remaining stations. Table 2.2 presents the values of the parameters characterizing the velocity profile at the five measuring stations, for a free-stream velocity of $\overline{U}_e \simeq 90$ cm/s. They will be useful as a reference when analyzing the unsteady flow results.

Figure 2.25 shows the correlation between C_f and Re_θ according to the present measurements, and a line representing the experimental results of ten different investigations [Coles (1962)], including one performed at IIHR [Landweber and Siao (1958)]. The agreement is very good, except, perhaps, at station 1. This may be due to the fact that the flow was not yet fully turbulent at this station. Figure 2.26 presents the variation of π with Re_θ, together with the "normal curve" given by Coles (1962). Except for the points corresponding to station 3, which show excellent agreement with the "normal curve", the present results are consistently lower. This may be because of the relatively high free-stream turbulence intensity (1 to 1.2%) in the present experiments [Coles (1962)], which, in turn, is evidently due to the absence of screens in the calming chamber (see section 2.2).

The four velocity profiles at station 5 are replotted in Fig. 2.27 in the outer coordinates and compared with the results of Klebanoff (1954) corresponding to $Re_\theta \simeq 7800$. The agreement is excellent for the largest free-stream velocity, for which $Re_\theta = 5840$, and, as expected, gets poorer for lower velocities due to the incomplete development of the wake component.

The distributions of the turbulence properties, $\overline{u^2}$, $\overline{v^2}$ and $-\overline{uv}$ at station 5, normalized by the shear velocity u_*, at station 5, are presented in Figs. 2.28 to 2.30, together with the results of Klebanoff. The comparisons are considered to be satisfactory at the higher free-stream velocities and become poorer (as expected) at the lower ones.

The results show that the facility is, in general, able to produce a standard steady boundary-layer flow. Note that, in addition, they provide the data needed for the "in situ" calibration of the HFG, during the measurement of the wall shear stress.

Table 2.1

Measurement (Random) Errors

Quantity	Time-Mean	Amplitude	Phase (deg.)
U/U_e	0.005	0.005	0.8
$u^2/U_e^2 \times 10^3$	0.15	0.20	10
$v^2/U_e^2 \times 10^3$	0.11	0.16	9
$-uv/U_e^2 \times 10^3$	0.15	0.15	10
C_f	0.0001	0.0002	4

Table 2.2

Parameters for Steady Flow at $\overline{U}_e = 90$ cm/s

Station	x(cm)	δ_*(mm)	θ(mm)	H	C_f	δ(mm)	Π
1	48	1.785	1.003	1.780	0.004373	14.46	0.1011
2	69	2.141	1.359	1.575	0.004164	17.29	0.1621
3	90	2.879	2.012	1.431	0.003660	20.87	0.4027
4	142	4.465	3.285	1.359	0.003373	33.05	0.3975
5	203	5.217	3.895	1.339	0.003276	39.73	0.3769

LEGEND

ITEM NO.	DESCRIPTION
1	CONSTANT HEAD TANK
2	24" BUTTERFLY VALVE WITH ACTUATOR
3	DIFFUSER I
4	DIFFUSER II
5	DIFFUSER III
6	VANED ELBOW
7	CIRCULAR TO SQUARE TRANSITION
8	DISTANCE PIECE
9	ALUMINUM HONEYCOMB
10	SETTLING CHAMBER
11	THREE DIMENSIONAL CONTRACTION
12	TEST SECTION
13	DISTANCE PIECE
14	TRANSITION PIECE
15	SLOTTED CYLINDER
16	ROTATING SLEEVE
17	DISCHARGE ENCLOSURE
18	3 HP VARIABLE SPEED SCR DRIVE FOR SLEEVE

Figure 2.1. Lay-out of the water tunnel.

BC : BRAGG CELL
BS : BEAM SPLITTER
PR : POLARISATION ROTATOR
SM : STEERING MODULE
PD : PHOTO DIODE
PMT: PHOTO MULTIPLIER TUBE
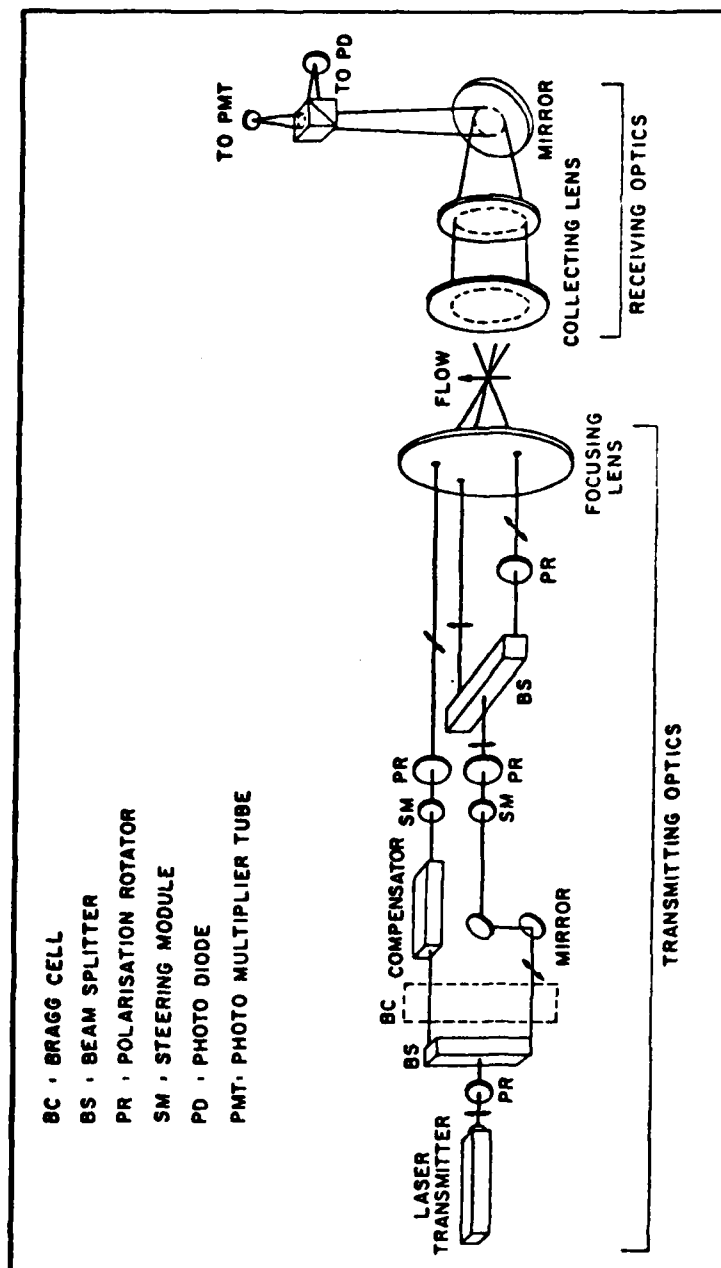
Figure 2.2.   Optical Arrangement of LDA
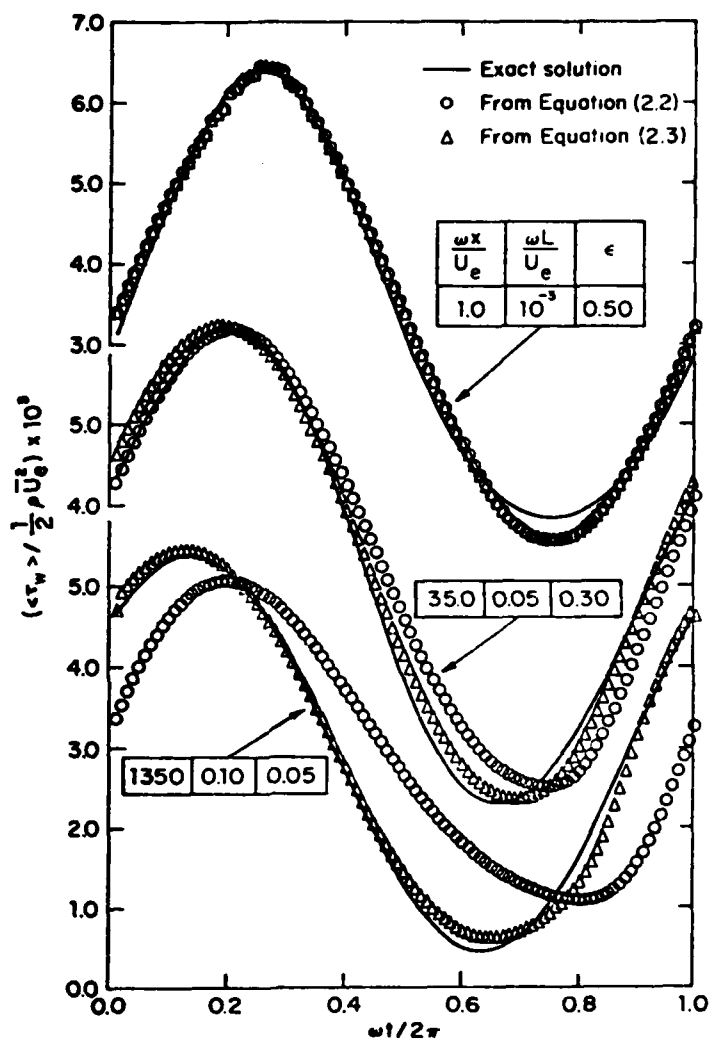
Figure 2.3. Calculation of the wall shear stress from the wall heat transfer in unsteady flow. L is the effective length of the heated element.
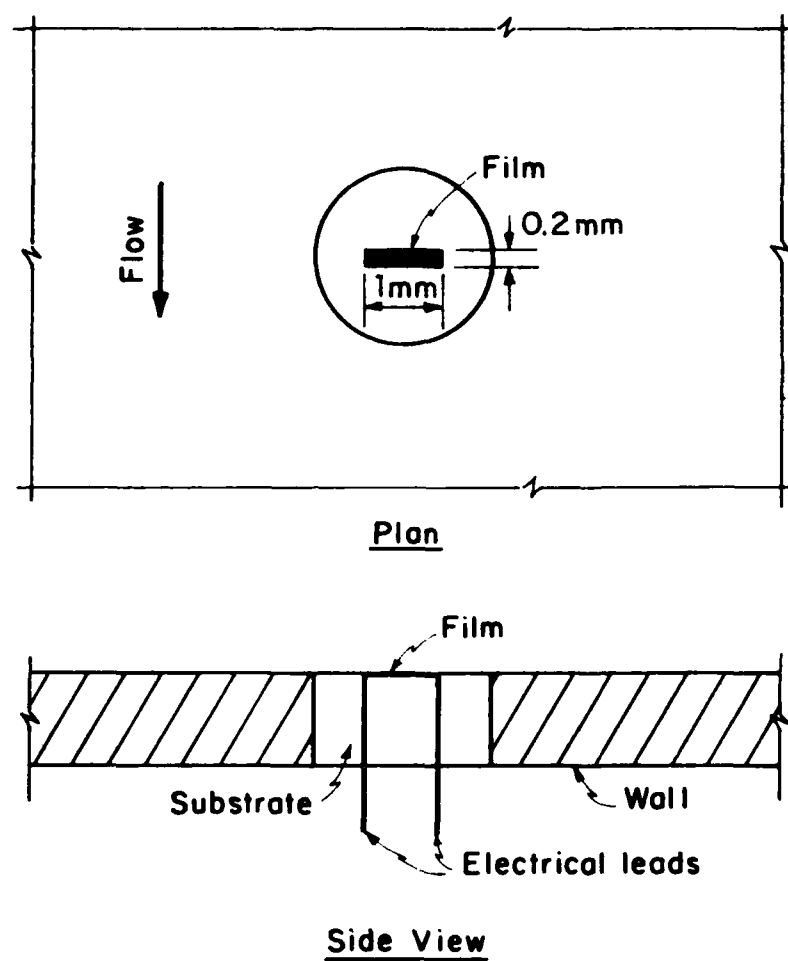
Figure 2.4. Sketch of the heat-flux gage (HFG).
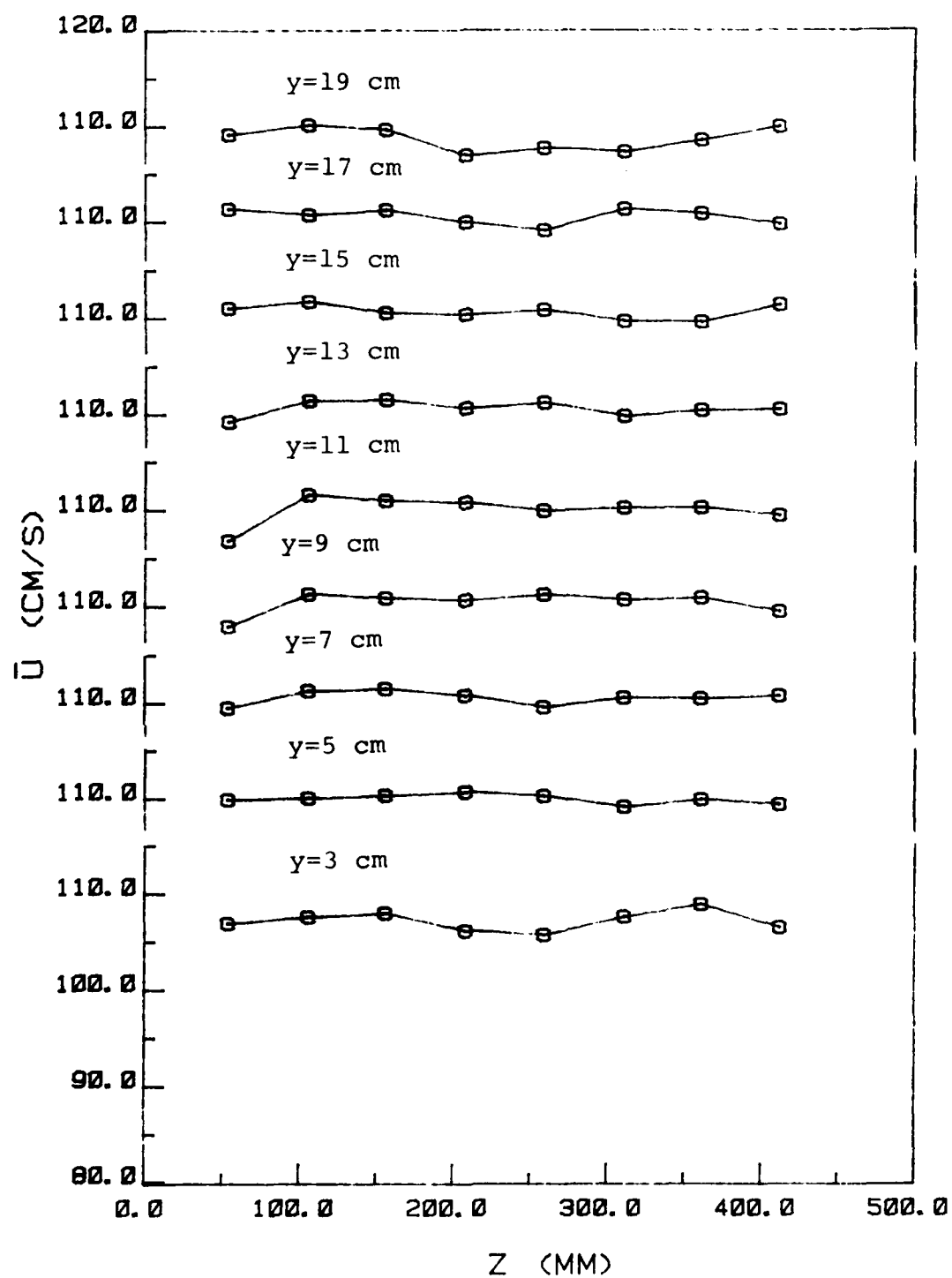
Figure 2.5.   Check of flow uniformity at x = 190 cm.
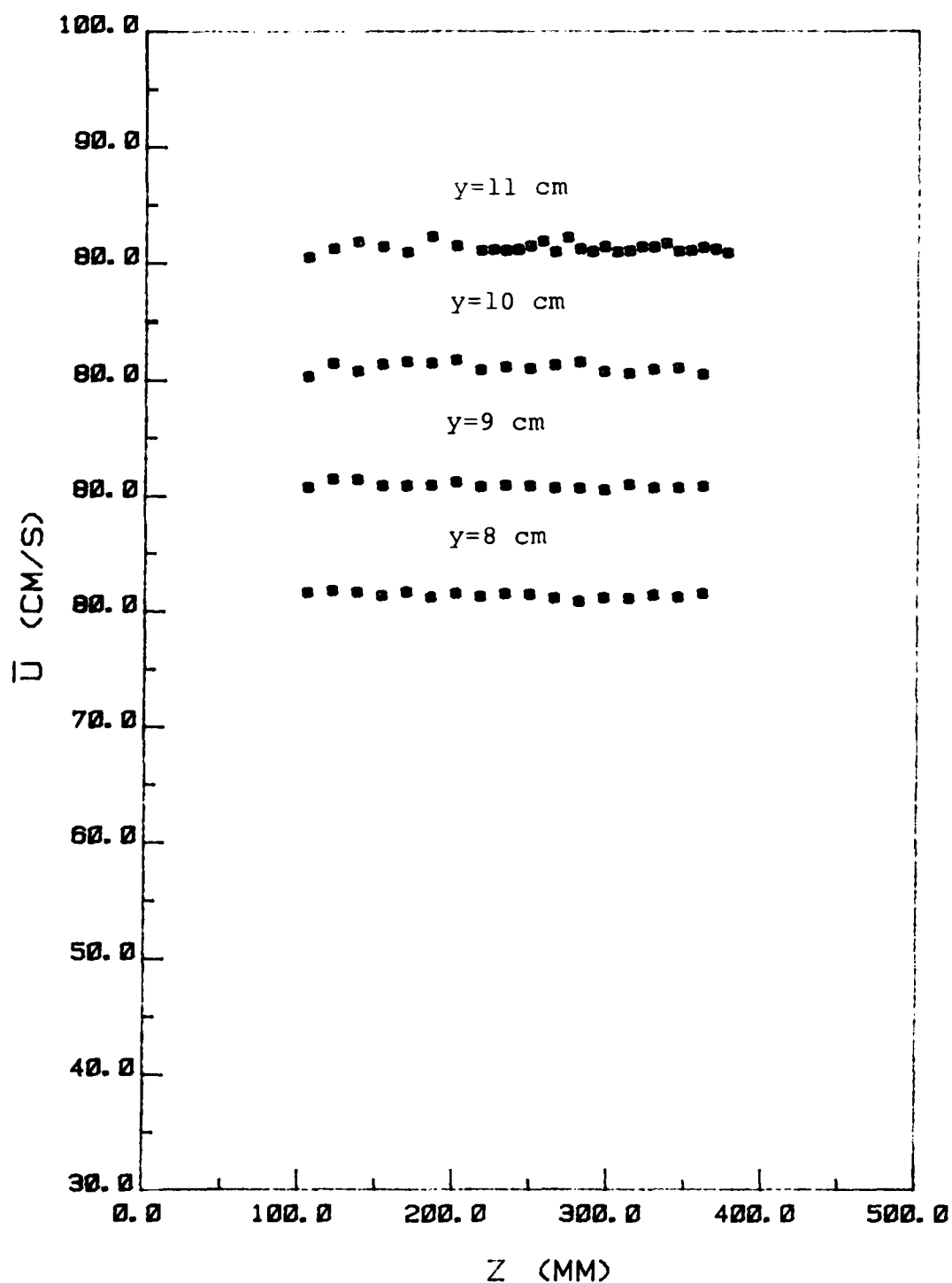
Figure 2.6. Check of two-dimensionality in the core region, x = 190 cm.
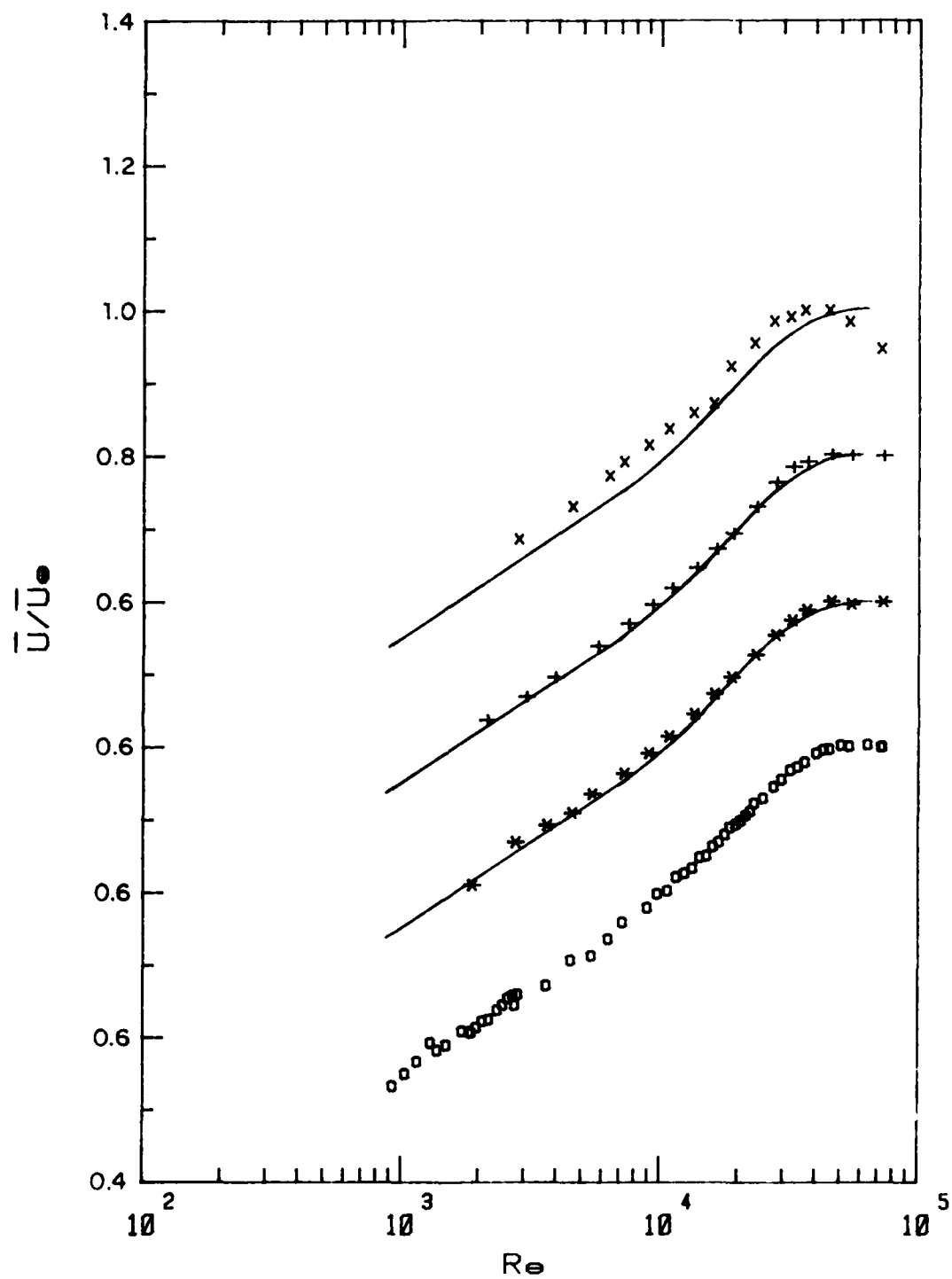
Figure 2.7.   Check of two-dimensionality for $\bar{U}$.   o , --- ,
              z = 18.9 cm; *, z = 16.2 cm; +, z = 13.6 cm;
              x, z = 8.3 cm.
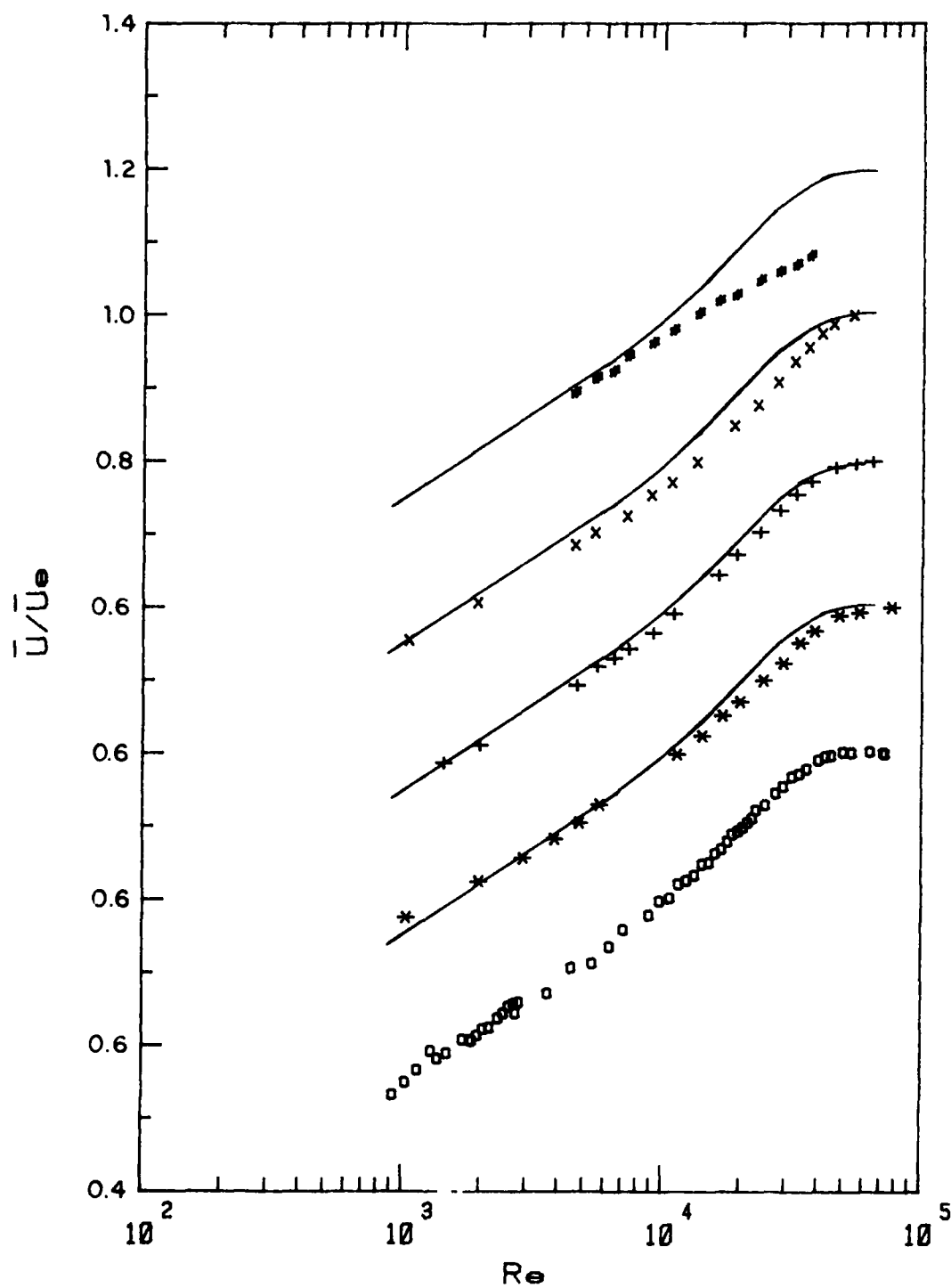
Figure 2.8.   Check of two-dimensionality for $\bar{U}$.   o , —— ,
z = 18.9 cm; *, z = 24.3 cm; +, z = 29.6 cm; x,
z = 34.9 cm; #, z = 40.2 cm.
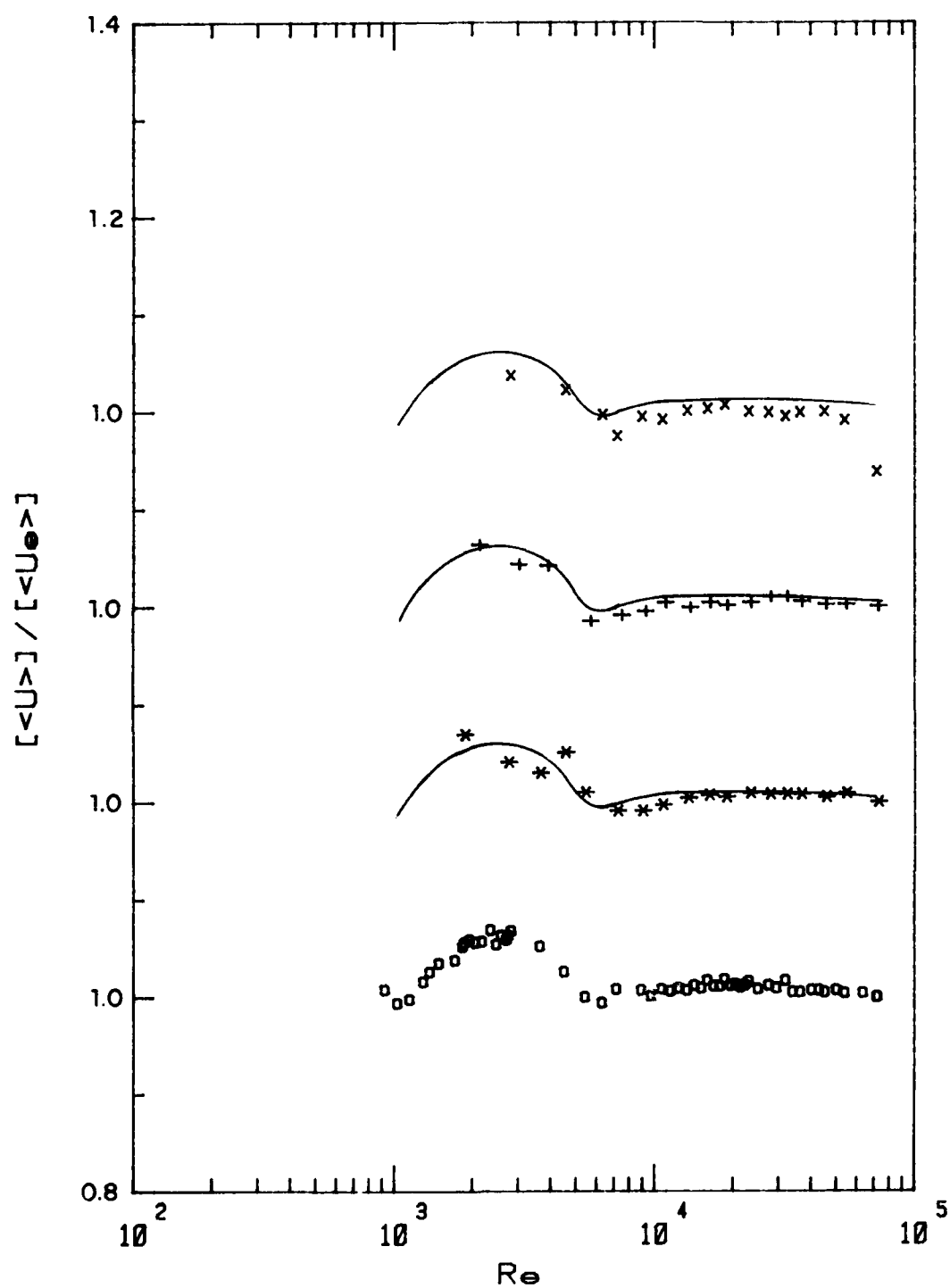
Figure 2.9.   Check of two-dimensionality for $[<U>]$.   Symbols as in Fig. 2.7.
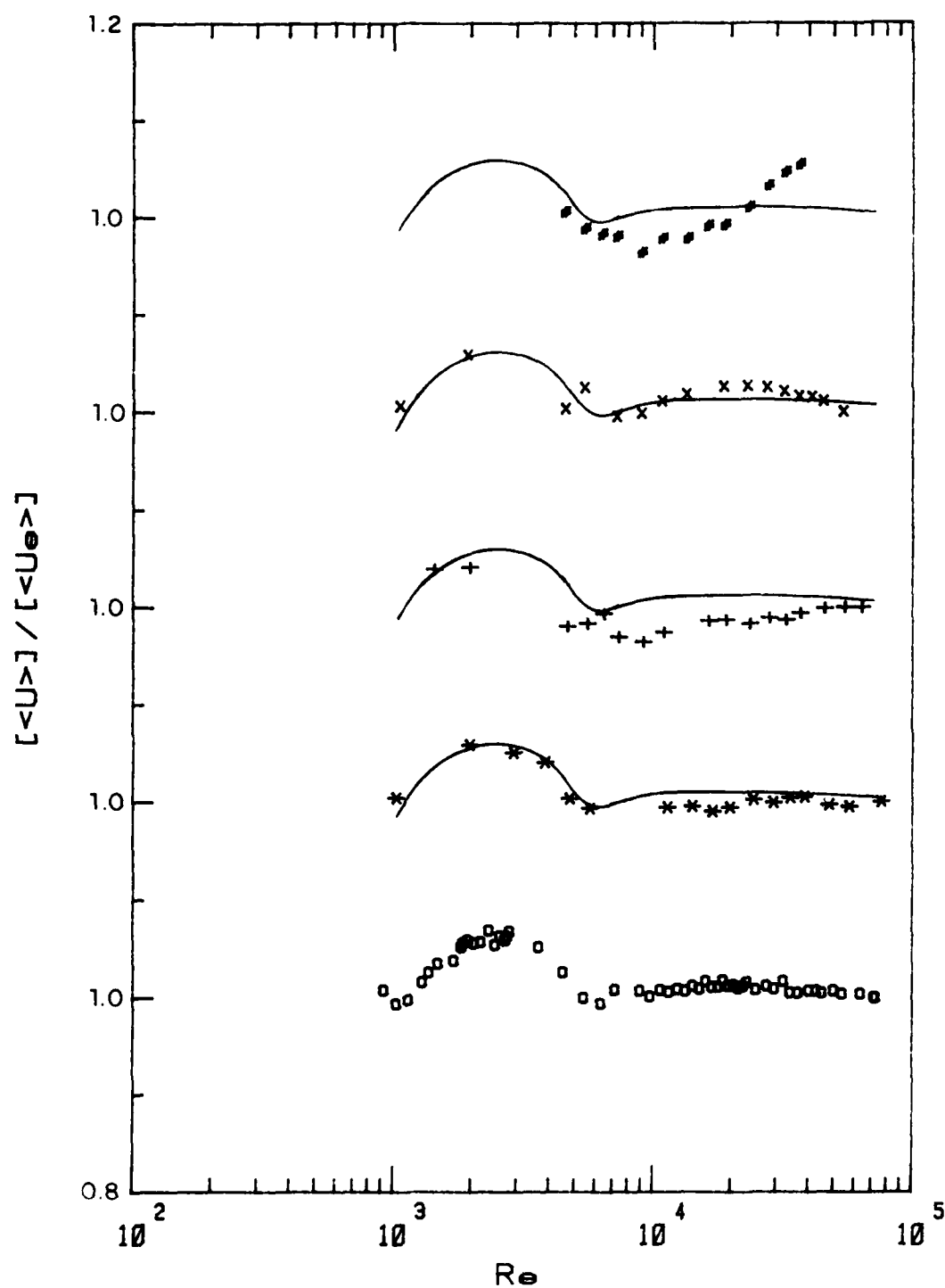
Figure 2.10. Check of two-dimensionality for [<U>]. Symbols as in Fig. 2.8.
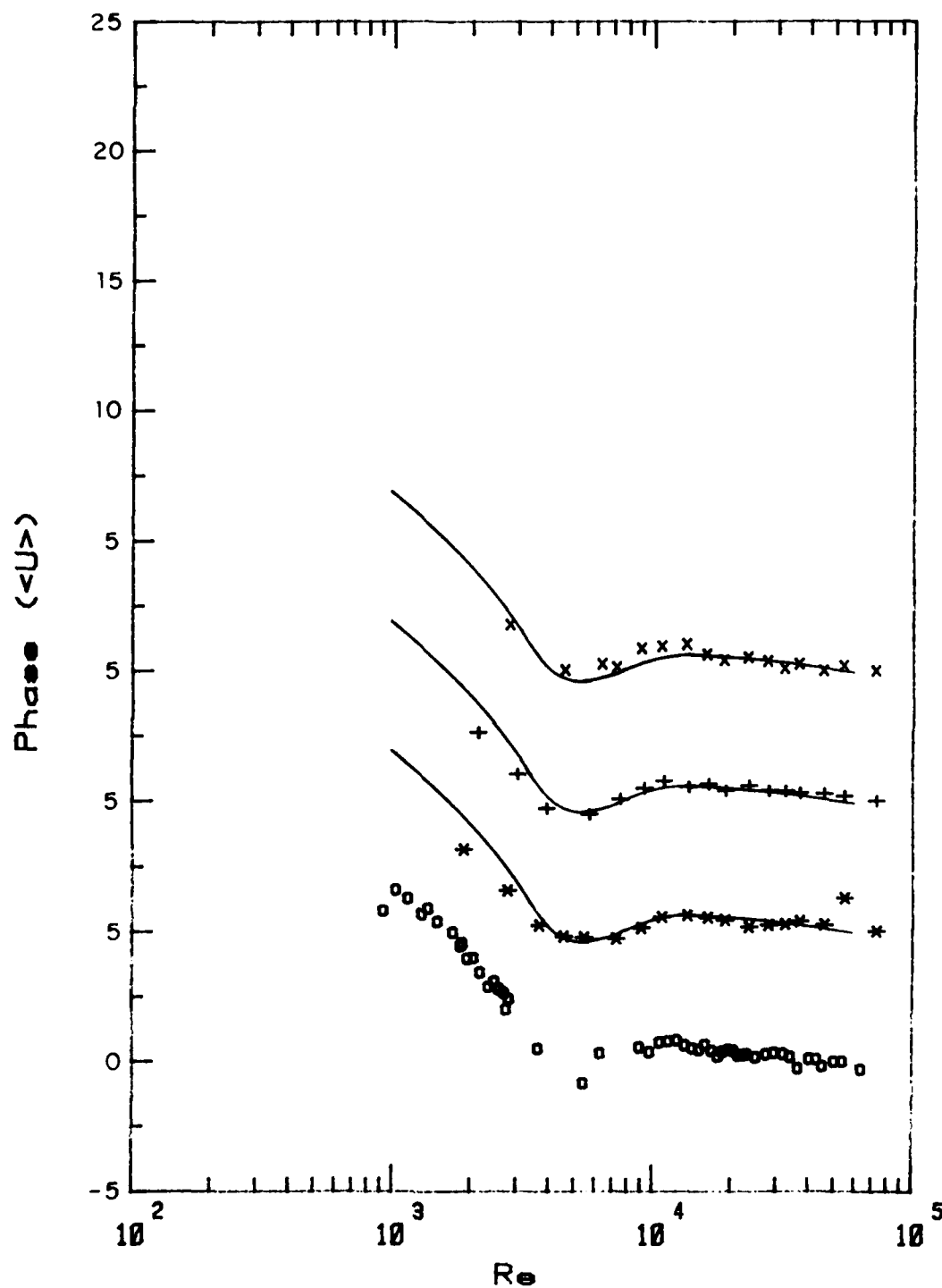
Figure 2.11. Check of two-dimensionality for the phase of
⟨U⟩. Symbols as in Fig. 2.7.
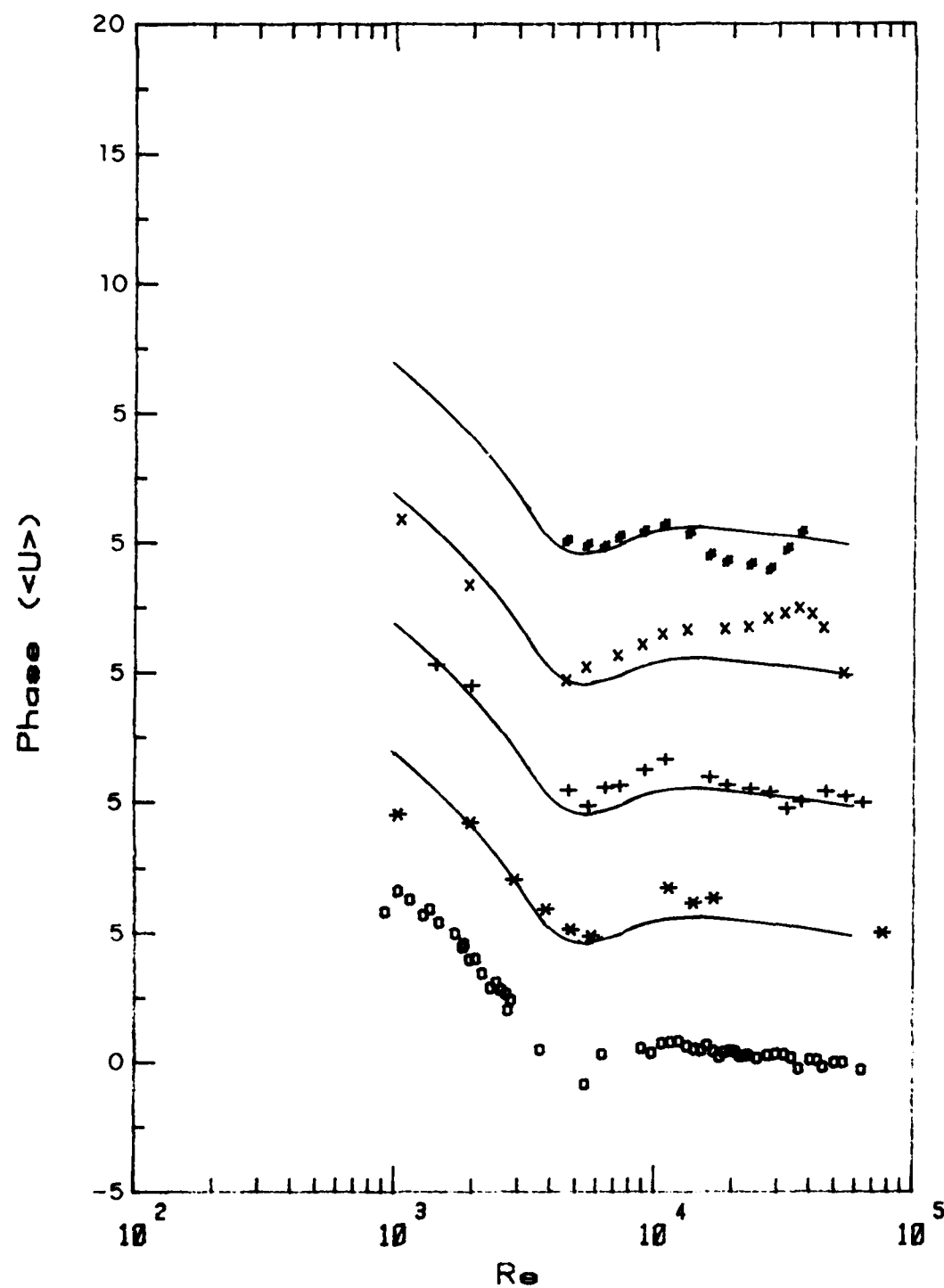
Figure 2.12.   Check of two-dimensionality for the phase of
‹U›.   Symbols as in Fig. 2.8.
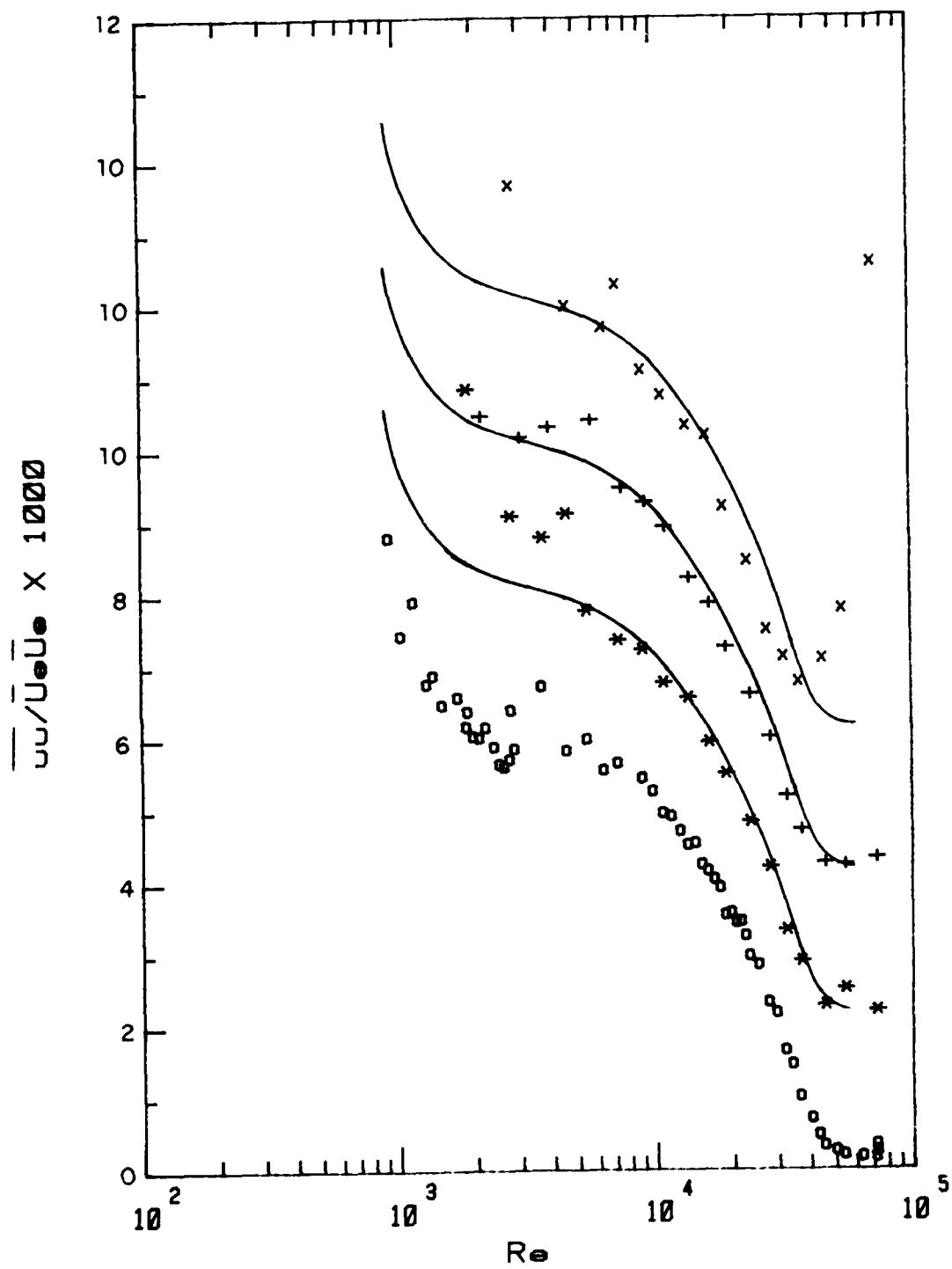
Figure 2.13. Check of two-dimensionality for u^2.
Symbols as in Fig. 2.7.
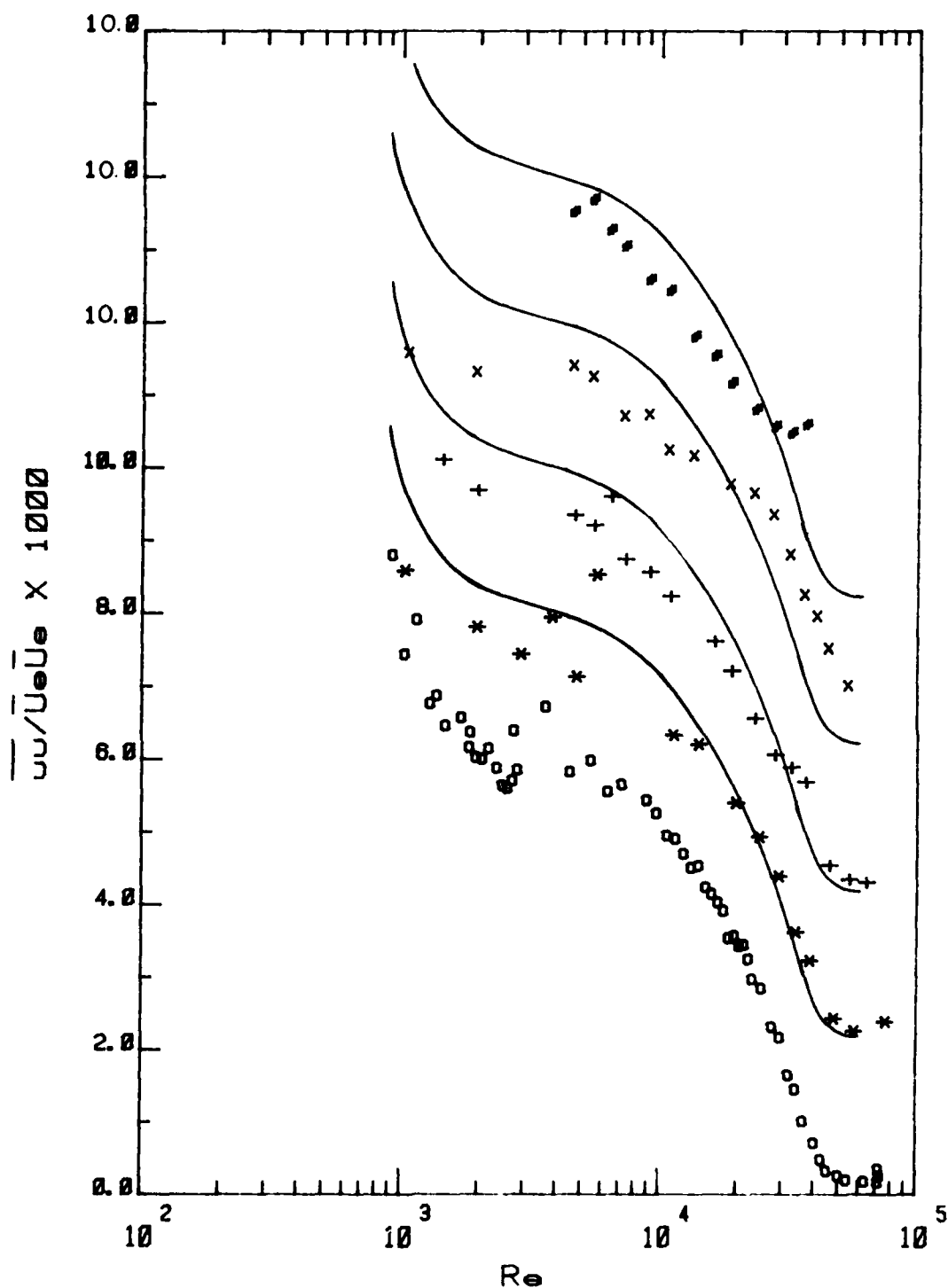
Figure 2.14.   Check of two-dimensionality for u^2.
Symbols as in Fig. 2.8.
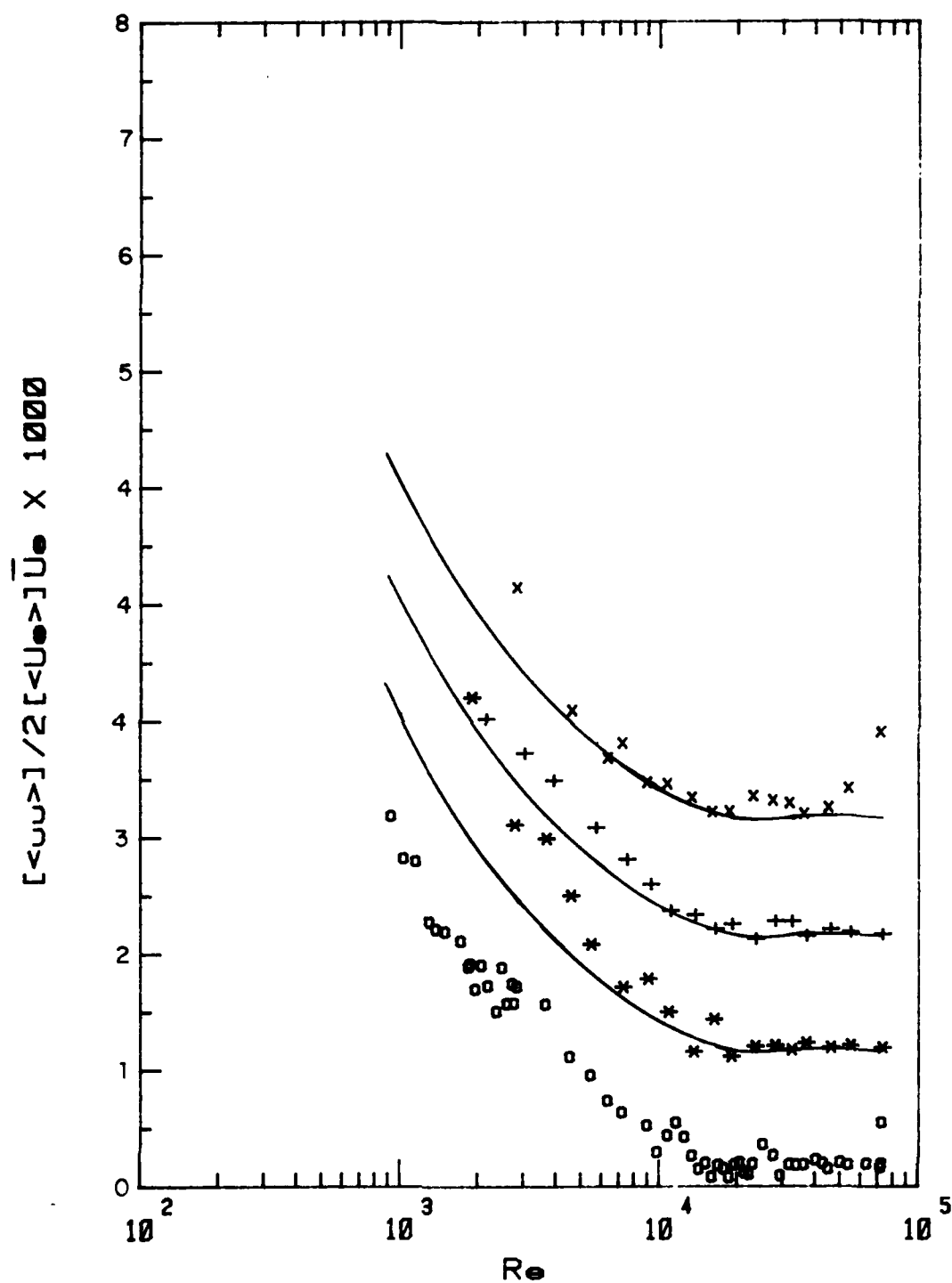
Figure 2.15.   Check of two-dimensionality for $[<u^2>]$.
Symbols as in Fig. 2.7.
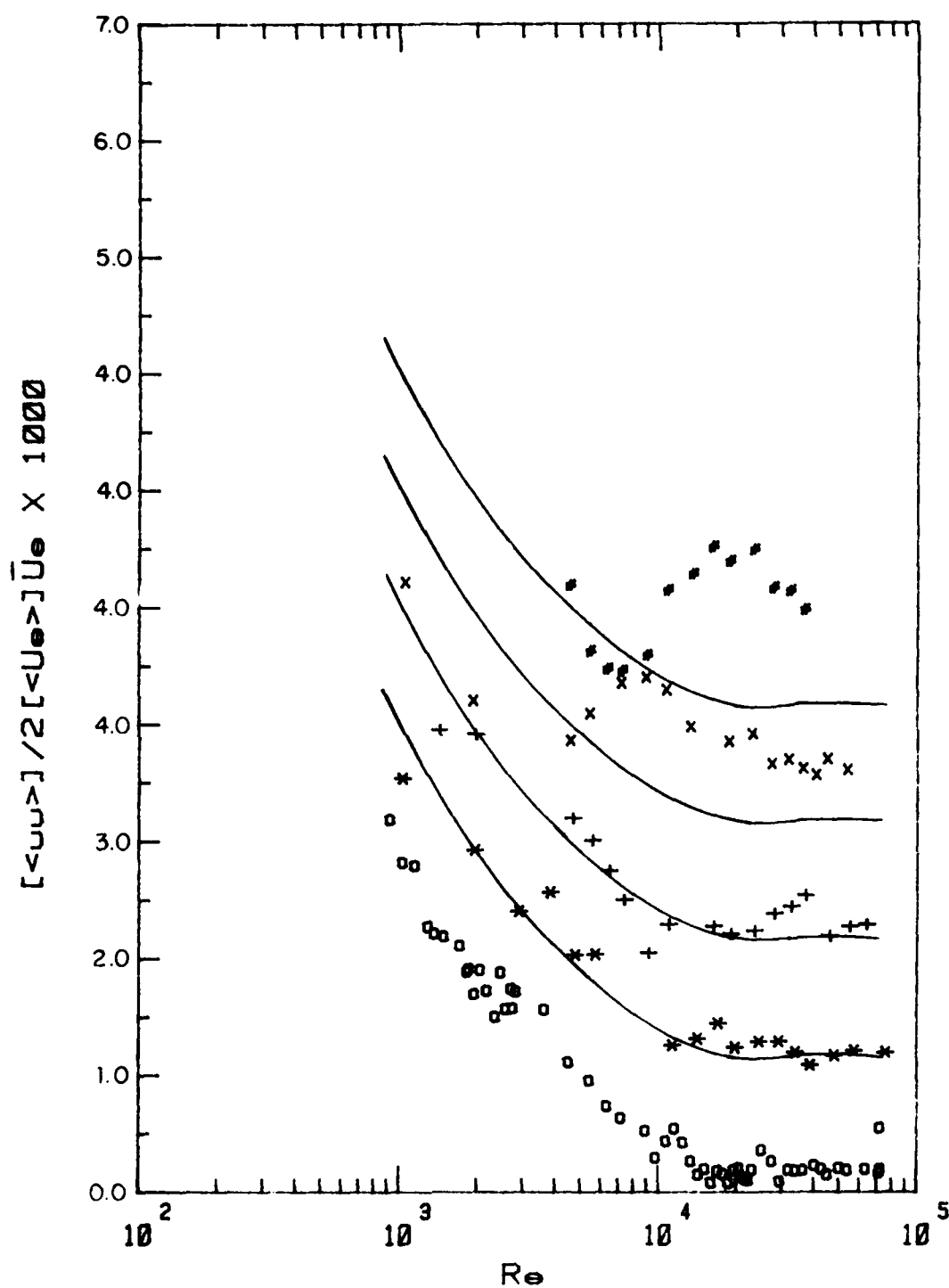
Figure 2.16. Check of two-dimensionality for $[<u^2>]$. Symbols as in Fig. 2.8.
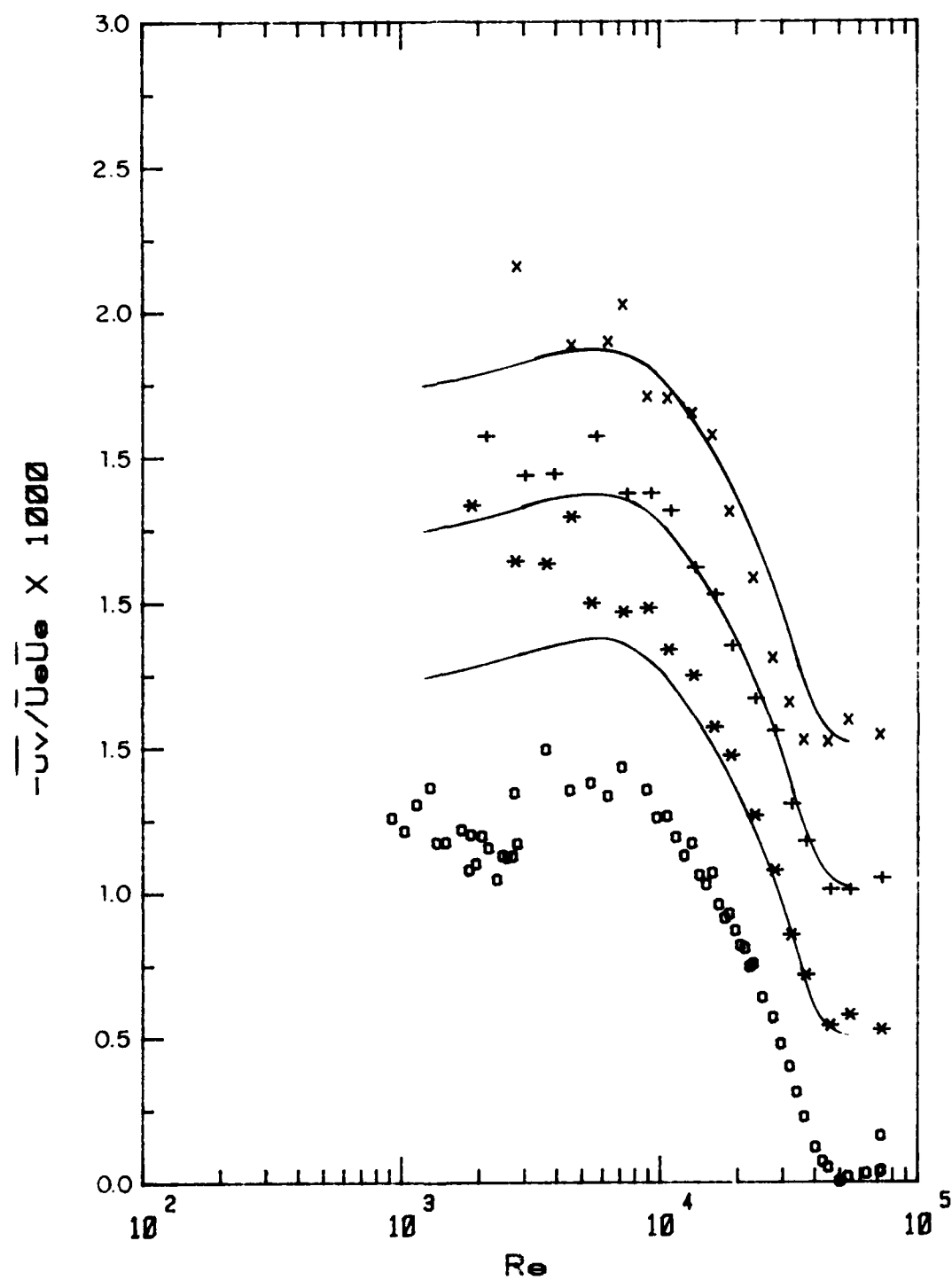
Figure 2.17. Check of two-dimensionality of - $\overline{uv}$. Symbols as in Fig. 2.7.
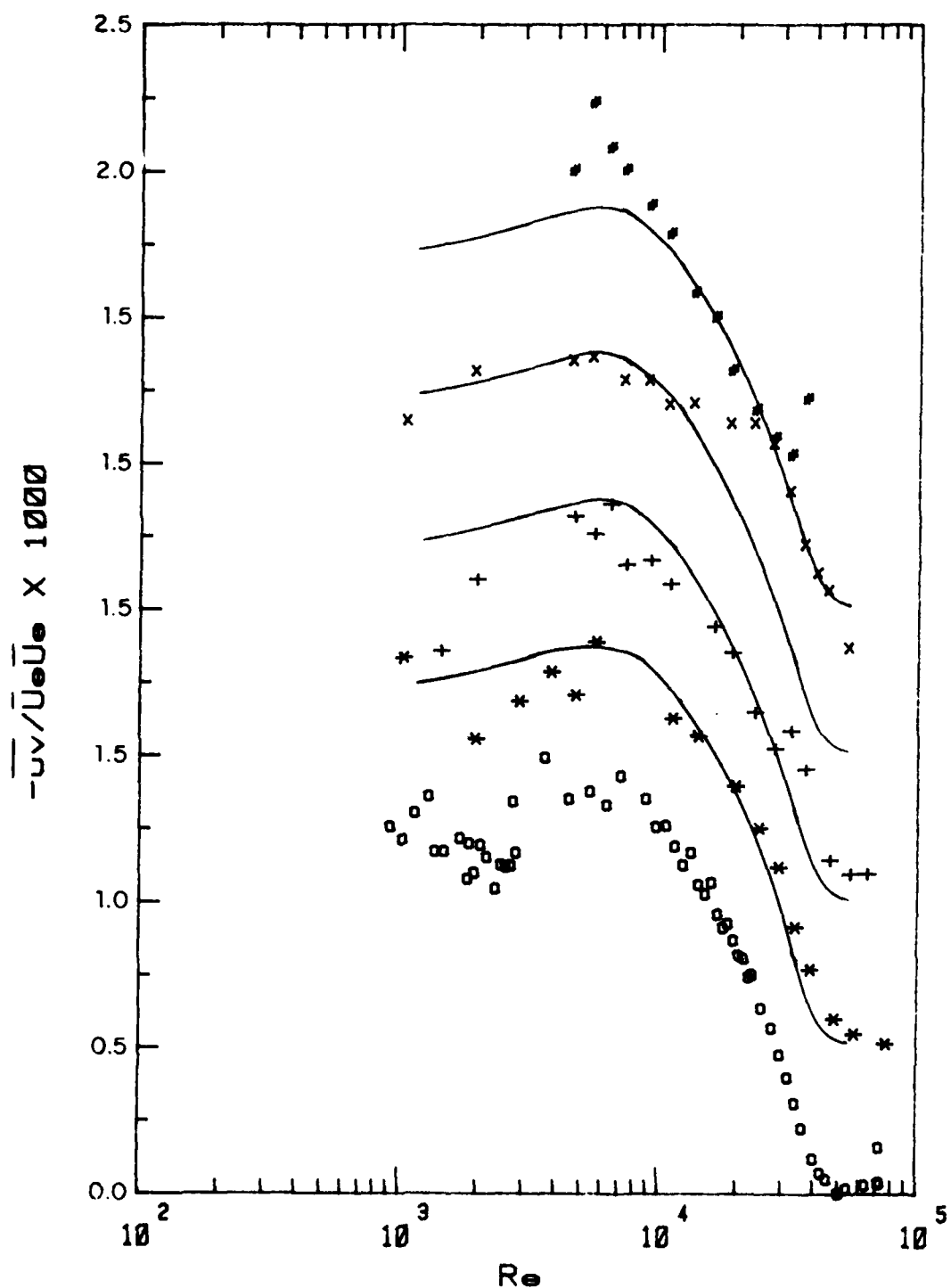
Figure 2.18. Check of two-dimensionality for - $\overline{uv}$. Symbols as in Fig. 2.8.
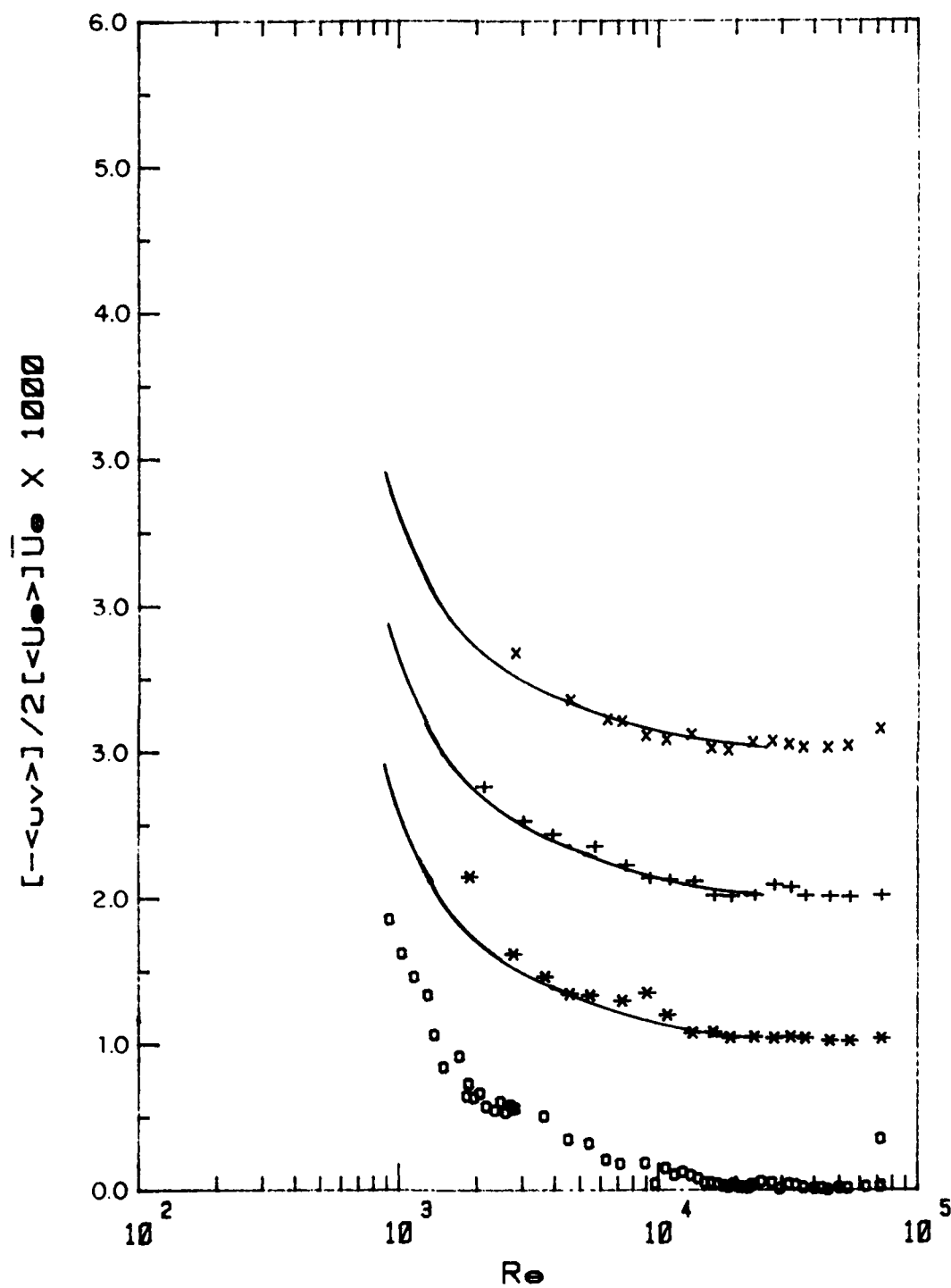
Figure 2.19.   Check of two-dimensionality for [-<uv>].
Symbols as in Fig. 2.7.

48
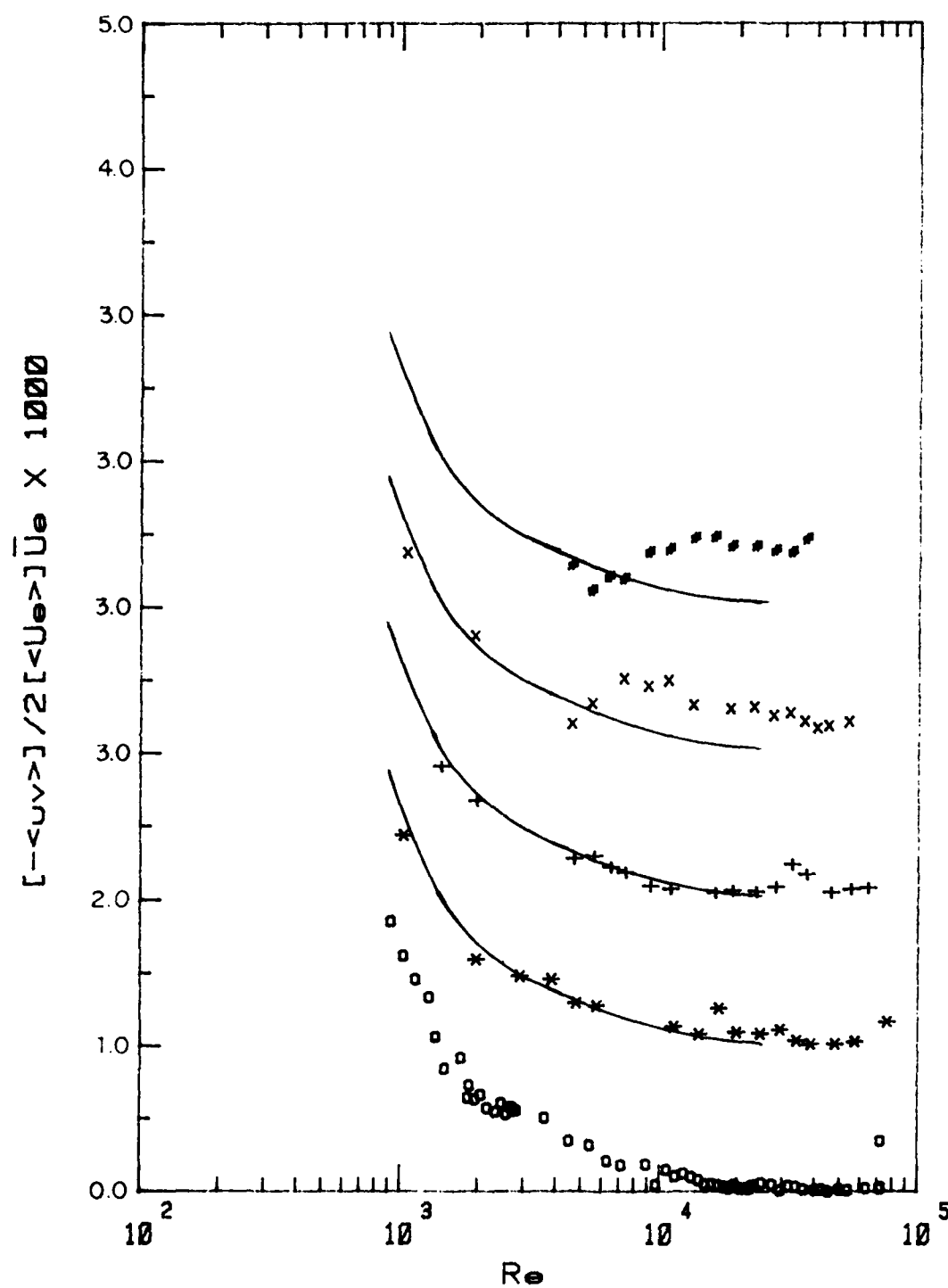
Figure 2.20.   Check of two-dimensionality for [-<uv>].
Symbols as in Fig. 2.8.
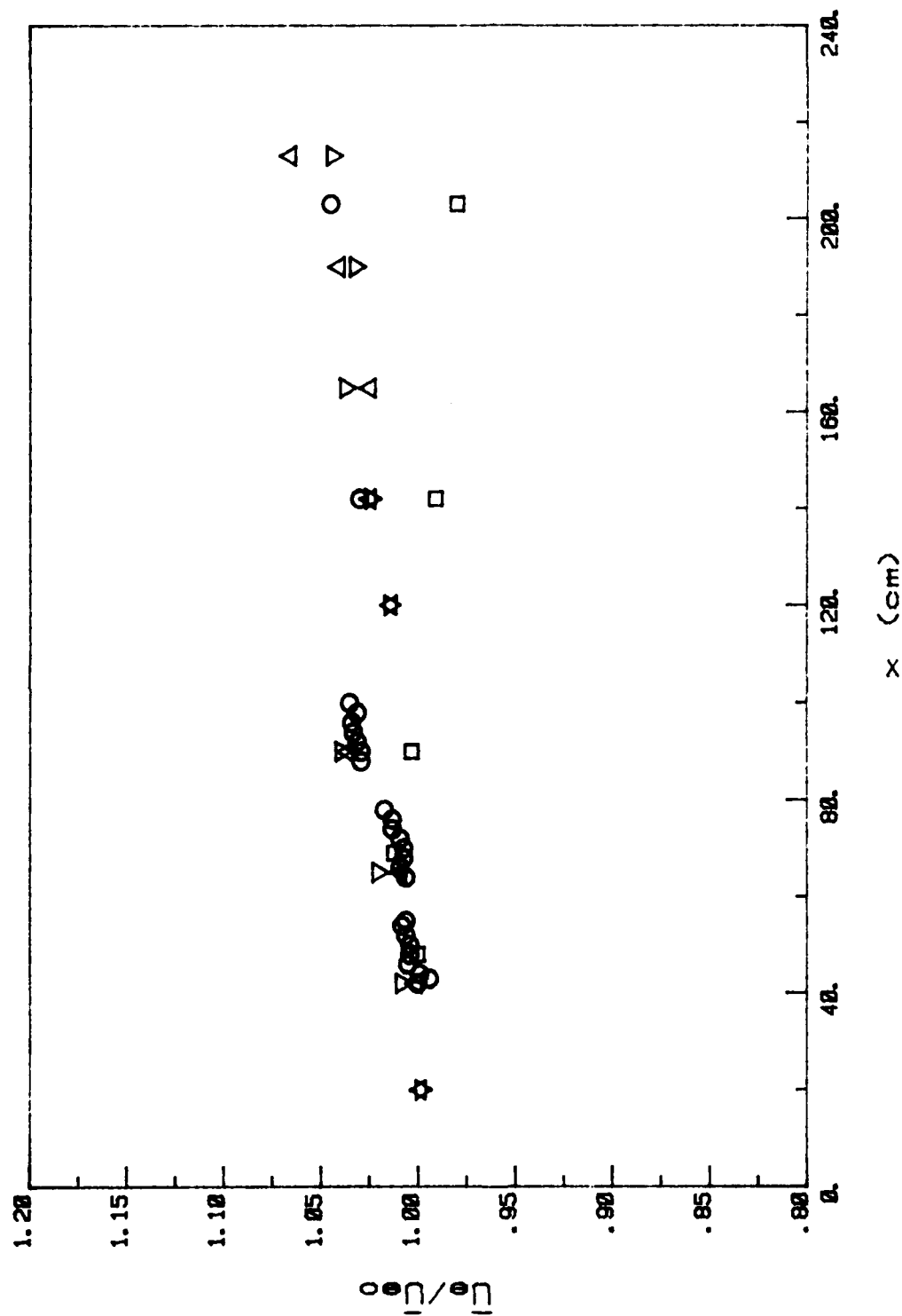
Figure 2.21. Longitudinal distribution of the time-mean free-stream velocity. △, ▽, steady flow; □, unsteady flow at 0.5 Hz; ○, unsteady flow at 2 Hz.

Figure 2.22. Longitudinal distribution of the free-stream amplitude of oscillation. Symbols as in Fig. 2.21.
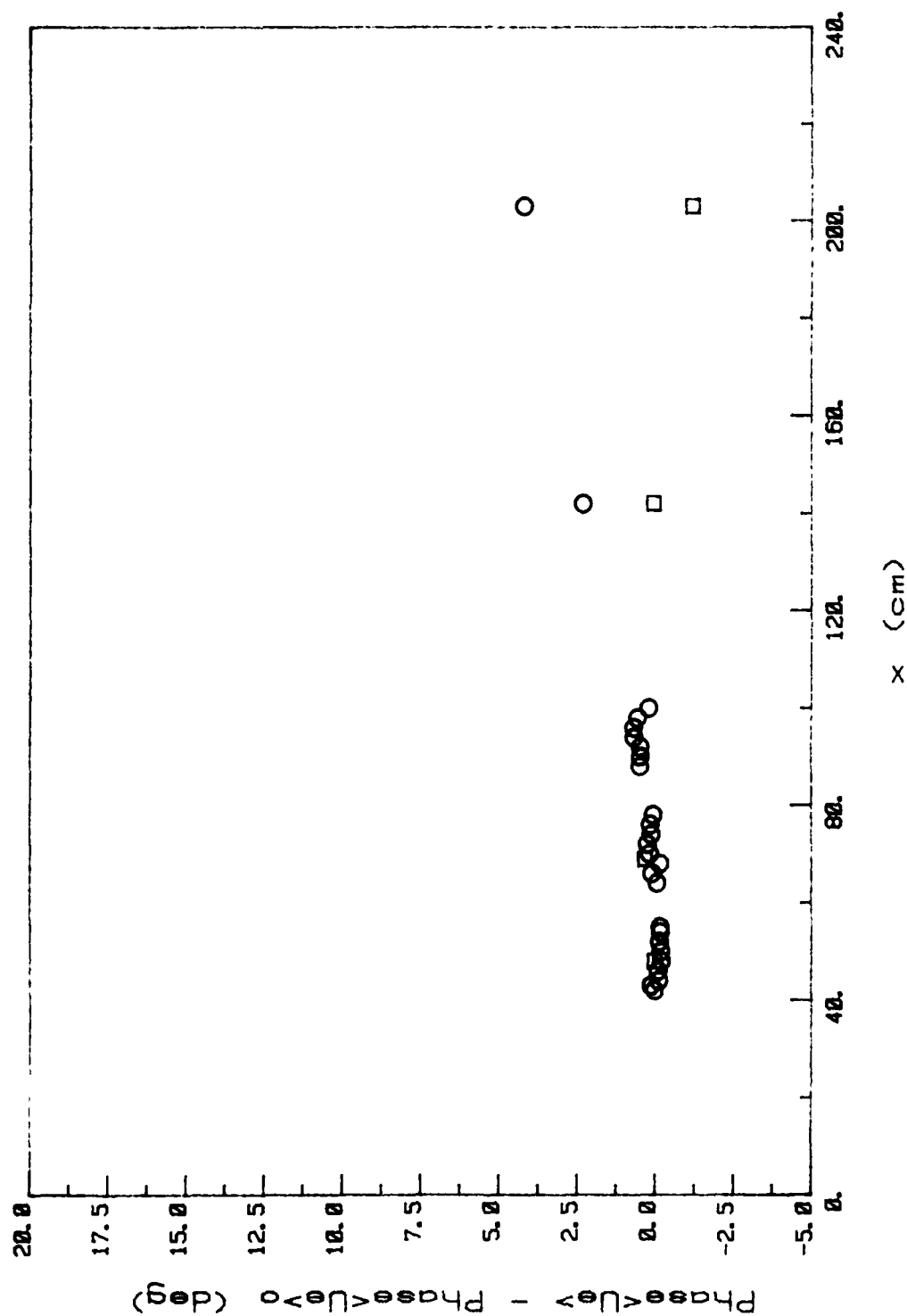
Figure 2.23. Longitudinal distribution of the free-stream phase of oscillation.
Symbols as in Fig. 2.21.
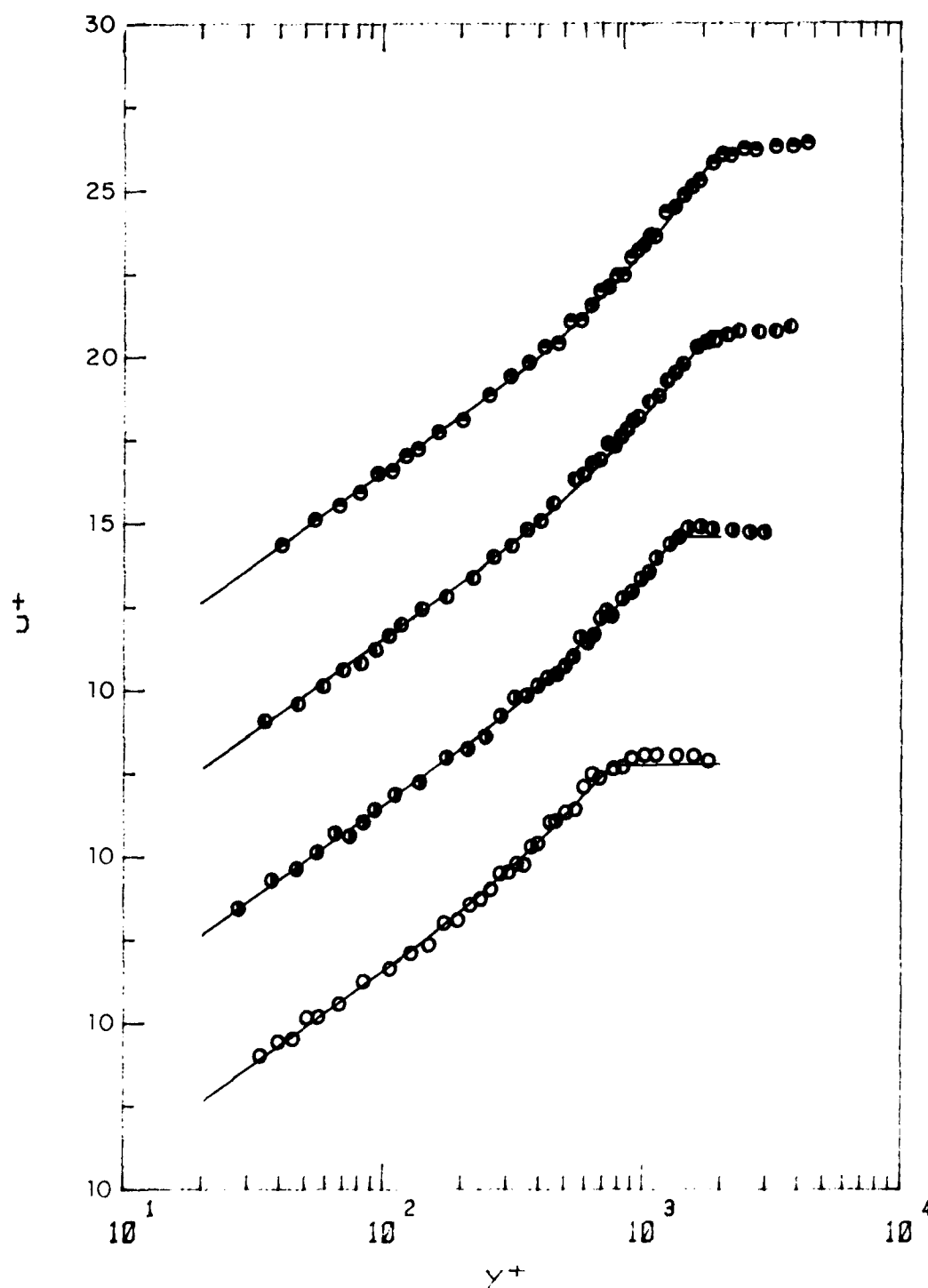
Figure 2.24. Steady velocity profiles at station 5 in the inner coordinates. 0, U_e = 50.69 cm/s; 0, U_e = 90.18 cm/s; 0, U_e = 119.74 cm/s; 0, U_e = 141.77 cm/s; —, Coles' fit.
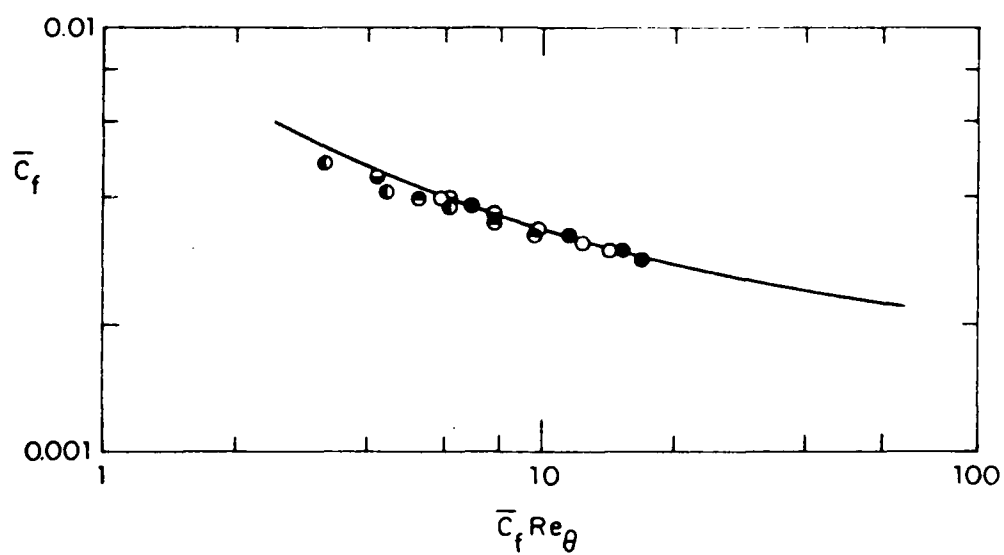
Figure 2.25. Correlation between $\bar{C}_f$ and Re_θ for steady flow. ◐, station 1; ◑, 2; ◒, 3; O, 4; ●, 5; —, 'normal' curve [Coles (1962)].
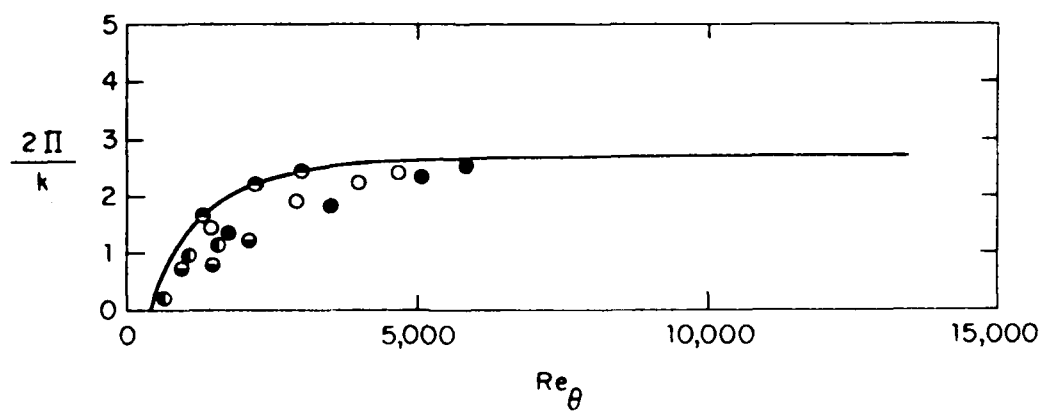
Figure 2.26. Correlation between τ and Re_θ for steady flow. Symbols as in Fig. 2.25.
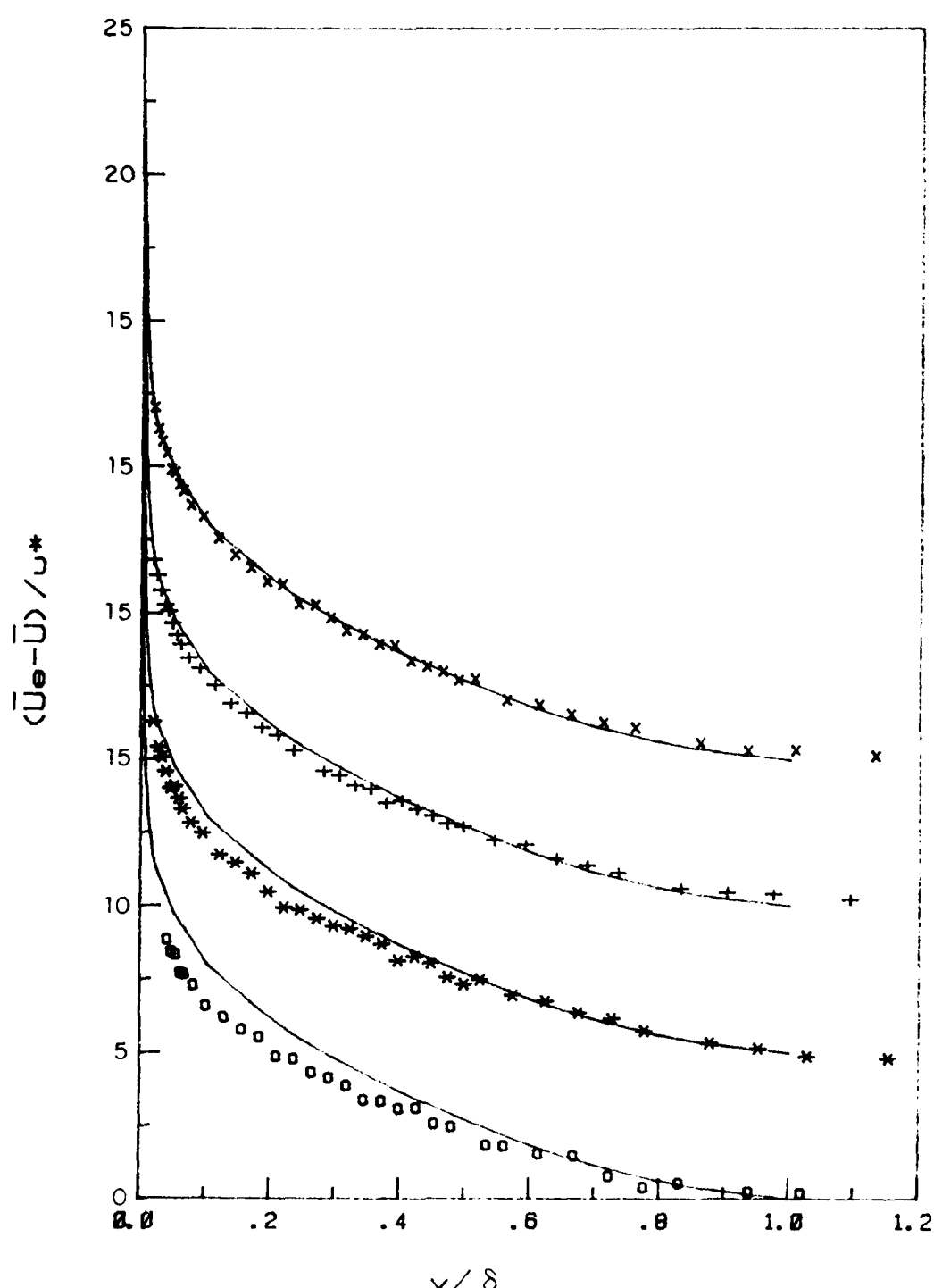
Figure 2.27. Steady velocity profiles at station 5 in the outer coordinates. $\circ$, $\bar{U}_e = 50.69$ cm/s; $*$, $\bar{U}_e = 90.18$ cm/s; $+$, $\bar{U}_e = 119.74$ cm/s; $\times$, $\bar{U}_e = 141.77$ cm/s; —, Klebanoff's data (1954).
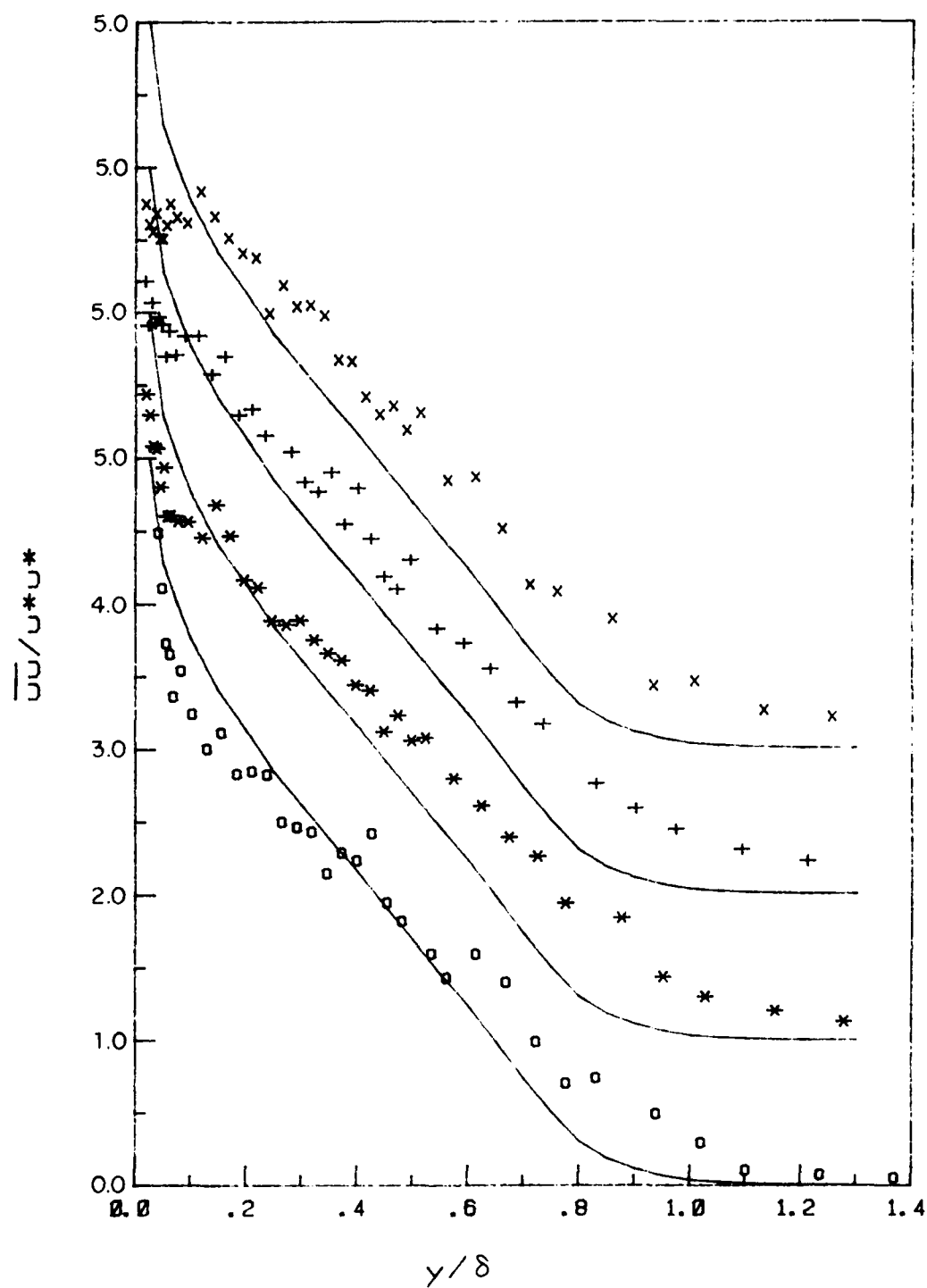
Figure 2.28. Steady-flow distribution for $\overline{u^2}$ at station 5.
Symbols as in Fig. 2.27.
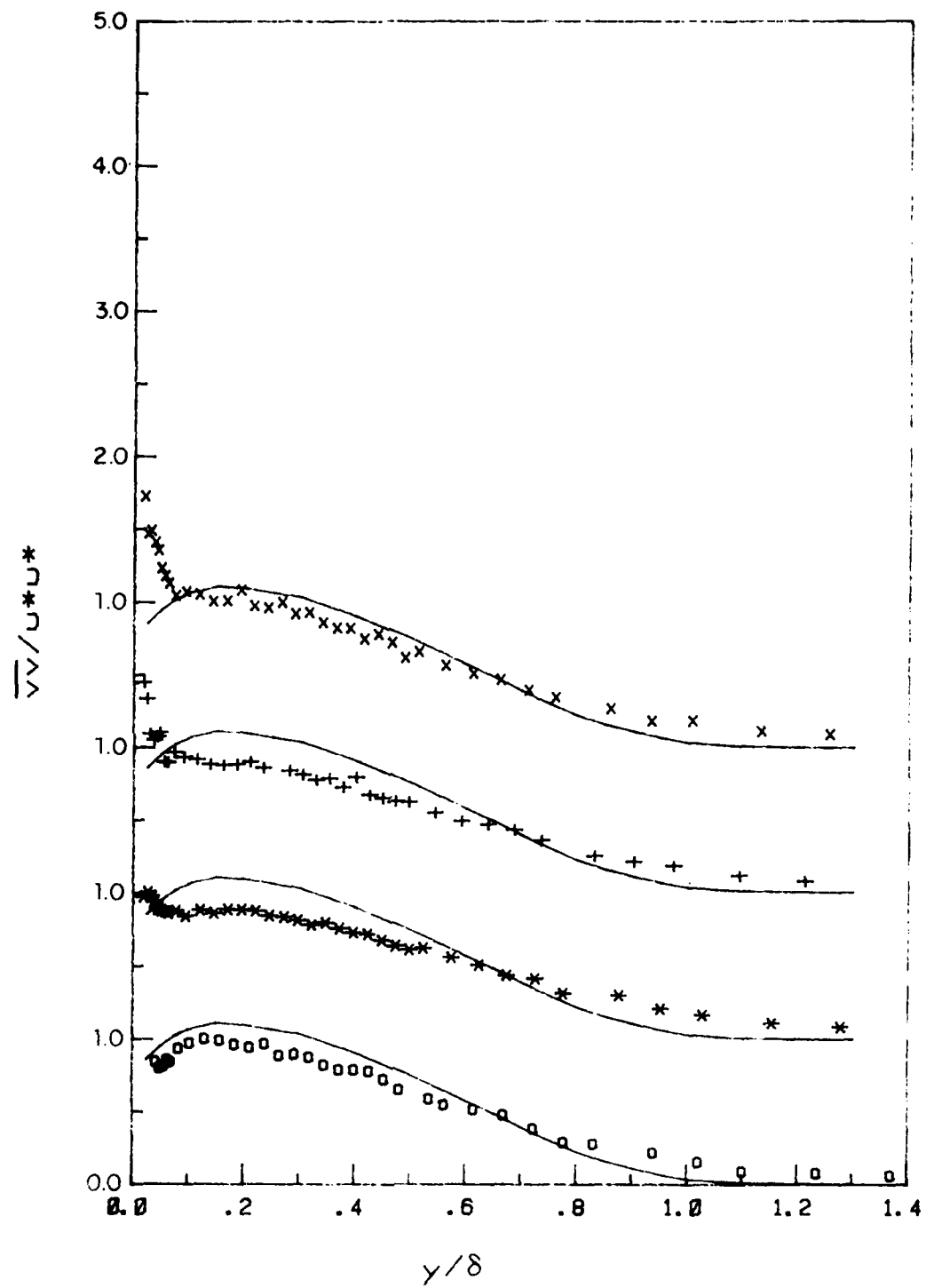
Figure 2.29. Steady-flow distribution for v^2 at station 5. Symbols as in Fig. 2.27.
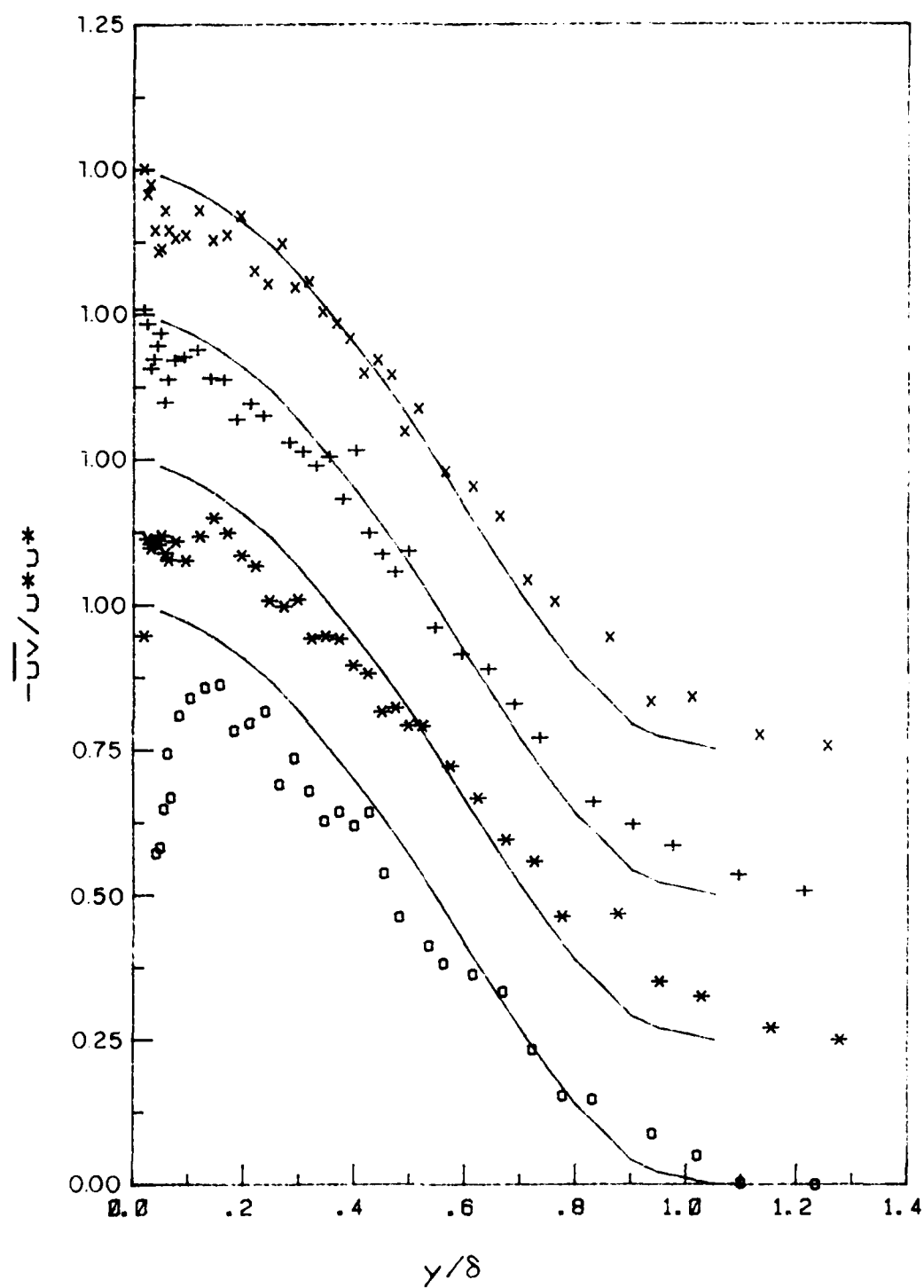
Figure 2.30.   Steady-flow distribution for - ūv at station 5.
Symbols as in Fig. 2.27.

CHAPTER 3

EXPERIMENTAL RESULTS

3.1. General

In this chapter, the main experimental results on unsteady boundary layers are presented and discussed. Emphasis is placed on the comparison among the steady, quasi-steady and unsteady flows. In the study of the oscillatory motion, the first harmonic of the Fourier decomposition of the flow quantities is analyzed in detail, and only a relatively short discussion is included on the behavior of the complete periodic flow.

It is pointed out that, in the interest of brevity, only typical results are presented here. As already mentioned, all the processed data for both steady and unsteady flows are stored on digital tape and are available to any interested reader.

3.2. Time-Mean Flow

The time-mean flow may be expected to differ from the steady flow at the time-mean Reynolds number due to the nonlinearity of the problem. This nonlinear behavior arises, mathematically speaking, from the nonlinearity of the Navier-Stokes equations. However, at the amplitude of oscillation studied in the present experiments, nonlinear effects are found to be practically insignificant, in agreement with previous investigations.

3.2.1. Velocity and Wall Shear Stress

The time-mean velocity for stations 5 and 1 are shown, respectively, in Figs. 3.1 and 3.2 for both forcing frequencies, together with the corresponding quasi-steady (zero-frequency) velocity distribution for the same amplitude of oscillation. The latter distributions were obtained for each station by averaging over the steady distributions corresponding to the complete range of free-stream velocities included in the oscillation [i.e., from $(1-\varepsilon) U_0$ to $(1-\varepsilon) U_0$]. These steady velocity distributions were represented by Coles' profiles [Eq. (2.7)], whose parameters were related to the free-stream velocity by means of relations $u_*(U_e)$, $\Pi(U_e)$ and $\delta(U_e)$ deduced from the present steady flow measurements. The quasi-steady distributions so obtained were found practically to coincide with the corresponding steady-flow velocity profiles at the time-mean free-stream velocity. This confirms that nonlinear effects on the velocity are not significant. On the other hand, the time-mean velocity distributions for both frequencies of oscillation, while being very similar to each other, are seen to differ from the steady-flow distributions. This difference between the steady and unsteady flow velocities is in disagreement with previous experimental results, and has to be explained. A first insight into the nature of this problem is provided by the analysis of the behavior of the parameters Re_θ, H and C_f.

Figures 3.3 and 3.4 present the evolution of Re_θ and H with Re_x for the steady flow at the time-mean velocity and the time-mean unsteady flows. They show, as expected, the same trends as the

velocity profiles. The values of the parameters corresponding to the two unsteady experiments are practically equal to each other, and they differ from the ones for the steady flow. This difference tends to disappear when moving downstream. This seems to indicate that there is a 'Reynolds number effect', which vanishes asymptotically for large Reynolds numbers, i.e., when the flow is completely developed. The results for the time-mean wall shear stress are shown in Fig. 3.5. It seems that the time-mean unsteady value for the smaller frequency is slightly larger than for the higher frequency, and very close to the wall shear stress for the steady flow at the time-mean free-stream velocity. This latter value, in turn, is always smaller than the quasi-steady value. Thus, the trend seems to be a slight decrease in time-mean wall shear stress with the frequency. It is interesting to note that this is opposite to the trend observed by Ramaprian and Tu (1982) in pipe flow. In any case, the magnitude of the decrease is too small to be quantified from the present measurements, which have an uncertainty of ± 1%.

From the experimental results shown, it is obvious that the outer and inner layers are responding quite differently to the imposed oscillation. On the one hand, the inner flow (whose behavior is illustrated by that of C_f) does not seem to be very much affected. On the other hand, the outer flow (whose response is characterized by those of Re_θ and H) is significantly changed by unsteadiness, though the differences tend to disappear for large Re_x. This mismatch is well illustrated in Fig. 3.6, where the relation between C_f and Re_θ for the unsteady flow experiments is

compared with the experimental data reviewed by Coles (1962). It is seen that they do not follow the "normal" law for a standard steady turbulent boundary layer, except for the largest Re_θ values.

In order to understand the details of behavior of the outer and inner flow in the unsteady flow regime, it is necessary to analyze the complete velocity profile. Figures 3.7 and 3.8 present the velocity distributions in the inner coordinates for the five stations and the two frequencies. The measured value of the time-mean shear velocity is used as the scaling velocity. Lines representing the universal logarithmic law ($u^+ = 5.5 \log y^+ + 5.5$) and the quasi-steady velocity distribution are also shown. It is observed that the time-mean unsteady velocity profiles do not follow the universal law, except asymptotically at large Reynolds numbers (i.e., at the more downstream stations). However, they show a logarithmic region, but with a slightly different slope and a significantly different additive constant.

In fact, these time-mean distributions, like their steady counterparts, also belong to the Coles family of velocity profiles [see Eq. (2.7)]. The corresponding parameters (C_f, δ and π), for each flow and each station, are presented in Table 3.1, together with the ones for the steady flow at the time-mean velocity, as a reference. Note that, in the case of the unsteady flows, the physical interpretation of Coles' parameters is not obvious except for δ, which can be considered as the boundary layer thickness for the time-mean flow. It is this quantity that is used in Figs. 3.9 and 3.10 to present the velocity-defect distribution in the outer

coordinates. Also shown are the quasi-steady profiles and a line representing Klebanoff's data (1954), considered to be the standard distribution for steady flow at large Reynolds numbers. It is seen that both the unsteady and quasi-steady distributions approach Klebanoff's profile for large Re_x, the unsteady profiles doing so faster, though nonmonotonically. In any case, the approach is from 'below', showing that there is development of the wake component in the downstream direction.

It is interesting to go back and study the significance of Coles' parameters for the time-mean velocity profile in unsteady flow. The values of the parameter C_f are also shown in Fig. 3.5. It is observed that, except at the last stations, they do not correspond to the correct value of the time-mean wall shear stress (unlike in steady flow). However, when plotted in the Coles-plot of C_f vs. $C_f Re_\theta$ (see Fig. 3.6), they fall on the 'normal' line. Hence, they can be interpreted as the skin friction coefficient for a 'normal' steady turbulent boundary layer at the given Re_θ. As for Π, it can still be regarded as a measure of the strength of the wake component relative to the logarithmic region. Its variation with Re_θ is presented in Fig. 3.11. Comparison with Fig. 2.26 shows that the distribution is 'normal' by the present standards.

These last results demonstrate that, in the unsteady boundary layer, the mean _outer_ flow can be considered to be the same as that in a 'normal' steady boundary layer at the same Re_θ. From this point of view, the observed difference between the velocity distributions at a given location, in steady and unsteady flows, can be interpreted

as being due to a relative shift in the virtual origins for the two cases. This is also strongly suggested by Fig. 3.3, from which one can obtain, by extrapolation, the approximate position, x_V, of the virtual origin. It is found that $x_V \simeq 7$ cm for the steady flow and $x_V \simeq -75$ cm for both the time-mean unsteady flows. Hence, the effect of the imposed oscillation on the outer flow is to promote a rapid development towards its asymptotic structure. Note that the response seems to be quantitatively similar for both frequencies. However, from Table 3.1 or Fig. 3.11 it is observed that Π actually varies significantly from one frequency to the other at a given station. Since both the unsteady profiles have similar values of Re_θ at all stations, this difference must be due to the effect of unsteadiness. We shall call it the "frequency effect". It is plausible (and consistent with other results, as shown in the next section) to assume that frequency effects manifest themselves as an increase in Π. Hence, they seem to be important at the last station for $f = 0.5$ Hz and at the first three stations for $f = 2$ Hz.

In conclusion, it can be said that the imposed oscillation acts very differently on the inner and outer layers. The inner flow responds rather weakly. The outer flow, on the other hand, is strongly affected. The changes in the outer flow can be interpreted, in general, as a combination of rather strong Reynolds number effects, which are due to shift of the virtual origin of the turbulent boundary layer, and relatively mild frequency effects which increase the wake-component strength. The former are almost independent of frequency and decrease in the downstream direction,

i.e., with increasing length Reynolds numbers. It is seen that the main differences, between the time-mean velocity distribution and that for steady flow at the time-mean free-stream velocity observed in the present experiments, is due to their different 'history'. In the limit of large Reynolds number, they nearly coincide with each other (in agreement with previous experimental results), except for small residual effects which depend on the oscillatory frequency. Some correlation (though not an explanation) will be found for these frequency effects later in this work (see chapter 5).

3.2.2. Turbulence Properties

The distributions of the mean-square longitudinal turbulent intensity, $\overline{u^2}$, for the five stations and for both the frequencies, are presented in Figs. 3.12 to 3.16 in the outer coordinates. Also shown are the corresponding distributions in steady flow at the time-mean velocity, and the data of Klebanoff (1954), considered to be the asymptotic limit for large Reynolds numbers. It is, in fact, seen that this limit is slowly but continuously approached by the present steady-flow data for increasing values of Re_x.

The behavior of the distributions in the unsteady flows is rather interesting when compared with the steady flow. In fact, trends not previously observed can be clearly distinguished. First, it is to be noted that, at large Reynolds numbers, the steady-flow profiles are not very sensitive to Reynolds-number variations. This is related to the above-mentioned insensitivity to nonlinear effects, and can be checked by comparing the distributions for stations 3, 4,

and 5, which are very similar to each other. Significant changes occur, however, for stations 1 and 2, where Re_θ is relatively small. Hence, for these stations an additional line is drawn, corresponding to the distribution in steady flow at station 3. This may be used as the reference steady-flow distribution for a value of Re_θ similar to those for the unsteady-flow profiles at those stations. The difference between this reference distribution and the actual steady-flow profile is a Reynolds number effect. In turn, any departure of the unsteady-flow distribution from the reference profile has to be considered as a frequency effect. It is observed, from the figures, that frequency effects show up as a positive departure, at the two downstream stations for $f = 0.5$ Hz and at the two upstream stations for $f = 2$ Hz. These differences, though not very large, are significant and consistent with the discussion on the effects of unsteadiness on the velocity profile.

Similar trends are observed for the mean-square transverse turbulent intensity $\overline{v^2}$. Figure 3.17 presents the results for station 5, where frequency effects are seen to be present for $f = 0.5$ Hz, while Fig. 3.18 shows the distributions for station 3, where very significant departures due to frequency effects are observed for $f = 2$ Hz. Notice the tendency of the $\overline{v^2}$-distributions to increase very close to the wall. This is believed to be associated with the (small) oscillation of the test surface. Figures 3.19 and 3.20 illustrate the behavior of the turbulent Reynolds shear stress. Note that, now, no significant frequency effects are observed for station 3 at any frequency.

3.3. Oscillatory Motion

Only the behavior of the amplitude and phase of the first harmonic of the flow quantities is studied in the following sections, as it is the most energetic component of the oscillatory motion. A brief discussion of the complete ensemble-averaged flow and its departure from a sinusoidal response is presented in a later section.

3.3.1. Velocity

Stations 5 and 3 are selected as representative of the behavior of the oscillatory motion. The corresponding results for the amplitude of oscillation of the velocity are shown, respectively, in Figs. 3.21 and 3.22. An overshoot, typical of periodic flow, can be seen in each case. Its magnitude is of the order of 7-8% of the free-stream amplitude, and decreases slowly with the position along the plate and the oscillation frequency. The extent of amplitude variation, however, varies significantly both with x and f. Beyond the amplitude overshoot, and closer to the outer edge of the boundary layer, the flow undergoes constant amplitude oscillations at the free-stream amplitude, i.e., it is an inviscid or slug-flow oscillation. The unsteady viscous effects can be considered to be confined within the zone of significant amplitude variation. A measure of the extent of unsteady viscous effects is provided by the distance, y_M, from the wall to the point of maximum amplitude. This distance, referred to the local boundary layer thickness, is presented in Table 3.2 for each station and the two frequencies. Also the corresponding relative Stokes-layer thickness, namely

$\sqrt{\dfrac{2\nu}{\omega}}/\delta$, is tabulated as a reference, which measures the extent of unsteady viscous effects in a hypothetical periodic laminar boundary layer of the same thickness and oscillated at the same frequency. It is observed that y_M/δ decreases in the downstream direction, for a given frequency, and also decreases with frequency, for a given station. However, it is interesting to note that when y_M is normalized by $\overline{u}_*/\omega$, it remains essentially constant with both frequency and position along the plate, as shown in the last column of Table 3.2. In any case, y_M/δ is always very much larger than the relative Stokes-layer thickness, showing that unsteady viscous effects propagate over a much wider region in turbulent flow. These results are in agreement with previous investigations. The table also suggests that, from the point of view of unsteady viscous effects, there is a continuous transition between what happens at station 5 at the lower frequency and at station 1 at the higher one. All these trends will be shown to be consistent with the theory developed in the next chapter.

Figures 3.23 and 3.24 present the distribution of the phase lead, relative to the free-stream velocity, of the velocity oscillation. It increases monotonically towards the wall, in some cases after attaining a small phase lag. This agrees with previous experimental results. At the closest point (at about 1 mm from the wall) the phase lead is, for all stations, in the range 10-13 degrees for $f = 0.5$ Hz and 7-9 degrees for $f = 2$ Hz. The significant phase variations extend over, roughly, the same distance as the amplitude variations. Also shown in these figures are the phases of the

corresponding wall shear stress (see below), except for station 5 at f = 2 Hz, in which case it goes out of the range of this figure. They suggest that some nonmonotonic behavior may occur close to the wall for the low-frequency cases. However, measurements could not be obtained closer than 1 mm from the wall in the present experiments.

3.3.2. Turbulence Properties

The amplitude of oscillation of the turbulence properties $\langle u^2 \rangle$, $\langle v^2 \rangle$ and $-\langle uv \rangle$ are normalized by $2[\langle U_e \rangle] \overline{U}_e$. The logic behind this nondimensionalization is that the resulting quantity, say the amplitude of $\langle u^2 \rangle$, should be essentially equal, in quasi-steady flow, to the steady-flow value of $\overline{u^2}/\overline{U}_e^2$ (see chapter 4). Hence, any departure from the steady-flow distribution indicates that the quantity $\langle u^2 \rangle$ is not varying in a quasi-steady manner. Figures 3.25 and 3.26 present the amplitude of oscillation for $\langle u^2 \rangle$. Departures from the quasi-steady behavior are, as expected, very important for both the frequencies (compare with Figs. 3.12 and 3.14). On the other hand, the region of significant variation of the amplitude are now more extended (roughly doubled) than for the velocity. Beyond this region the amplitude is essentially zero, indicating a state of frozen turbulence, in agreement with previous investigations. For station 3 (Fig. 3.26) and f = 0.5 Hz, a secondary peak in the amplitude is observed close to the outer edge of the boundary layer. The origin of this disturbance, which also shows up at other locations and at the higher frequency, could not be satisfactorily explained.

The phase of $\langle u^2 \rangle$, relative to the free-stream velocity, is presented in Figs. 3.27 and 3.28. It is actually interpreted as a phase lag, which tends to zero at or close to the wall (where the turbulence is produced), and increases to 360 degrees at the outer edge of the region with strong unsteady viscous effects, which will be called the "unsteady layer" (indicated by a vertical line for $f = 2$ Hz). The scatter observed beyond this, for $f = 2$ Hz, is a result of the very small (spurious) amplitude of oscillation in that region.

Similar results are obtained for $\langle v^2 \rangle$, as depicted in Figs. 3.29 to 3.32. This time, however, the unsteady viscous effects extend over a slightly smaller region. Note the anomaly in the phase distributions at $f = 2$ Hz over the outer region (Figs. 3.31 and 3.32). The amplitude of this disturbance, however, is very small, as seen from Figs. 3.29 and 3.30.

Lastly, Figs. 3.33 to 3.36 present the amplitude and phase of the Reynolds shear stress, which show a behavior very much analogous to that of $\langle u^2 \rangle$.

The amplitude and phase distributions of the turbulence properties are in general agreement with those measured by Ramaprian and Tu (1982) and Mizushina et al., (1975) in periodic pipe flow. It is seen that, as observed by these investigators, the phase lag of $\langle u^2 \rangle$ increases approximately linearly through the unsteady layer. This can be interpreted as if the disturbance in the turbulence (generated near the wall) imposed by the oscillation diffuses outward with a constant velocity. Now, the distance travelled by the disturbance in one oscillation period, due to diffusion, corresponds

to the thickness of the unsteady layer. If this thickness can be regarded to be characterized by y_M, the relation $\omega y_M/\overline{u}_\star \approx 1$ indicated by Table 3.2 suggests that the diffusion velocity is constant and is roughly equal to $\overline{u}_\star$. Another significant point to be noted is that both $\langle u^2 \rangle$ and $- \langle uv \rangle$ are out of phase with $\langle U \rangle$ over most part of the unsteady layer, a result which is in agreement with the observations of Ramaprian and Tu (1982). This points to the limitation of quasi-steady eddy viscosity models that relate $\langle uv \rangle$ to $\langle U \rangle$. A careful examination of Figures 3.27, 3.28, 3.35 and 3.36 also shows that $\langle u^2 \rangle$ and $-\langle uv \rangle$ have a relative phase difference which varies across the unsteady layer. This is, again, in agreement with the earlier results in pipe flow and shows that the turbulence structure is not in 'equilibrium' during the oscillation cycle.

3.3.3. Wall Shear Stress

Figure 3.37 presents the amplitude of oscillation of the wall shear stress, normalized in the same manner as the turbulence properties. Comparison with the time-mean results, represented by the shaded region, shows that there is some departure from the quasi-steady distribution for the amplitude at all the stations. This departure is larger, as expected, for the higher frequency. However, the deviation from quasi-steady flow is not as strong as that observed in the case of the turbulence properties in the outer layer.

The phase of the wall shear stress is the more reliable quantity measured with the HFG. The reason is that it is not very sensitive to the calibration constants. Figure 3.38 presents the results for

the four measuring stations. It is observed that the phase lead increases in the downstream direction for a given frequency, and also increases with the frequency for a given station.

Additional experiments were done with the HFG at station 5 varying the frequency of oscillation, but using the sleeve designed for $f = 0.5$ Hz (see section 2.2). The results for the time-mean wall shear stress are shown in Fig. 3.39. A weak tendency to decrease with the frequency is observed. The quasi-steady value corresponding to this station is also shown in this figure, and seems to agree well with the general trend. The amplitude of oscillation is shown in Fig. 3.40, where also the time-mean results are represented as a shaded region. Again, there is a weak departure from a quasi-steady amplitude distribution. The phase variation is presented in Fig. 3.41, where results obtained using the sleeve designed for $f = 2$ Hz are also shown. A monotonic and roughly linear increase with the frequency is observed.

3.4. Ensemble-Averaged Flow

Though the harmonic motion with the forcing frequency is the most energetic component, higher harmonic motions are not negligible for the present amplitude of oscillation. Only the ensemble averaged velocity can be considered sinusoidal with little error, as illustrated in Fig. 3.42, where the phasewise variation of the free-stream velocity is shown. For any location across the boundary layer, higher harmonic contributions to $\langle U \rangle$ were found to be less than 1% of the fundamental.

This is not the case for the turbulence properties. Figures 3.43 to 3.45 present their variation with phase position for different locations relative to the wall, at station 5 and f = 2 Hz. One location (y/δ = .47) corresponds to the region where the turbulence structure is 'frozen'; another (y/δ .068) to the zone of maximum oscillation amplitude; and a third (y/δ = .023) to the measurement point closest to the wall. The contribution from the higher harmonics, relative to the fundamental, is of the order of 15-20% at $y/\delta \simeq$ .07 and increases up to about 40% at $y/\delta \simeq$ .02. Similar results were observed in the lower frequency experiment. Higher harmonic contributions in this case ranged from 10-20% at the zone of maximum amplitude (y/δ = .22) to about 30% at the closest measuring point.

Figure 3.46 shows the phasewise variation of the ensemble averaged wall shear stress in some typical cases. Higher harmonics in $\langle \tau_w \rangle$ were found to be of the order of 7-10% for f = 0.5 Hz and 15-20% for f = 2Hz, relative to the fundamental.

3.5. Derived Quantities

The experimental information can be used to calculate some secondary quantities that are important from a theoretical and/or practical point of view. Some of these are presented and briefly discussed next.

Figures 3.47 to 3.49 show the phasewise variation of the integral parameters for a few phase positions along the cycle, at station 5 and for both frequencies. It is seen that the time-mean

value as well as the amplitude of oscillation are, for each parameter, very similar for both the frequencies. The relative amplitude is roughly 43% for the displacement thickness, 33% for the momentum thickness and only 12% for the shape parameter. In quasi-steady flow, these integral parameters are 180 degrees out of phase with the free-stream velocity. It is observed that this is still roughly the case for the 0.5-Hz experiment, but that for the 2-Hz experiment there seems to be a phase lead, relative to the quasi-steady case, of about 30 degrees. It is seen that there is significant distortion from the sinusoidal behavior.

It was found, from a detailed study of the data, that the ensemble-averaged velocity profiles for given phase positions do not belong to the Coles' family. However, it seems to be still possible to distinguish a logarithmic region close to the wall which matches with some of the lines in a Clauser-plot, though smetimes this is a difficult and ambiguous task. The "skin friction coefficient" so obtained, for station 5, is presented in Fig. 3.50. Compared to the results of the wall shear stress measurements, their mean values and amplitudes are low, specially for the 0.5 Hz case. This means that the conventional Clauser-plot cannot be used to obtain the phasewise distribution of the wall shear stress.

Another important and useful quantity is the eddy viscosity. Its ensemble-averaged value is defined as

$$\langle \nu_t \rangle \equiv \frac{-\langle uv \rangle}{\frac{\partial \langle U \rangle}{\partial y}} \tag{3.1}$$

To obtain a meaningful estimate of this value, it is crucial to smooth the variation of $\langle U \rangle$ with y before proceeding with the differentiation. This is difficult and very laborious to do with the whole set of ensemble-averaged velocity profiles. A simpler method can be used by invoking the small-amplitude approximation. Utilizing the complex notation, one can write

$$\langle U \rangle = \overline{U} + \epsilon U_1 e^{i\omega t} \tag{3.2}$$

$$-\langle uv \rangle \equiv \tau = \overline{\tau} + \epsilon \tau_1 e^{i\omega t} \tag{3.3}$$

$$\langle \nu_t \rangle = \overline{\nu}_t + \epsilon \nu_{t1} e^{i\omega t} \tag{3.4}$$

Introducing Eqs. (3.2) to (3.4) into Eq. (3.1), the following expressions for the time-mean value and the complex amplitude of the eddy viscosity follow:

$$\overline{\nu}_t = \frac{\overline{\tau}}{\frac{\partial \overline{U}}{\partial y}} \tag{3.5}$$

$$\nu_{t1} = \frac{\tau_1 - \overline{\nu}_t \frac{\partial U_1}{\partial y}}{\frac{\partial \overline{U}}{\partial y}} \tag{3.6}$$

Thus, the smoothing procedure is now only needed for $\overline{U}$ and U_1 (which includes both the "in-phase" and "out-of-phase" components). Coles' fit is used for $\overline{U}$, while U_1 is represented by a piecewise polynomial

fit. Figure 3.51 presents the time-mean distribution for station 5 and both frequencies. A line is also shown, representing the distribution of $\overline{\nu}_t$ in steady flow. As in the case of the turbulent shear stress, the time-mean distribution of $\overline{\nu}_t$ for the higher frequency agrees very well with that in steady flow, but the distribution for $f = 0.5$ Hz shows a departure due to frequency effects. Figures 3.52 and 3.53 present the amplitude and phase of the oscillatory component. Note, that for $f = 2$ Hz the eddy viscosity is frozen in the outer region (as is to be expected since both $\langle - \rangle$ and $\partial\langle U \rangle/\partial y$ are frozen).

Table 3.1

Coles' Parameters for the Time-Mean Unsteady Flows
and the Steady Flow at the Time-Mean Free-Stream Velocity

Station	f(Hz)	$\overline{C}_f$	δ(mm)	Π
1	2	0.003533	20.22	0.5159
	0.5	0.003642	21.13	0.3895
	0	0.004373	14.46	0.1011
2	2	0.003516	24.78	0.4159
	0.5	0.003609	27.21	0.2783
	0	0.004164	17.29	0.1621
3	2	0.003433	28.74	0.4062
	0.5	0.003507	30.17	0.3116
	0	0.003660	20.87	0.4027
4	2	0.003204	36.58	0.4979
	0.5	0.003177	36.32	0.5037
	0	0.003373	33.05	0.3975
5	2	0.003072	45.10	0.5061
	0.5	0.002967	46.60	0.5850
	0	0.003276	39.73	0.3769

Table 3.2

Relative Distance to the Point of
Maximum Amplitude of Oscillation

f(Hz)	Station	y_M/δ	$\sqrt{2\nu/\omega}\,/\delta$	$\omega y_M/\bar{u}_*$
0.5	1	0.526	0.038	0.83
	2	0.490	0.029	0.98
	3	0.425	0.026	0.96
	4	0.254	0.022	0.73
	5	0.240	0.017	0.84
2	1	0.115	0.020	0.74
	2	0.121	0.016	0.96
	3	0.120	0.014	1.00
	4	0.067	0.011	0.79
	5	0.065	0.009	0.93
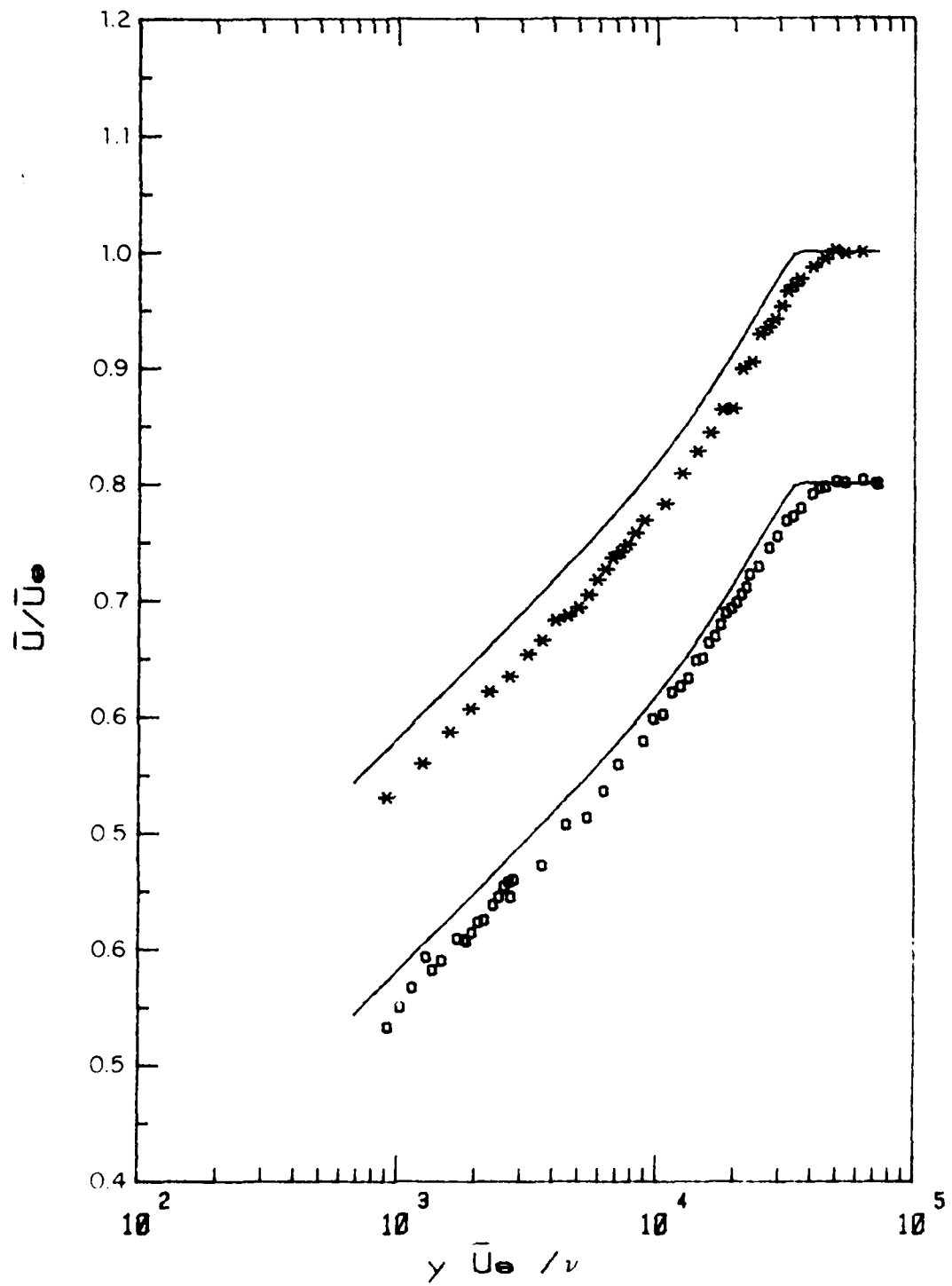
Figure 3.1. Time-mean velocity profile at station 5.
*, f = 0.5 Hz; o, f = 2 Hz; ——, quasi-
steady.

MICROCOPY RESOLUTION TEST CHART

NATIONAL BUREAU OF STANDARDS 1963 A

$\overline{U} / \overline{U}_e$

$y \ \overline{U}_e \ / \ \nu$
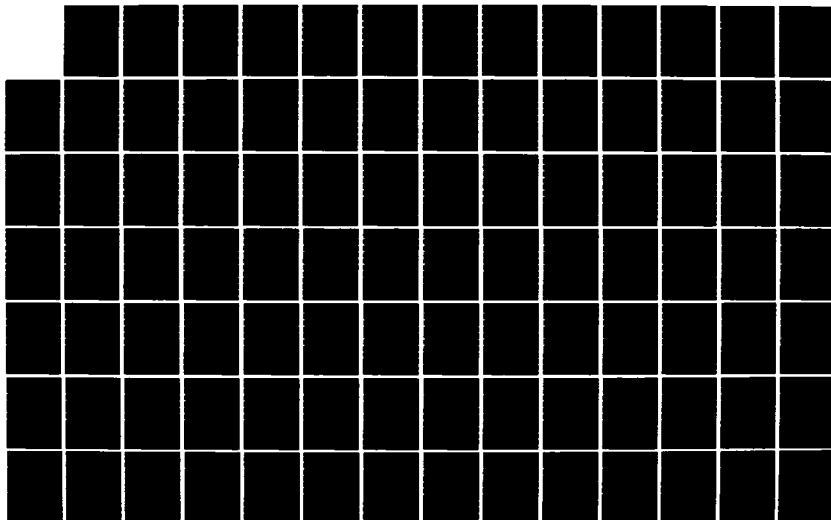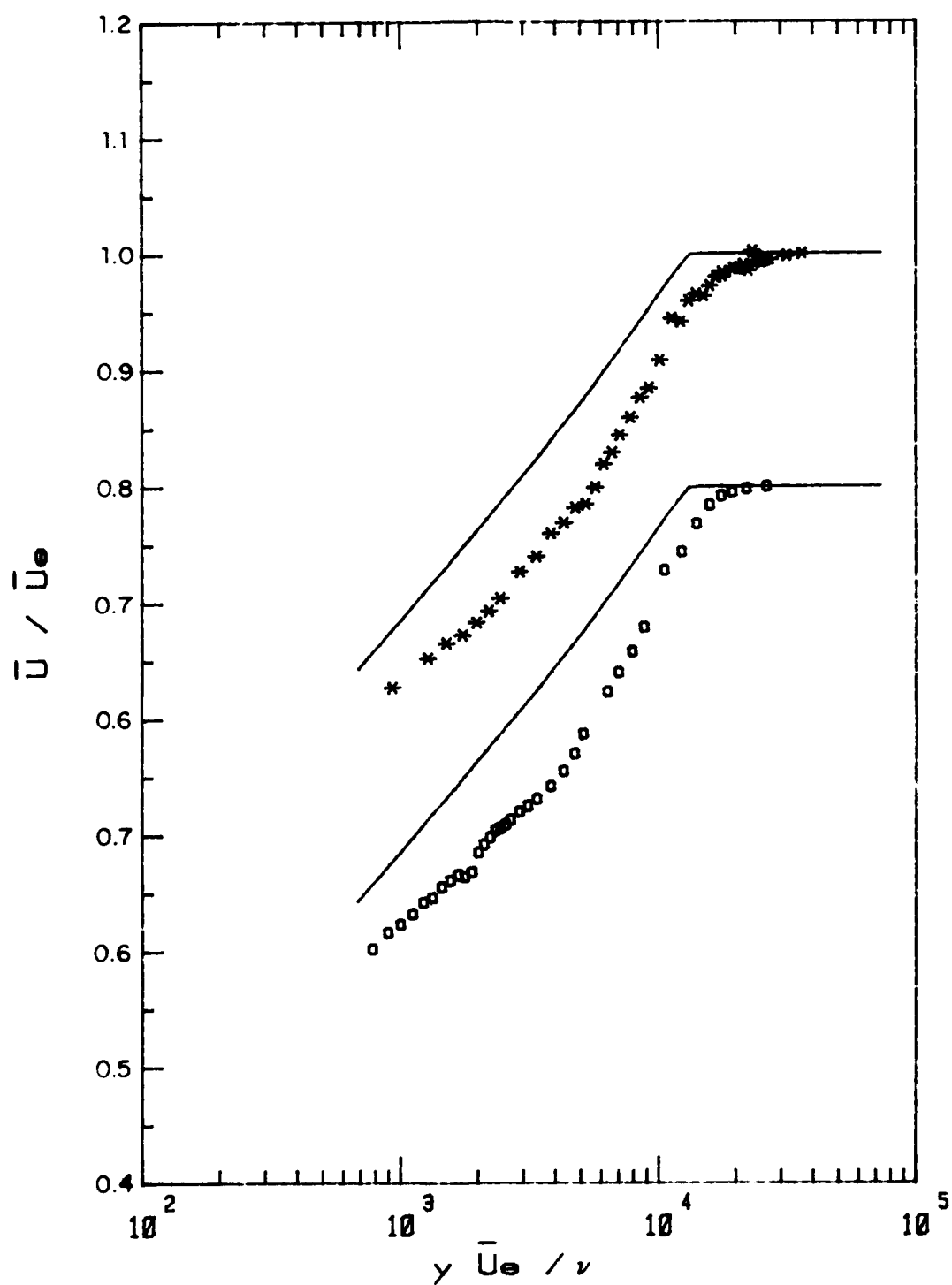
Figure 3.2. Time-mean velocity profile at station 1. Symbols as in Fig. 3.1.
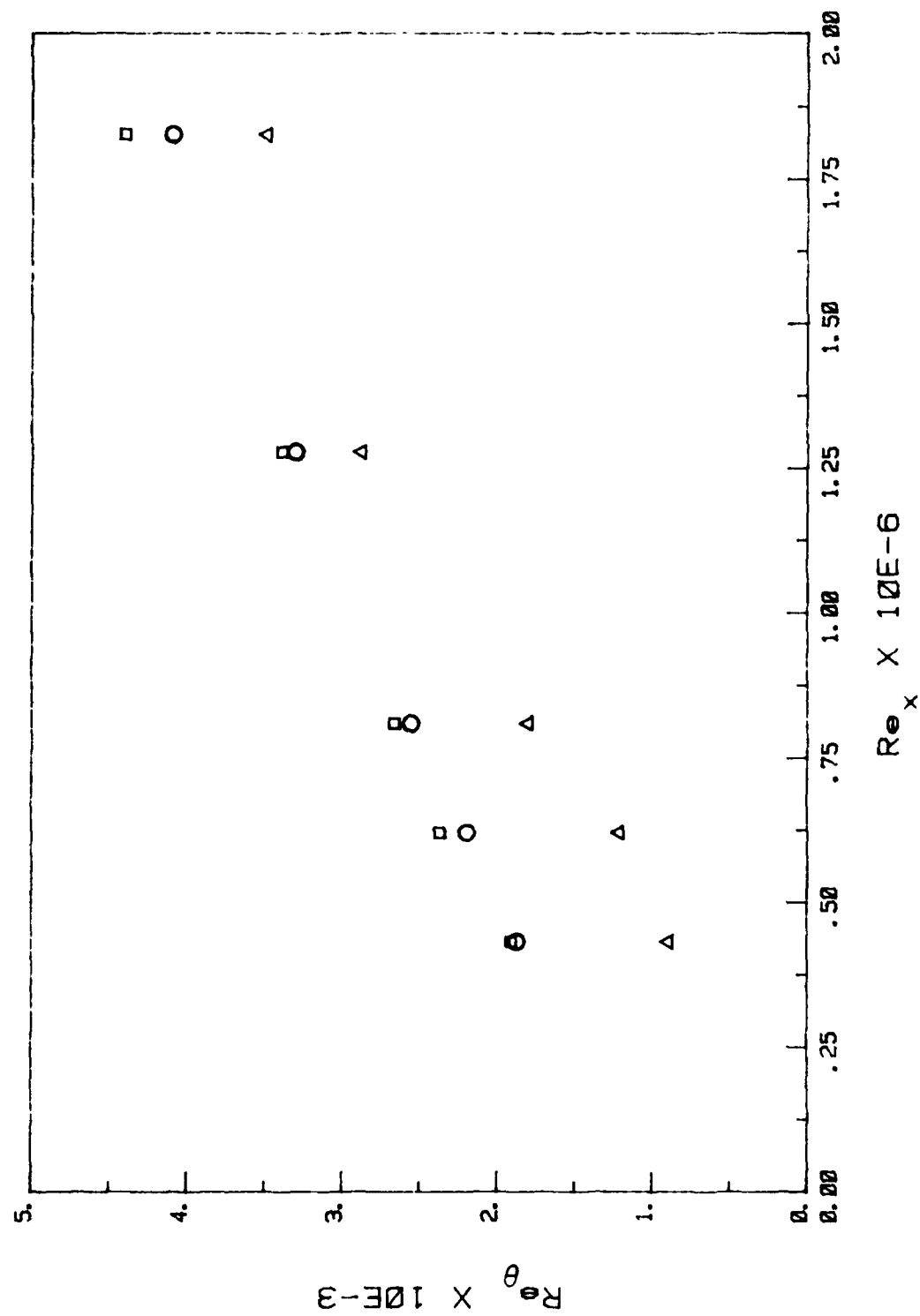
Figure 3.3. Longitudinal distribution of Re_θ. $\triangle$, steady flow; $\square$, f = 0.5 Hz; 0, f = 2 Hz.
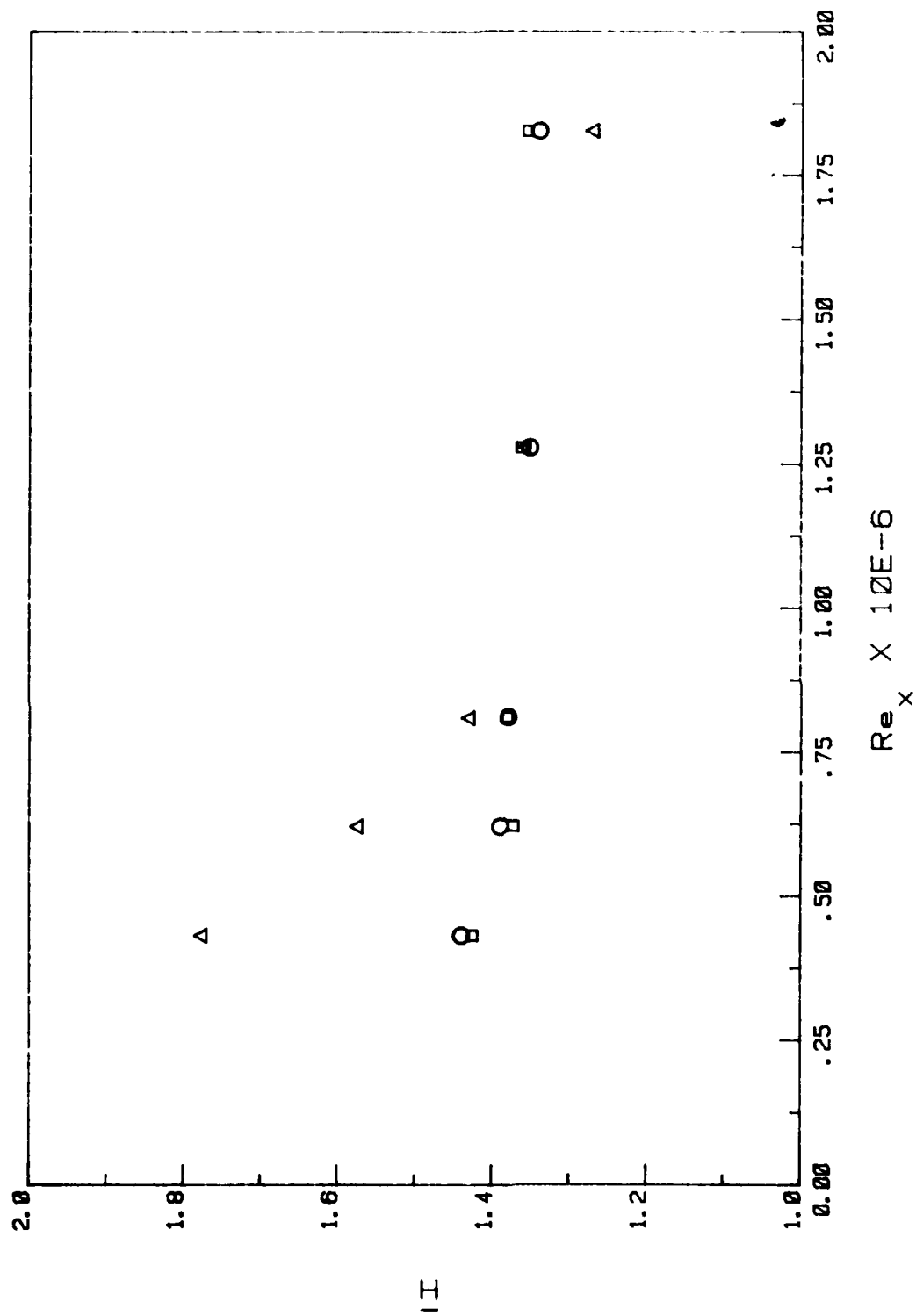
Figure 3.4. Longitudinal distribution of H. Symbols as in Fig. 3.3.
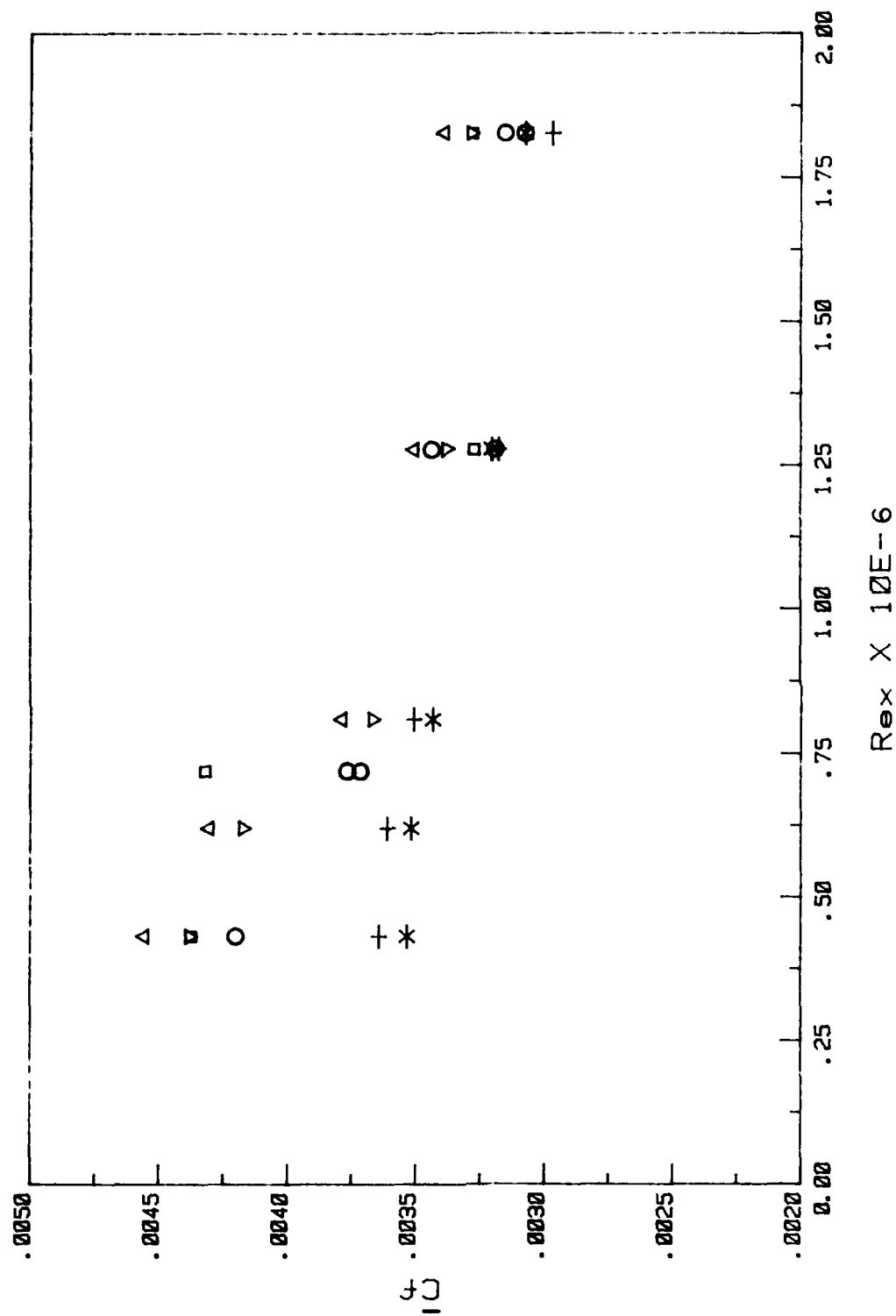
Figure 3.5. Longitudinal distribution of C_f. $\triangledown$, steady flow;
$\triangle$, quasi-steady flow; $\square$, $f = 0.5$ Hz; O, $f = 2$ Hz; $+$, Clauser value
for $f = 0.5$ Hz; $*$, Clauser value for $f = 2$ Hz.
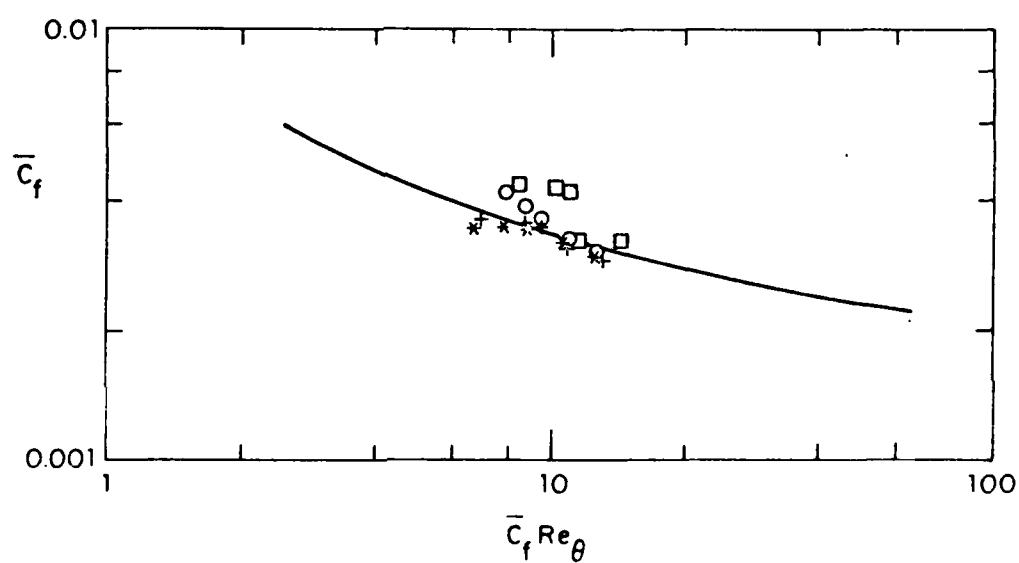
Figure 3.6. Correlation between $\bar{C}_f$ and Re_θ for unsteady flow.
□, f = 0.5 Hz; O, f = 2 Hz; +, Coles parameter
for f = 0.5 Hz; *, Coles parameter for f = 2 Hz;
——, 'normal curve' [Coles (1962)].
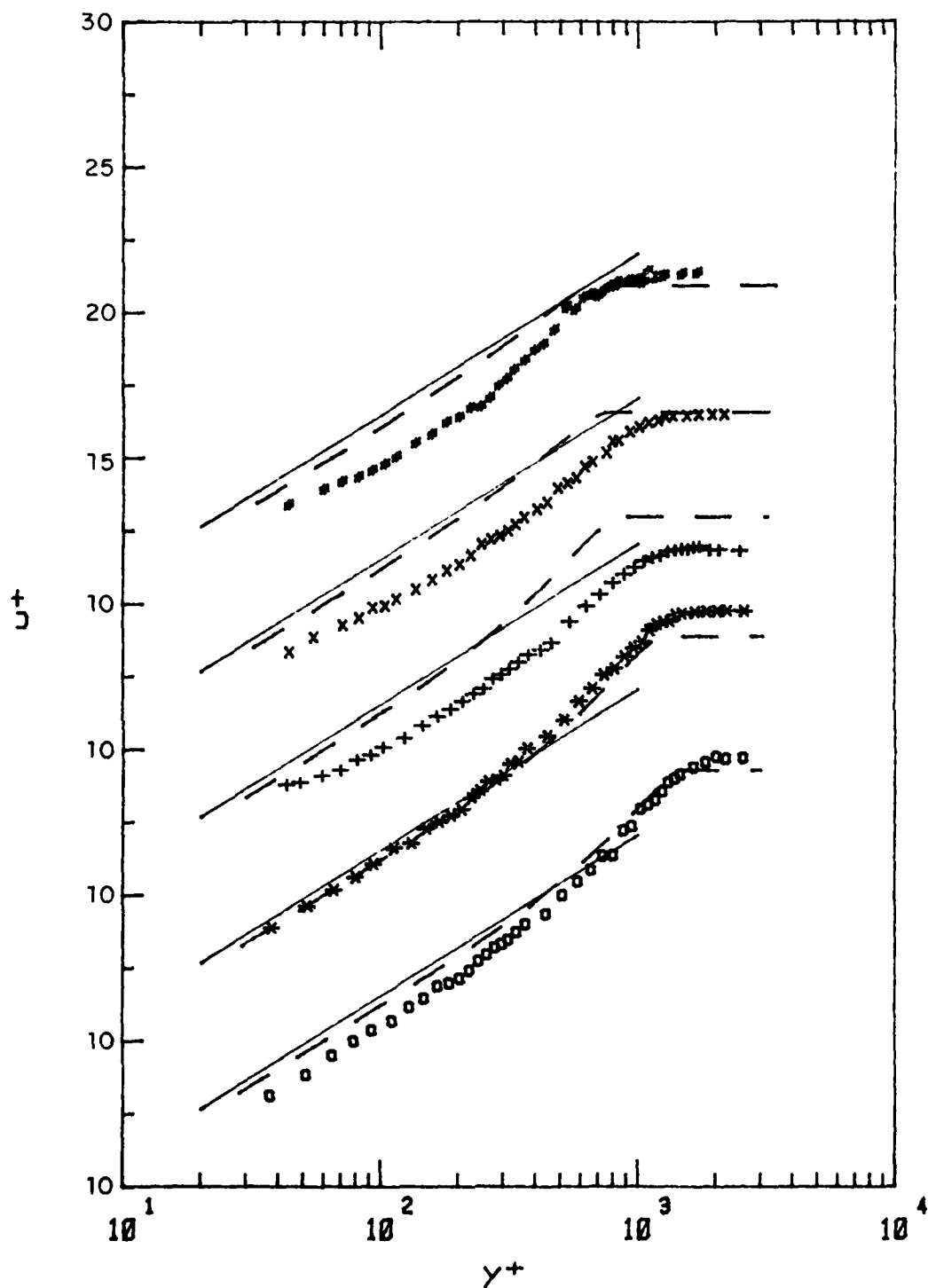
Figure 3.7. Time-mean velocity profiles in the inner coordinates for f = 0.5 Hz. #, station 1; x, 2; +, 3; *, 4; o, 5; ——, universal logarithmic law; ---, quasi-steady distribution.
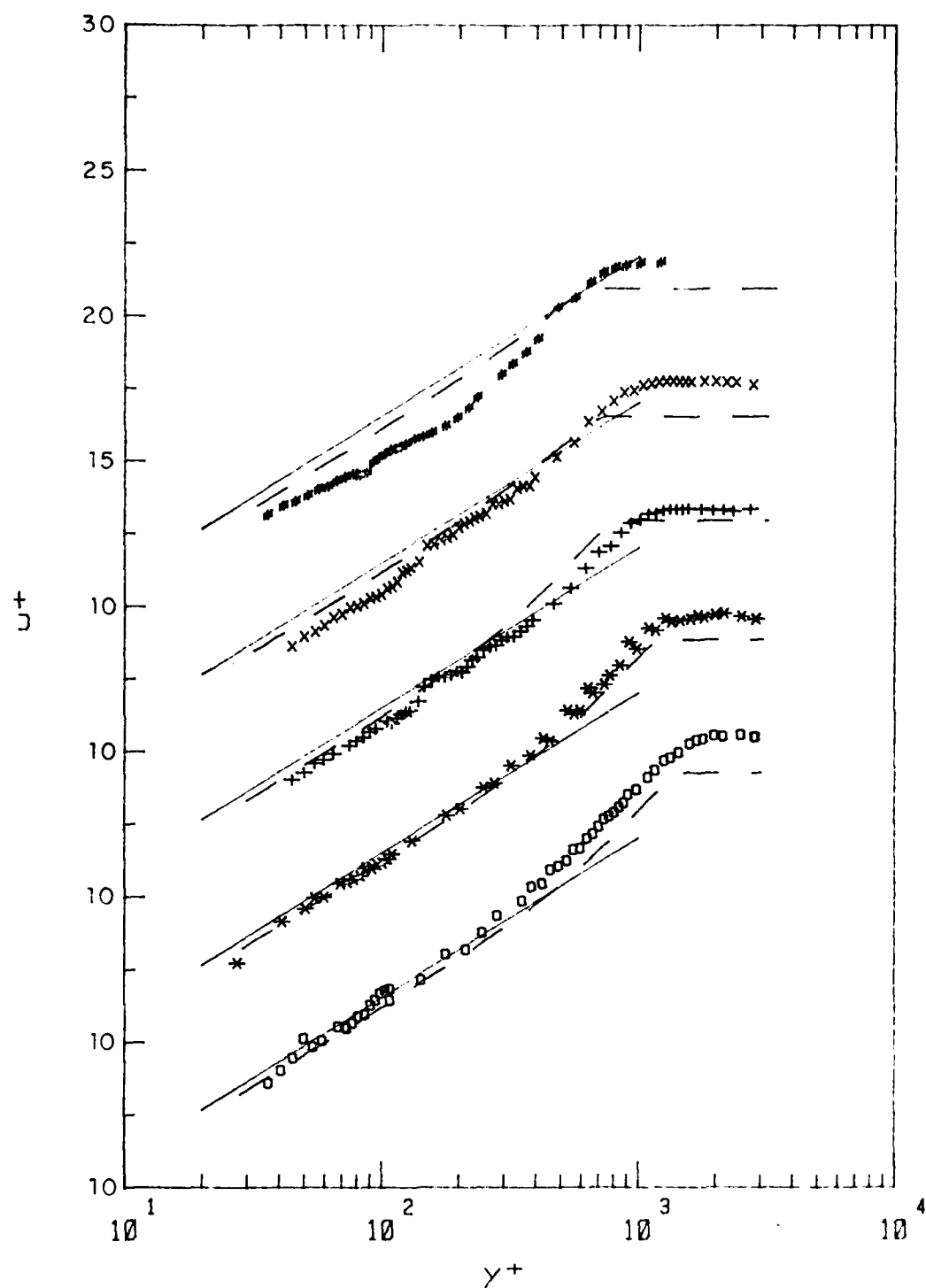
Figure 3.8. Time-mean velocity profiles in the inner coordinates
for f = 2 Hz. Symbols as in Fig. 3.7.
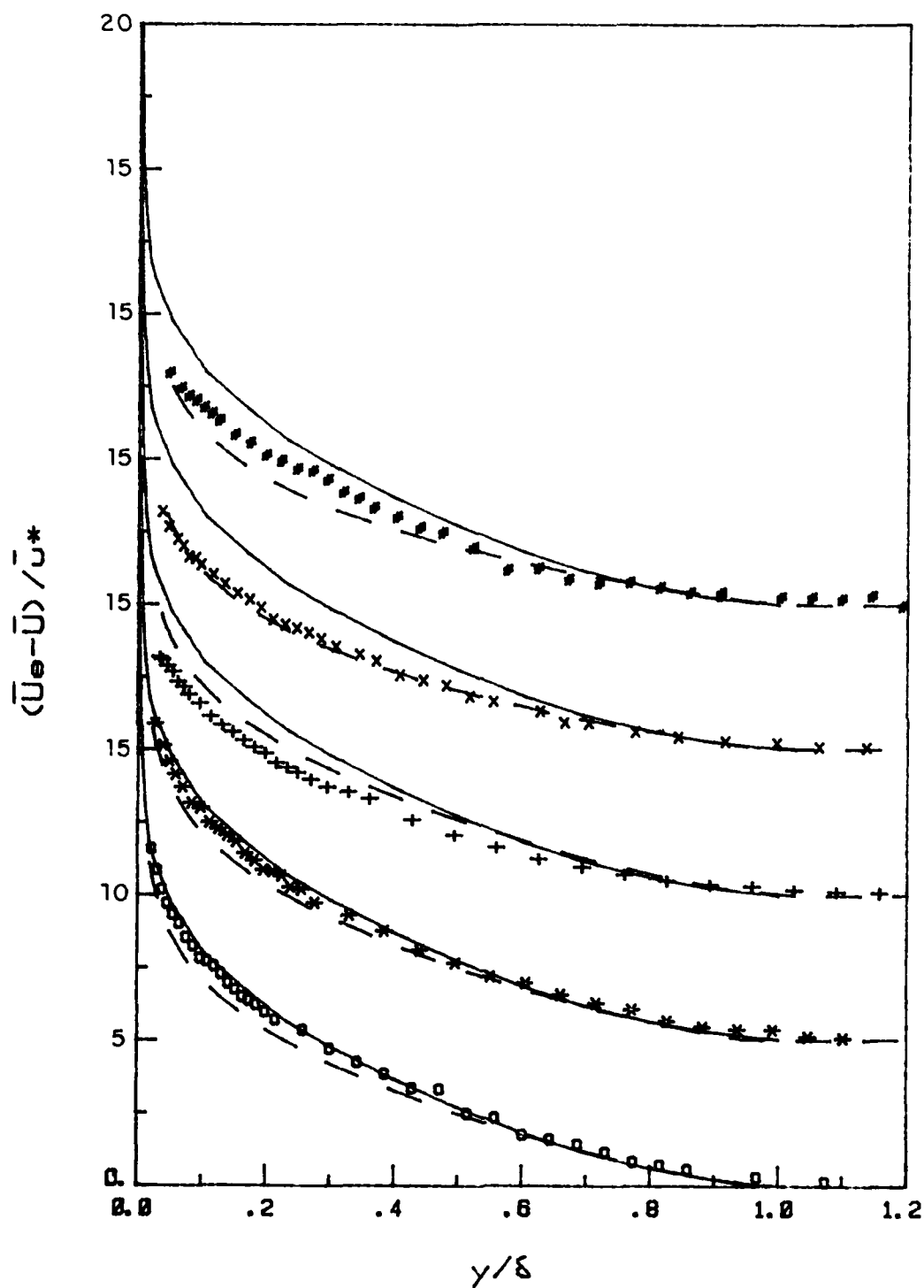
Figure 3.9. Time-mean velocity profiles in the outer
coordinates for f = 0.5 Hz; ——, Klebanoff
data (1954). Other symbols as in Fig. 3.7.
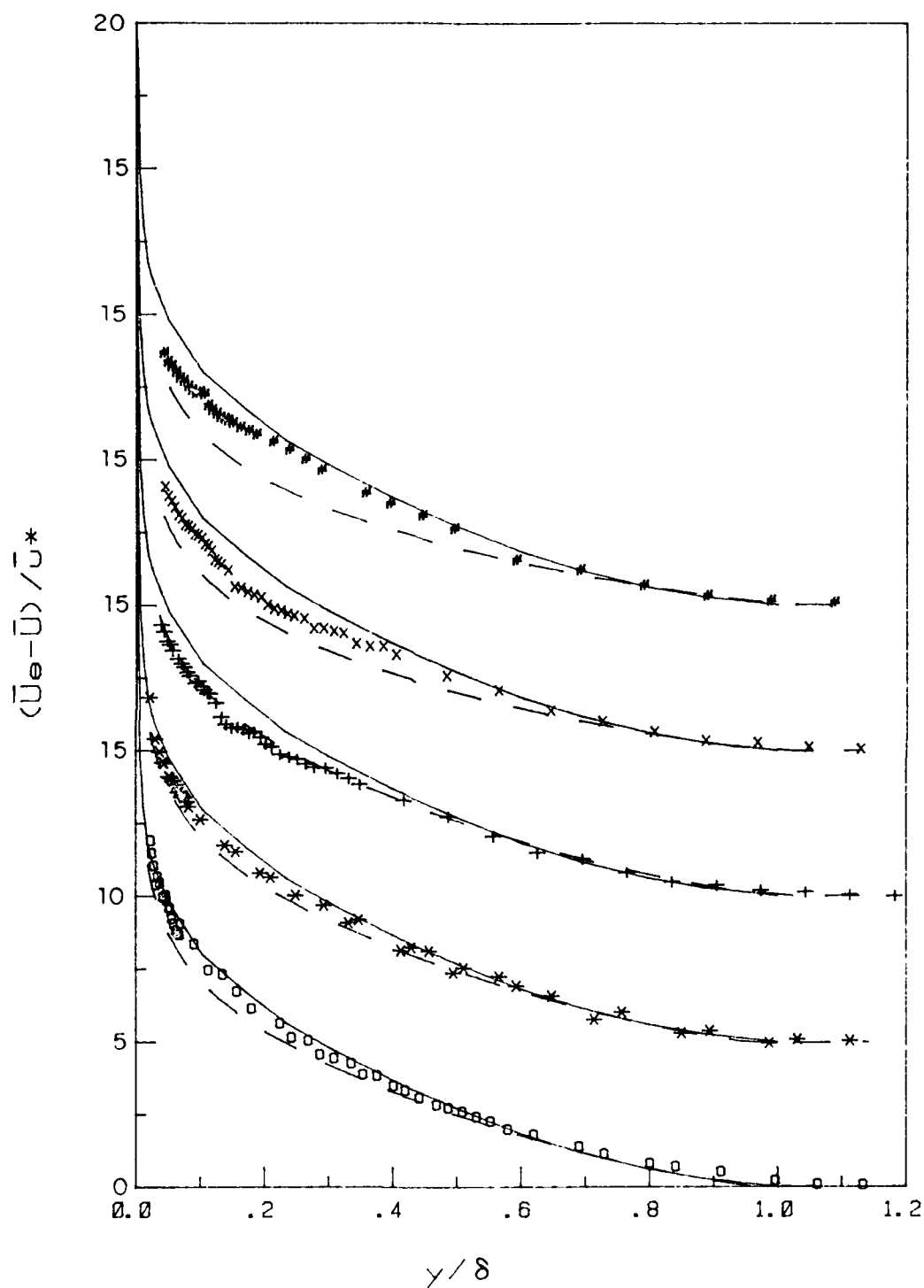
Figure 3.10. Time-mean velocity profiles in the outer
coordinates for f = 2 Hz. Symbols as in
Fig. 3.9.
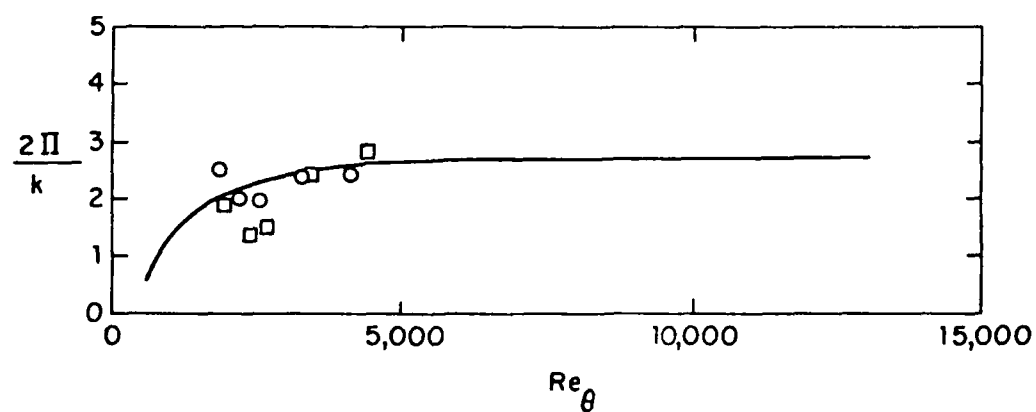
Figure 3.11. Correlation between Π and Re_θ for the
time-mean unsteady flow.$\square$, $f = 0.5$ Hz;
$\bigcirc$, $f = 2$ Hz.
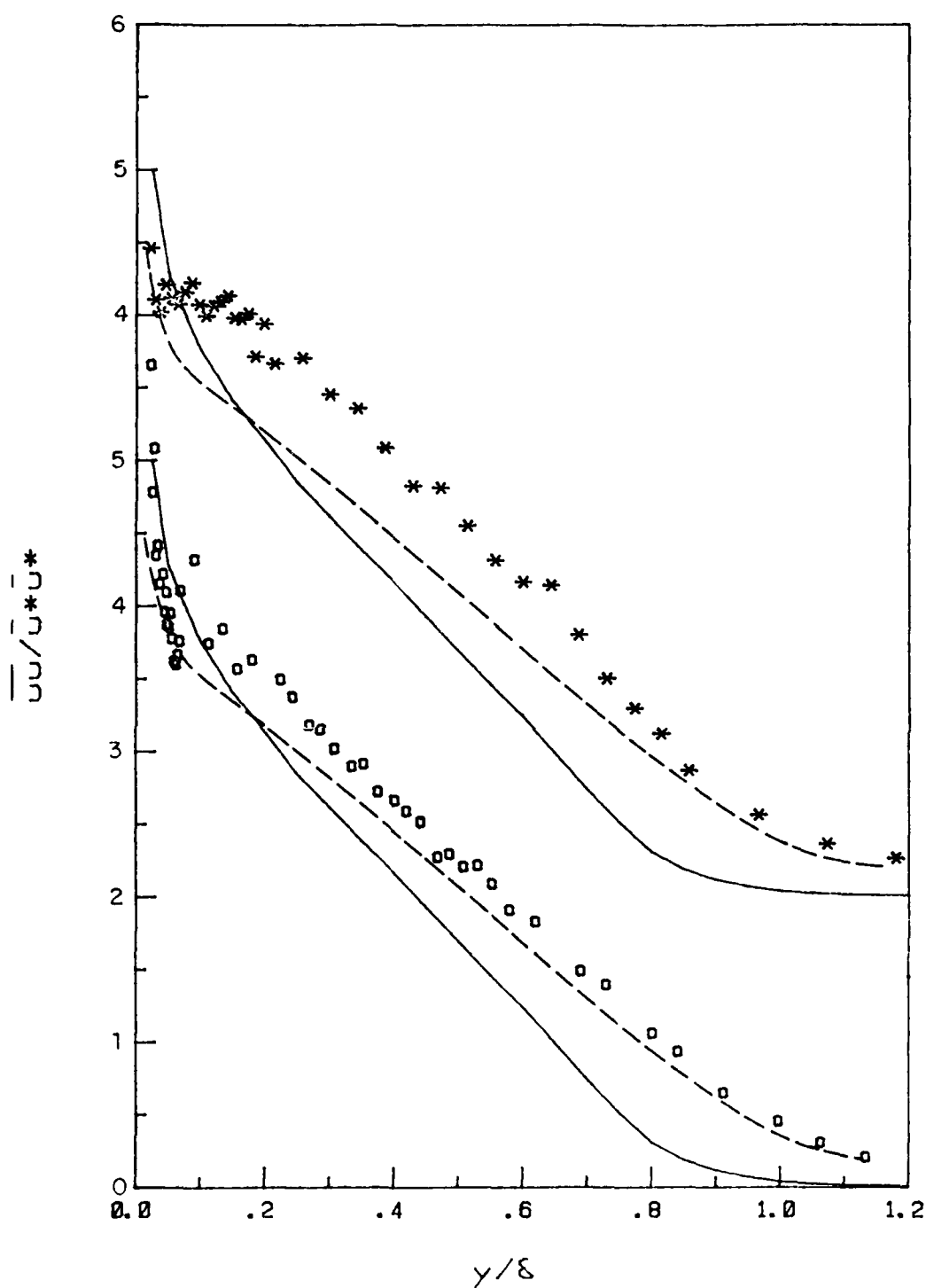
Figure 3.12. Time-mean distribution for $\langle u^2 \rangle$ at station 5.
*, f = 0.5 Hz; o, f = 2 Hz; ---, steady flow;
——, Klebanoff's data (1954).
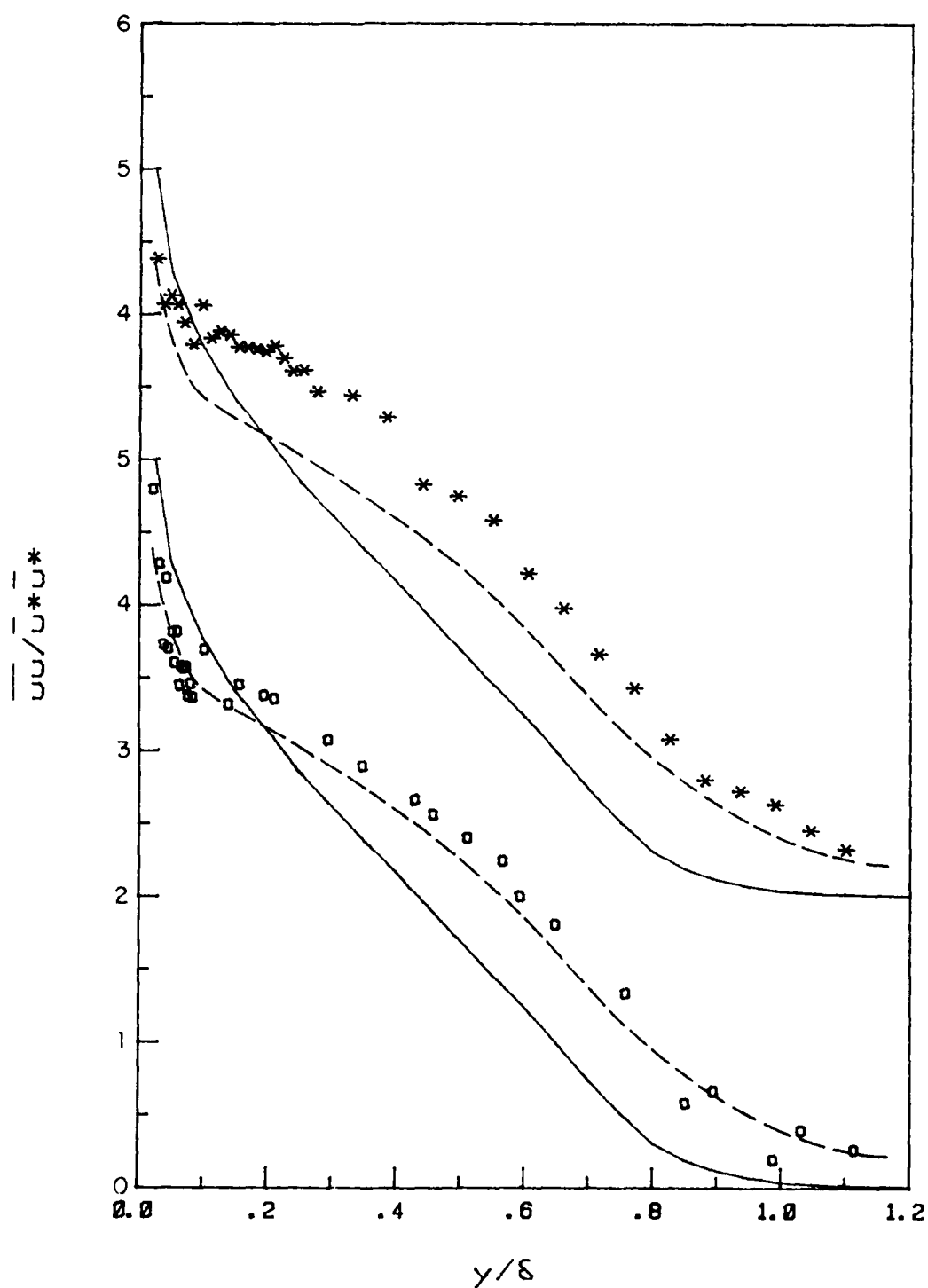
Figure 3.13. Time-mean distribution for $\langle u^2 \rangle$ at station 4. Symbols as in Fig. 3.12.
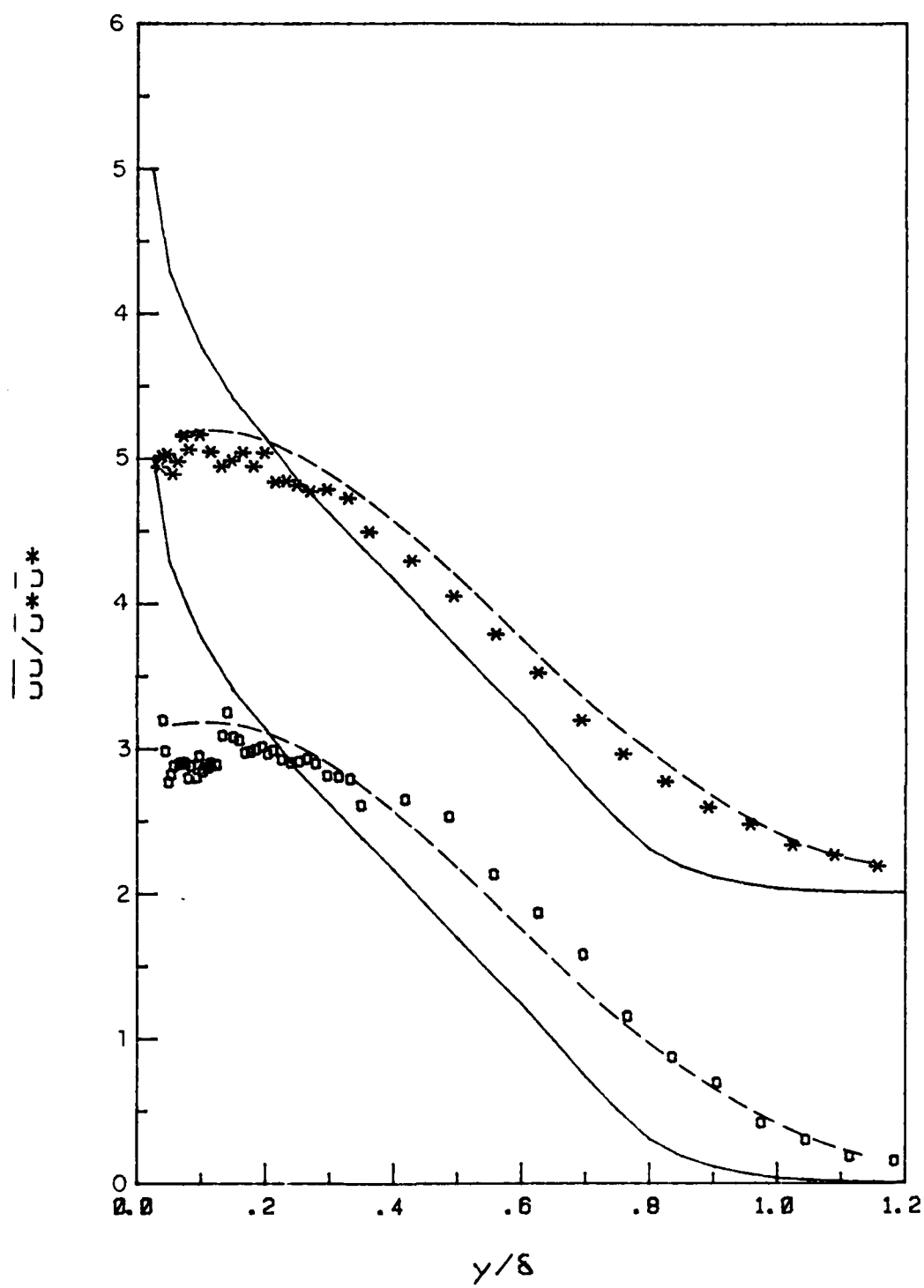
Figure 3.14.   Time-mean distribution for $\langle u^2 \rangle$ at station 3.
Symbols as in Fig. 3.12.
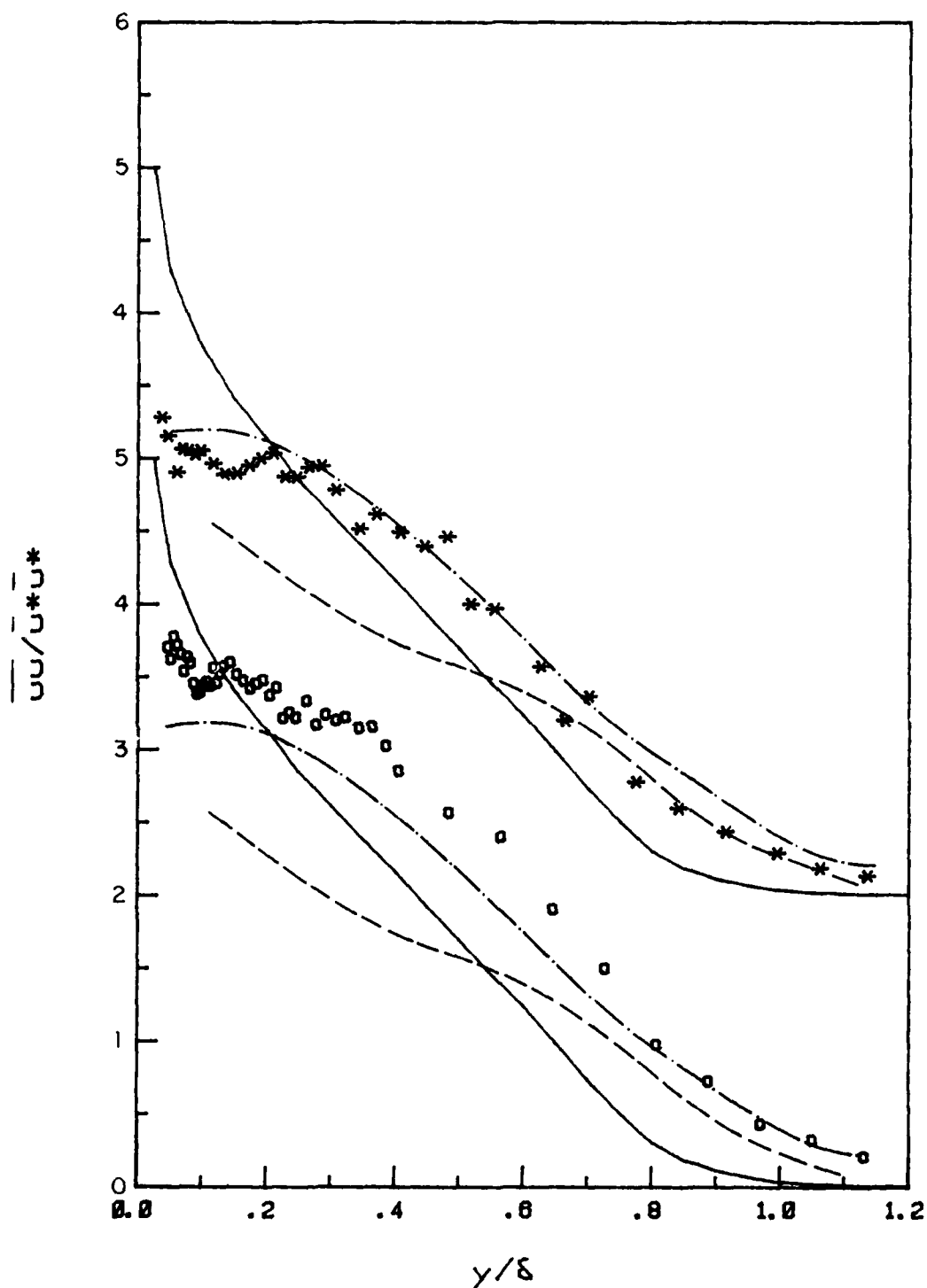
Figure 3.15. Time-mean distribution for $\langle u^2 \rangle$ at station 2. — · —, steady flow at station 3. Other symbols as in Fig. 3.12.
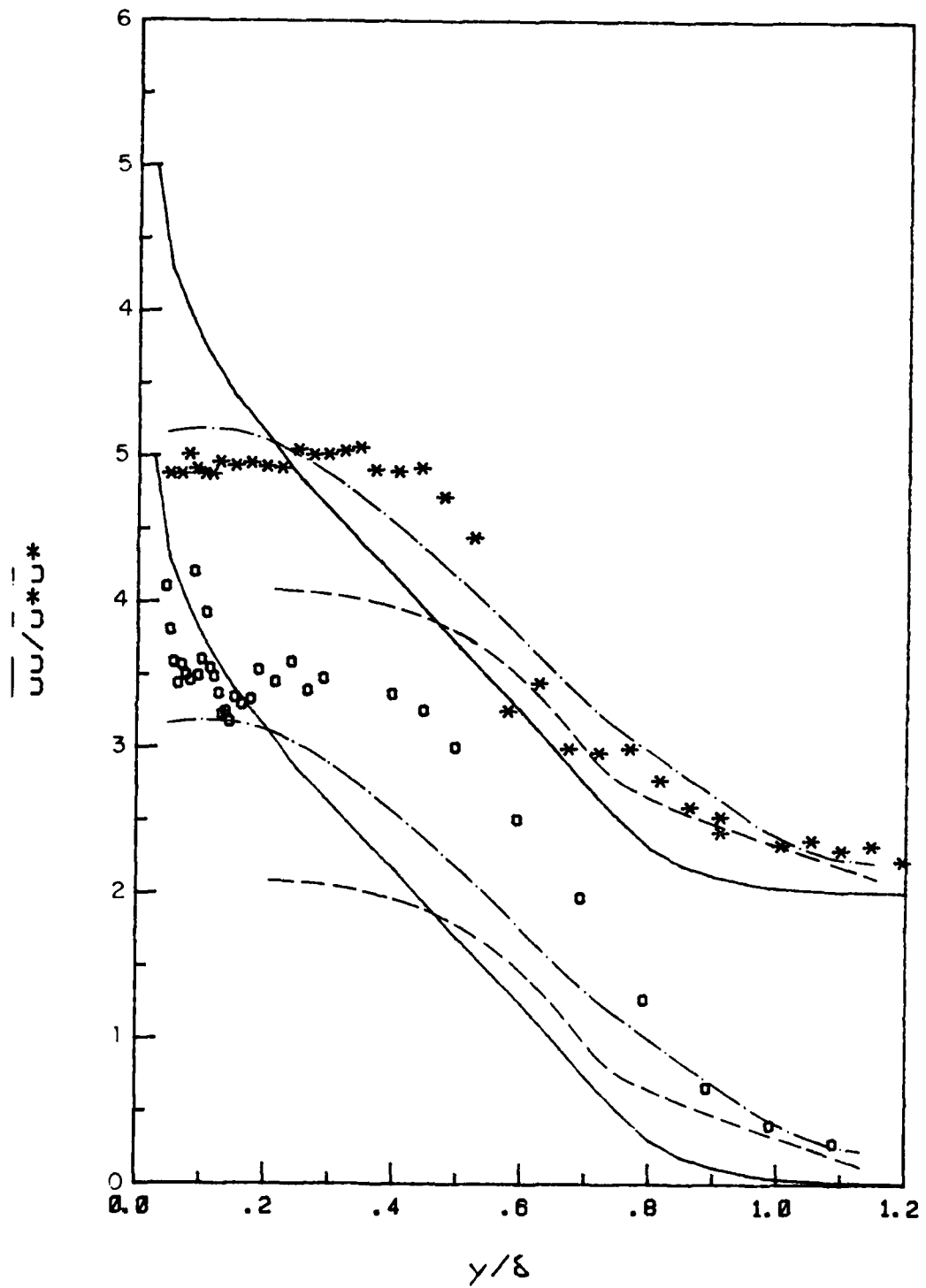
Figure 3.16. Time-mean distribution for $\langle u^2 \rangle$ at station 1.
—·—, steady flow at station 3. Other
symbols as in Fig. 3.12.
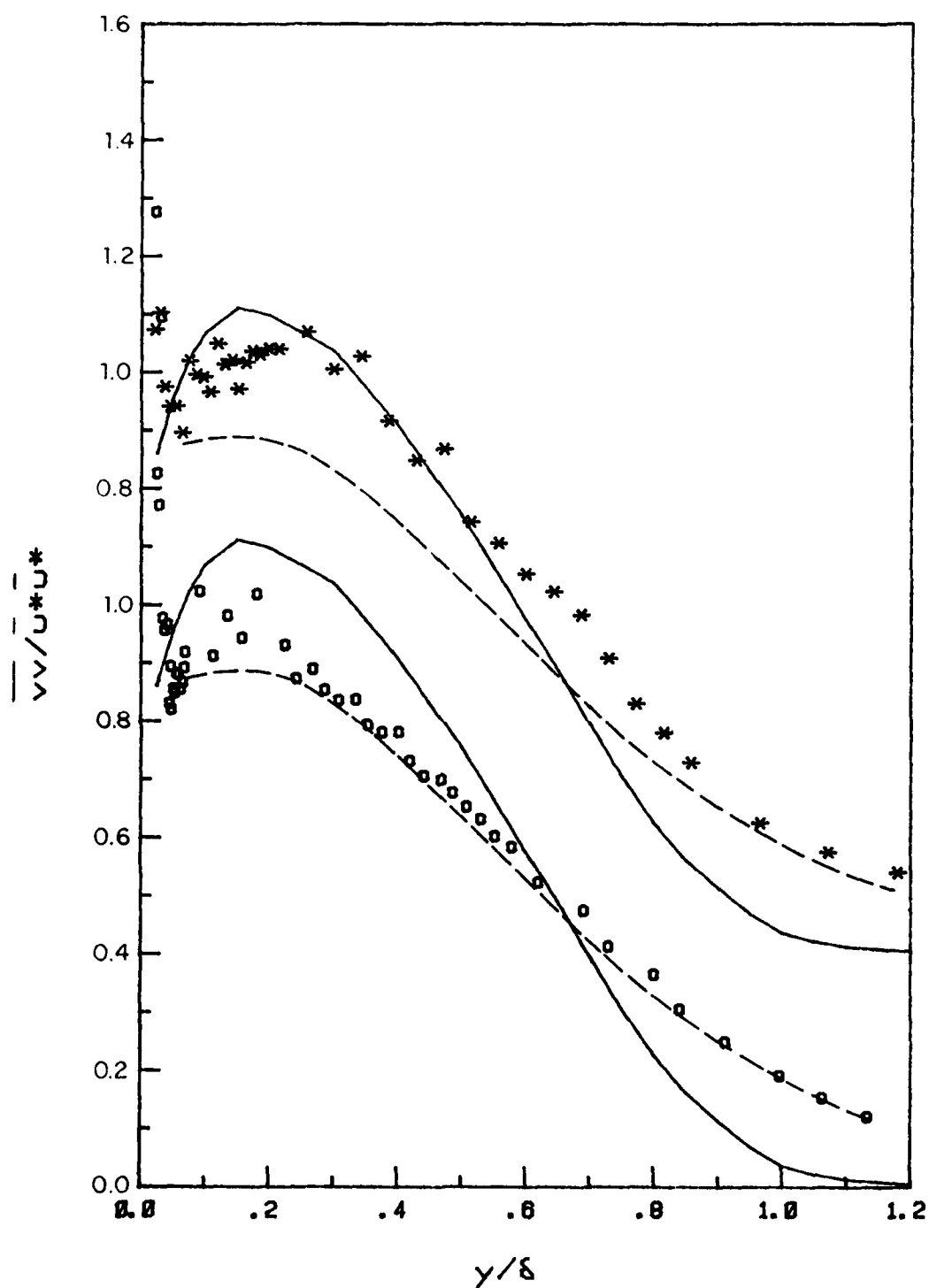
Figure 3.17. Time-mean distribution for $\langle v^2 \rangle$ at station 5.
Symbols as in Fig. 3.12.
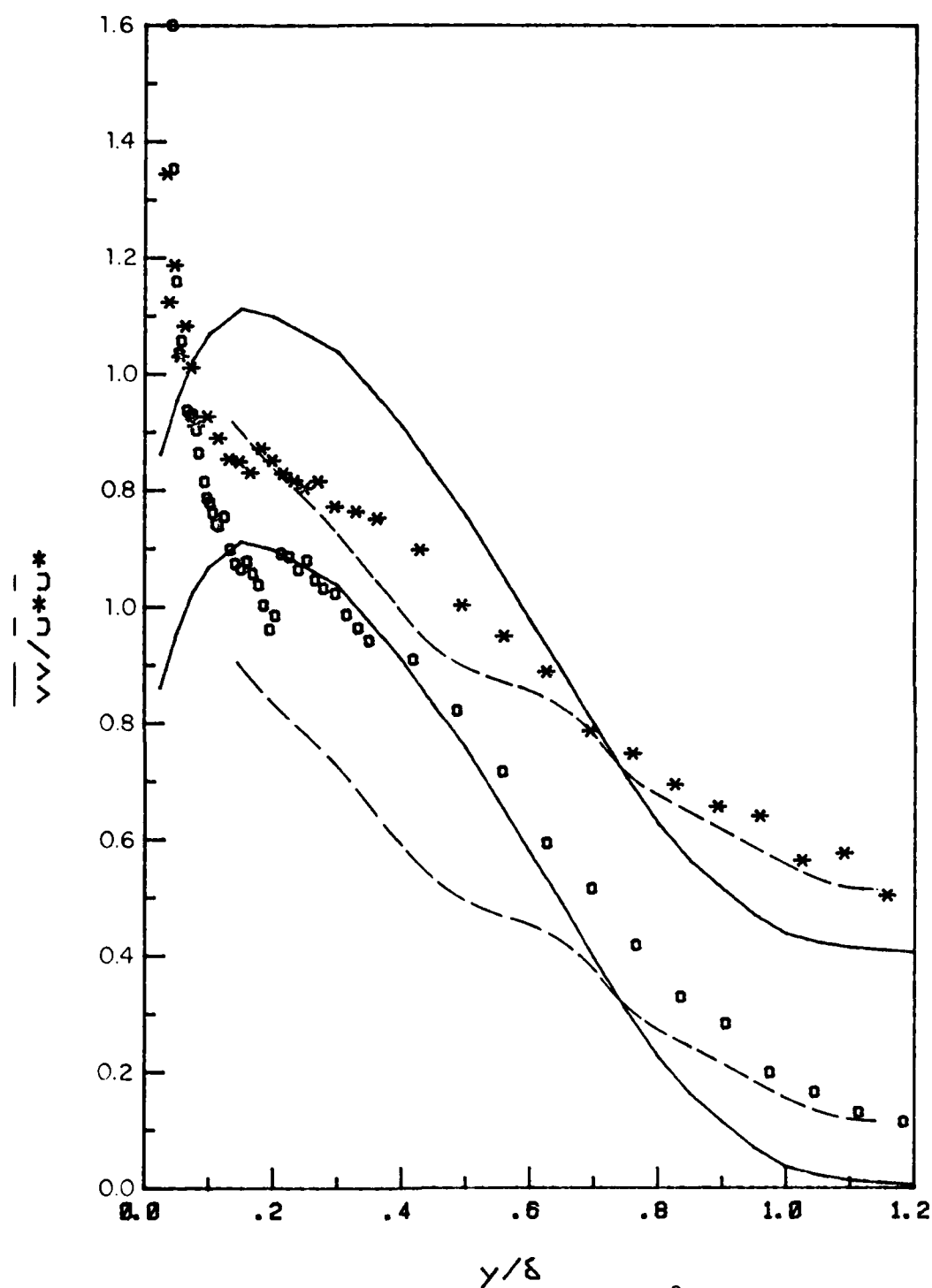
Figure 3.18. Time-mean distribution for $\langle v^2 \rangle$ at station 3. Symbols as in Fig. 3.12.
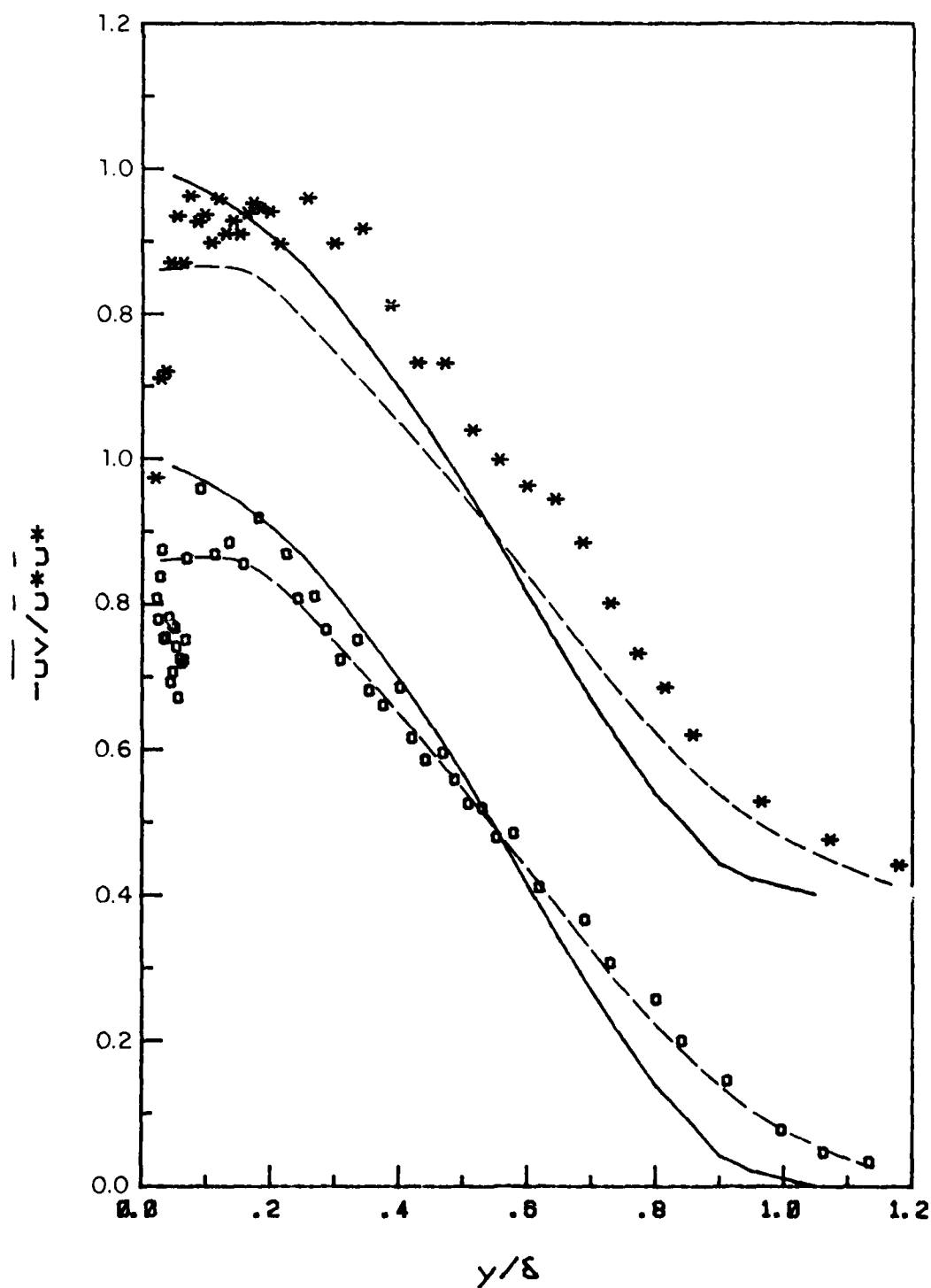
Figure 3.19. Time-mean distribution for - <uv> at station 5. Symbols as in Fig. 3.12.
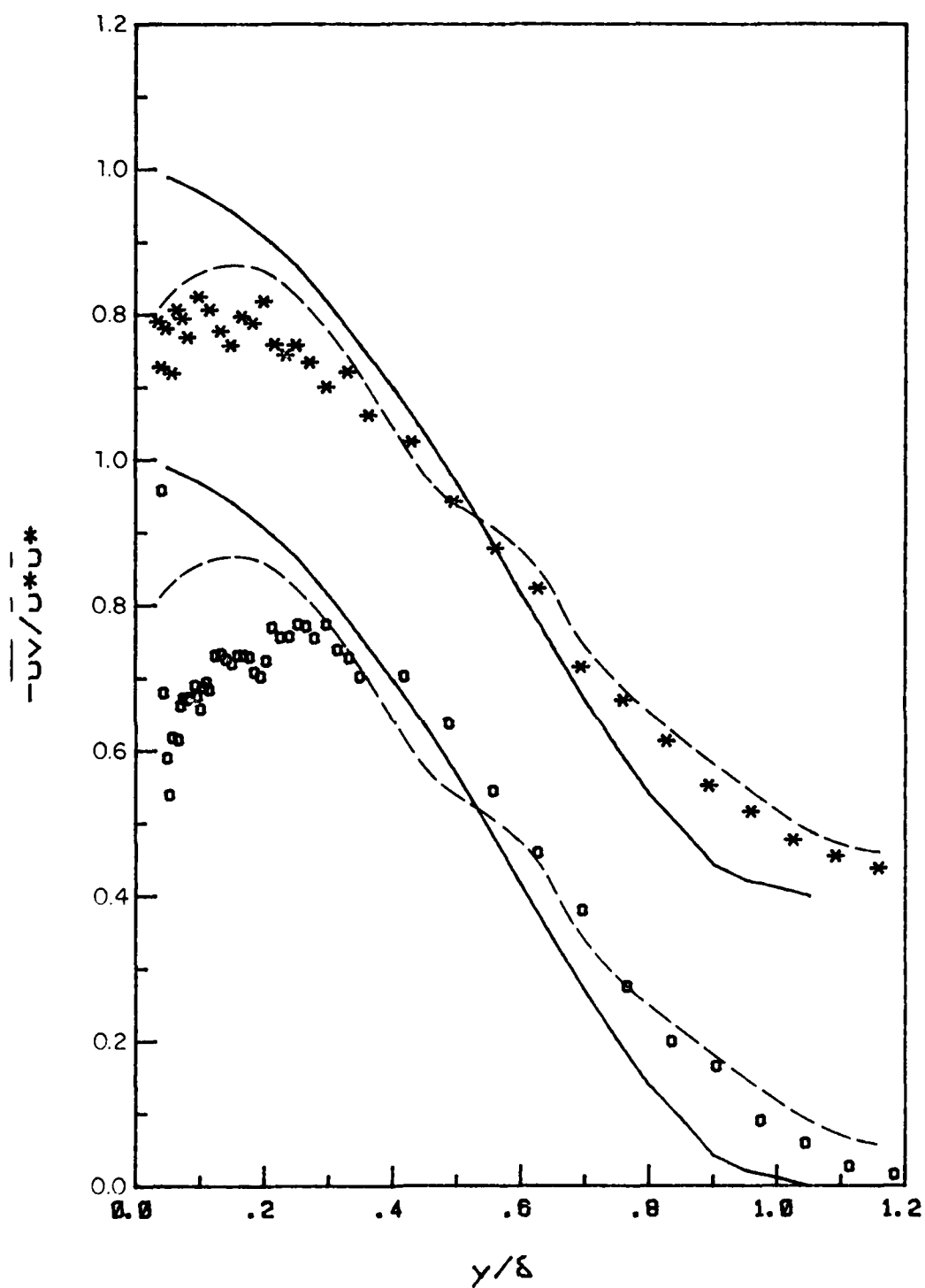
Figure 3.20. Time-mean distribution for - <uv> at station 3. Symbols as in Fig. 3.12.

Figure 3.21. Amplitude distribution for the velocity at station 5. *, f = 0.5 Hz; o, f = 2 Hz.
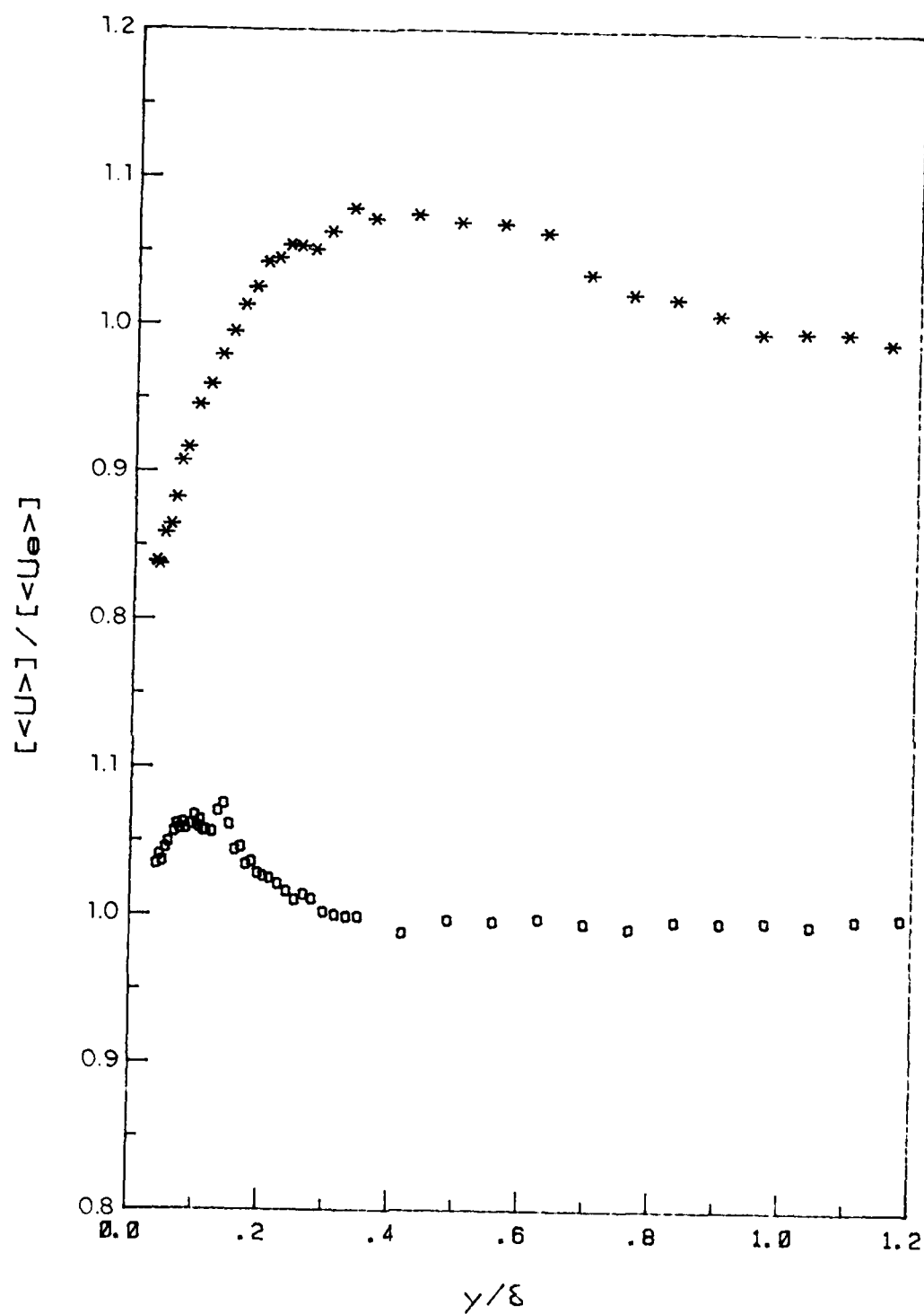
Figure 3.22. Amplitude distribution for the velocity at station 3. Symbols as in Fig. 3.21.
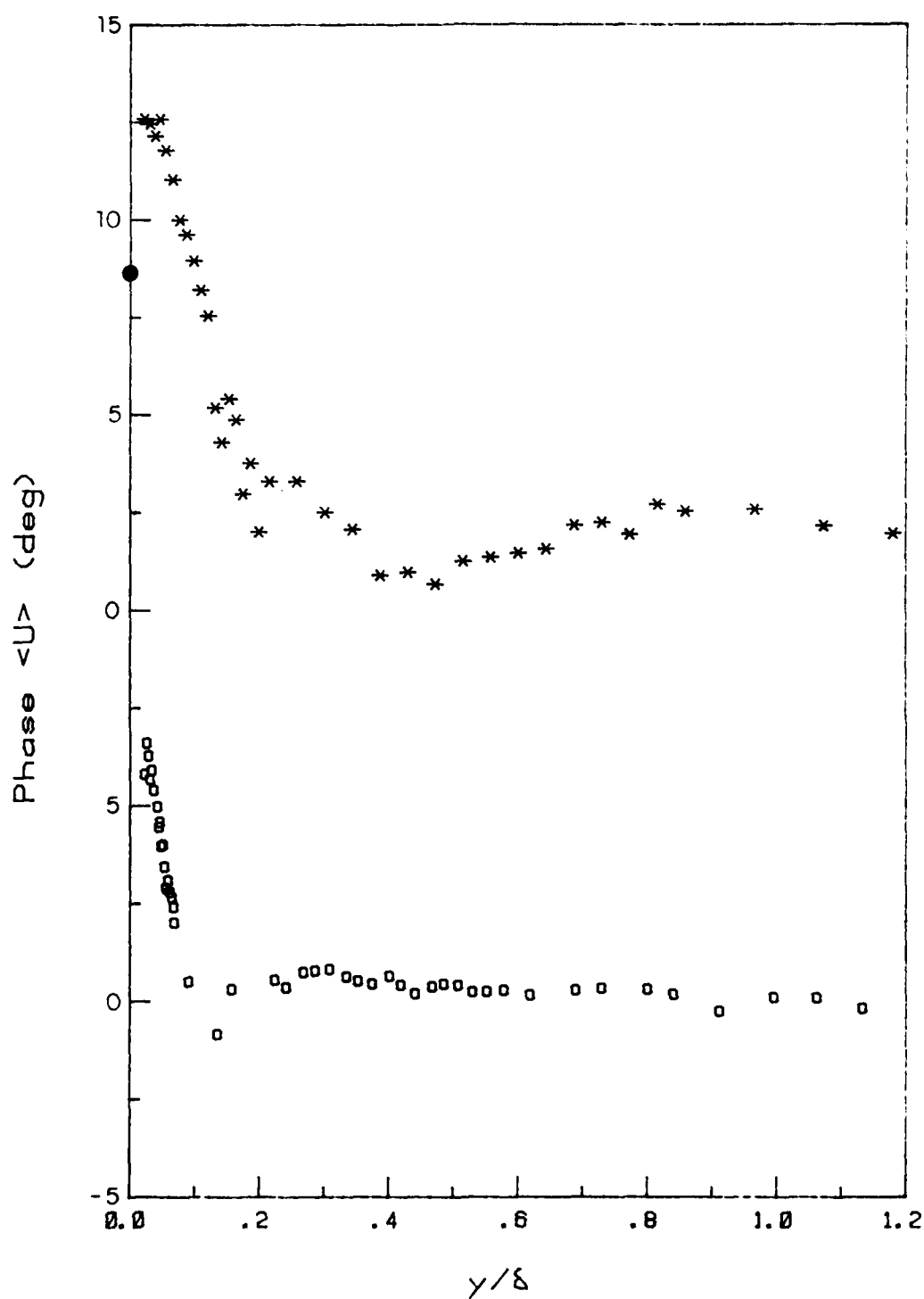
Figure 3.23. Phase distribution for the velocity at station 5.
●, phase of the wall shear stress for f = 0.5 Hz.
Other symbols as in Fig. 3.21.
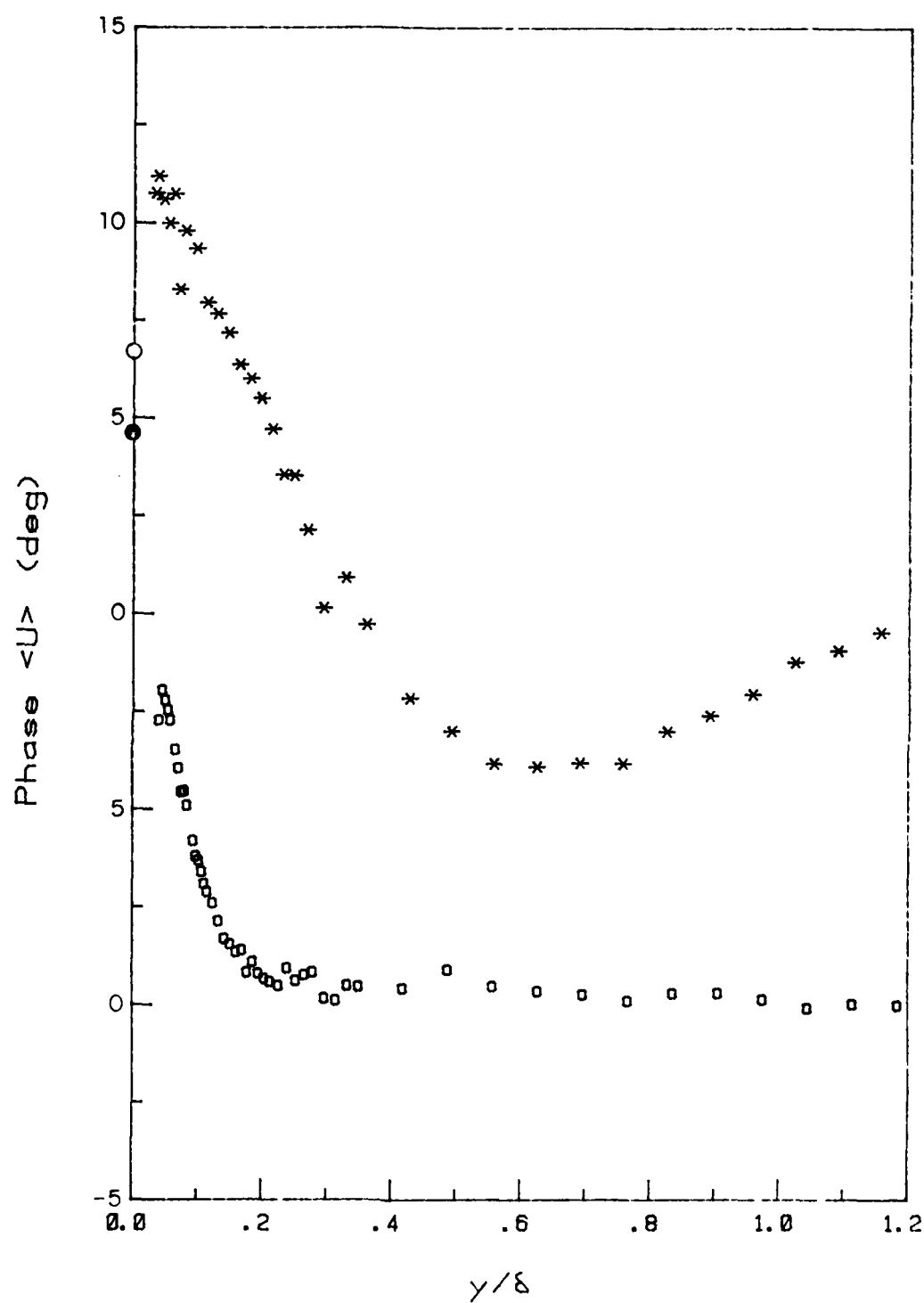
Figure 3.24. Phase distribution for the velocity at station 3. ●, phase of the wall shear stress for f = 0.5 Hz; O, f = 2 Hz. Other symbols as in Fig. 3.21.
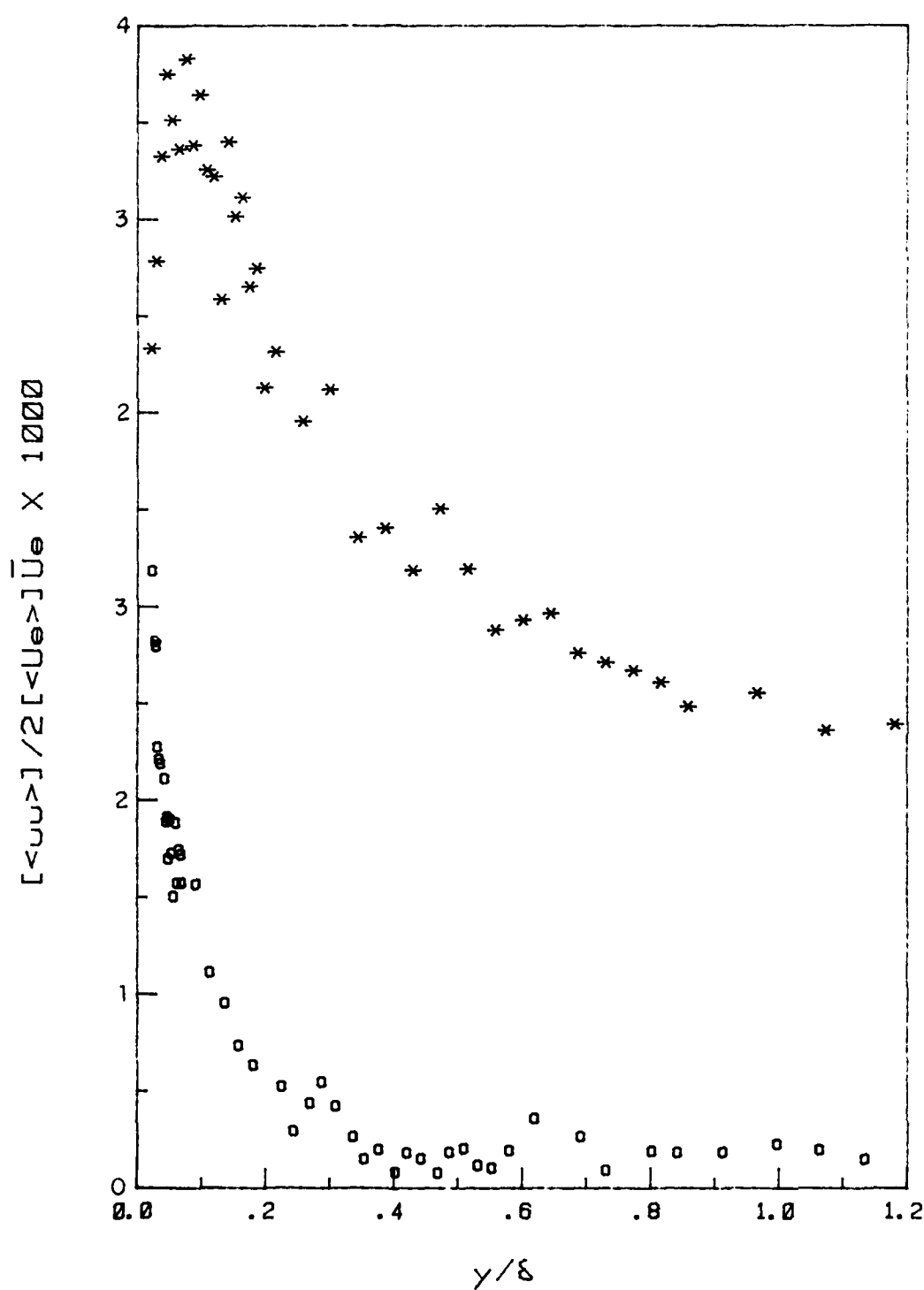
Figure 3.25. Amplitude distribution for $<u^2>$ at station 5. Symbols as in Fig. 3.21.
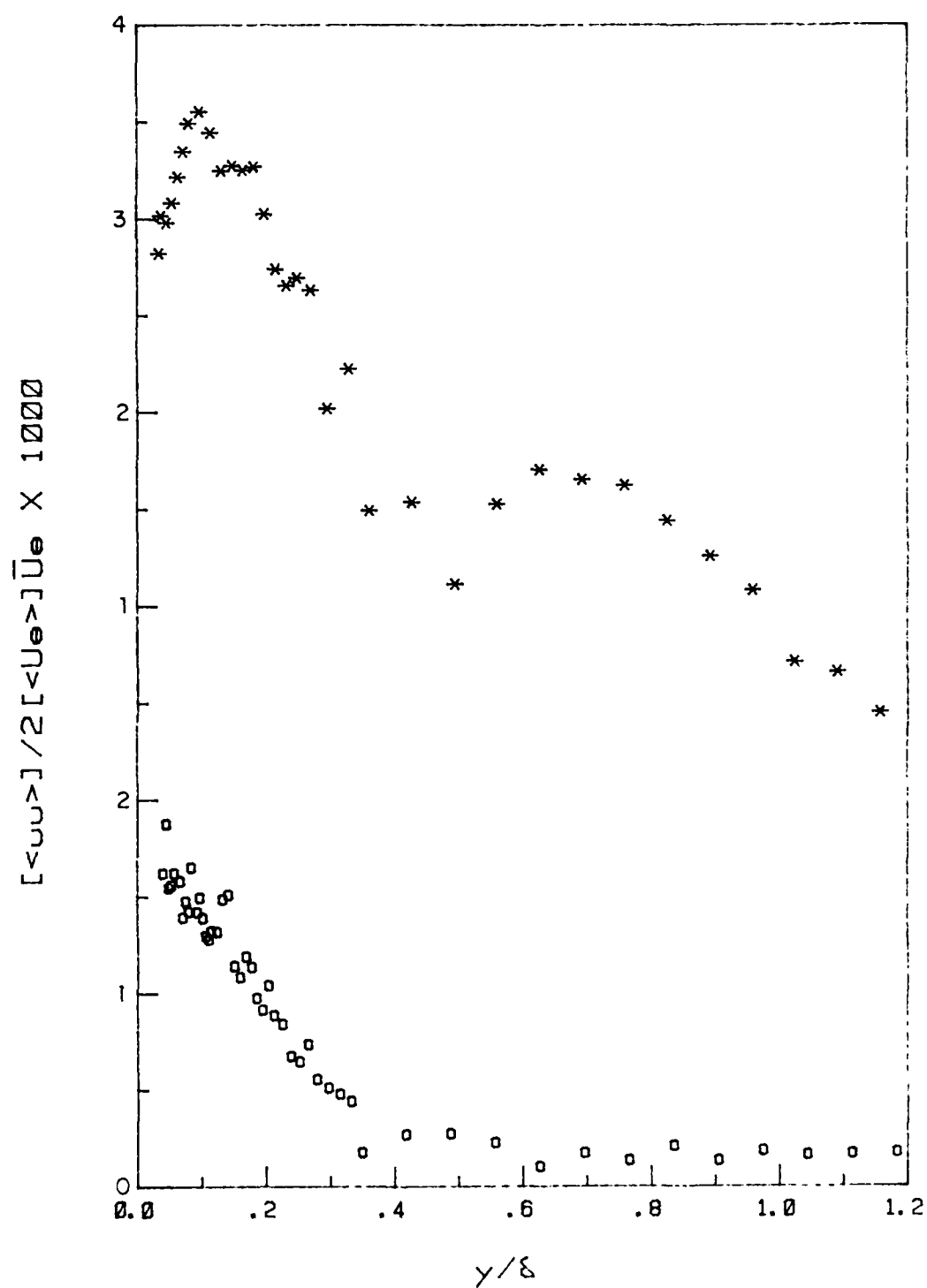
Figure 3.26. Amplitude distribution for $\langle u^2 \rangle$ at station 3. Symbols as in Fig. 3.21.
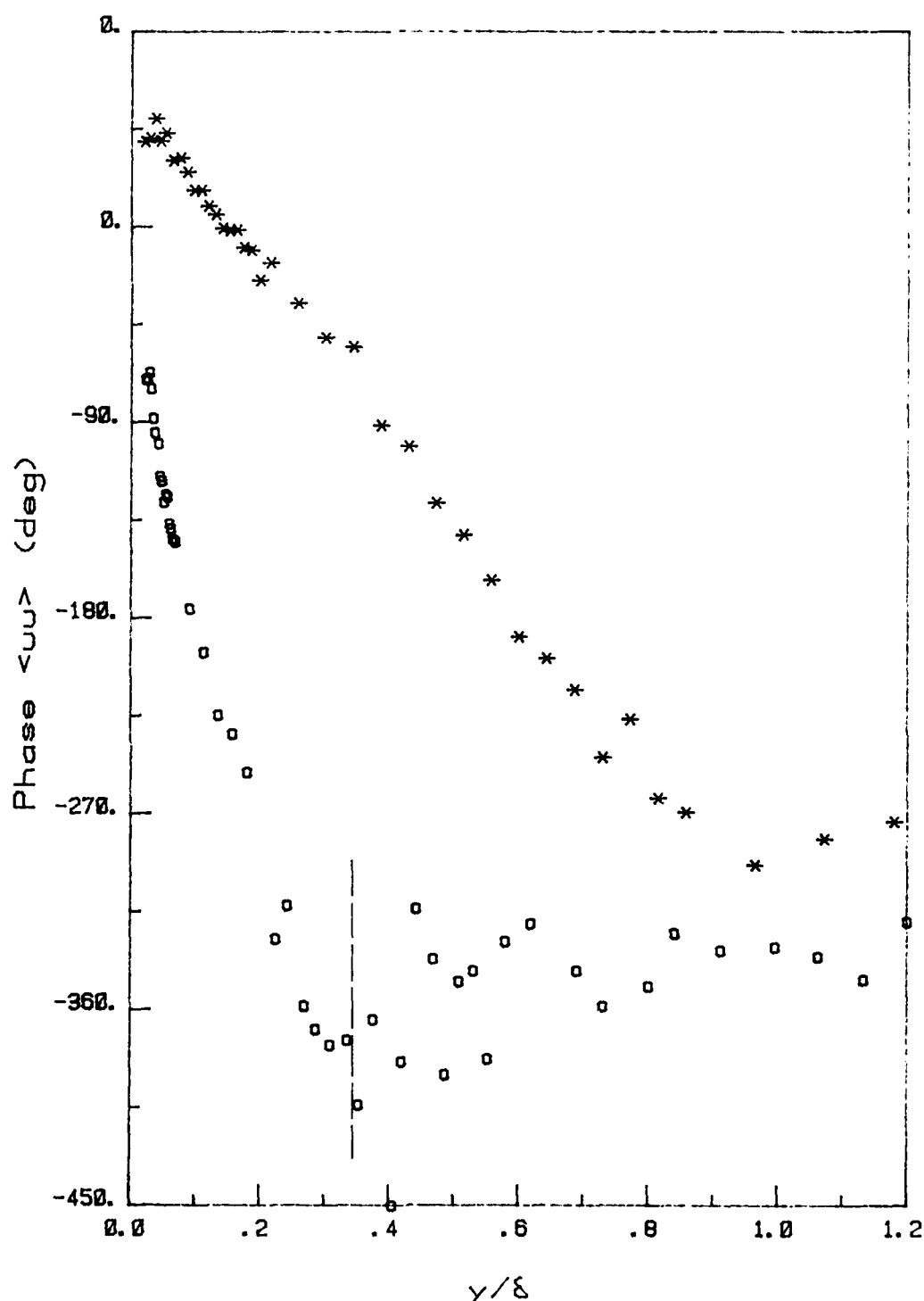
Figure 3.27. Phase distribution for $<u^2>$ at station 5. ---, edge of unsteady layer. Other symbols as in Fig. 3.21.
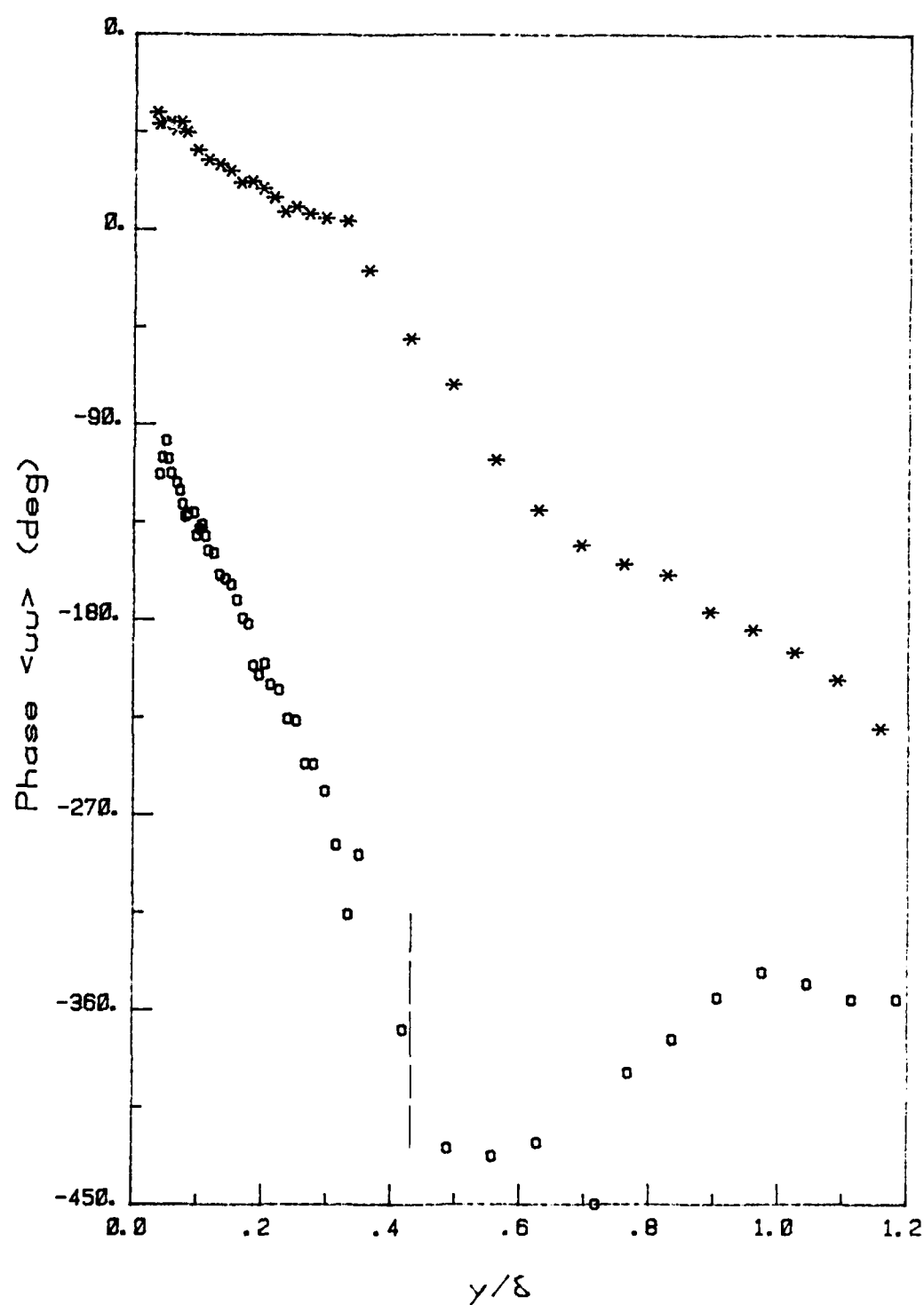
Figure 3.28. Phase distribution for $\langle u^2 \rangle$ at station 3.
---, edge of unsteady layer. Other symbols
as in Fig. 3.21.
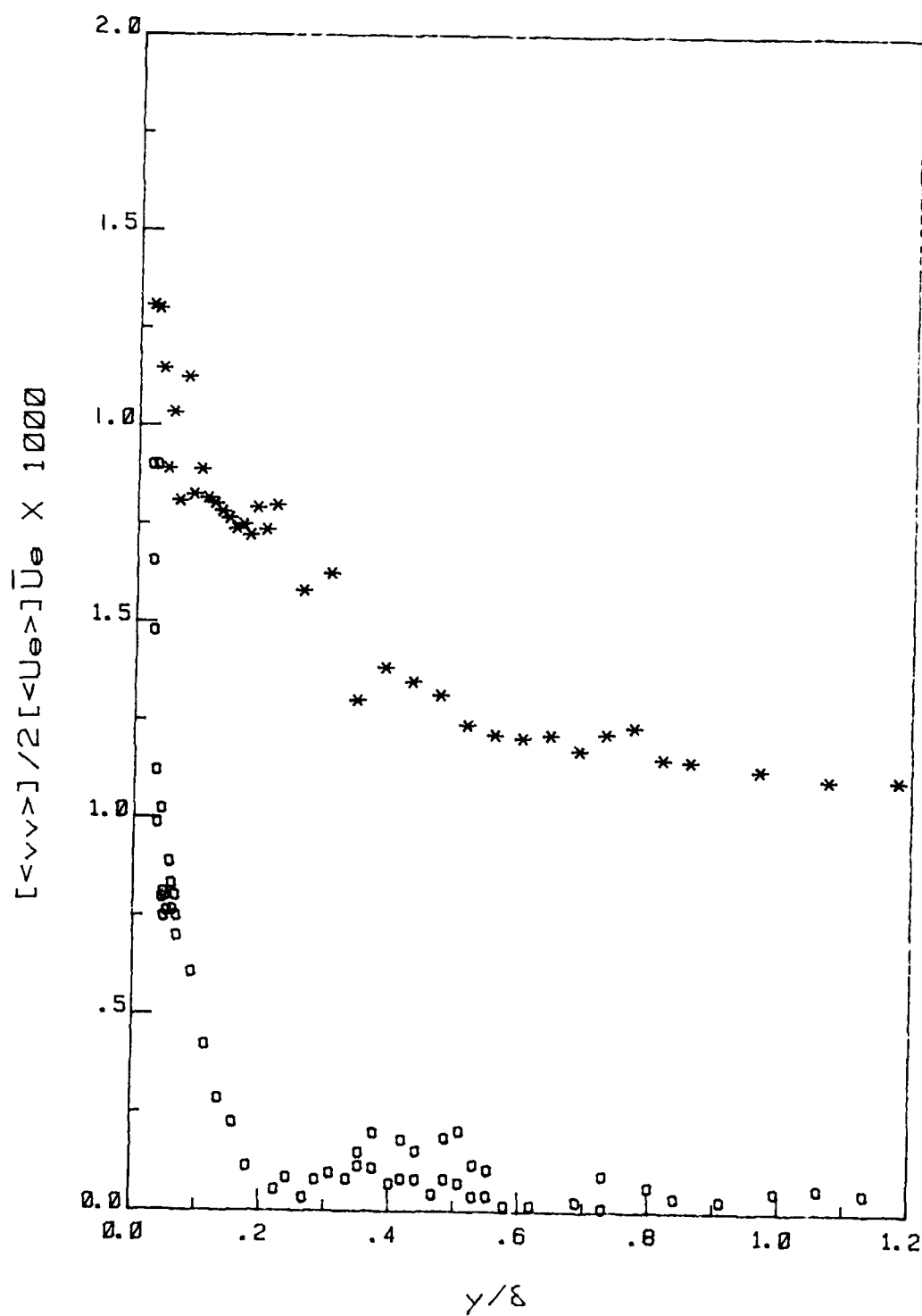
Figure 3.29. Amplitude distribution for $<v^2>$ at station 5. Symbols as in Fig. 3.21.
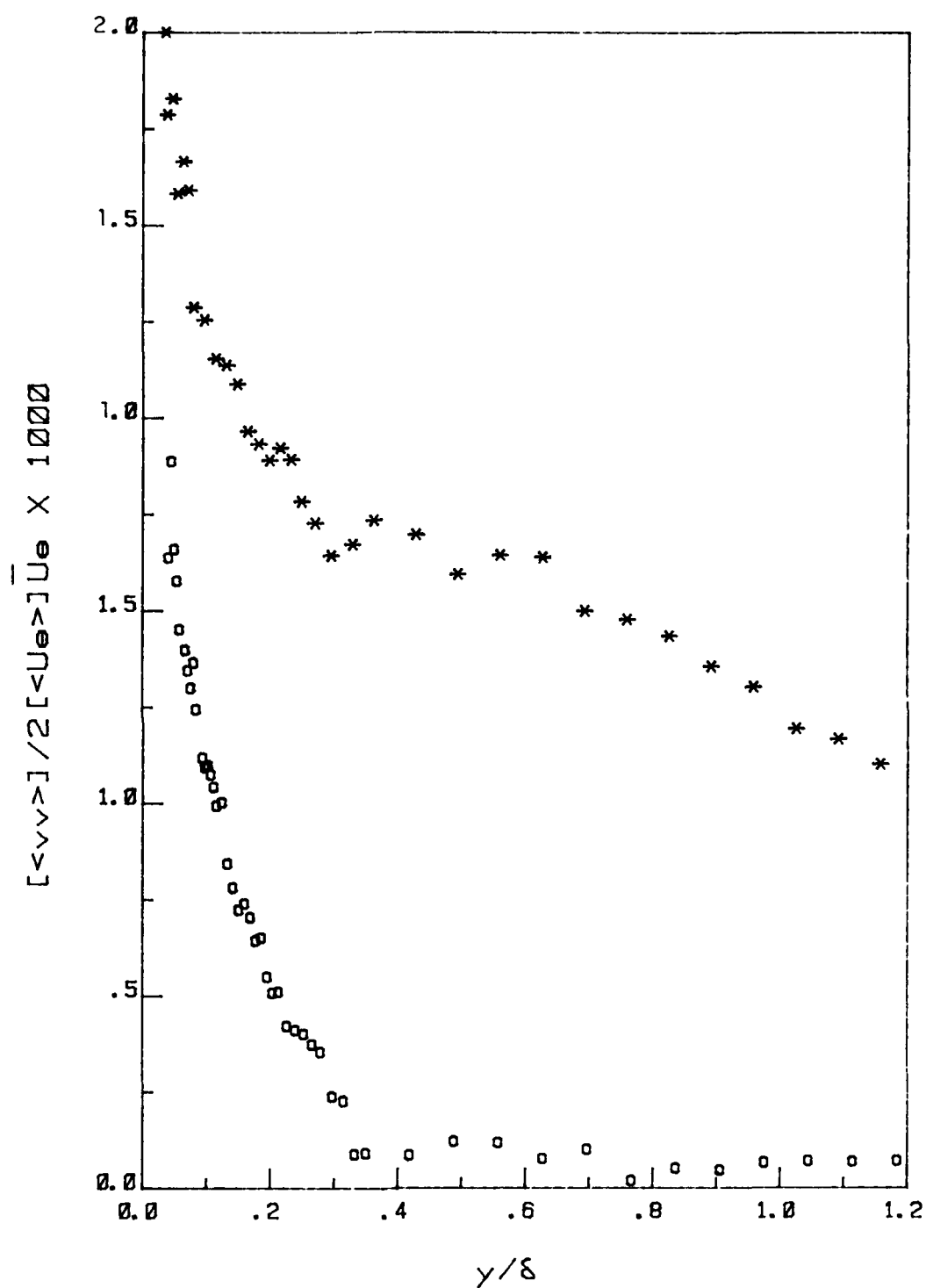
Figure 3.30. Amplitude distribution for $<v^2>$ at station 3. Symbols as in Fig. 3.21.
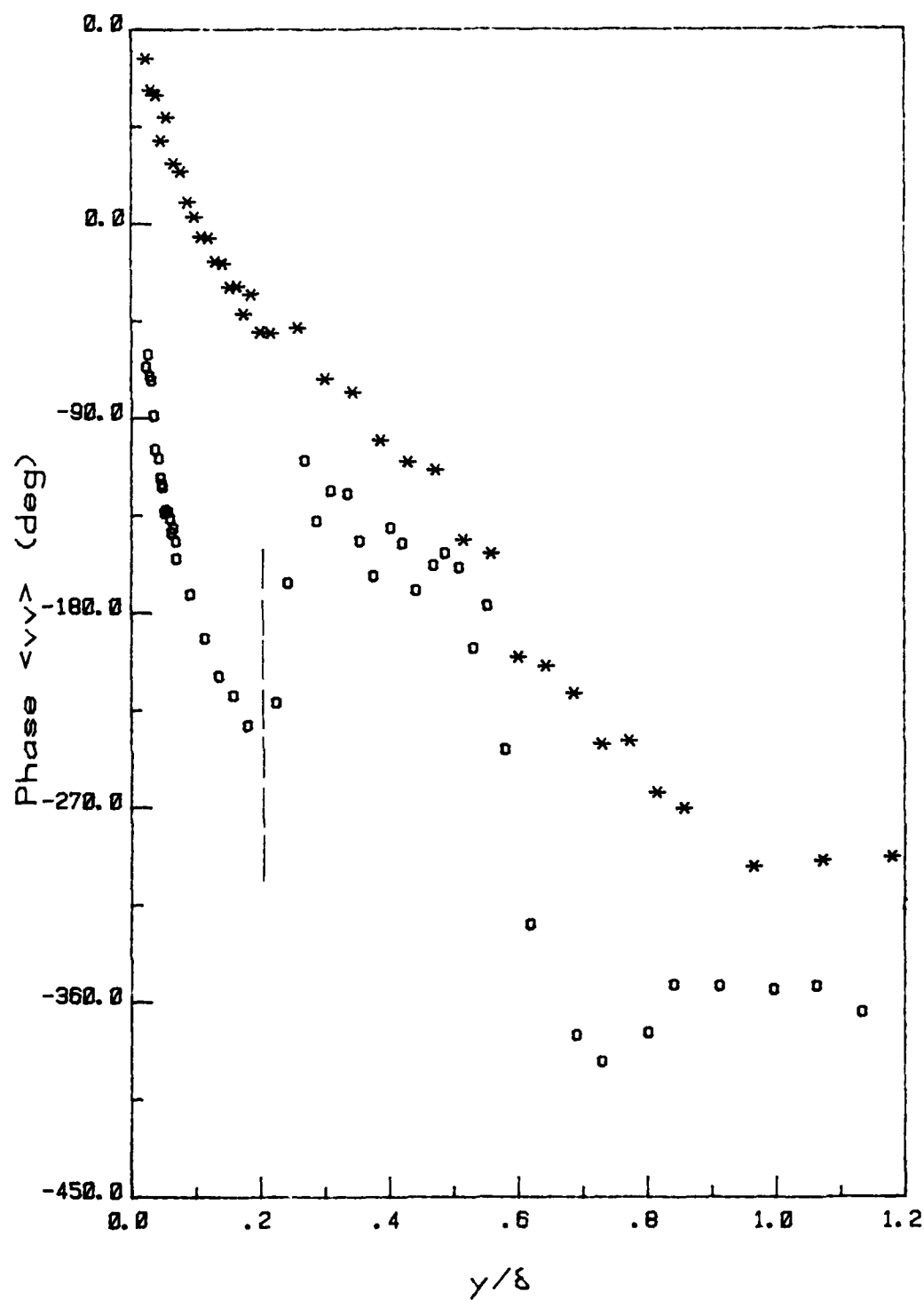
Figure 3.31. Phase distribution for $\langle v^2 \rangle$ at station 5.
---, edge of unsteady layer. Other symbols
as in Fig. 3.21.
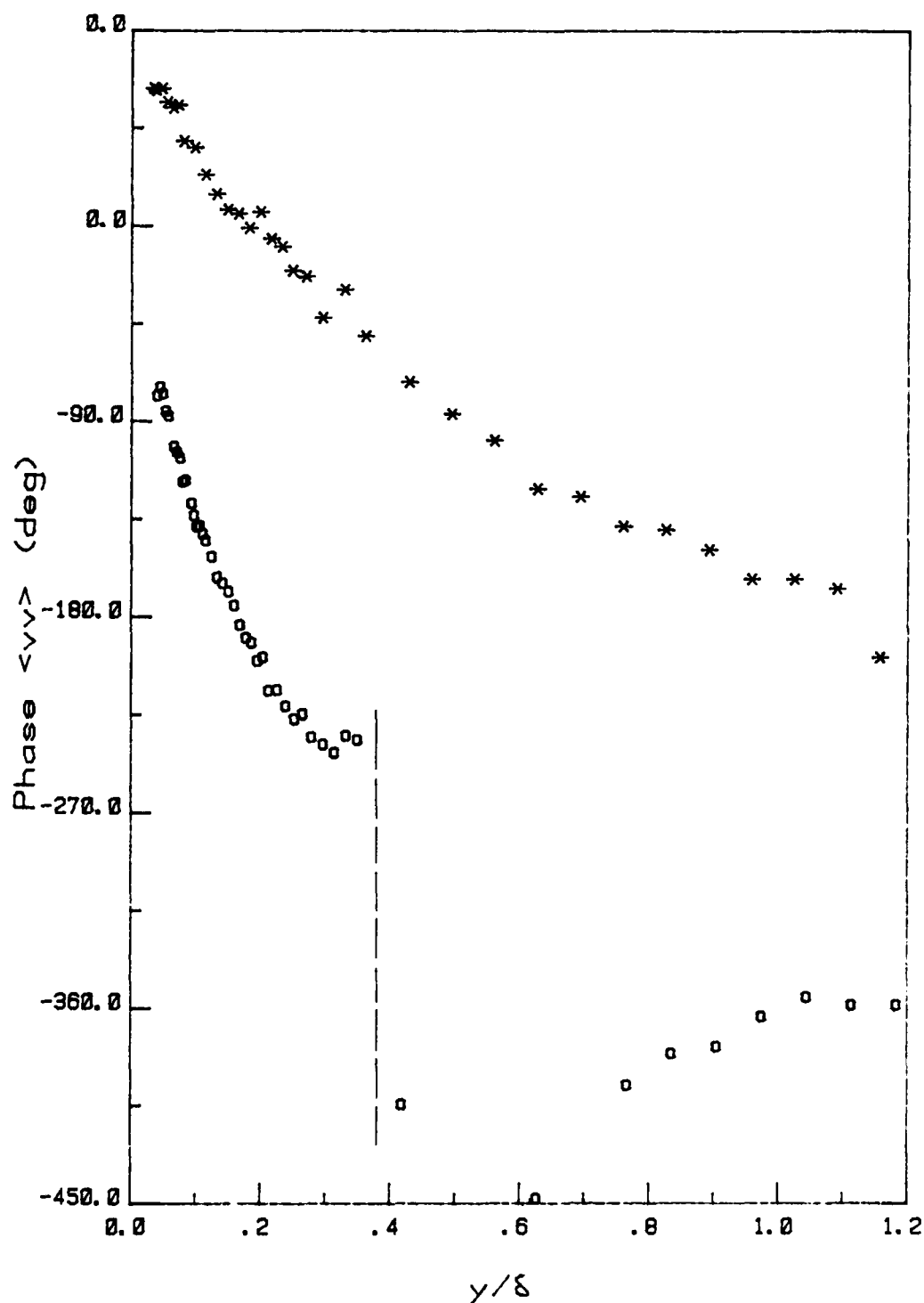
Figure 3.32. Phase distribution for $<v^2>$ at station 3.
---, edge of unsteady layer. Other symbols
as in Fig. 3.21.
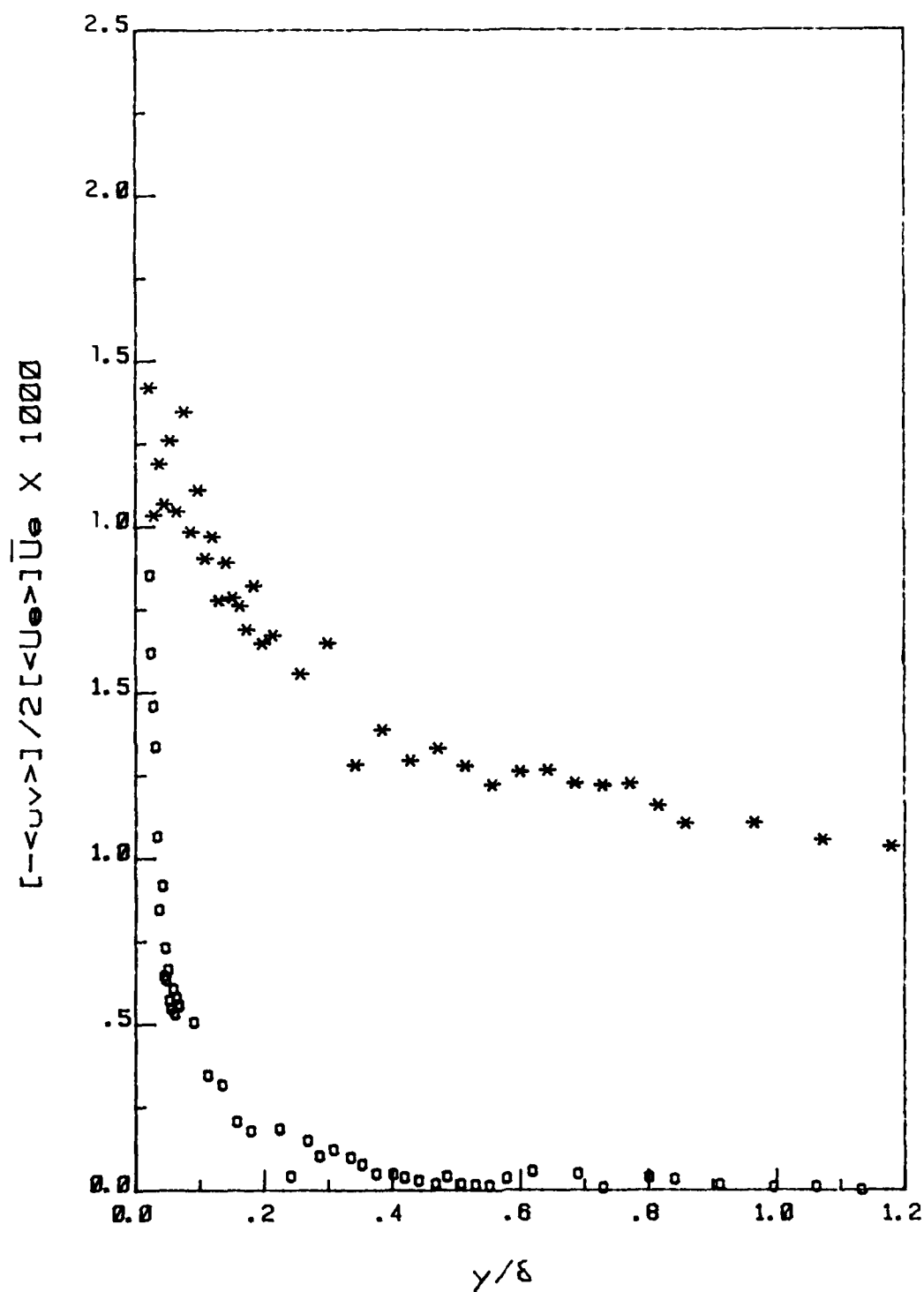
Figure 3.33. Amplitude distribution for - <uv> at station 5. Symbols as in Fig. 3.21.
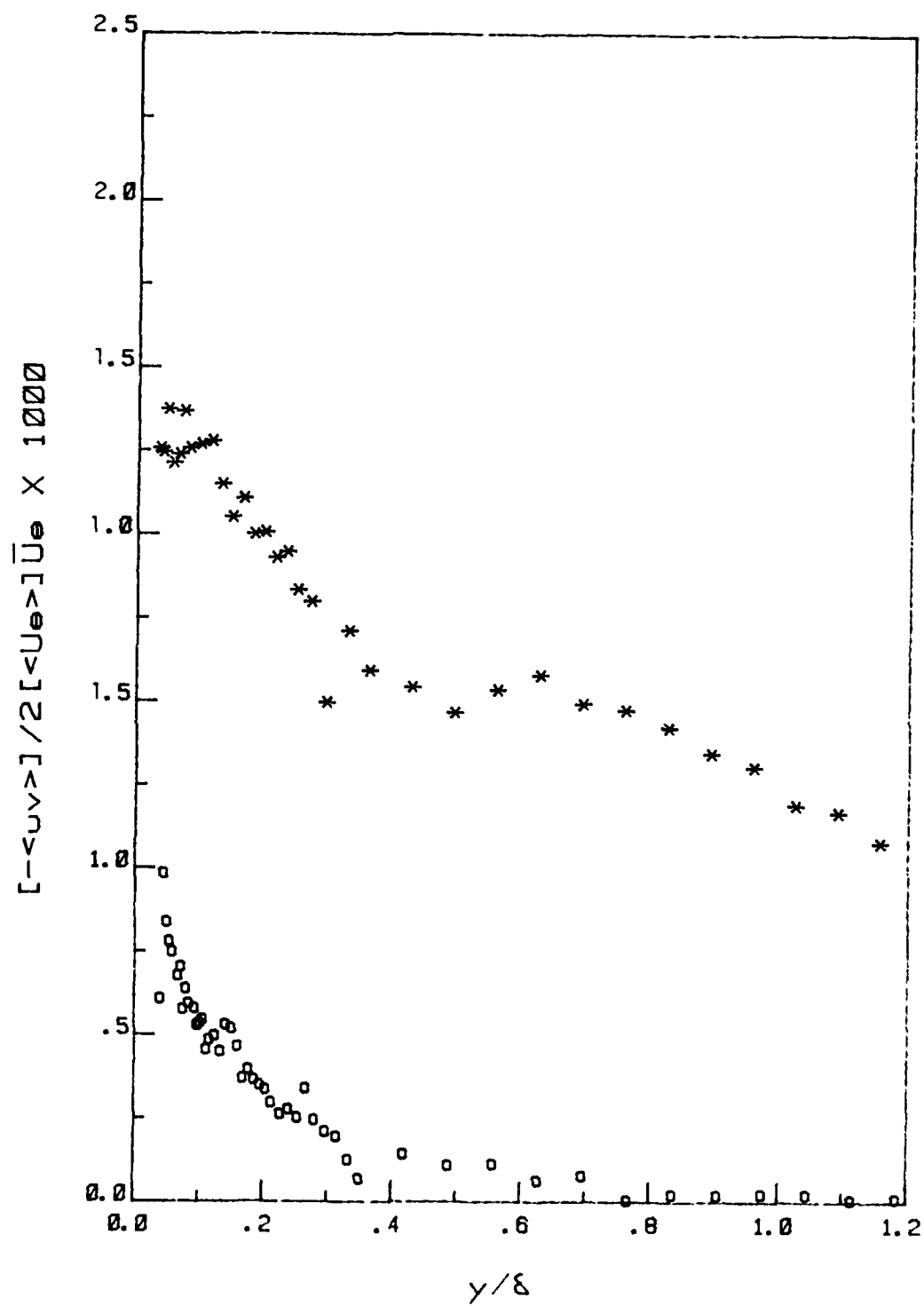
Figure 3.34. Amplitude distribution for - ‹uv› at station 3.
Symbols as in Fig. 3.21.
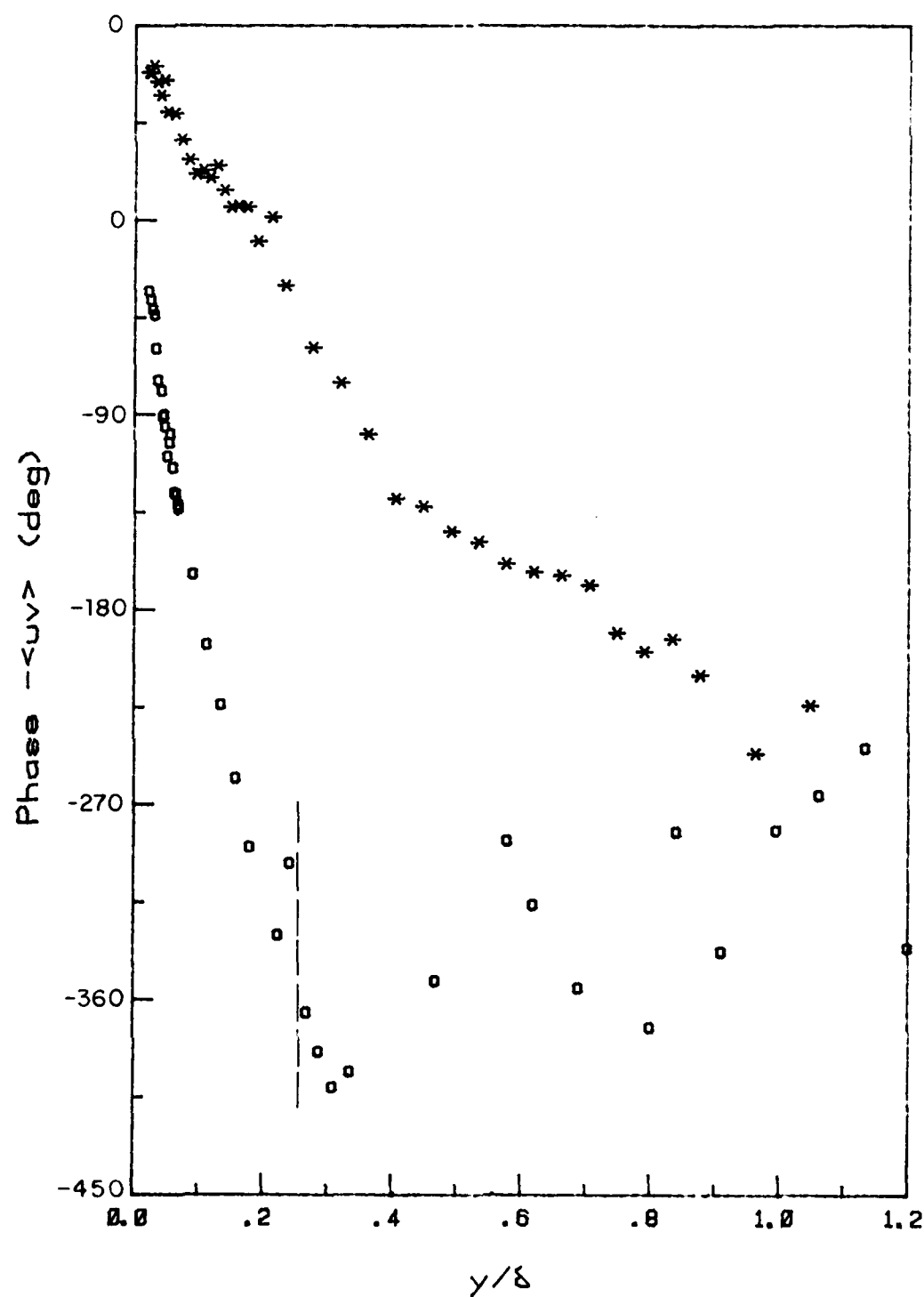
Figure 3.35. Phase distribution for - <uv> at station 5.
---, edge of unsteady layer. Other symbols
as in Fig. 3.21.
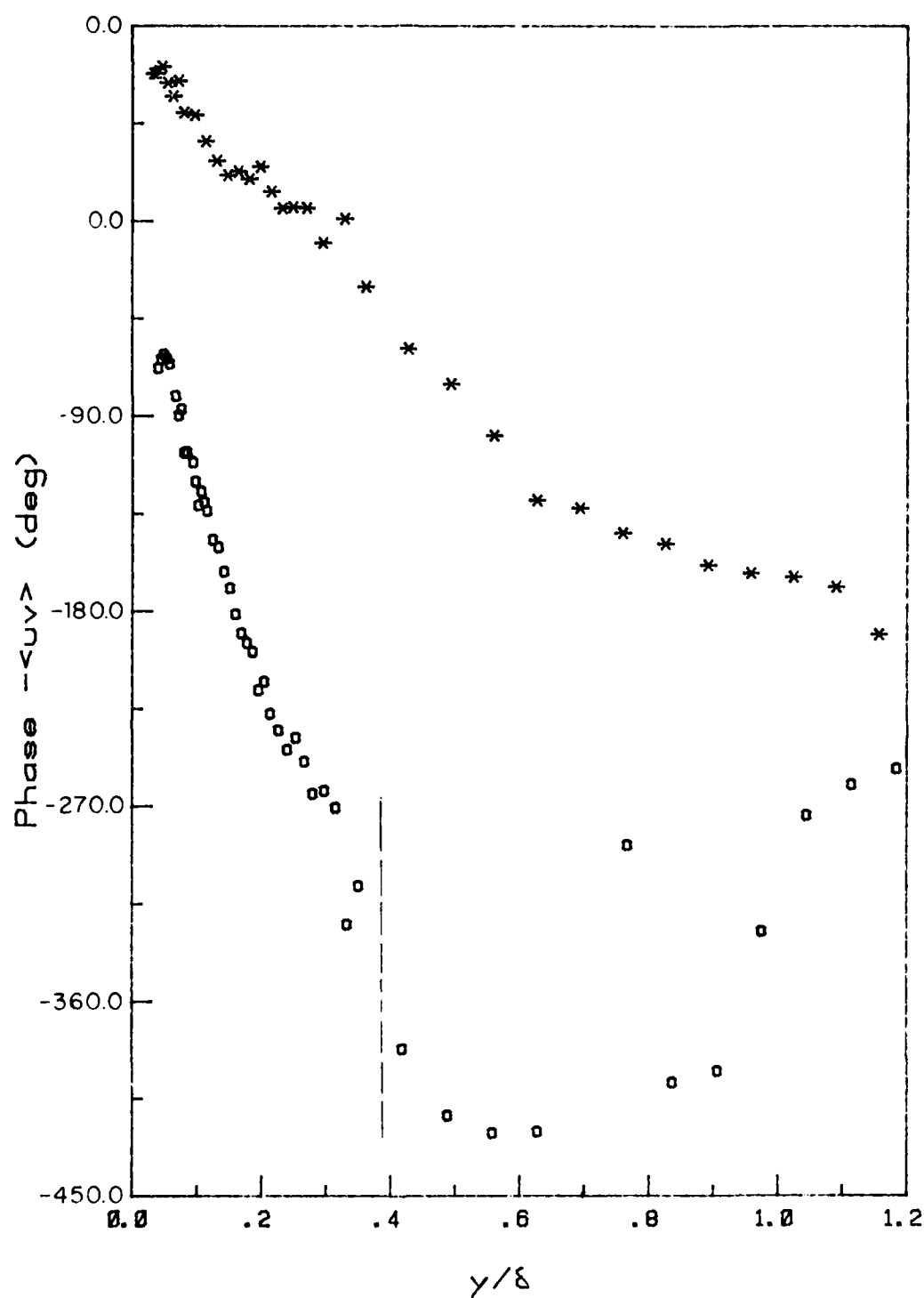
Figure 3.36. Phase distribution for - <uv> at station 3.
---, edge of unsteady layer. Other symbols
as in Fig. 3.21.
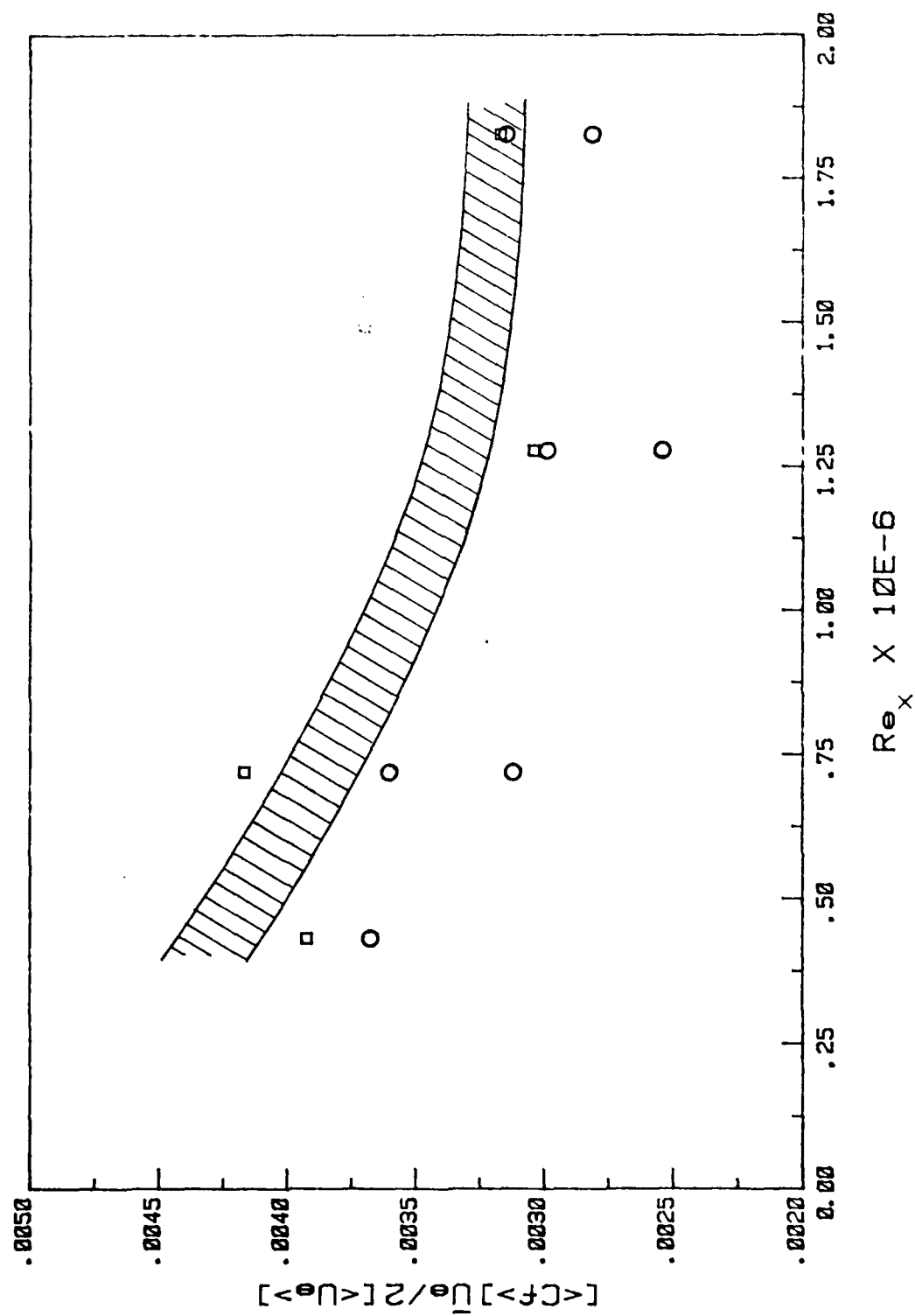
Figure 3.37. Longitudinal distribution of $[\langle C_f \rangle]$. □, f = 0.5 Hz; 0, f = 2 Hz; ▨, quasi-steady.
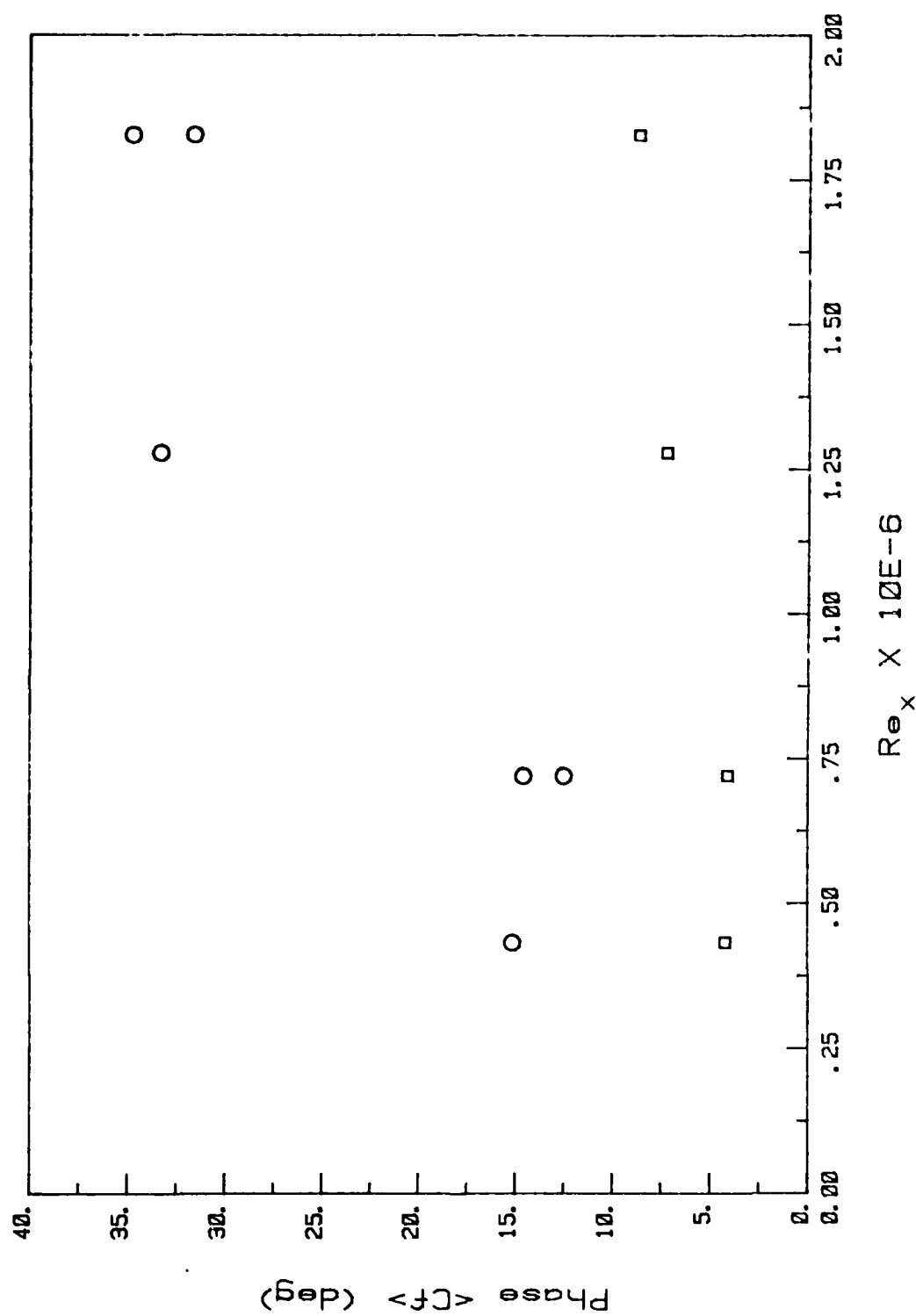
Figure 3.38. Longitudinal distribution of the phase of $<C_f>$. Symbols as in Fig. 3.37.
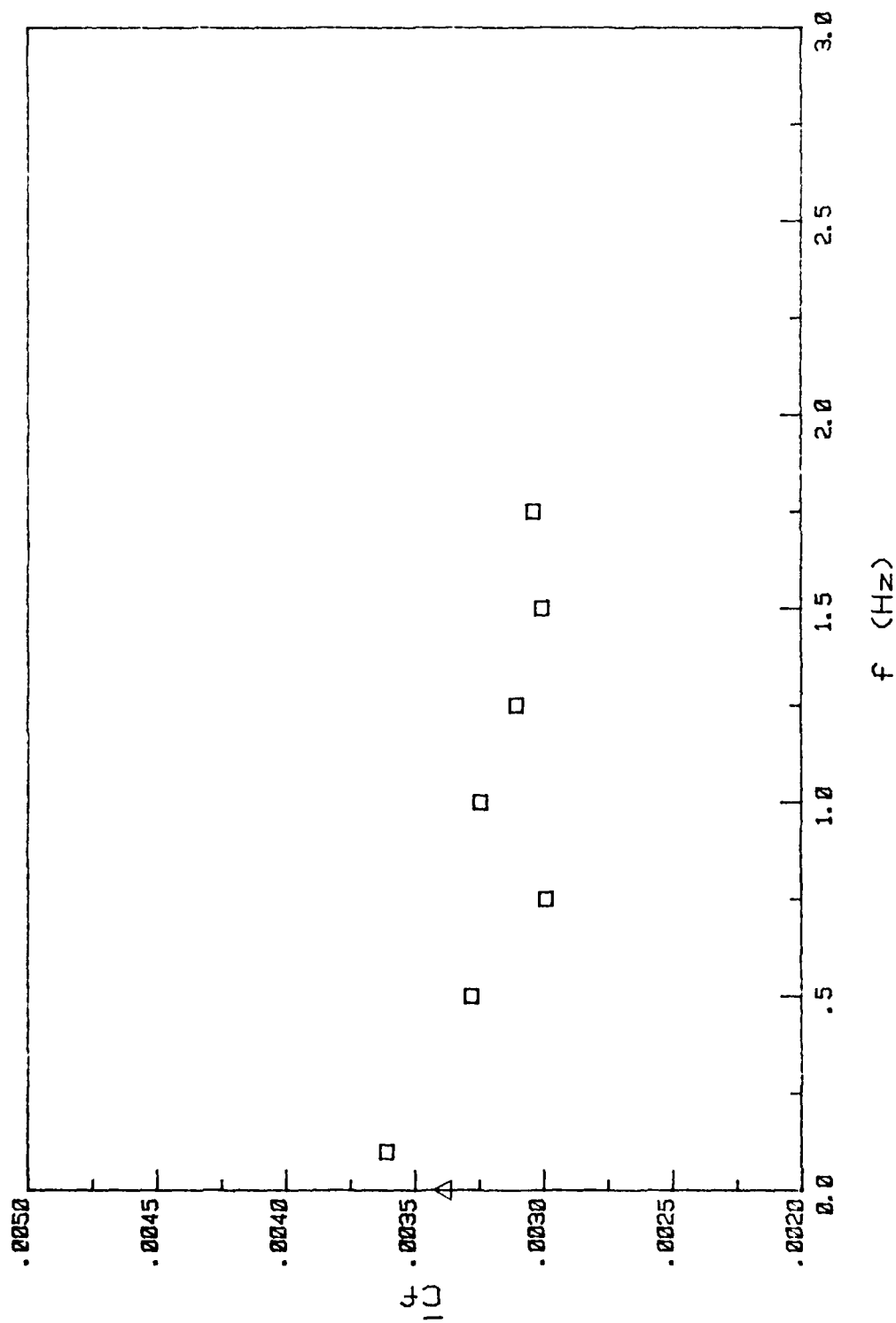
Figure 3.39. Frequency variation of $\overline{C_f}$ at station 5. $\triangle$, quasi-steady value.
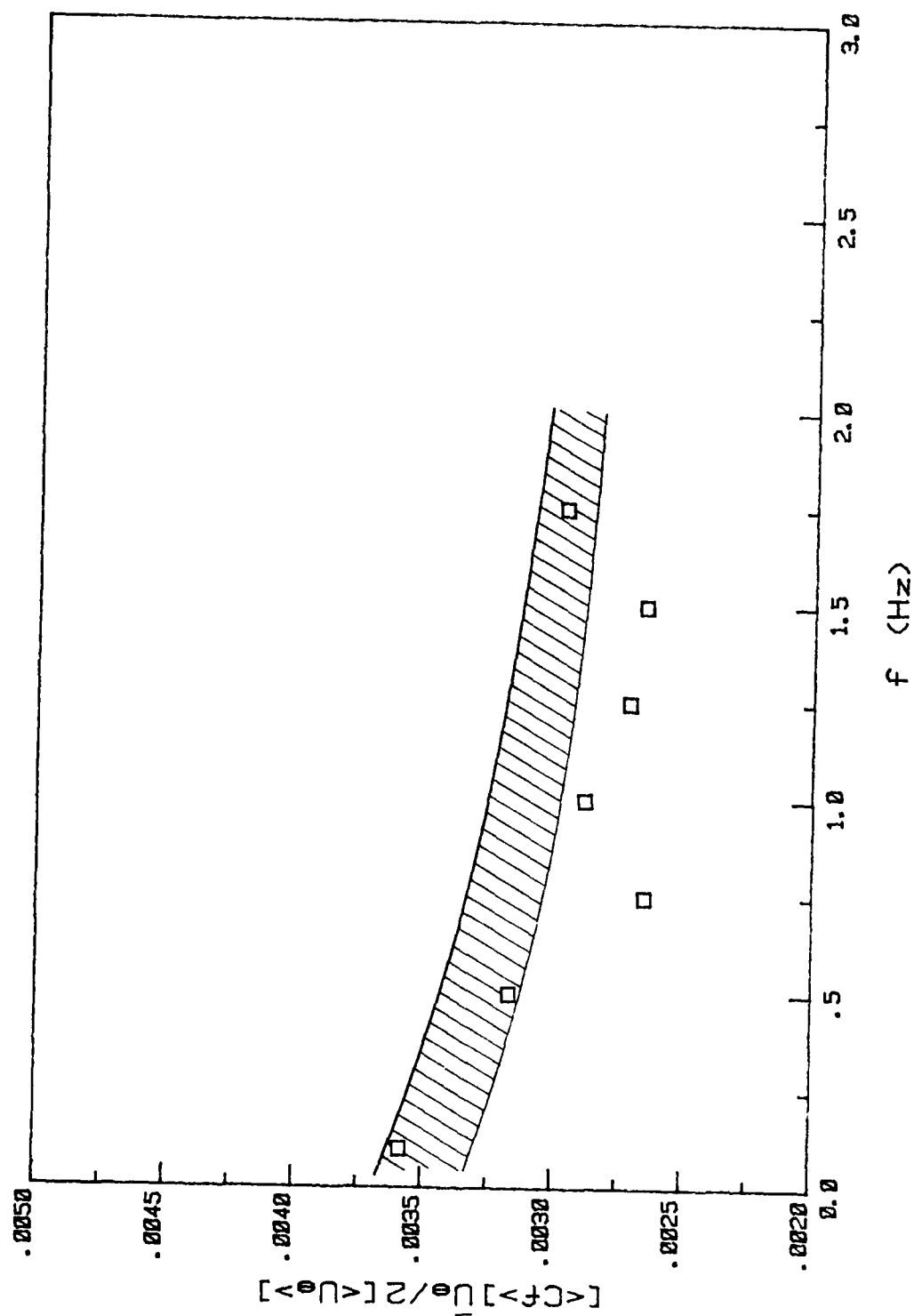
Figure 3.40. Frequency variation of $[<C_f>]$. ▨, quasi-steady distribution.

The plot has an x-axis labeled f (Hz) ranging from 0.0 to 3.0, and a y-axis labeled $[<C_f>]\bar{U}e/2[<U_e>]$ ranging from .0020 to .0050.

113
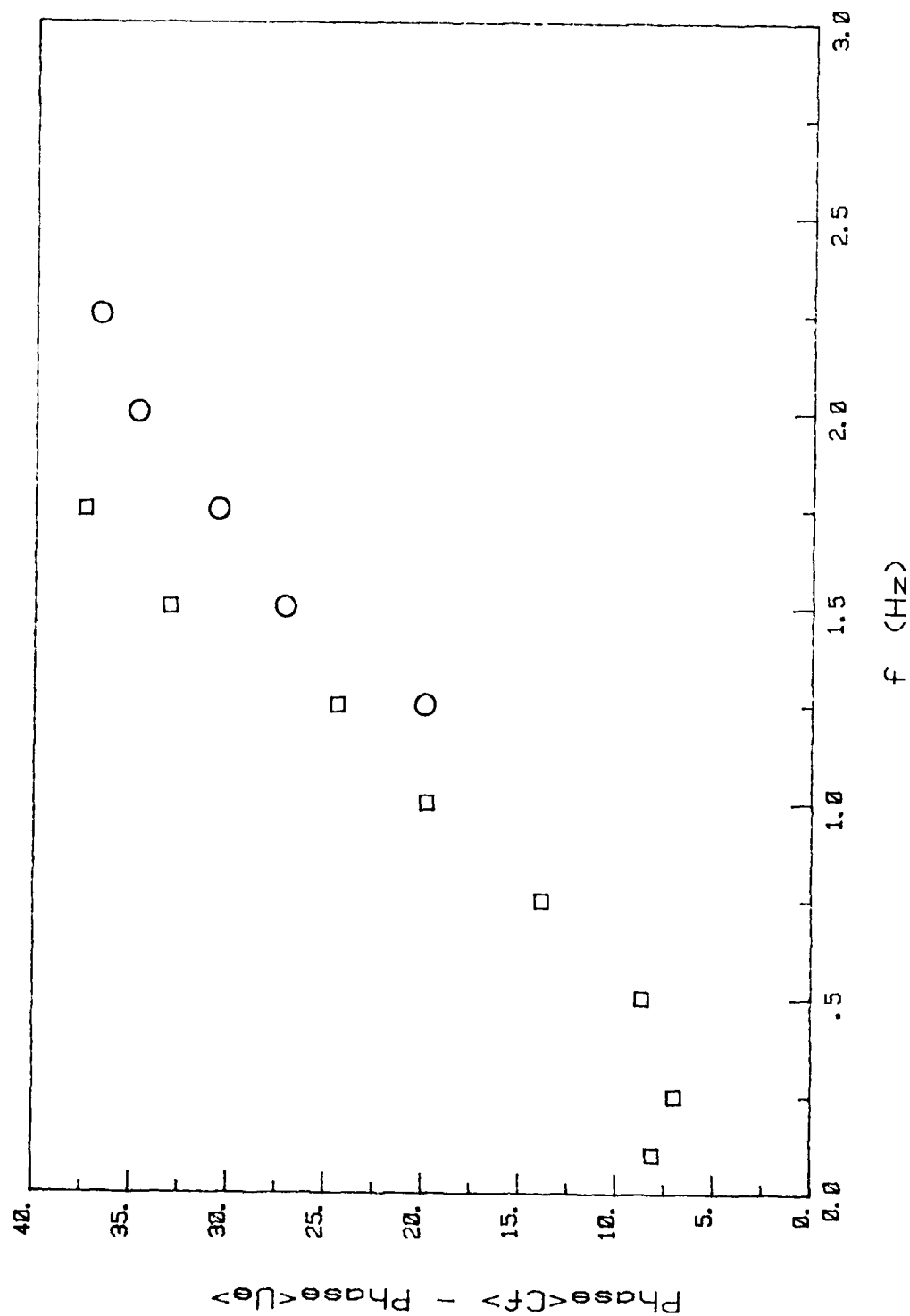
Figure 3.41. Frequency variation of the phase of $<C_f>$. □ , using the sleeve for
f = 0.5 Hz; 0, f = 2 Hz.
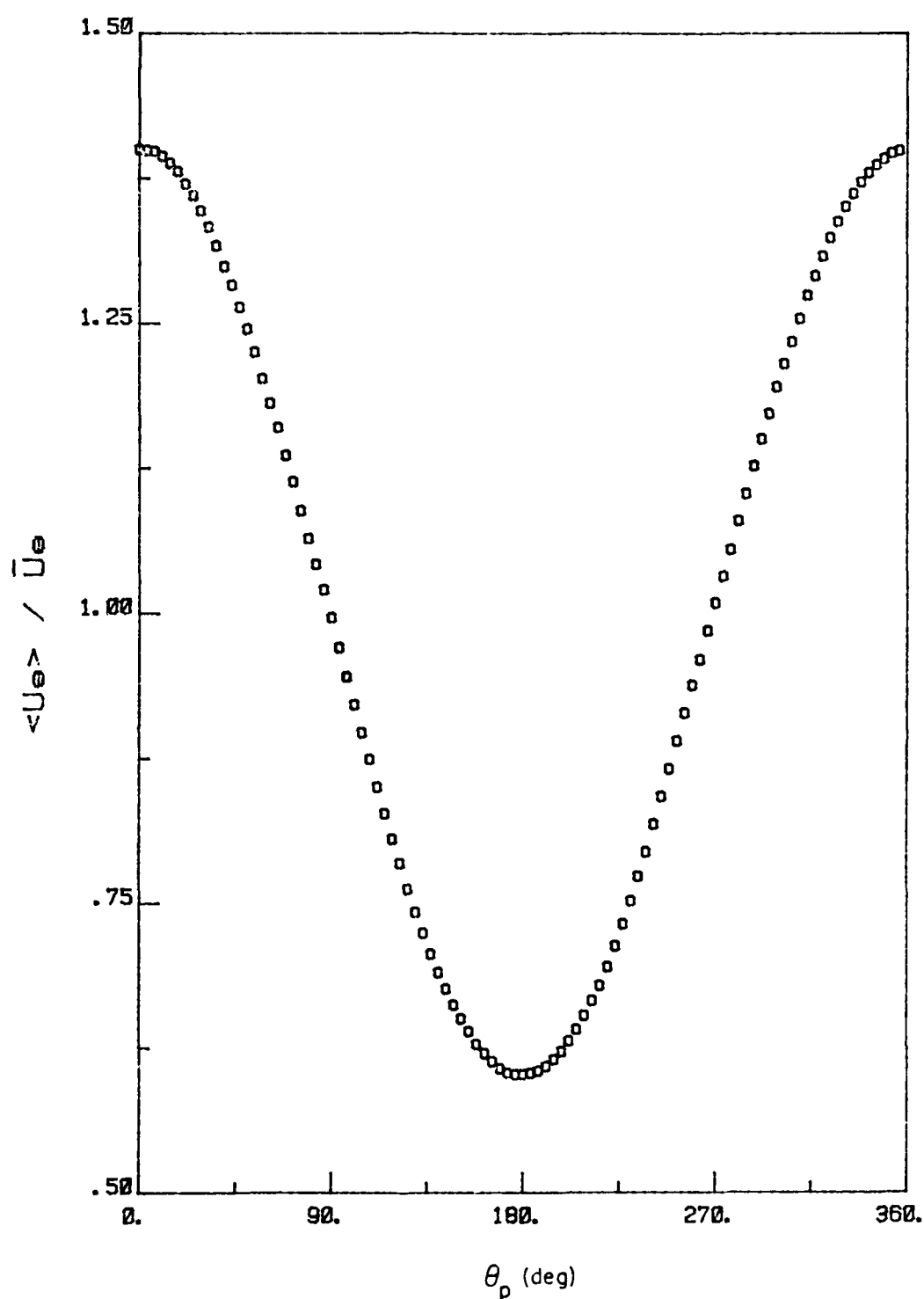
Figure 3.42. Phasewise variation of the free-stream velocity at station 5 and f = 2 Hz.
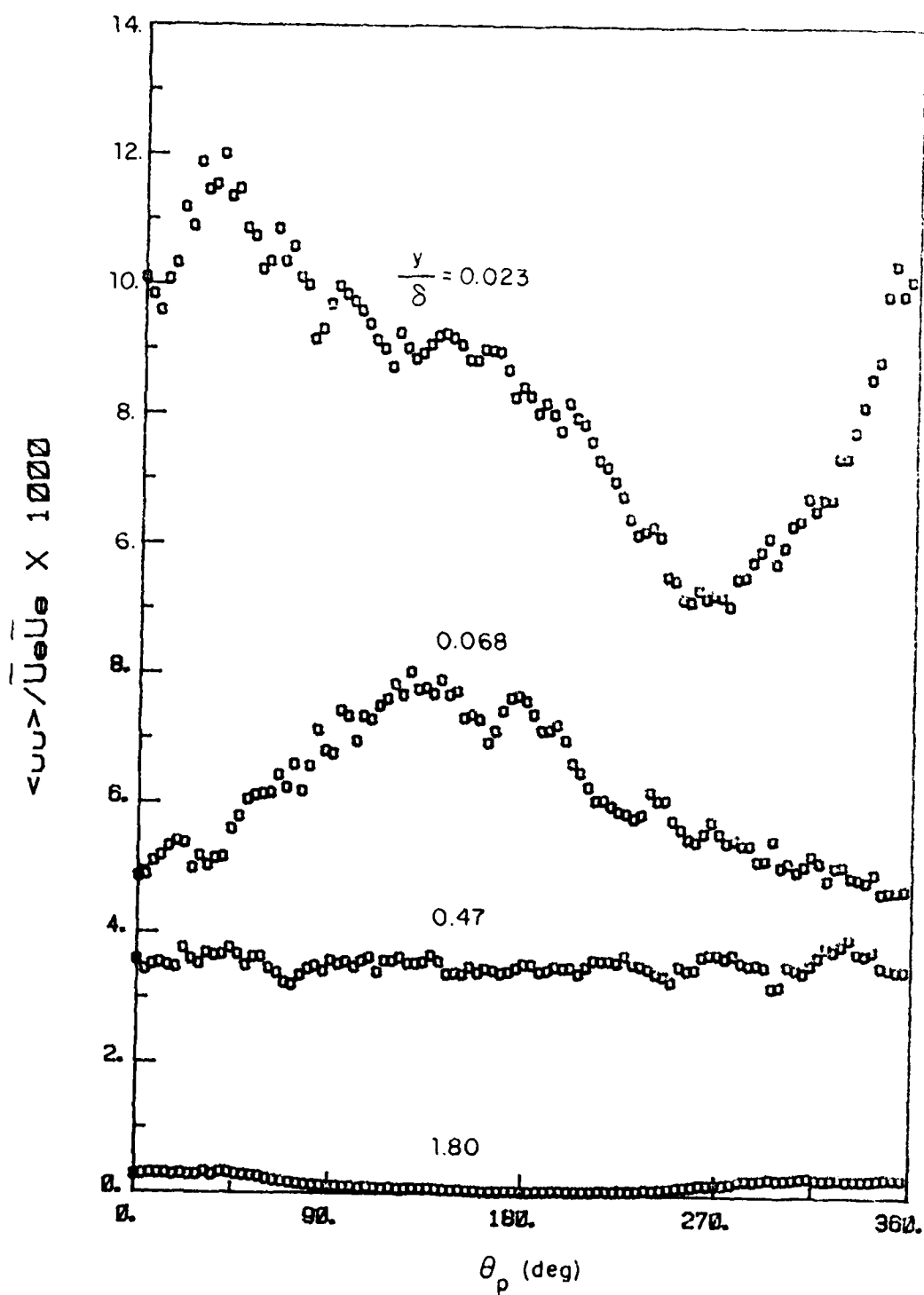
Figure 3.43. Phasewise variation of $<u^2>$ at station 5 and $f = 2$ Hz.
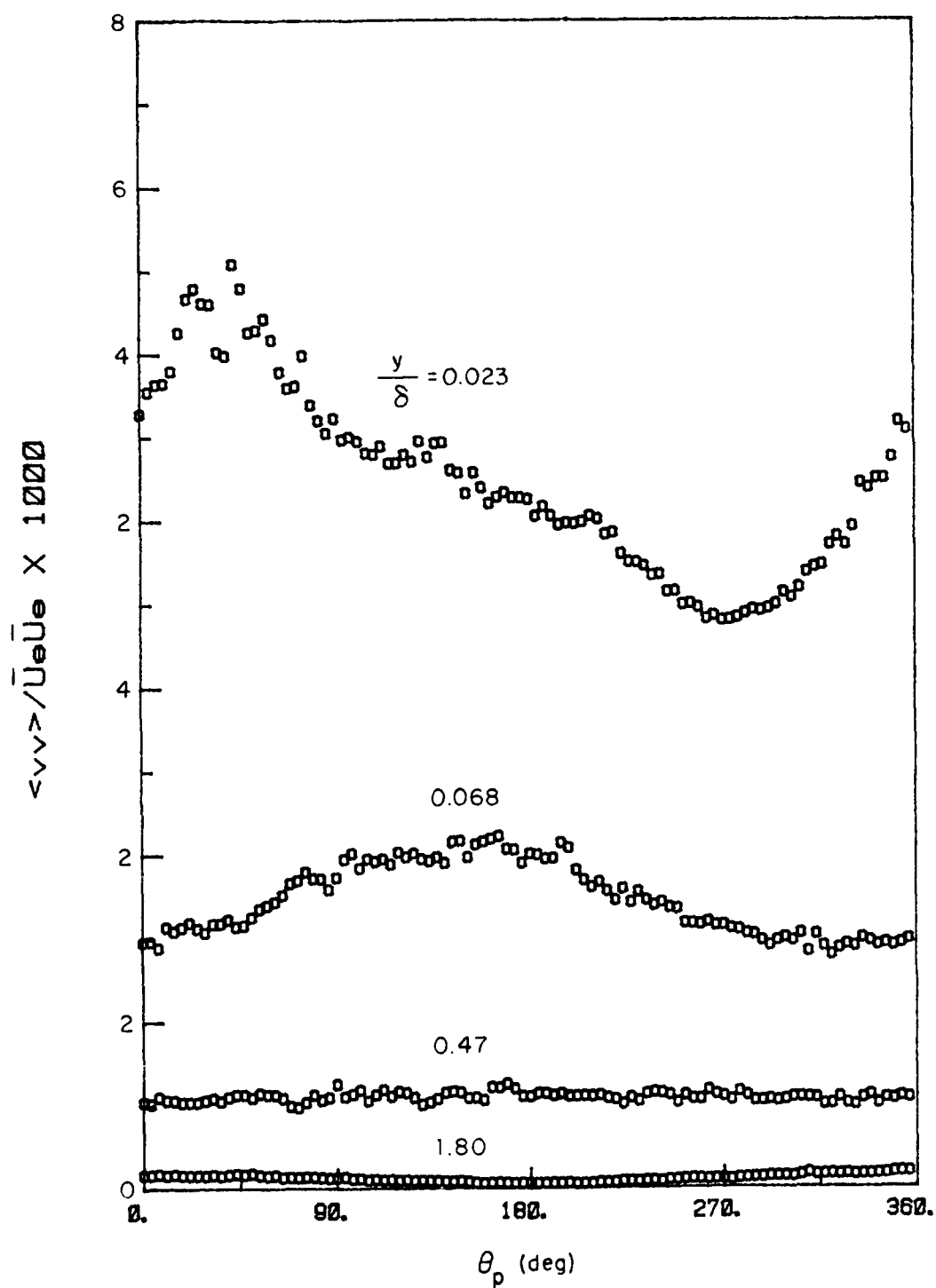
Figure 3.44.   Phasewise variation of $<v^2>$ at station 5 and
              f = 2 Hz.
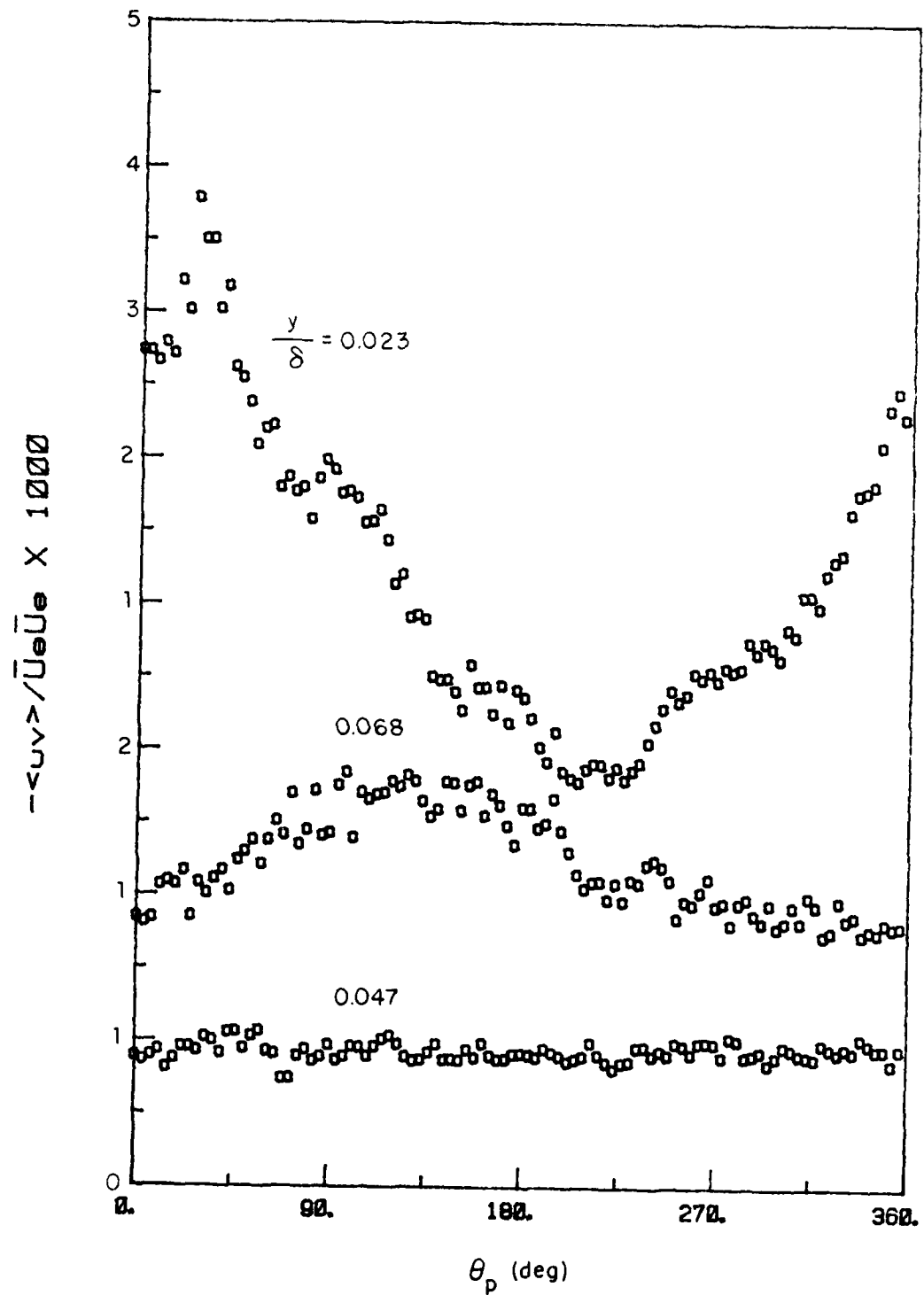
Figure 3.45. Phasewise variation of − <uv> at station 5 and f = 2 Hz.
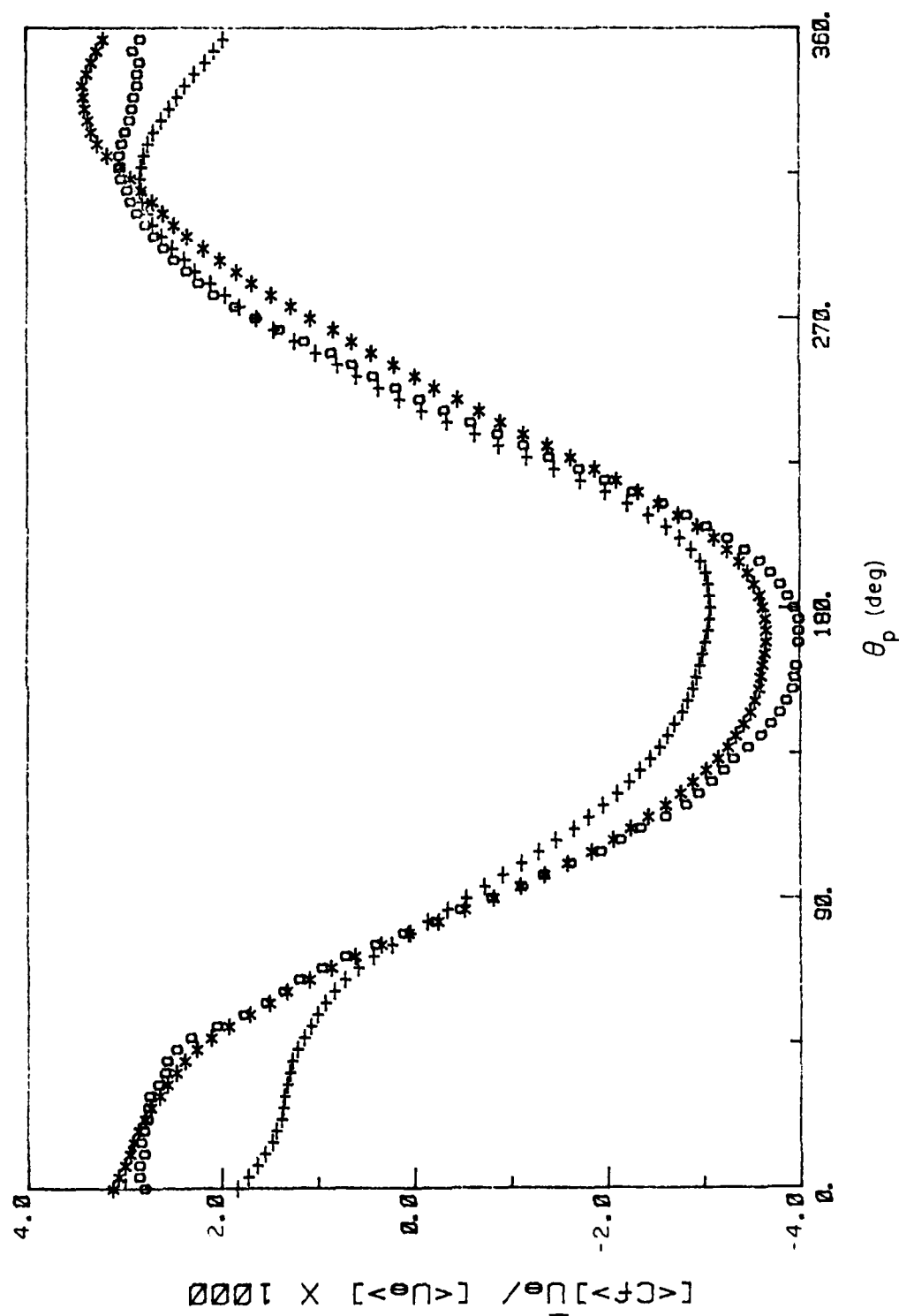
Figure 3.46. Phasewise variation of $[<C_f>]$ at $f = 2$ Hz. o , x = 48 cm; *, x = 80 cm; +, x = 203 cm.
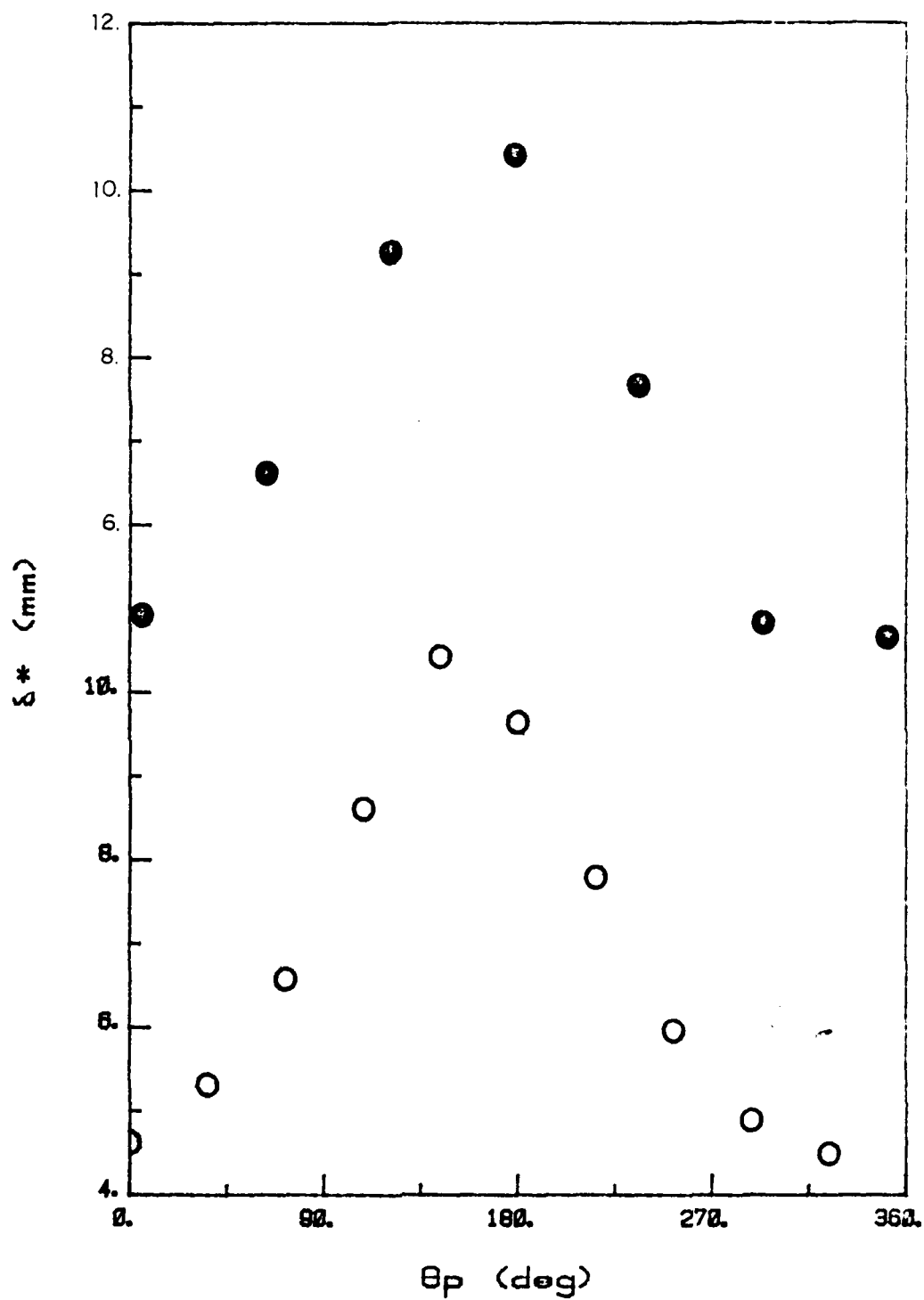
Figure 3.47. Phasewise distribution of $\langle \delta_* \rangle$. ●, f = 0.5 Hz; 0, f = 2 Hz.
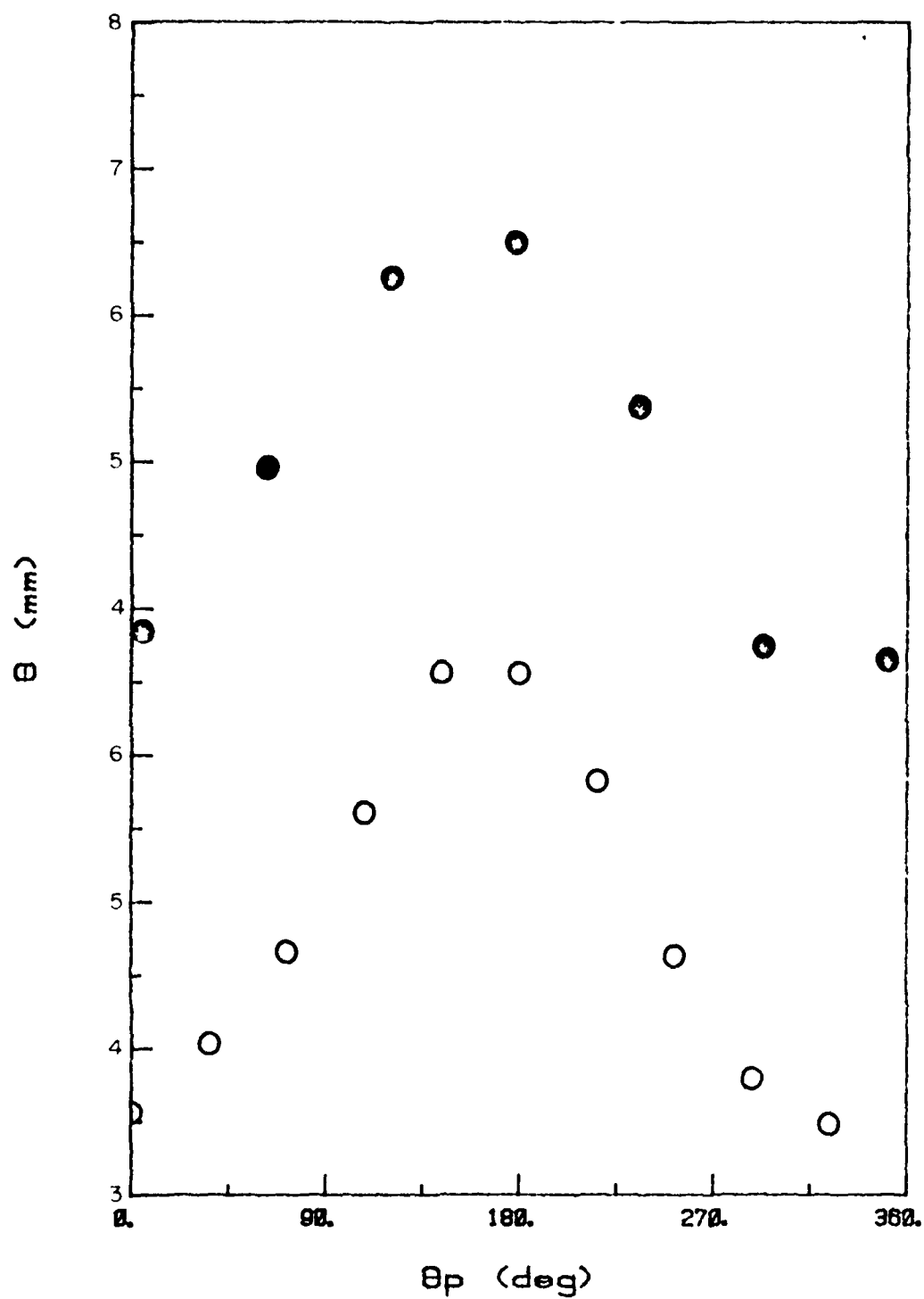
Figure 3.48. Phasewise distribution of <θ>. Symbols as in
Fig. 3.47.

Figure 3.49. Phasewise distribution of <H>. Symbols as in
Fig. 3.47.
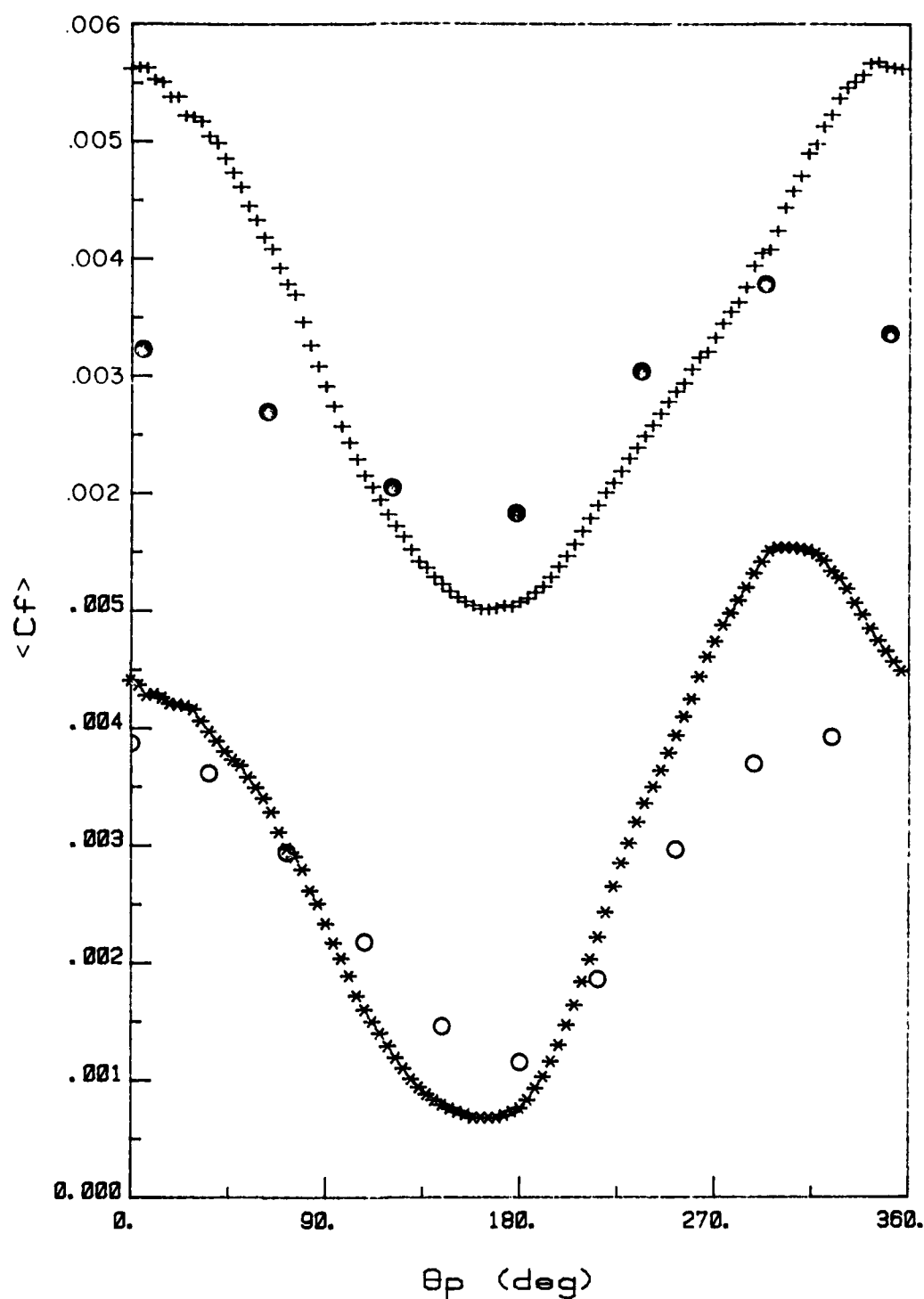
Figure 3.50. Phasewise distribution of $<C_f>$. O, f = 2 Hz, from Clauser-plot; ●, f = 0.5 Hz, from Clauser-plot; *, f = 2 Hz, measured; +, f = 0.5 Hz, measured.
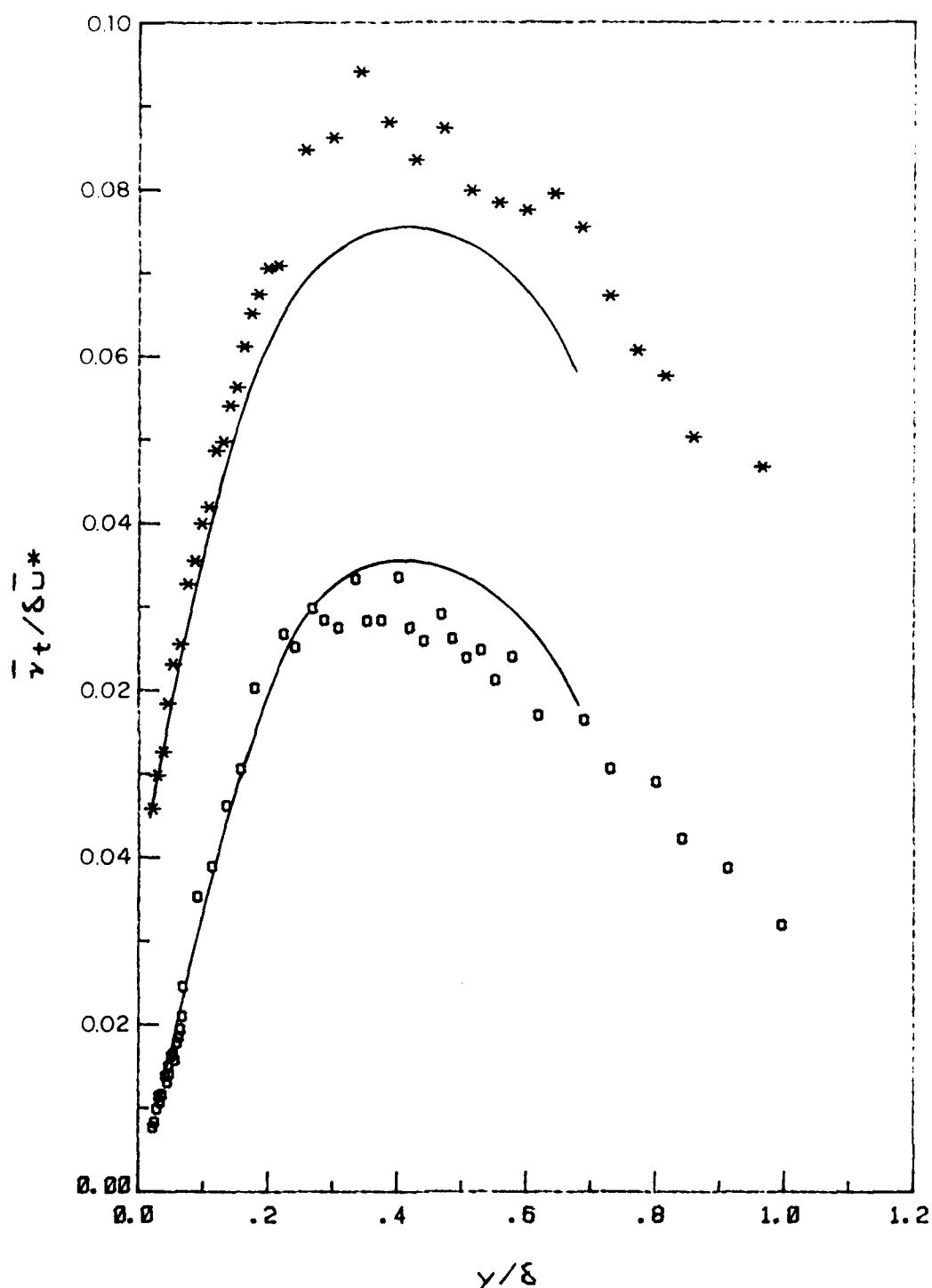
Figure 3.51. Time-mean distribution for $\langle v_t \rangle$. *, f = 0.5 Hz, o , f = 2 Hz ; —— , quasi-steady
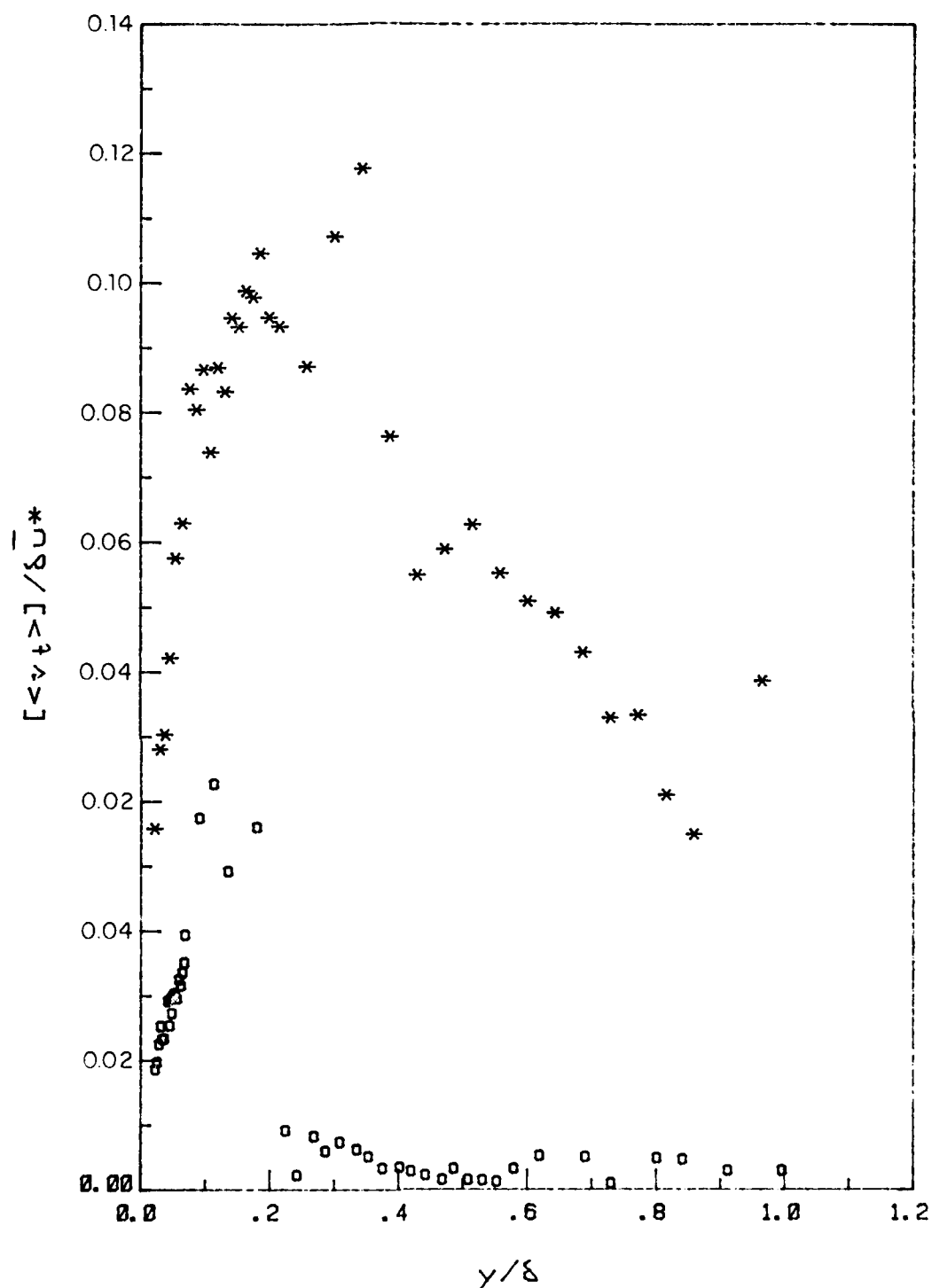
Figure 3.52. Amplitude distribution for $\langle v_t \rangle$. Symbols as in Fig. 3.51.
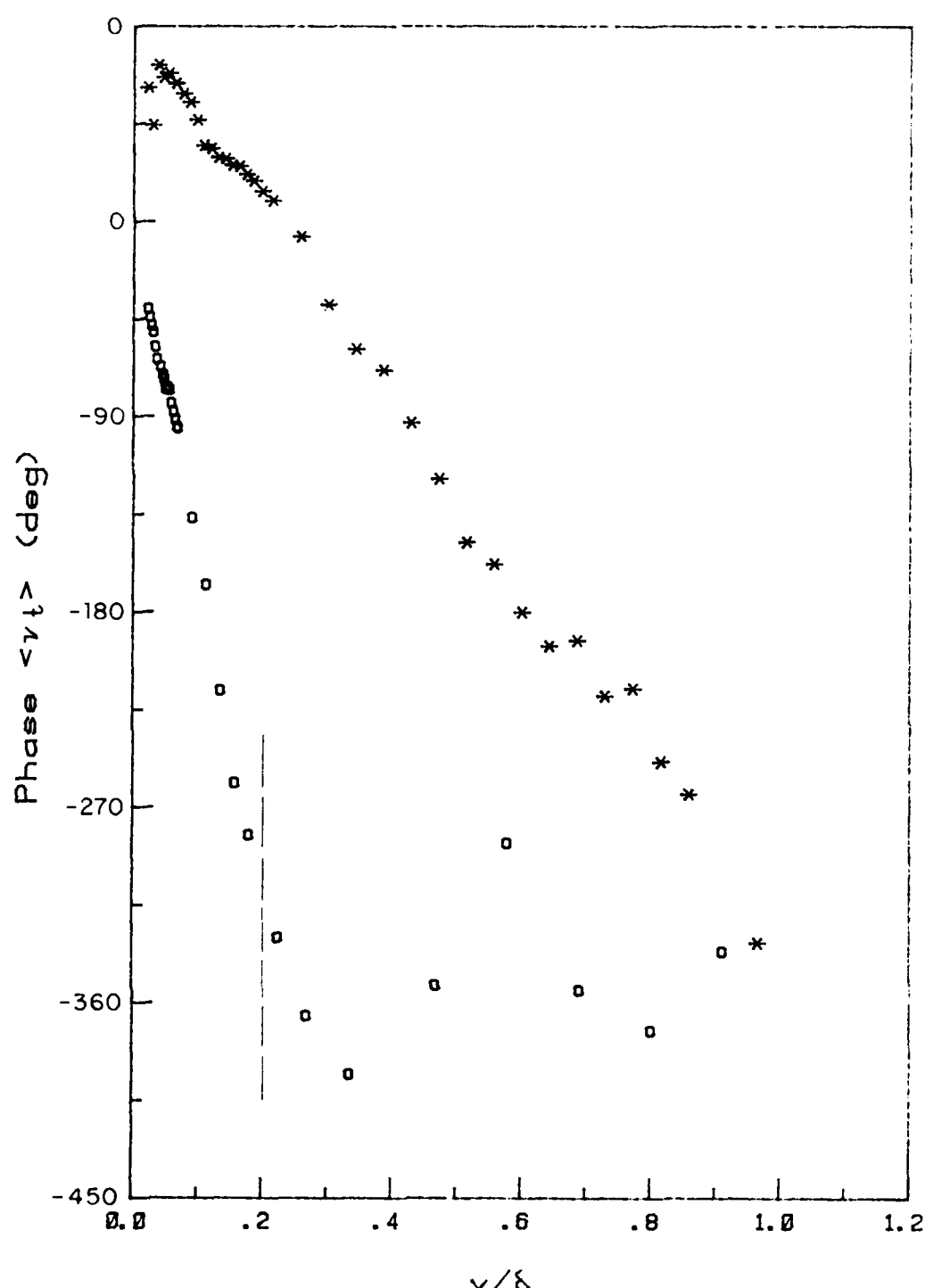
Figure 3.53. Phase distribution for $\langle \nu_t \rangle$. ---, edge of unsteady layer. Other symbols as in Fig. 3.51.

CHAP   4

A GENERAL THE   FOR UNSTEADY

PERIODIC T   ILENT FLOWS

4.1. General

The stumbling block in the analysis of turbulent flows, both in the steady and unsteady regimes, is the well-known closure problem. This arises as a consequence of the statistical approach, that provides a hierarchy of equations in which correlations of a given order are related to the next-order correlations. As an attempt to overcome this difficulty, the so-called turbulence models have been introduced. Essentially, they amount to truncating the sequence of equations at a certain level, and relating the remaining highest-order correlations to the lower-order ones through "models" based on ad hoc physical arguments and experimental data [see Bradshaw (1976)].

Though useful for engineering purposes, the turbulence models do not seem to be the appropriate tool to provide new physical insight into the turbulence process. Such insight has been obtained primarily from experiments and, to some extent, from simple, yet powerful, dimensional analysis. In fact, a combination of a minimum of experimental information, dimensional analysis and singular perturbation theory has proved useful, in recent times, in providing quite general asymptotic results for large Reynolds numbers, in the

form of similarity laws for many categories of steady turbulent shear flows [see Tennekes and Lumley (1980)]. The power of this approach (and, perhaps, its major limitation) is that it works on the open system of equations, thus avoiding the anomalies introduced by a specific turbulence model. While in the case of steady flows such analysis has merely reconfirmed already well-established experimental knowledge, it is used in the present work as a predicting tool to obtain similarity laws for unsteady turbulent flows. Some of these results are verified in the next chapter, using the available experimental information.

In analyzing the behavior of the velocity in unsteady (periodic) flows, the tendency has been to search for similarity laws (e.g., law of the wall, logarithmic law, etc.) in the instantaneous (ensemble-averaged) velocity profiles [Cousteix et al. (1981)], with little success. In the present work, instead, the velocity profile is decomposed into its time-mean and oscillatory components, and each one of them is studied separately.

4.2. Equations

The analysis is started from the ensemble-averaged unsteady turbulent boundary-layer equations for an incompressible, two-dimensional flow [Patel and Nash (1971)]

$$\frac{\partial \langle U \rangle}{\partial x} + \frac{\partial \langle V \rangle}{\partial y} = 0 \tag{4.1}$$

$$\frac{\partial \langle U \rangle}{\partial t} + \langle U \rangle \frac{\partial \langle U \rangle}{\partial x} + \langle V \rangle \frac{\partial \langle U \rangle}{\partial y} = -\frac{1}{\rho} \frac{\partial \langle p \rangle}{\partial x} + \nu \frac{\partial^2 \langle U \rangle}{\partial y^2} + \frac{\partial \langle \tau \rangle}{\partial y} \tag{4.2}$$

$$- \frac{1}{\rho} \frac{\partial \langle p \rangle}{\partial x} = \frac{\partial U_e}{\partial t} + U_e \frac{\partial U_e}{\partial x} \qquad (4.3)$$

The inclusion of the unsteady terms in Eqs. (4.2) and (4.3) does not involve any additional hypothesis beyond the classical boundary-layer assumption for steady turbulent flows. Briefly, this assumption states that the length scale of the motion normal to the wall is much smaller than that along the wall. As a consequence, diffusion in the longitudinal direction can be neglected, and the pressure can be considered to remain constant in the transverse direction. Actually, in turbulent flow, this last conclusion requires one to neglect also the contribution of the normal Reynolds stress $\langle v^2 \rangle$, which can be done safely except near the separation point. Then, the longitudinal pressure gradient is a known quantity in boundary-layer theory, and is related to the free-stream velocity by Eq. (4.3). Likewise, in Eq. (4.2) the contribution due to the normal turbulent stress $\langle u^2 \rangle$ has been neglected, for which the same considerations apply as for $\langle v^2 \rangle$. The above equations are subject to the following boundary conditions

$$\langle U \rangle = 0, \ \langle V \rangle = 0 \ \text{ at } y = 0$$
$$\langle U \rangle \rightarrow U_e \quad \text{as } y \rightarrow \infty \qquad (4.4)$$
$$\langle \tau \rangle = 0 \qquad \text{at } y = 0$$

The upstream boundary conditions, i.e., the specification of $\langle U \rangle$ at the first station, is somewhat complicated. However, the analysis

will concentrate on the search for asymptotic self-similarity laws, which do not need this information.

The following particular form of the periodic free-stream velocity is now assumed:

$$U_e(t) = U_0 \ (1 + \epsilon \sin \omega t) \tag{4.5}$$

where both the time-mean value, U_0, and the relative amplitude of oscillation, ϵ, are constants. Note that, from Eq. (4.5), $\overline{U}_e = U_0$, i.e., the time-mean flow is a "flat plate" type of boundary layer, in the sense that it is not subjected to any effective pressure gradient. In fact, the time-mean quantities are related through the following equations:

$$\frac{\partial \overline{U}}{\partial x} + \frac{\partial \overline{V}}{\partial y} = 0 \tag{4.6}$$

$$\overline{U} \frac{\partial \overline{U}}{\partial x} + \overline{V} \frac{\partial \overline{U}}{\partial y} = \nu \frac{\partial^2 \overline{U}}{\partial y^2} + \frac{\partial \overline{\tau}}{\partial y} - \frac{\partial \overline{U_p^2}}{\partial x} - \frac{\partial \overline{U_p V_p}}{\partial y} \tag{4.7}$$

and boundary conditions

$$\overline{U} = 0, \quad \overline{V} = 0 \qquad \text{at } y = 0$$

$$\overline{U} \rightarrow U_0 \qquad \qquad \text{as } y \rightarrow \infty \tag{4.8}$$

$$\overline{\tau} = 0 \qquad \qquad \text{at } y = 0$$

resulting from time-averaging Eqs. (4.1) to (4.4). The last two terms of Eq. (4.7) are the Reynolds stresses due to the oscillatory motion. They are of the order ϵ^2, and can be neglected provided the amplitude of oscillation of the freestream is sufficiently small, i.e., $\epsilon \ll 1$. Assuming this to be the case, the above system reduces to the standard boundary-layer equations for a flat plate. However, differences with respect to the corresponding steady motion (i.e., the one produced by a free-stream velocity $U_e = U_0$) could, in principle, arise if the time-mean turbulent shear stress, $\bar{\tau}$, is affected by unsteadiness. It has been speculated that this could happen if the forcing frequency $f = \omega/2\pi$ is high enough to interact with the most energetic turbulent frequencies [Ramaprian and Tu (1982)]. A measure of this frequency range is provided by the bursting frequency, f_b, which in a boundary layer can be correlated with global quantities through the approximate relation [Rao et al. (1971)]

$$\frac{U_0}{f_b \delta} \approx 5 \qquad (4.9)$$

Ramaprian and Tu (1982) give some experimental evidence. Past and present experiments have indicated that, in any case, the resulting variation in the time-mean velocity profile relative to the corresponding steady profile is small for large Reynolds numbers. It can, therefore, be neglected for purposes of the perturbation analysis presented here.

The assumption $\varepsilon \ll 1$ allows a linear analysis in the amplitude to be performed. This means that only motions at the forcing frequency are considered to be significant, i.e., higher harmonic oscillations can be neglected. The advantage of the complex notation can, then, be utilized, defining

$$U = \overline{U} + \varepsilon U_1 \, e^{i\omega t} \qquad (4.10)$$

$$V = \overline{V} + \varepsilon V_1 \, e^{i\omega t} \qquad (4.11)$$

$$\tau = \overline{\tau} + \varepsilon \, \tau_1 \, e^{i\omega t} \qquad (4.12)$$

and restating Eq. (4.5) as

$$U_e = U_0 (1 + \varepsilon \, e^{i\omega t}) \qquad (4.13)$$

Note that U_1, V_1 and τ_1 are all, in general, complex quantities. Introducing Eqs. (4.10) to (4.13) into Eqs. (4.1) to (4.4), and using Eqs. (4.6) to (4.8), the equations and boundary conditions for the oscillatory components are obtained as [Telionis (1981)]

$$\frac{\partial U_1}{\partial x} + \frac{\partial V_1}{\partial y} = 0 \qquad (4.14)$$

$$i\omega(U_1 - U_0) + \overline{U} \frac{\partial U_1}{\partial x} + U_1 \frac{\partial \overline{U}}{\partial x} + \overline{V} \frac{\partial U_1}{\partial y} + V_1 \frac{\partial \overline{U}}{\partial y}$$

$$= \nu \frac{\partial^2 U_1}{\partial y^2} + \frac{\partial \tau_1}{\partial y} \qquad (4.15)$$

$$U_1 = 0, \quad V_1 = 0 \qquad \text{at } y = 0$$

$$U_1 \rightarrow U_0 \qquad\qquad \text{as } y \rightarrow \infty \qquad\qquad (4.16)$$

$$\tau_1 = 0 \qquad\qquad\quad \text{at } y = 0$$

Before undertaking the analysis of Eqs. (4.14) to (4.16), the asymptotic behavior of the time-mean flow for large Reynolds number is briefly discussed, in the next section.

4.3. Asymptotic Characteristics of the
Time-Mean Flow at Large Reynolds Numbers

As pointed out in the previous section, the time-mean velocity is practically the same as for the corresponding steady flow, to the first order in the amplitude of oscillation. Tennekes and Lumley (1980) presented an asymptotic analysis of the steady flow for very large Reynolds numbers, without using any closure hypothesis for the turbulent shear stress. Their results, then, can be assumed to apply also to the time-mean unsteady flow. Their main conclusions, with reference to the present context, can be summarized as follows:

(i) There exist two distinctly different length scales for the motion, which determine a double-layer structure: an outer layer characterized by the (local) boundary layer thickness, δ, and an inner layer with length scale ν/u_*. The quantities $\delta(x)$ and $u_*(x)$ will be assumed to correspond to the steady flow at the time-mean velocity. Alternatively, they could be chosen as the time-mean values in unsteady flow which cannot differ much from the previous

ones due to the small amplitude of oscillation. Furthermore, as the boundary layer thickness, δ, is an ill-defined quantity, a thickness, Δ, defined by

$$\Delta \equiv \int_0^\infty \frac{\overline{U}(U_0 - \overline{U})}{U_0 u_*} \, dy = \frac{U_0}{u_*} \theta \qquad (4.17)$$

will be used instead. Note that the ratio of the two length scales defines the following Reynolds number:

$$R_* \equiv \frac{u_* \Delta}{\nu} \qquad (4.18)$$

With the present definition of Δ, Eq. (4.17), it follows that $R_* = Re_\theta \equiv U_0 \theta / \nu$. However, it is better to work with R_* in order to be able to generalize the results to fully developed flow in pipes and two-dimensional channels (see section 4.6).

(ii) The velocity scale for both the layers is u_*. Then, the time scales are $t_0 \equiv \Delta / u_*$ and $t_i \equiv \nu / u_*^2$ for the outer and inner layers, respectively.

(iii) In the limit $R_* \to \infty$, the following relations hold:

$$\frac{\overline{U} - U_0}{u_*} = F\left(\frac{y}{\Delta}\right) \qquad \text{for the outer layer} \qquad (4.19)$$

$$\frac{\overline{U}}{u_*} = f\left(\frac{y u_*}{\nu}\right) \qquad \text{for the inner layer} \qquad (4.20)$$

where the functions F and f can only be obtained from experiments. This indeterminacy arises because the system of equations is not

closed. Eqs. (4.19) and (4.20) are the well-known "velocity-defect law" and "law of the wall".

(iv) For $R_* \to \infty$, there exists a region where the outer and inner layers overlap. In this "inertial sublayer" Eqs. (4.19) and (4.20) are both valid, leading to the following results

$$\frac{\overline{U}}{u_*} = \frac{1}{k} \ln \left(\frac{y u_*}{\nu} \right) + B \qquad (4.21)$$

$$\frac{\overline{U} - U_o}{u_*} = \frac{1}{k} \ln \left(\frac{y}{\Delta} \right) + D \qquad (4.22)$$

where k (von Karman constant), B and D are constant and independent of the Reynolds number R_*. Equation (4.21) or (4.22) is the well-known "logarithmic law".

(v) Subtracting Eq. (4.22) from Eq. (4.21) yields

$$\frac{1}{E} \equiv \frac{U_o}{u_*} = \frac{1}{k} \ln R_* + B\text{-}D \qquad (4.23)$$

which is called the "logarithmic friction law", as it allows the determination of the shear velocity (and, then, the wall shear stress) if the constants k, B and D and the boundary layer thickness Δ are known.

(vi) If L is the length scale in the longitudinal direction, then $\Delta/L \to 0$ as $R_* \to \infty$. Equation (4.23) also shows that $E \to 0$ as $R_* \to \infty$. However, the ratio $\gamma = u_* L / U_o \Delta$ remains finite in the limit. The length scale L can be correlated to local quantities by performing an order-of-magnitude analysis in the momentum integral

equation, which for a steady flow at zero pressure gradient is simply [White (1974)]

$$\frac{d\theta}{dx} = E^2 \qquad (4.24)$$

Then, L can be defined as

$$L \equiv \frac{\theta}{E^2} \qquad (4.25)$$

Notice that, from Eqs. (4.17) and (4.25), it follows that $\gamma = 1$, and hence the definition of L is consistent with the asymptotic requirement that γ should remain finite.

The foregoing results will be very usef in the analysis of the oscillatory motion, discussed in the following section.

4.4. Asymptotic Characteristics of the
Oscillatory Motion

The imposed oscillation introduces a third time scale, ω^{-1}, into the problem. Its relation to the outer and inner time scales can be described by the following two frequency parameters

$$\tilde{\omega} \equiv \frac{t_o}{\omega^{-1}} = \frac{\omega\Delta}{u_\star} = \frac{\omega L}{U_o} \qquad (4.26)$$

$$\alpha \equiv \frac{\omega^{-1}}{t_i} = \frac{u_\star^2}{\omega\nu} = \frac{R_\star}{\tilde{\omega}} \qquad (4.27)$$

In addition, a third length scale, namely u_*/ω, appears, being associated with the imposed oscillation. This defines an "unsteady layer" whose thickness bears to the outer and inner thicknesses the same relation as the corresponding time scales, and is thus described by the same parameters, i.e., $\tilde{\omega}$ and α, defined above.

Various flow regimes can be distinguished, according to the values of the foregoing parameters. For $\tilde{\omega} \lesssim 1$, one has that $\omega^{-1} \gtrsim t_0$ and hence, significant unsteady effects must be expected in the outer layer. In fact, the unsteady layer is merged with the outer layer. On the contrary, $\alpha = R_*/\tilde{\omega} \gtrsim R_* \gg 1$, i.e., $\omega^{-1} \gg t_i$ indicates that the inner layer responds instantly to the excitation, i.e., in a quasi-steady manner. This will be called the "low frequency regime". Note that, in the particular case, $\tilde{\omega} \ll 1$, the outer layer will also show an instantaneous response, i.e., the entire boundary layer will behave in a quasi-steady manner.

The other extreme situation arises when $\tilde{\omega} \gtrsim R_*$ i.e. $\alpha \lesssim 1$, in which case $\omega^{-1} \lesssim t_i$. In this case, the unsteady layer will be actually submerged in the inner layer. The effects of unsteadiness are, therefore, significant in the inner layer. On the other hand, since $\omega^{-1} \ll t_0$, there is not enough time for the turbulent flow in the outer layer to respond to the imposed oscillation and hence this layer will move as a rigid body, i.e., it will perform inviscid or slug-flow oscillations. In fact, even the outer part of the inner layer may exhibit the slug-flow behavior. This situation will be named "very high frequency regime".

The situation $1 \ll \tilde{\omega} \ll R_\star$ which lies between the two limiting cases, described above, needs careful study. Since, under this condition, the inner and outer time scales are such that $t_i \ll \omega^{-1} \ll t_0$, one should expect that there will be quasi-steady flow in the inner layer, while a slug-flow is present in the outer layer. Furthermore, the fact that $\nu/u_\star \ll u_\star/\omega \ll \Delta$ in this flow, suggest that the unsteady layer lies between the outer and inner layers. Only in this unsteady layer, then, the unsteady viscous effects are significant. In fact, it has been found to be useful in the analysis to subdivide this regime further into two distinct regimes: an "intermediate frequency regime", for which $1 \ll \tilde{\omega} \lesssim R_\star^{1/2}$ (or, equivalently, $R_\star^{1/2} \lesssim \alpha \ll R_\star$), and a "high frequency regime", with $R_\star^{1/2} \ll \tilde{\omega} \ll R_\star$ (or, equivalently, $1 \ll \alpha \ll R_\star^{1/2}$). Notice that $\tilde{\omega} = R_\star^{1/2}$ corresponds to the case $\omega^{-1} = (t_0 t_i)^{1/2}$, i.e. the geometric mean of the outer and inner time scales, for which $\tilde{\omega} = \alpha$.

Each one of these four frequency regimes is analyzed in detail in the following sub-sections.

4.4.1. Low Frequency Regime

This regime, as explained above, is characterized by the conditions $\tilde{\omega} \lesssim 1$, $\alpha \gtrsim R_\star$. The outer layer, where unsteady effects are expected to be important, is analyzed first. For this purpose, the following dimensionless variables are introduced:

$$\eta = \frac{y}{\Delta} \qquad\qquad \xi = \int_0^x \frac{dx}{L}$$

$$F = \frac{\overline{U} - U_0}{u_\star} \qquad \widetilde{U}_1 = \frac{U_1 - U_0}{u_\star}$$

$$F_v = \frac{L\overline{V}}{\Delta u_\star} \qquad \widetilde{V}_1 = \frac{LV_1}{\Delta u_\star} \tag{4.28}$$

$$\widetilde{\tau}_1 = \frac{\tau_1}{u_\star^{\,2}}$$

The quantity F defined in Eq. (4.28) is the same as in Eq. (4.19), and hence $F = F(\eta)$. The definition of the variable $\widetilde{U}_1$, in turn, stems from the similarity between the equations and boundary conditions for $\overline{U}$ and U_1. On the other hand, the nondimensionalization of the transverse velocity components in Eq. (4.28) is suggested by the respective continuity equations. Finally, the scale $u_\star^{\,2}$ for the oscillatory component of the turbulent shear stress, τ_1, arises from the following quasi-steady argument. As already mentioned in Chapter 3, it is well known, from experiments in steady flow, that $\tau/U_e^{\,2}$ depends only weakly on U_e (i.e., on the Reynolds number). Considering it to remain constant, to a first approximation, when U_e is varied by ΔU_e, the variation $\Delta\tau$ in τ is related to ΔU_e by

$$\frac{\Delta\tau}{\tau} = \frac{2\Delta U_e}{U_e} \tag{4.29}$$

Equation (4.29), together with Eq. (4.12) and (4.13), show that $\tau_1 = O(u_\star^2)$ in quasi-steady flow. As shown in chapter 3, experiments however suggest that $u_\star^2$ is, in fact, the appropriate scale also for any finite frequency.

Introducing the definitions (4.28) into Eqs. (4.14) and (4.15) one obtains

$$\frac{\partial \widetilde{U}_1}{\partial \xi} - \beta_1 \eta \frac{\partial \widetilde{U}_1}{\partial \eta} + \beta_2 \, \widetilde{U}_1 + \frac{\partial \widetilde{V}_1}{\partial \eta} = 0 \qquad (4.30)$$

$$i \widetilde{\omega} \, \widetilde{U}_1 + (1 + EF) \, (\frac{\partial \widetilde{U}_1}{\partial \xi} - \beta_1 \eta \frac{\partial \widetilde{U}_1}{\partial \eta} + \beta_2 \, \widetilde{U}_1)$$

$$+ (1 + E\widetilde{U}_1) \, (-\beta_1 \eta \frac{dF}{d\eta} + \beta_2 F) + E \, (F_v \frac{\partial \widetilde{U}_1}{\partial \eta} + \widetilde{V}_1 \frac{dF}{d\eta})$$

$$= \frac{1}{R_\star} \frac{\partial^2 \widetilde{U}_1}{\partial \eta^2} + \frac{\partial \widetilde{\tau}_1}{\partial \eta} \qquad (4.31)$$

where

$$\beta_1 \equiv \frac{L}{\Delta} \frac{d\Delta}{dx} \qquad (4.32)$$

$$\beta_2 \equiv \frac{L}{u_\star} \frac{du_\star}{dx} \qquad (4.33)$$

In the limit $R_\star \to \infty$, Eq. (4.31) reduces, to the lowest order, to

$$i \widetilde{\omega} \, \widetilde{U}_1 + \frac{\partial \widetilde{U}_1}{d\xi} - \beta_1 \eta \frac{\partial \widetilde{U}_1}{\partial \eta} + \beta_2 \, \widetilde{U}_1 - \beta_1 \eta \frac{dF}{d\eta} + \beta_2 F$$

$$= \frac{\partial \widetilde{\tau}_1}{\partial \eta} \qquad (4.34)$$

The outer boundary condition for U_1 in Eq. (4.16), can be expressed now as

$$\tilde{U}_1 \to o \qquad \text{as } \eta \to \infty \qquad (4.35)$$

According to Eq. (4.34), viscous effects on the oscillatory motion are negligible in the outer layer, to this order of approximation. One the other hand, from both Eqs. (4.30) and (4.34) it is observed that, for similarity solutions to exist, i.e., solutions independent of the streamwise coordinate ξ, it is necessary that the coefficients β_1 and β_2 be constant. Not surprisingly, these are the same conditions as those necessary to achieve self-preservation in the time-mean flow [Yajnik (1970)]. Now, from Eqs. (4.17), (4.24), and (4.25), it can easily be shown that $\beta_1 = 1 - \beta_2$. Hence, the only necessary condition for similarity is

$$\frac{\theta U_o^2}{u_\star^3} \frac{du_\star}{dx} = \text{const.} \qquad (4.36)$$

Now, for very high Reynolds numbers one has that $u_\star/U_o \simeq$ const. This shows that Eq. (4.36) is satisfied, with the constant on the right hand side equal to zero, and that similarity is, in fact, possible in this case. Then, a "velocity-defect law" for the oscillatory motion can be expected to hold in the form

$$\tilde{U}_1 \equiv \frac{U_1 - U_o}{u_\star} = F_1 \left(\frac{y}{\Delta}; \tilde{\omega}\right) \qquad (4.37)$$

where F_1 is a complex function that must be determined from experiments. Note that Eq. (4.37) is not a self-preserving solution for any physical (constant ω) oscillatory flow, because $\tilde{\omega}$ still

depends on x (or ξ). Self-similarity in a given flow can be achieved only in the quasi-steady limit, i.e., for $\tilde{\omega} \ll 1$, for which the effects of the local acceleration and the pressure gradient [lumped together in the first term of Eq. (4.34)] are negligible. In this case, it can be shown that $F_1(\eta)$ is practically coincident with $F(\eta)$. However, Eq. (4.37) should still be useful in providing the link between oscillatory motions at different frequencies.

Next, the inner layer is analyzed. The nondimensionalization is carried out using similar criteria as for the outer layer, with the results

$$y^+ = \frac{y u_\star}{\nu} \qquad\qquad \xi = \int_0^x \frac{dx}{L}$$

$$f = \frac{\overline{U}}{u_\star} \qquad\qquad U_1^+ = \frac{U_1}{u_\star}$$

$$f_v = \frac{L\overline{V}}{\nu} \qquad\qquad V_1^+ = \frac{L V_1}{\nu} \tag{4.38}$$

$$\tau_1^+ = \frac{\tau_1}{u_\star^2}$$

Note that the function f in Eq. (4.38) is the same as in Eq. (4.20); then, $f = f(y^+)$. Introducing the definitions (4.38) into Eqs. (4.14) and (4.15) yields

$$\frac{\partial U_1^+}{\partial \xi} + \beta_2 y^+ \frac{\partial U_1^+}{\partial y^+} + \beta_2 U_1^+ + \frac{\partial V_1^+}{\partial y^+} = 0 \tag{4.39}$$

$$\frac{i}{\alpha E}(E U_1^+ - 1) + \frac{E}{R_\star}\left[f\left(\frac{\partial U_1^+}{\partial \xi} + \beta_2 y^+ \frac{\partial U_1^+}{\partial y^+} + \cdots \right. \right.$$

$$+ \beta_2 U_1^+ \left(y^+ \frac{df^+}{dy^+} + f\right) + f_v \frac{\partial U_1^+}{\partial y^+} + V_1^+ \frac{df}{dy^+}\,\Big]$$

$$= \frac{\partial^2 U_1^+}{\partial y^{+2}} + \frac{\partial \tau_1^+}{\partial y^+} \qquad (4.40)$$

When $R_* \to \infty$, the zero order approximation of Eq. (4.40) is simply

$$\frac{\partial^2 U_1^+}{\partial y^{+2}} + \frac{\partial \tau_1^+}{\partial y^+} = 0 \qquad (4.41)$$

i.e., a balance between viscous and turbulent diffusion. The inner boundary conditions of Eq. (4.16), are now rewritten as

$$U_1^+ = 0, \quad V_1^+ = 0 \qquad \text{at } y^+ = 0$$

$$\qquad (4.42)$$

$$\tau_1^+ = 0 \qquad\qquad \text{at } y^+ = 0$$

Note that (as expected) Eq. (4.41) will yield quasi-steady solutions, since it does not depend on $\tilde{\omega}$. Furthermore, self-similarity can be expected to hold in the form of a "law of the wall", i.e.

$$U_1^+ \equiv \frac{U_1}{u_*} = f_1 \left(\frac{yu_*}{\nu}\right) \qquad (4.43)$$

with the function f_1 to be determined.

Now, as in the case of the time-mean flow, an asymptotic matching procedure can be applied to the inner and outer solutions for the oscillatory flow. The procedure proposed by Van Dyke (1973) will be followed here. Symbolically, it states that

$$O_m I_n (\ ) = I_n O_m (\ ) \qquad (4.44)$$

In words, Eq. (4.44) expresses that the m-term outer expansion of the n-term inner expansion of the quantity between brackets equals the n-term inner expansion of its m-term outer expansion. In the present case, the expansions are in terms of the large parameter R_*, and the quantity chosen to be matched is $U_1^+ = U_1/u_*$. Now, as in the inner layer U_1^+ is assumed to satisfy Eq. (4.43), it does not have any explicit dependence on R_*. Hence the inner expansion of U_1^+ consists of only one term, namely $f_1(y^+)$. On the other hand, from Eqs. (4.23), (4.37) and (4.38), one gets the following outer expansion

$$U_1^+ (n; R_*) = \frac{1}{k} \ln R_* + [B-D + F_1 (n ; \tilde{\omega})] \qquad (4.45)$$

i.e., a two term-expansion, with the leading term growing very large for $R_* \rightarrow \infty$. The matching procedure is started with $m = n = 1$. Then,

$$I_1 O_1 (U_1^+) = I_1 (\frac{1}{k} \ln R_*) = \frac{1}{k} \ln R_* \qquad (4.46)$$

$$O_1 I_1 (U_1^+) = O_1 [f_1 (R_* n)] \qquad (4.47)$$

From the matching principle, Eq. (4.44), and from Eqs. (4.46) and (4.47), one obtains

$$O_1 [f_1 (R_* n)] = \frac{1}{k} \ln R_* \qquad (4.48)$$

which is satisfied only if

$$f_1(y^+) \to \frac{1}{k} \ln y^+ + B_1 \qquad \text{as } y^+ \to \infty \qquad (4.49)$$

where B_1 is an unknown constant. Eq. (4.49) shows that the law of the wall merges with a logarithmic law when y^+ is large. The next step in the matching is to take $m = 2$ and $n = 1$. Then,

$$I_1 O_2(U_1^+) \qquad = I_1 [\frac{1}{k} \ln R_\star + B - D + F_1(\frac{y^+}{R_\star}; \tilde{\omega})]$$

$$= \frac{1}{k} \ln R_\star + I_1 [F_1 (\frac{y^+}{R_\star}; \tilde{\omega})] \qquad (4.50)$$

$$O_2 I_1 (U_1^+) \qquad = O_2 [f_1(R_\star n)]$$

$$= \frac{1}{k} \ln (R_\star n) + B_1 \qquad (4.51)$$

Equation (4.49) has been used in Eq. (4.51). From Eqs. (4.44), (4.50) and (4.51) one obtains

$$I_1 [F_1(\frac{y^+}{R_\star}; \tilde{\omega})] = \frac{1}{k} \ln n + B_1 \qquad (4.52)$$

which means that

$$F_1(n; \tilde{\omega}) \to \frac{1}{k} \ln n + D_1 \qquad \text{as } n \to 0 \qquad (4.53)$$

where D_1 is a new constant. From Eq. (4.53) it is seen that the velocity defect law also merges with a logarithmic law when $\eta \to 0$. Interestingly, Eqs. (4.49) and (4.53) show that <u>the slope of the logarithmic curve, $1/k$, is the same as for the time-mean flow.</u>

4.4.2. Very High Frequency Regime

The conditions satisfied by the frequency parameters are now $\tilde{\omega} \gtrsim R_*$, $\alpha \lesssim 1$. The lowest order approximation of Eq. (4.31) is, then, simply

$$\tilde{U}_1 = 0 \qquad (4.54)$$

i.e., a balance between local acceleration and pressure gradient. Equation (4.54) shows that the outer layer performs rigid body oscillations, as expected.

On the other hand, when the zero order approximation is sought in the inner momentum equation, Eq. (4.40), a contradiction is found, since the leading term is a constant. This indicates that there exists a scaling problem. In fact, Eq. (4.54) suggests that changes in the velocity of the order of U_0 must occur within the inner layer in order to match the outer solution. Hence, the following alternative nondimensionalization is proposed:

$$U_1^{++} = \frac{U_1 - U_0}{U_0} = E U_1^+ - 1 \qquad (4.55)$$

$$V_1^{++} = \frac{u_* L V_1}{U_0 \nu} \qquad (4.56)$$

after which, the zero-order approximation of Eq. (4.40) becomes

$$iU_1^{++} = \alpha \frac{\partial^2 U_1^{++}}{\partial y^{+2}} \tag{4.57}$$

i.e. a balance between local acceleration, pressure gradient and viscous diffusion. In turn, the inner boundary condition for the velocity is, from Eqs. (4.42) and (4.55),

$$U_1^{++} = -1 \qquad \text{at } y^+ = 0 \tag{4.58}$$

while the matching condition with the outer layer simply becomes, from Eq. (4.54)

$$U_1^{++} \to 0 \qquad \text{as } y^+ \to \infty \tag{4.59}$$

The solution to Eqs. (4.57) to (4.59) is the well-known Stokes or shear-wave solution, namely

$$U_1^{++} = -\exp\left[-\frac{(1+i)}{\sqrt{2\alpha}} y^+\right] \tag{4.60}$$

which is obviously self-similar in the inner coordinates. Hence, for these very high frequencies, the oscillatory motion behaves as in laminar flow [Lighthill (1954)]. Note, from Eq. (4.60), that the main change in the oscillatory velocity occurs in a layer whose width is of the order of δ_s, where

$$\delta_S = \sqrt{2\alpha}\, \frac{\nu}{u_\star} = \sqrt{\frac{2\nu}{\omega}} \qquad\qquad (4.61)$$

is the Stokes thickness. For $\alpha \sim 1$, the Stokes layer thickness is of the same order as the inner layer thickness. However, for $\alpha \ll 1$ ($\tilde{\omega} \gg R_\star$), δ_S becomes much smaller than the thickness of the inner layer, which will then perform slug-like oscillations, just like the outer layer.

4.4.3. Intermediate Frequency Regime

The conditions that characterize this frequency regime are $1 \ll \tilde{\omega} \lesssim R_\star^{1/2} \lesssim \alpha \ll R_\star$. Hence, the zero order approximation in both $R_\star$ and $\tilde{\omega}$ of the outer momentum equation, Eq. (4.31), is again Eq. (4.54), i.e. there exists an outer slug flow, as in the very high frequency regime.

In turn, taking into account that $\alpha E \gtrsim (R_\star^{1/2}/\ln R_\star) \to \infty$, as $R_\star \to \infty$, Eq. (4.40) for the inner layer reduces to Eq. (4.41). Hence, there is a quasi-steady motion in the inner layer, and a law-of-the-wall like Eq. (4.43) can be expected to hold. Note that, this time, nothing suggests that the scaling for the oscillatory velocity is wrong: neither the momentum equation nor the matching with the outer layer, as this is performed through the unsteady layer, analyzed next.

The dimensionless variables for the unsteady layer are defined as follows:

$$\tilde{y} = \frac{\omega y}{u_\star} \qquad\qquad \xi = \int_0^x \frac{dx}{L}$$

$$F = \frac{\overline{U} - U_0}{u_*} \qquad\qquad \hat{U}_1 = \frac{U_1 - U_0}{u_*}$$

$$\hat{F}_v = \frac{\omega L \overline{V}}{u_*^2} \qquad\qquad \hat{V}_1 = \frac{\omega L \hat{U}_1}{u_*^2} \qquad\qquad (4.62)$$

$$\hat{\tau}_1 = \frac{\tau_1}{u_*^2}$$

Note that F now depends both on $\hat{y}$ and ξ. The scaling for U_1 seems to be appropriate to bridge the gap between the inner and outer flows. Introducing the definitions (4.62) into Eqs. (4.14) and (4.15) one obtains

$$\frac{\partial \hat{U}_1}{\partial \xi} - \beta_2 \hat{y} \frac{\partial \hat{U}_1}{\partial \hat{y}} + \beta_2 \hat{U}_1 + \frac{\partial \hat{V}_1}{\partial \hat{y}} = 0 \qquad\qquad (4.63)$$

$$i\hat{U}_1 + \tilde{\omega}^{-1} \left[\frac{\partial}{\partial \xi} (\hat{U}_1 + F) - \beta_2 \hat{y} \frac{\partial}{\partial \hat{y}} (\hat{U}_1 + F) \right.$$

$$\left. + \beta_2 (\hat{U}_1 + F) \right] = \frac{\partial \hat{\tau}_1}{\partial \hat{y}} \qquad\qquad (4.64)$$

To zero order in $\tilde{\omega}^{-1}$, Eq. (4.64) reduces to

$$i\hat{U}_1 = \frac{\partial \hat{\tau}_1}{\partial \hat{y}} \qquad\qquad (4.65)$$

i.e., a balance between local acceleration, pressure gradient and turbulent diffusion. Eq. (4.65) admits self-similar solutions in the form of a velocity defect law, i.e.

$$\hat{U}_1 = \frac{U_1 - U_0}{u_\star} = F_2\left(\frac{\omega y}{u_\star}\right) \tag{4.66}$$

with F_2 to be determined. Matching with the outer layer simply requires

$$F_2(\hat{y}) \to 0 \qquad \text{as } \hat{y} \to \infty \tag{4.67}$$

On the other hand, matching with the inner layer, using Van Dyke's principle, is more cumbersome than in the low-frequency regime, as the three parameters $\tilde{\omega}$, α and $R_\star$ are now assumed to grow very large. For $1 \ll \tilde{\omega} \ll R_\star^{1/2}$, however, $\tilde{\omega}$ may be considered fixed when $R_\star \to \infty$, and the matching principle indicates, as before, the existence of a logarithmic region. As $\tilde{\omega} \to R_\star^{1/2}$, this region would tend to disappear.

4.4.4. High Frequency Regime

This regime is characterized by the conditions $1 \ll \alpha \ll R_\star^{1/2} \ll \tilde{\omega} \ll R_\star$. The outer layer motion, hence, continues to be a slug flow oscillation, as Eq. (4.31) reduces to Eq. (4.54).

In the inner layer, Eq. (4.40) leads again to a contradiction, as $\alpha E \to 0$ when $R_\star \to \infty$ (α is now fixed when $R_\star \to \infty$). Using the alternate scaling proposed for the very high frequency regime, Eqs. (4.55) and (4.56), the zero-order approximation of Eq. (4.40) is then

$$\frac{\partial^2 U_1^{++}}{\partial y^{+2}} = 0 \tag{4.68}$$

Eq. (4.68) shows that the only significant mechanism is now viscous
diffusion, which must be counteracting the difference in shear stress
at the two ends of the inner layer, i.e., it is undergoing a Couette
motion.   From Eq. (4.68) and the inner boundary condition, Eq.
(4.58), the following solution is obtained

$$u_1^{++} - a y^+ - 1 \qquad (4.69)$$

where a is a constant that depends on the conditions in the unsteady
layer.

The analysis of the unsteady layer does not differ at all from
the one for the intermediate frequency-regime case. Thus, Eqs.
(4.65) to (4.67) are still expected to hold. Matching with the inner
layer, in turn, requires that F_2 become a linear function of its
argument when this becomes very small. Using Eq. (4.69), this can be
written as

$$F_2(\hat{y}) \to \frac{a\,x\hat{y}-1}{E} \qquad \text{as } \hat{y} \to 0 \qquad (4.70)$$

4.4.5. Summary of Results

The main results of the foregoing analysis are now summarized.
The original concept introduced is that of a triple-layered structure
imposed by unsteadiness, as schematized in Fig. 4.1(b). This is
superimposed on the original two-layer structure, already present in
steady flow, shown in Fig. 4.1(a). The different flow regimes are

defined according to the way the unsteady structure overlaps the steady structure. This is schematically represented in Fig. 4.2. Different similarity laws hold in the different layers, for each frequency regime. These laws were derived in terms of the complex quantity U_1, defined by Eq. (4.10). They are restated below in a form, that is more convenient to use in practice.

For a free-stream velocity given by Eq. (4.5), the longitudinal velocity component given by Eq. (4.10) is written as

$$U = \overline{U} + \varepsilon \, (U_{11} \sin \omega t - U_{12} \cos \omega t) \qquad (4.71)$$

where U_{11} and U_{12} are, respectively, the in-phase and out-of-phase components of the oscillatory motion. To obtain the results for U_{11} and U_{12} from those for U_1, it is only necessary to replace U_1 by $(U_{11} - iU_{12})$ in the various relations derived earlier. The following are the results for U_{11} and U_{12}.

(i)   Low frequency regime: $\tilde{\omega} \lesssim 1, \ \alpha \gtrsim R_*$

(a) Outer layer (coincident with unsteady layer)

$$\frac{U_{11} - U_0}{u_*} = F_{11} \left(\frac{y}{\Delta}; \tilde{\omega} \right) \qquad (4.72)$$

$$\frac{U_{12}}{u_*} = F_{12} \left(\frac{y}{\Delta}; \tilde{\omega} \right) \qquad (4.73)$$

$$F_{11} \left(\frac{y}{\Delta}; \tilde{\omega} \right) \to \frac{1}{k} \ln \left(\frac{y}{\Delta} \right) + D_{11} \qquad \text{as } \frac{y}{\Delta} \to 0 \qquad (4.74)$$

$$F_{12}\left(\frac{y}{\Delta}; \tilde{\omega}\right) \rightarrow D_{12} \qquad \text{as } \frac{y}{\Delta} \rightarrow 0 \qquad (4.75)$$

where F_{11}, F_{12} are unknown functions and D_{11}, D_{12} unknown constants.

(b) Inner layer:

$$\frac{U_{11}}{u_\star} = f_{11}\left(\frac{yu_\star}{\nu}\right) \qquad (4.76)$$

$$\frac{U_{12}}{u_\star} = f_{12}\left(\frac{yu_\star}{\nu}\right) \qquad (4.77)$$

$$f_{11}\left(\frac{yu_\star}{\nu}\right) \rightarrow \frac{1}{k}\ln\left(\frac{yu_\star}{\nu}\right) + B_{11} \qquad \text{as } \frac{yu_\star}{\nu} \rightarrow \infty \qquad (4.78)$$

$$f_{12}\left(\frac{yu_\star}{\nu}\right) \rightarrow B_{12} \qquad \text{as } \frac{yu_\star}{\nu} \rightarrow \infty \qquad (4.79)$$

where f_{11}, f_{12} are unknown functions and B_{11}, B_{12} unknown constants.

(ii) Intermediate frequency regime: $1 \ll \tilde{\omega} \lesssim R_\star^{1/2} \lesssim \alpha \ll R_\star$

(a) Outer layer:

$$U_{11} = U_5 \qquad (4.80)$$

$$U_{12} = \tilde{} \qquad (4.81)$$

(b) Unsteady layer:

$$\frac{U_{11}-U_0}{u_\star} = F_{21}\left(\frac{\omega y}{u_\star}\right) \qquad (4.82)$$

$$\frac{U_{12}}{u_\star} = F_{22}\left(\frac{\omega y}{u_\star}\right) \qquad (4.83)$$

where F_{21}, F_{22} are unknown functions.

(c) Inner layer:

$$\frac{U_{11}}{u_\star} = f_{11}\left(\frac{yu_\star}{\nu}\right) \qquad (4.84)$$

$$\frac{U_{12}}{u_\star} = f_{12}\left(\frac{yu_\star}{\nu}\right) \qquad (4.85)$$

(iii) High frequency regime: $1 \ll \alpha \ll R_\star^{1/2} \ll \tilde{\omega} \ll R_\star$

(a) Outer layer: same results as for the intermediate frequency regime.

(b) Unsteady layer: similar results as for the intermediate frequency regime.

(c) Inner layer:

$$\frac{U_{11}-U_0}{U_0} = a_1\,\frac{yu_\star}{\nu} - 1 \qquad (4.86)$$

$$\frac{U_{12}}{U_0} = a_2 \frac{yu_*}{\nu} \tag{4.37}$$

where a_1 and a_2 are unknown constants.

(iv) Very high frequency regime: $\tilde{\omega} \gtrsim R_*$, $\alpha \lesssim 1$

    (a) Outer layer: same results as for the intermediate frequency regime.

    (b) Inner layer (coincident with unsteady layer)

$$\frac{U_{11}-U_0}{U_0} = - e^{-\frac{y^+}{\sqrt{2\alpha}}} \cos\left(\frac{y^+}{\sqrt{2\alpha}}\right) \tag{4.88}$$

$$\frac{U_{12}}{U_0} = - e^{-\frac{y^+}{\sqrt{2\alpha}}} \sin\left(\frac{y^+}{\sqrt{2\alpha}}\right) \tag{4.89}$$

The foregoing results are asymptotic limits for $R_* \to \infty$. Hence, they should be referred to as "weak" similarity laws [Yajnik (1970)], in the sense that they hold only to the lowest order asymptotic analysis. Deviations from these asymptotic laws should be expected in practice, due to the finite value of R_*.

4.5. Generalization to Nonzero Time-Mean Pressure Gradient Boundary Layer

The concepts developed so far for zero time-mean pressure gradient flows admit a relatively simple extension to other types of flow. Not only does such an extension widen their range of

application, but also enables one to verify some of the general
conclusions using the available experimental information. In this
section, the general case of nonzero time-mean pressure gradient
boundary layers is examined. Fully developed channel and pipe flows
are analyzed in the next section.

Consider a general harmonic free-stream oscillation of the form

$$U_e(x,t) = U_\infty(x) [1 + \varepsilon(x) \sin \omega t] \qquad (4.90)$$

with $\varepsilon \ll 1$. To the first order in the relative amplitude, ε, the
driving pressure gradient is, from Eqs. (4.3) and (4.90),

$$-\frac{1}{\rho} \frac{\partial \langle p \rangle}{\partial x} = U_\infty \frac{dU_\infty}{dx} + \omega \varepsilon U_\infty \cos \omega t$$

$$+ U_\infty \left(2\varepsilon \frac{dU_\infty}{dx} + U_\infty \frac{d\varepsilon}{dx} \right) \sin \omega t \qquad (4.91)$$

The two extra contributions, namely the first and the last terms on
the right hand side of Eq. (4.91), will produce modifications in the
time-mean flow and the oscillatory motion, respectively, relative to
the case of zero time-mean pressure gradient. Note that, rigorously
speaking, flows with U_∞ = const., $\varepsilon = \varepsilon(x)$ would belong to the
category of zero pressure-gradient flows. However, this name will be
reserved for the situation in which both U_∞ and ε are constant.

4.5.1. Time-Mean Flow

The discussion on the features of the time-mean flow of section 4.3 can be generalized to include the present case in the following manner [Tennekes and Lumley (1972)].

(i) The normalized boundary layer thickness, Δ, used as the length scale for the outer layer is redefined as

$$\Delta = \int_0^\infty \frac{\bar{U}(U_\infty - \bar{U})}{U_\infty u_\star} \, dy = \frac{U_\infty}{u_\star} \delta \qquad (4.92)$$

which is a more general expression than Eq. (4.17).

(ii) In addition to the outer and inner time scales, the longitudinal variation of the free-stream velocity introduces its own time scale, namely $|dU_\infty/dx|^{-1}$. Its ratios to the preceding time scales define, respectively, the following two parameters:

$$\Pi_1 = \frac{U_\infty}{u_\star^2} \frac{dU_\infty}{dx} \qquad (4.93)$$

$$\Pi_2 = \frac{U_\infty}{u_\star^2} \frac{dU_\infty}{dx} \qquad (4.94)$$

Π_1 is the well known Clauser equilibrium parameter [see White (1974)]. In turn, if $dU_\infty/dx \ll U_\infty/L$ [see (vi) below], then Π_2 may in turn be neglected in the asymptotic limit, i.e., the longitudinal time-scale is

infinitely large compared to the scale of the inner layer
at this order of approximation.

(iii) When $R_\star \to \infty$, the velocity-defect law, Eq. (4.19),
generalizes to

$$\frac{\overline{U}-U_\infty}{u_\star} = F\left(\frac{y}{\Delta}; \gamma_1\right) \tag{4.95}$$

For Eq. (4.95) to hold, it is required that $d\gamma_1/dx = 0$.
This condition defines the so called equilibrium boundary
layers, for which Eq. (4.95) gives a self-preserving
velocity profile (in the outer layer). On the other hand,
the law of the wall, Eq. (4.20), is still valid.

(iv) The logarithmic laws, Eqs. (4.21) and (4.22), are
satisfied as long as γ_1 remains finite [see (vi) below].
However, the extent of the inertial sublayer and the value
of D in Eq. (4.22) depend on γ_1.

(v) A logarithmic friction law like that of Eq. (4.23) holds
for finite γ_1.

(vi) The momentum integral equation for steady flow is [White
(1974)]

$$\frac{d\theta}{dx} + (2+H) \; \frac{1}{U_\infty} \frac{dU}{dx} = l^2 \tag{4.96}$$

Equation (4.96) shows that, in addition to the longitudinal length scale l defined by Eq. (4.25), a second length scale, $l_\infty = U_\infty/(dU_\infty/dx)$, is imposed by the spatial variation of the free stream. It will be assumed that $l_\infty \gtrsim l$, i.e. rapidly accelerating or decelerating flows are excluded. Then, $dU_\infty/dx \lesssim U_\infty/l$, as assumed above, and $\gamma_1 \lesssim 1$.

4.5.2. Oscillatory Motion

Regarding the oscillatory motion, the discussion presented at the beginning of section 4.4 still applies, if in Eq. (4.26) U_0 is changed to U_∞. Retaining the definitions (4.10) to (4.12) and updating Eq. (4.13) to

$$U_e = U_\infty (1 + \varepsilon e^{i\omega t}) \tag{4.97}$$

Equation (4.15) can now be generalized as

$$i\omega(U_1-U_o) + U \frac{d}{dx}(U_1-U_o) + \dots \tag{4.98}$$

The outer scaling of Eq. (4.28) is still appropriate if U_0 is replaced by U_∞. Then, an expression analogous to Eq. (4.31) results, except for the following additional term on its left hand side

$$- (\gamma_1 + \gamma_2) (\tilde{U}_1 + F) \tag{4.99}$$

where

$$\gamma_2 = - \frac{L}{\varepsilon} \frac{d\varepsilon}{dx} \tag{4.100}$$

is a new "equilibrium" parameter. In the low frequency regime, then, in order for a similarity law like Eq. (4.37) to hold (with U_0 replaced by U_∞), it is necessary that, in addition to satisfying Eq. (4.36), both γ_1 and γ_2 be constant. For the remaining flow regimes, in turn, $\tilde{\omega} \gg 1$ and, hence, the flow will be slug-like in the outer layer, as for zero-pressure-gradient flows.

The analysis for the inner layer remains exactly the same as before because, as explained above, γ^+ [Eq. (4.94)] vanishes at the lowest order of approximation. Finally, the equation for the unsteady layer, in the intermediate and high frequency regimes, is still analogous to Eq. (4.64), except for the following additional term on its left hand side

$$- \tilde{\omega}^{-1} (\gamma_1 + \gamma_2) (\tilde{U}_1 + F) \tag{4.101}$$

where the same scaling as before is used, namely Eq. (4.62), with U_0 replaced by U_∞. As $\tilde{\omega} \gg 1$ for both regimes, Eq. (4.65) is again valid to the lowest order of approximation and, hence, a similarity

law like that in Eq. (4.66) can be expected to hold (with U_0 replaced by U_∞).

Though the above discussion was limited to equilibrium boundary layers, only a few of the results are actually restricted by this condition. First, for nonequilibrium boundary layers, the velocity-defect law, Eq. (4.95), is not valid, as the profile will also depend on its "history", i.e., its upstream evolution. However, a logarithmic region still exists (for finite Y_1) though its extent (and the value of D) will depend on the history. Then, the only difference in the results for the oscillatory motion is that no similarity law, like that of Eq. (4.37), will hold in the outer layer for the low frequency regime.

4.6. Extension to Fully Developed Channel

and Pipe Flows

In fully developed flow all the properties are invariant in the longitudinal direction. In particular, the shear velocity, u_*, is a constant (in the corresponding steady flow). Also, since the convection terms vanish (as does the cross-stream velocity $\langle V \rangle$) the problem becomes linear and the results are valid for any amplitude of oscillation, not necessarily small, provided the instantaneous Reynolds number remains large throughout the cycle.

4.6.1. Two-Dimensional Channel Flow

Consider a channel of width $2a$, with the centerline velocity given by

$$U_c = U_0 (1 + \varepsilon e^{i\omega \tau}) \qquad (4.102)$$

and with the origin of the y-coordinates at the bottom wall. The asymptotic analysis of the time-mean flow for the lower half (the upper half is, obviously, symmetrical) provides results completely analogous to those for a boundary layer, presented in section 4.3, if the length scale Δ is replaced by h. This time, however, the length scale in the longitudinal direction is infinitely large and need not be considered. In turn, it is fairly easy to show that the equivalent to Eq. (4.15) is

$$i\omega (U_1 - U_0) = \nu \left(\frac{d^2 U_1}{dy^2} - \frac{d^2 U_1}{dy^2}\Big|_{y=h} \right) + \frac{d\tau_1}{dy} \qquad (4.103)$$

The second term on the right hand side of Eq. (4.103) is part of the pressure-gradient contribution. Again, the discussion at the beginning of section 4.4 applies, with $\tilde{\omega}$ now defined as

$$\tilde{\omega} = \frac{\omega h}{u_\star} \qquad (4.104)$$

The outer scaling is, in analogy with Eq. (4.28),

$$\eta = \frac{y}{h}$$

$$f_1 = \frac{U_1 - U_0}{u_\star} \qquad (4.105)$$

$$U_1 = \frac{U_1}{u_\star}$$

Introducing Eq. (4.105) into Eq. (4.103) and taking the limit $R_\star = u_\star h/\nu \to \infty$, one gets

$$U_1 = \frac{\partial_1}{\partial y} \qquad (4.106)$$

which, obviously, gives truly self-preserving solutions in the form of a "velocity-defect law", namely

$$U_1 = \frac{U_1 - U_1}{u_\star} = F_1 \left(\frac{y}{h}; \omega\right) \qquad (4.107)$$

Equation (4.107) is completely analogous to Eq. (4.37). Beyond the low frequency regime (i.e., for $\omega \gg 1$), Eq. (4.106) shows that $\bar{U}_1 = 0$ at the lowest order, i.e., the outer layer or "core region" undergoes slug-flow oscillations, as in boundary-layer flow.

The inner scaling, on the other hand, is the same as in the boundary-layer case, i.e., it is given by Eq. (4.38). To the zero order, Eq. (4.103) then reduces to

$$\frac{\partial^2 \bar{U}_1^+}{\partial y^2} + \frac{\partial \bar{U}_1^+}{\partial y} = \frac{\partial^2 \bar{U}_1^+}{\partial y^2}\bigg|_\star \qquad (4.108)$$

Eq. (4.108) is the counterpart of Eq. (4.41). The solutions to this equation will be in the form of a "law-of-the-wall", like that of Eq. (4.43). The extra term on the right-hand side of Eq. (4.108), compared to Eq. (4.41), indicates the influence of the finite width of

flow on the inner or "surface" layer. Note that it gives a nonzero contribution only in the low frequency regime. In fact, for $\omega \gg 1$, the flow in the core region is slug-like and, then, $d^2 U_1/dy^2 = 0$. In the high and very high frequency regimes, U_1 needs to be rescaled according to Eq. (4.55), as in boundary-layer flow, giving the same solutions, namely Eqs. (4.69) and (4.60), respectively.

The results for the unsteady layer, in the intermediate and high frequency regimes, are completely analogous to that for the boundary layer case.

4.6.2. Pipe Flow

Very similar results are obtained for pipe flow. If the radius of the pipe is R, the centerline velocity is given by Eq. (4.103) and the origin of the y-axis is chosen at the inner surface (a rather unusual choice for an axisymmetric flow), then the time-mean flow satisfies the same conditions as in boundary-layer flow (section 4.3), if Δ is replaced by R. The equation equivalent to Eq. (4.103) is

$$i\omega(U_1 - U_0) = \frac{1}{(R-y)} \frac{d}{dy} [(R-y)(\nu \frac{dU_1}{dy} + \tau_1)]$$

$$- [\frac{1}{(R-y)} \frac{d}{dy} [(R-y)(\nu \frac{dU_1}{dy} + \tau_1)]]_{y=R} \qquad (4.109)$$

If the outer scaling of Eq. (4.105) is used, with h replaced by R, the lowest order approximation of Eq. (4.109) in the core region becomes

$$i\tilde{\omega}\,\tilde{U}_1 = \frac{1}{(1-\eta)}\frac{d}{d\eta}[(1-\eta)\tilde{\tau}_1] - \{\frac{1}{(1-\eta)}\frac{d}{d\eta}[(1-\eta)\,\tilde{\tau}_1]\}_{\eta=1} \qquad (4.110)$$

Eq. (4.110) is the counterpart of Eq. (4.106), and gives also solutions of the form of Eq. (4.107), with h replaced by R.

Likewise, the equivalent to Eq. (4.108) is

$$\frac{1}{(R^+-y^+)}\frac{d}{dy^+}[(R^+-y^+)(\nu\frac{dU_1^+}{dy^+} + \tau_1^+)]$$

$$= \{\frac{1}{(R^+-y^+)}\frac{d}{dy^+}[(R^+-y^+)(\nu\frac{dU_1^+}{dy^+} + \tau_1^+)]\}_{y^+=R_*} \qquad (4.111)$$

Equation (4.111) gives solutions in the form of Eq. (4.43). Note that, as in channel flow, the term on the right hand side of Eq. (4.111) gives a nonnegligible contribution only in the low frequency regime. In fact, for $\tilde{\omega} \gg 1$ both dU_1/dy and τ_1 vanish in the core region. That τ_1 must be zero can be easily proved by considering series expansions in powers of $\tilde{\omega}$ for both $\tilde{U}_1$ and $\tilde{\tau}_1$, which, when inserted into the outer equation, give a set of homogeneous equations with homogeneous boundary conditions.

For the unsteady layer, finally, the equivalent to Eq. (4.65) is

$$i\hat{U}_1 = -\frac{1}{(\hat{R}-\hat{y})}\frac{d}{d\hat{y}}[(\hat{R}-\hat{y})\,\hat{\tau}_1] \qquad (4.112)$$

where $\hat{R} = R\omega/U_*$ and the standard scaling has been used. Eq. (4.112) provides solutions of the form of Eq. (4.69).
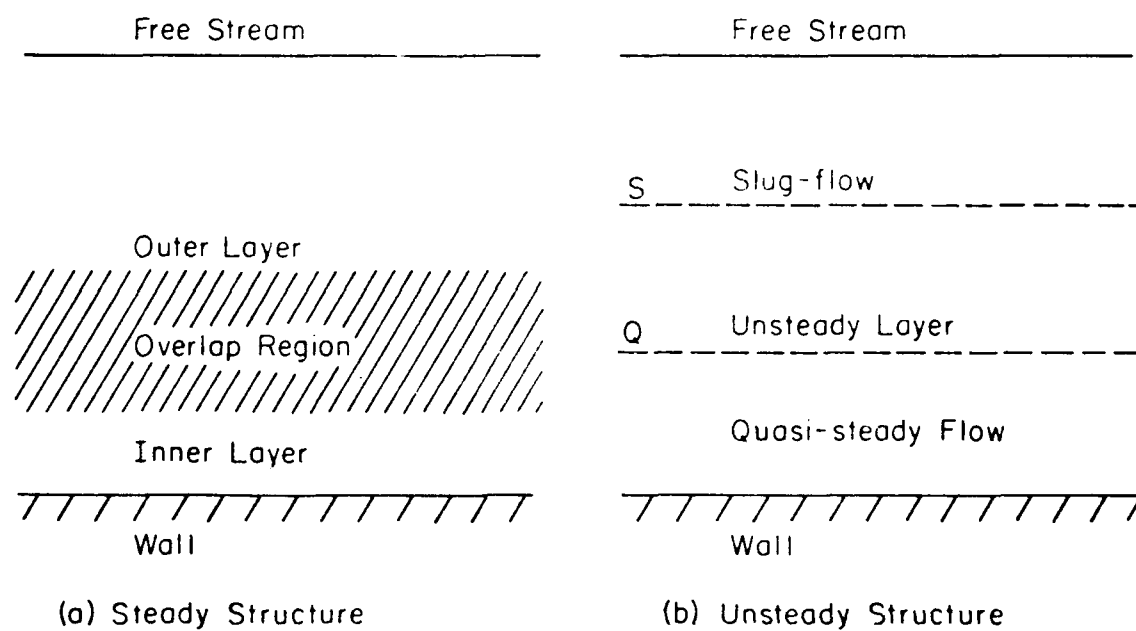
Figure 4.1. Schematic representation of the flow structure.

(a) Low Frequency Regime

(b) Intermediate Frequency Regime

Linear Flow, Eq. (4.69)

Stokes Flow, Eq. (4.60)

(c) High Frequency Regime

(d) Very High Frequency Regime
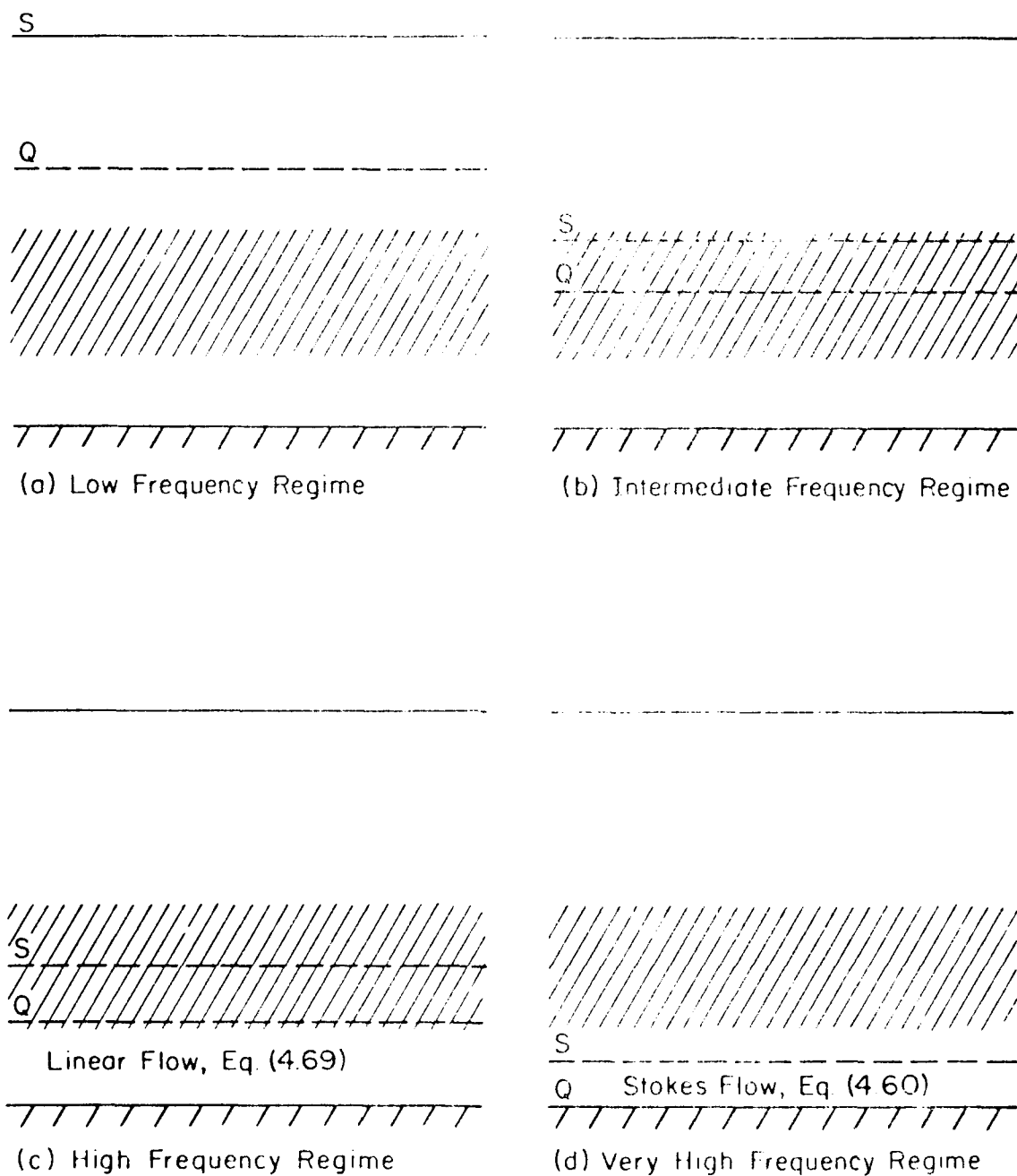
Figure 4.2. Schematic representation of the different flow
regimes in terms of the overlap between the
steady and unsteady structures.

CHAPTER 5

EXPERIMENTAL RESULTS IN
VIEW OF THE THEORY

5.1. General

The theory developed in the previous chapter is now applied to the experimental results. This not only constitutes a check, but also allows the identification, within experimental error, of some of the similarity laws to which the theory leads. In addition, a clear picture starts to emerge regarding the continuous transition of the oscillatory velocity profiles from the low to the very high frequency regime. Some of the concepts and ideas provided by the theory are also used to generalize its application to other flow quantities.

Table 5.1 shows the most relevant parameters for the present data at each station and for both the oscillating frequencies. It is observed that the majority of the situations correspond to the intermediate frequency regime. The remaining ones are in the transition range between the low and intermediate frequency regimes. Therefore, they are expected to have, to some extent, the main characteristics of both regimes.

5.2. Velocity

In this section, in addition to the present data, some experimental results from other studies on boundary-layer, channel,

and pipe flows are examined. This will not only demonstrate the generality of the theory, but will also provide a more comprehensive picture of the effect of unsteadiness on wall-bounded turbulent shear flows. Table 5.2 presents a list of these additional experiments, together with their most relevant parameters.

The cases in the low or transitional low-intermediate frequency regime must be expected to exhibit the "logarithmic law", Eq. (4.53) or Eqs. (4.74) and (4.75). Figure 5.1 presents the in-phase oscillatory component, U_{11}, in the inner coordinates, for experiments M1, M5, CA, T1 and J1. Data corresponding to intermediate and intermediate/high frequency regimes (experiments J2, J3 and J4) are also shown. A line corresponding to the universal logarithmic law for the mean velocity profile in steady flow is drawn. Its slope is used as a reference. It is readily observed that, in all the low and low-intermediate frequency regime experiments, there is a range in which the in-phase component varies logarithmically and with the universal slope, as predicted by the theory. Towards the outer edge, a "wake component" can be identified as for the steady-flow mean velocity profile, but extending deeper into the boundary layer. Note that this wake component is very strong for experiment J1 due to the time-mean adverse pressure gradient. This reduces considerably the extent of the logarithmic region (situated around $y^+ \approx$ ...).

The corresponding out-of-phase component, U_{12}, is shown in Fig. 5.2. It is seen that, in fact, there is a region of constant phase in the low and low-intermediate frequency experiments, in agreement with Eq. (4.75). This value generally corresponds to the edge of the

distribution, except for experiment J1 for which the region of constant value behaves like a saddle point. These results show that, like the time-mean flow, the oscillatory motion in the outer layer depends strongly on the particular flow conditions.

It is possible to obtain some more information from the foregoing figures. Comparing experiments M1, M5, GA and J1 in Fig. 5.1, it can be concluded that the additive constant in the logarithmic law [B_{11} in Eq. (4.78)] increases with $\tilde{\omega}$. The same effect is produced by the time-mean adverse pressure gradient, as seen from the data for experiment J1. It is more difficult to identify trends in the case of the constant associated with the out-of-phase component. This is because, since it is small in the zero or small time-mean pressure gradient cases, it is subjected to larger experimental errors. However, since it has to vanish for $\tilde{\omega} \to 0$ (quasi-steady flow) and for $\tilde{\omega} \to \infty$ (slug flow, except in a very thin Stokes layer) a nonmonotonic trend has to be expected, as is, in fact, suggested by the data. Note that the adverse pressure gradient, in turn, causes the constant to become positive (which means that there is a phase lag).

As already mentioned, figures 5.1 and 5.2 also present the data for experiments J2, J3, and J4. They are particularly useful because relatively accurate data extending to $y^+ = 1$ were obtained in these experiments. It is observed that experiments J2 and J3 show similar distributions, though the amplitude is relatively very much larger in the experiment J4. The vestiges of the logarithmic and constant-value regions can still be identified. On the other hand,
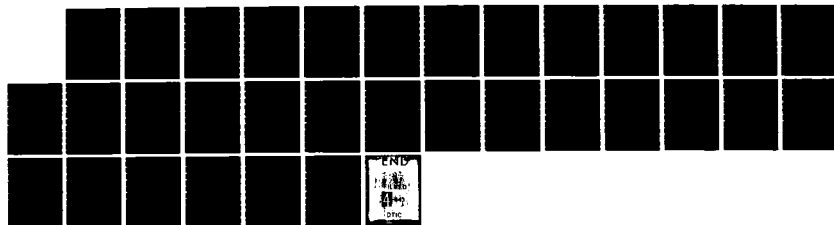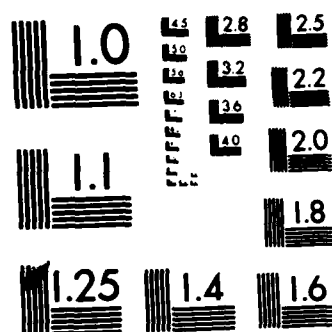
MICROCOPY RESOLUTION TEST CHART

NATIONAL BUREAU OF STANDARDS-1963-A

experiments J2 and J4 show that, with increasing $\tilde{\omega}$, a slug-flow region develops in the outer layer beginning from the outer edge. The out-of-phase component, in turn, is reduced in the inner layer, relative to the lower frequency cases J1 and J3. In fact, higher frequencies cause the local velocity to lead the free-stream velocity. This trend is opposite to that produced by the time-mean pressure gradient, which tends to produce a phase lag in the local velocity. It is also important to note that, at a given time-mean adverse pressure gradient (experiments J_1, J_2 or J_3, J_4), there is no significant change in the distribution of U_{11} in the inner layer. This supports the theory of Chapter 4 that the behavior of U_{11} in the inner layer is quasi-steady in the low to intermediate frequency range.

The previous discussion permits one to construct a general, though still speculative, picture of how the oscillatory components behave when the frequency parameter $\tilde{\omega}$ increases. Figure 5.3 refers to the case of a zero time-mean pressure gradient boundary layer. It is observed that there is a continuous transition between the "log + wake" profile for the low-frequency regime and the Stokes (viscous) solution for the very high-frequency regime.

According to the theory, in the intermediate-frequency regime there must exist an outer region of slug flow. That this is in fact the case for the present experimental results has already been shown in Chapter 3 (see Figs. 3.21 and 3.22). The same is true for the other experiments discussed in this section, as already mentioned with reference to experiments J2 and J4. Immediately next to this

layer, and closer to the wall, an intermediate unsteady layer develops where the "velocity defect law", Eq. (4.66) or Eqs. (4.82) and (4.83), must be satisfied. Figures 5.4 and 5.5 show the in-phase and out-of-phase velocity components, respectively, for all the present experimental data, plotted in the coordinates corresponding to the unsteady layer [see Eq. (4.62)]. The error in the asymptotic results is of the order $(\ln R_*)^{-1}$. Admitting an error of ± 0.5 (see Table 5.1), we conclude that the collapse is reasonably good for the truly intermediate frequency cases, in agreement with the theory. Deviations occur for the transitional low/intermediate frequency cases, specially for the out-of-phase component and closer to the outer edge of the unsteady layer. In these cases, the slug-flow region has nearly disappeared, so the unsteady layer extends practically up to the edge of the boundary layer. Hence, the deviations must result from the interaction with the free stream. In all the cases, the scatter for the out-of-phase component is much larger than for the in-phase component. This is, as already mentioned, due to the larger experimental errors in the measurement of U_{12}. It is significant to note that the location of the peak in the in-phase component, which is a measure of the extent of the unsteady layer, corresponds to $\hat{y} \simeq 1$.

Figures 5.6 and 5.7 present the results for experiments T2, J2, J4, AR and BK plotted in the "unsteady-layer coordinates". A typical set of data from the present experiments is also shown in the figure for comparison. It can be seen, again, that this normalization brings the data closer to one another, even though considerable

deviations still remain. However, these should *be interpreted with caution* due to the following reasons:

(i)   Except for the data set of experiment T2 and, of course, the present ones, all of the data were obtained from published graphs.

(ii)   The data of experiments J2, AR and BK, though closer to satisfy the small-amplitude assumption, may be subjected to larger experimental errors because, precisely, of the very low amplitudes of oscillation (see Table 5.2).

(iii)   In using the data set J2 and J4, the local boundary-layer thickness used by the originators to normalize the y-coordinates in their plots was not available and was therefore estimated.

There is a relatively good collapse of the results for the in-phase component in the near-wall region (see Fig. 5.5). In the outer part, some of the relative departures may be genuine and linked to the different characteristics of the outer flow. Similar comments can be made about the out-of-phase component (Fig. 5.7) which, again, show significant scatter in the near-wall region.

5.3. Other Flow Properties

Though the theory has been developed only for the oscillatory velocity components, the ideas can be extended to analyze other flow properties also. If the in-phase and out-of-phase components of the turbulence properties, namely $\langle u^2 \rangle$, $\langle v^2 \rangle$, and $\langle uv \rangle$, are defined in complete analogy with those for the velocity [see Eq. (4.71)], they must scale with u_*^2. To be consistent with earlier definitions (see chapter 3), they are normalized with $2u_*^2$. Their distributions in the unsteady-layer coordinates, for the present experiments, are shown in Figs. 5.8 to 5.13. With the same admitted error as for the velocity (± 0.5), the data for the in-phase component collapse fairly well for all the quantities, except for $\langle u^2 \rangle$ in the outer part of the unsteady layer. Deviations occur there for the transitional low/intermediate frequency cases (see Fig. 5.8). As in the case of the velocity, this must be attributed to interactions with the free stream, including some feeding of free-stream turbulence into the boundary layer. Less satisfactory is the performance of the out-of-phase components (Figs. 5.11 to 5.13), especially in the near-wall region. This can be due to a higher sensitivity of the turbulent quantities to the value of α. Note that the best data collapse is for $\langle uv \rangle$. The agreement improves when moving outwards, except for $\langle u^2 \rangle$, for which the same considerations as for the in-phase component apply.

As in the case of the turbulence properties, the in-phase and out-of-phase components of the wall shear stress $\langle \tau_w \rangle$ (obtained from $\langle C_f \rangle$) must scale with ρu_*^2. Figure 5.14 presents the amplitude of oscillation of the wall shear stress as a function of the frequency

parameter $\tilde{\omega}$. Included are the measurements at all stations and all frequencies. They merge satisfactorily within the admitted error, ±0.08 (obtained from that for [$<C_f>$]; see Table 2.1). It is observed that the amplitude remains fairly constant with $\tilde{\omega}$. There possibly exists a mild minimum around $\tilde{\omega} \approx 30$ to 35. The variation of the phase of $<\tau_w>$ with frequency is shown in Fig. 5.15. Again, there is a satisfactory correlation of the results. An approximately linear trend is observed in the variation of the phase angle with $\tilde{\omega}$.

Finally, the in-phase and out-of-phase components of the eddy viscosity, obtained from the measurements at station 5, and at both the frequencies, are plotted in Figs. 5.15 and 5.16. They are normalized by u_*^2/ω, as suggested by dimensional analysis. A relatively large uncertainty must be accepted because of the manner in which they are calculated. For example, they are very sensitive to the values of $\partial U_1/\partial y$, which are obtained from a piecewise fit to U_1 vs. y (see chapter 3). The collapse for the two sets of data is fairly good in the near-wall region, especially for the in-phase component. Large differences are observed in the outer part, which are believed to be associated with the above-mentioned calculation errors. The results corresponding to the lower-frequency data set are considered to be more reliable in this respect. The data, however, seem to confirm that neither a quasi-steady ($\nu_{t12}=0$) nor a frozen eddy-viscosity model ($\nu_{t11} = \nu_{t12} = 0$) is realistic at either of these frequencies.

5.4. Time-Mean Flow

As discussed in chapter 3, small but significant frequency effects are found in the outer distribution of the time-mean quantities, specially the turbulence properties. Though the theory developed does not deal with the time-mean flow (in fact, it assumes that it is equal to the steady flow at the time-mean free-stream velocity), the frequency parameters derived from the analysis can be used to correlate the observed departures.

The strongest frequency effects were observed in experiments M4, M5, M6 and M7. Hence, it can be said that frequency effects on the time-mean quantities, in the outer layer, can be expected in the range $8 \lesssim \tilde{\omega} \lesssim 20$. For $\tilde{\omega} < 8$, frequency effects are too weak. On the other hand, for $\tilde{\omega} > 20$, frequency effects, if present, must be confined to the near-wall region. In the outer layer the turbulence distribution is then frozen, so the time-averaged flow properties approach those in steady-flow at the time-mean velocity.

Table 5.1

Characterization of the Present Experiments

Experiment	M1	M2	M3	M4	M5	M6	M7	M8	M9	M10
Station No.	1	2	3	4	5	1	2	3	4	5
$f(Hz)$			0.5					2		
$\cdot(cm)$	0.213	0.244	0.283	0.380	0.463	0.213	0.244	0.283	0.380	0.463
E	0.0420	0.0419	0.0414	0.0400	0.0392	0.0420	0.0419	0.0414	0.0400	0.0392
$\Lambda(cm)$	5.07	5.83	6.84	9.49	11.8	5.07	5.83	6.84	9.49	11.8
$L(cm)$	121	139	165	237	301	121	139	165	237	301
$R_\star$	1920	2200	2550	3420	4170	1920	2200	2550	3420	4170
$R_\star^{1/2}$	43.8	46.9	50.5	58.5	64.5	43.8	46.9	50.5	58.5	64.5
$\tilde{\omega}$	4.21	4.85	5.76	8.28	10.5	16.8	19.4	23.0	33.1	42.1
σ	456	453	442	413	396	114	113	111	103	99.0
Freq. Regime	Low/Int	Low/Int	Low/Int	Low/Int	Int	Int	Int	Int	Int	Int

Table 5.2

Characterization of Other Experimental Studies

| Reference	Cousteix et al. (1977)	Ramaprian and Tu (1982)		Jarayaman et al. (1982)				Acharya and Reynolds (1975)	Binder and Kueny (1981)
Time-Mean Flow	Zero Pr. Gr.	Pipe Flow		Adverse Pr. Gr.		Strong Adverse Pr. Gr.		2-D Channel Flow	2-D Channel Flow
Fluid	Air	Water		Water		Water		Air	Water
Expt. Designation	CA	T1	T2	J1	J2	J3	J4	AR	BK
f(Hz)	43	0.5	3.6	0.1	2	0.1	2	24	0.66
U_∞ or U_o (cm/s)	3360	108.9	113.7	69.54	69.54	54.90	54.90	667.5	17.5
ϵ	0.35	0.64	0.15	0.05	0.05	0.25	0.25	0.036	0.056
u_* (cm/s)	139	4.95	4.83	2.42	2.42	1.46	1.46	31.4	0.80
θ or h or R(mm)	0.960	25.4	25.4	5.73	5.73	12.1	12.1	31.75	50
R_*	2150	1260	1230	3980	3980	6660	6660	605	400
$R_*^{1/2}$	46.4	35.5	35.0	63.1	63.1	81.6	81.6	24.6	20
$\tilde{3}$	4.51	1.61	11.9	4.27	85.5	19.6	392	16.4	26.0
α	477	779	103	932	46.6	339.8	77.9	37.0	15.4
Freq. Regime	Low/Int	Low	Int	Low/Int	Int	Int	Int/High	Int.	Int.
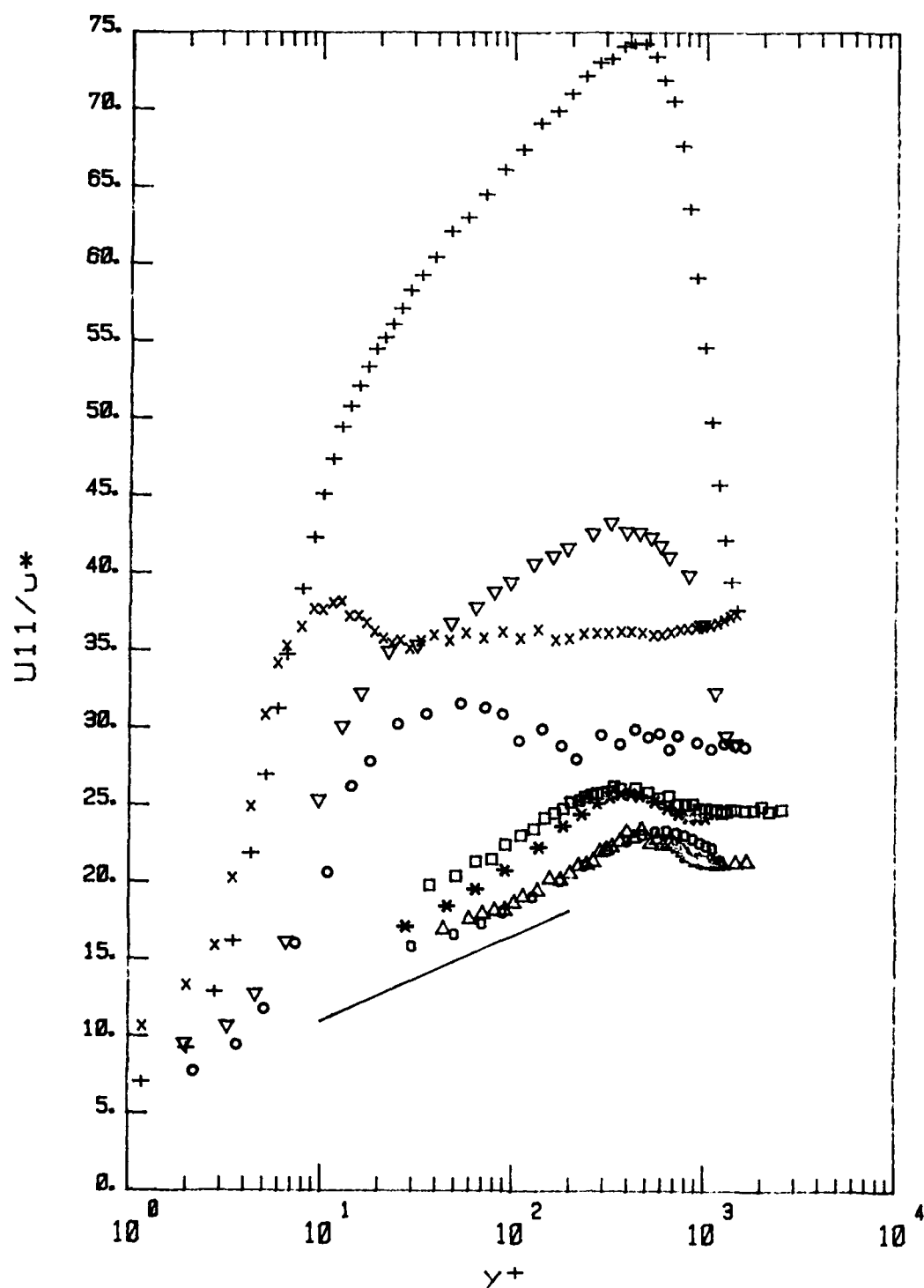
Figure 5.1. In-phase velocity component for the low and low/intermediate frequency regime. △, experiment M1: □ . M5: *. CA: O , T1: ▽, J1; ', J2; +, J3; x, J4; ——, universal logarithmic law.
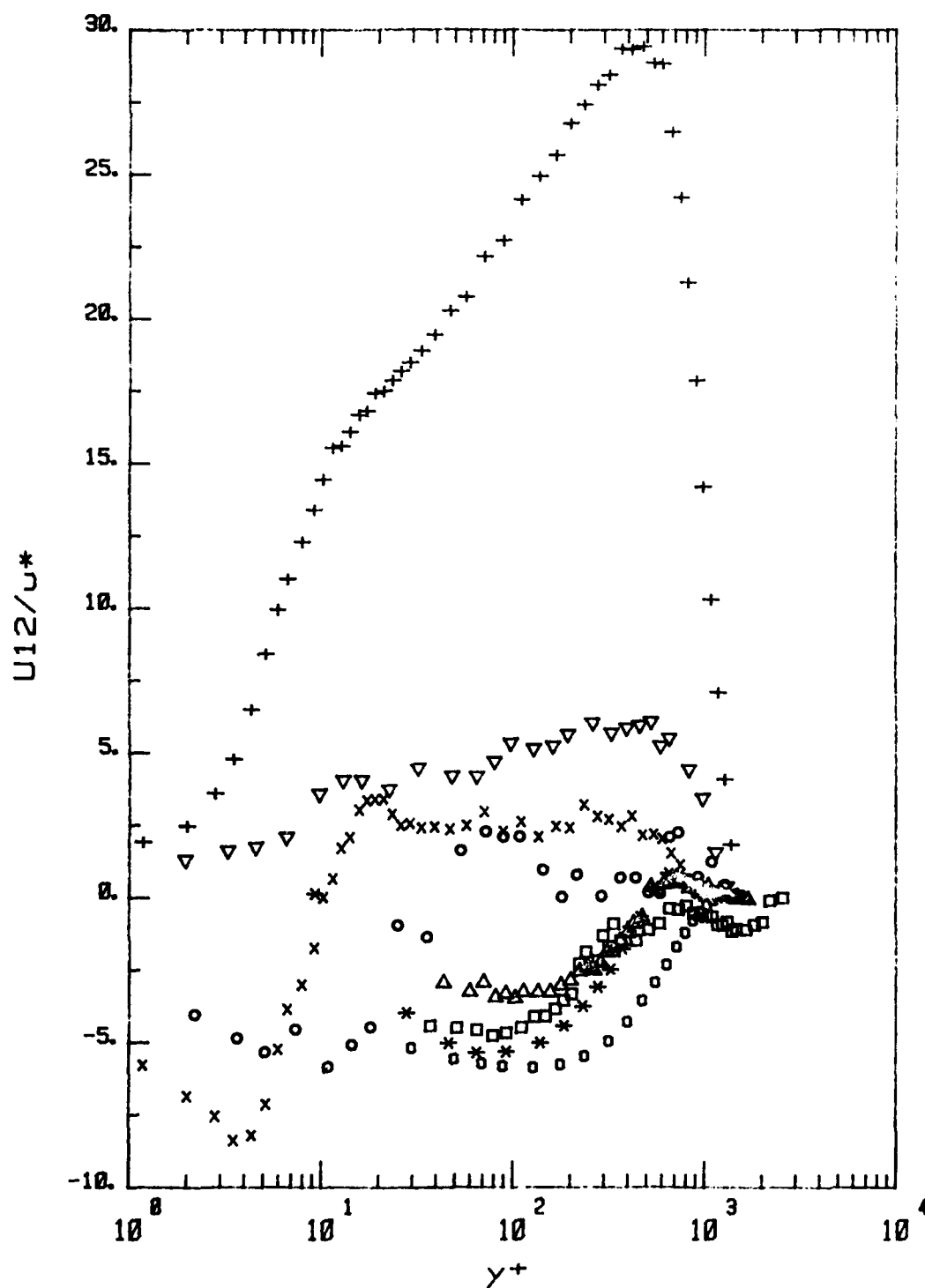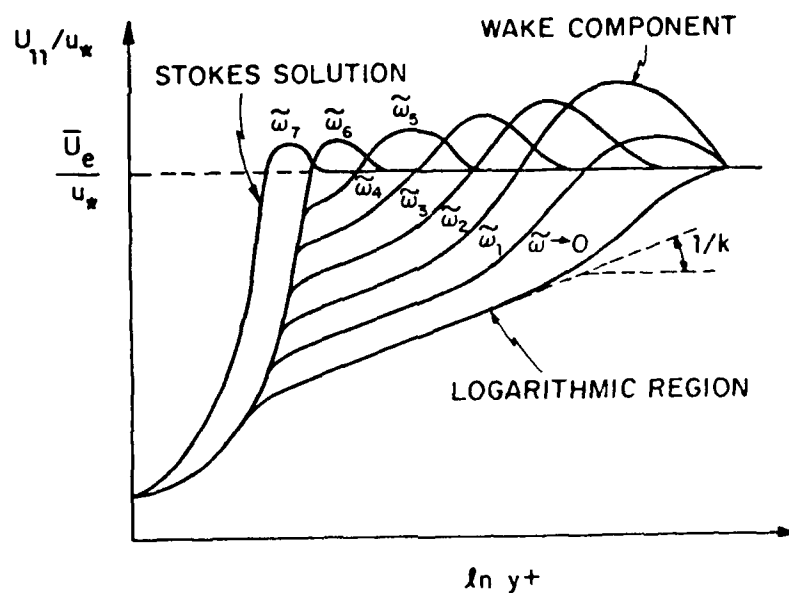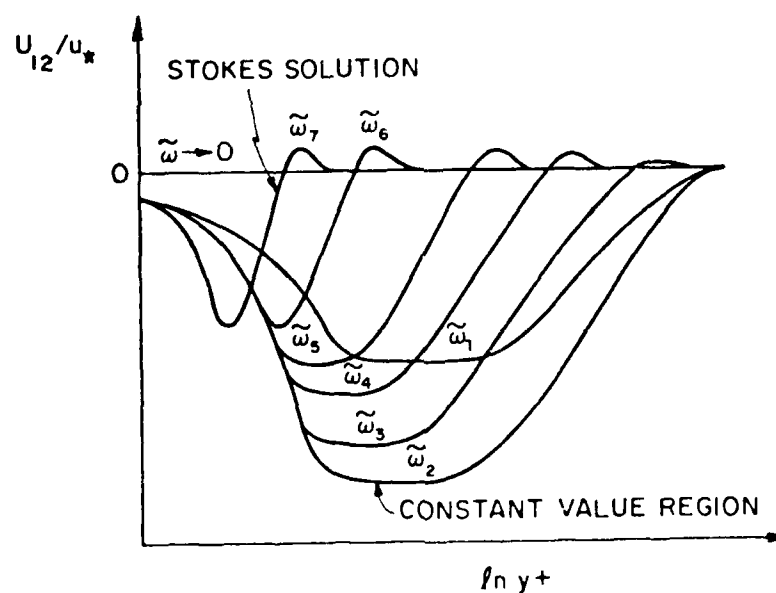
Figure 5.2.   Out-of-phase velocity component for the low
and low/intermediate frequency regime.
Symbols as in Fig. 5.1.

(a) IN-PHASE COMPONENT

(b) OUT-OF-PHASE COMPONENT

Figure 5.3. Qualitative representation of the evolution of the in-phase and out-of-phase velocity components with $0 < \tilde{\omega}_1 < \cdots < \tilde{\omega}_7$.
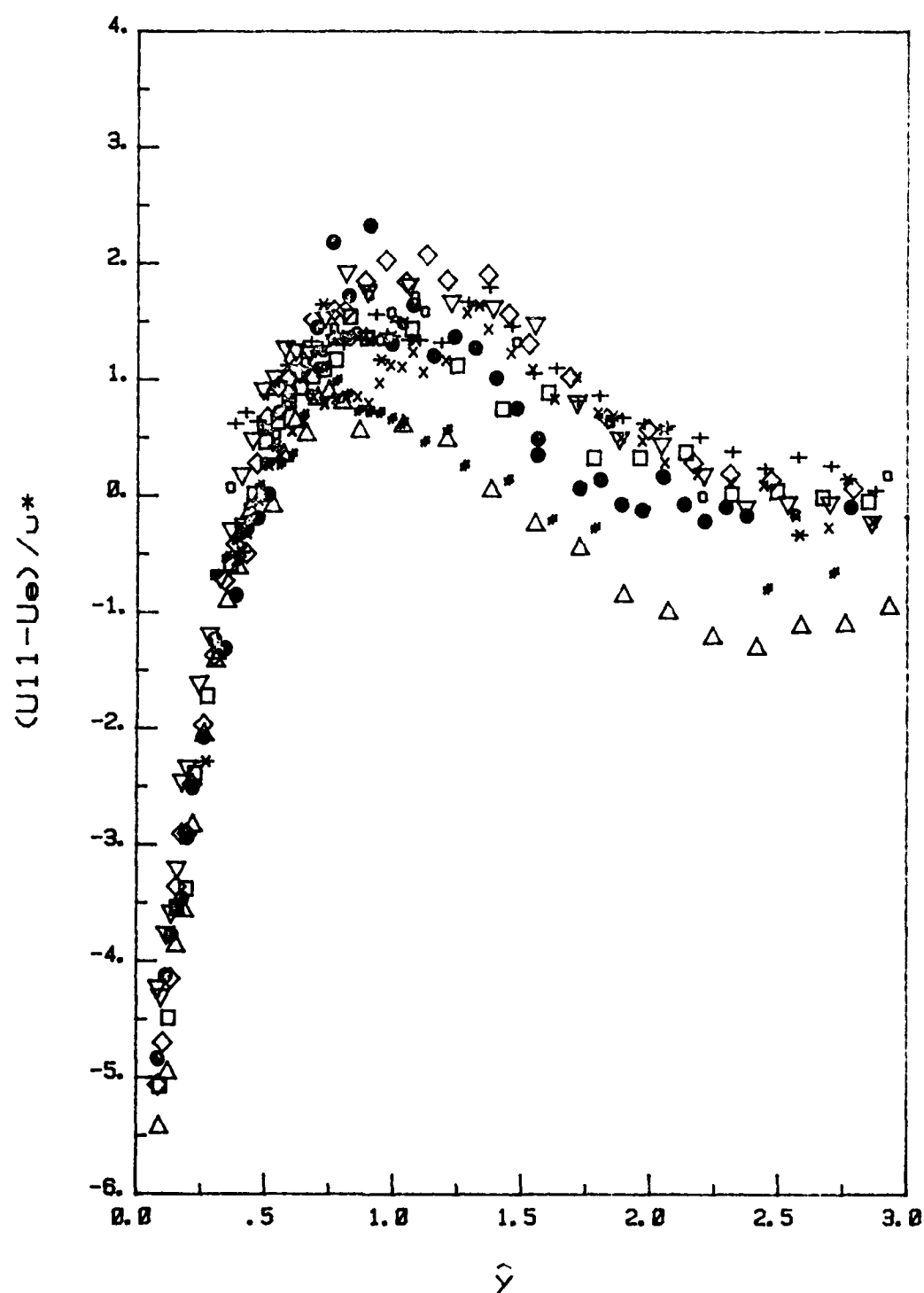
Figure 5.4.   In-phase velocity component in the unsteady
layer coordinates. $\mathbf{0}$, experiment M1; $\diamondsuit$, M2:
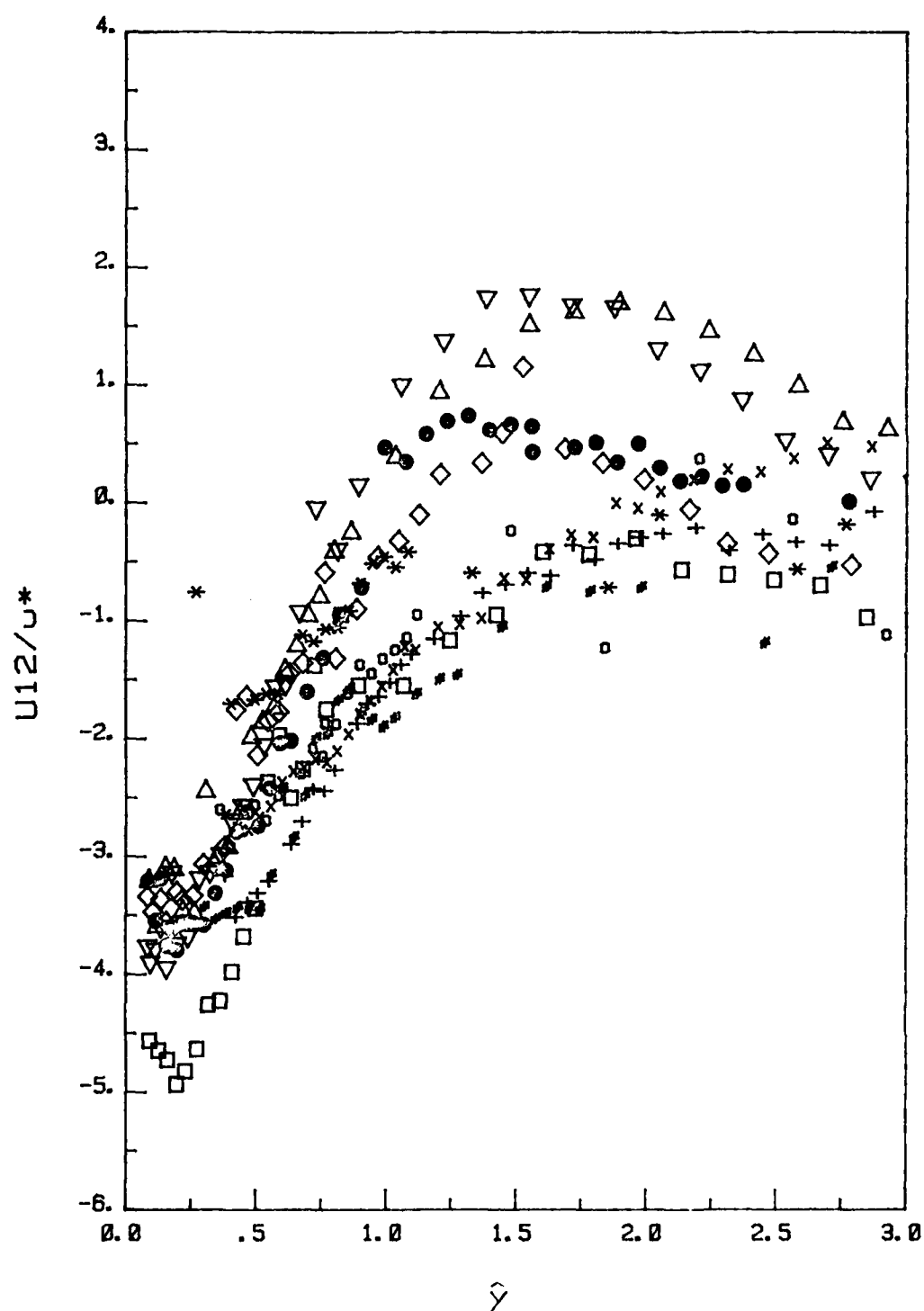$\triangledown$, M3; $\wedge$, M4; $\square$, M5; $\neq$, M6; x, M7; +, M8;
*, M9; 0, M10.

Figure 5.5. Out-of-phase velocity component in the unsteady
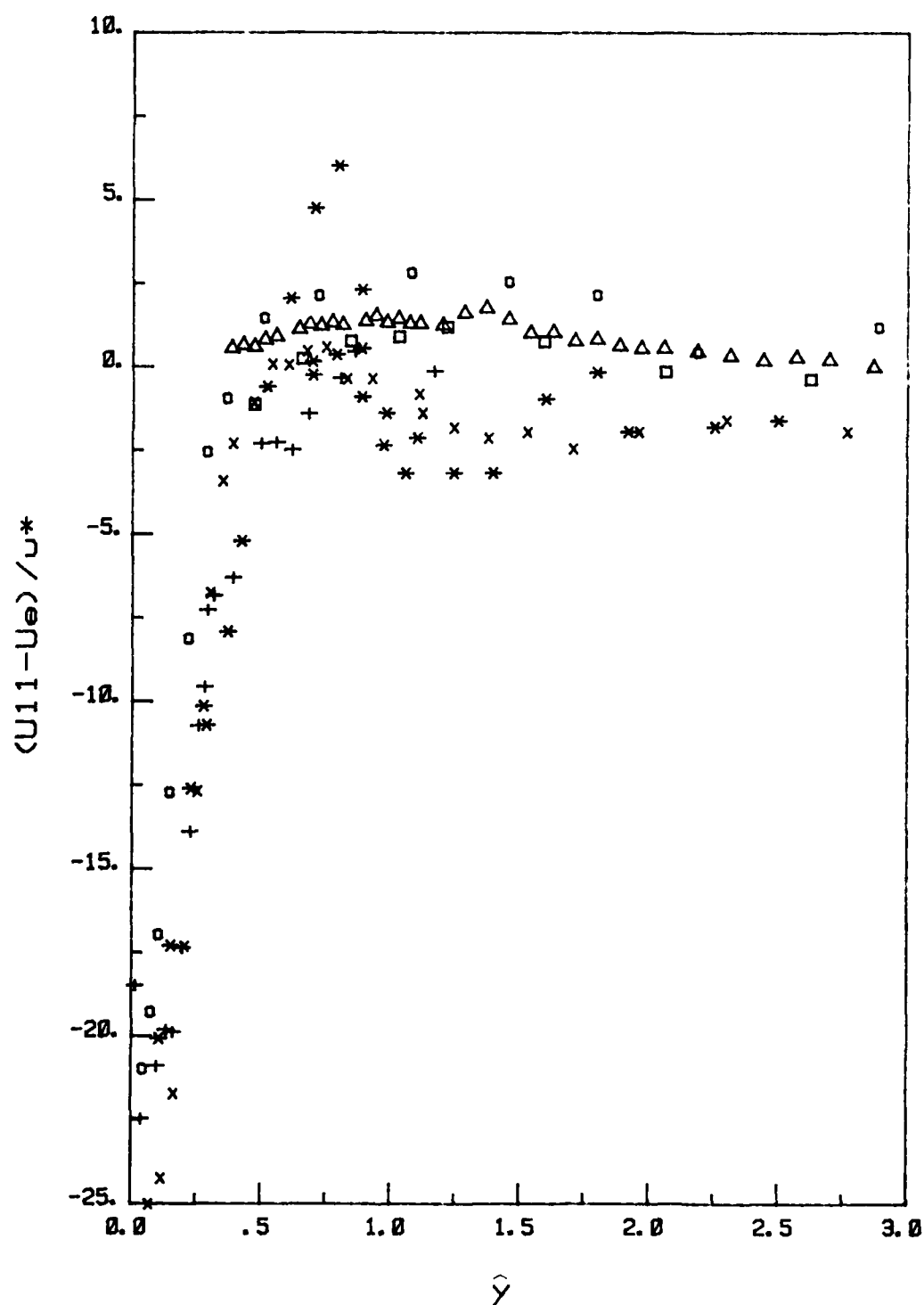layer coordinates. Symbols as in Fig. 5.4.

Figure 5.6. In-phase velocity component in the unsteady layer coordinates for the intermediate frequency regime. Δ, M8; □ , T2; 0, J2; x, J4; +, AR; *, BK.
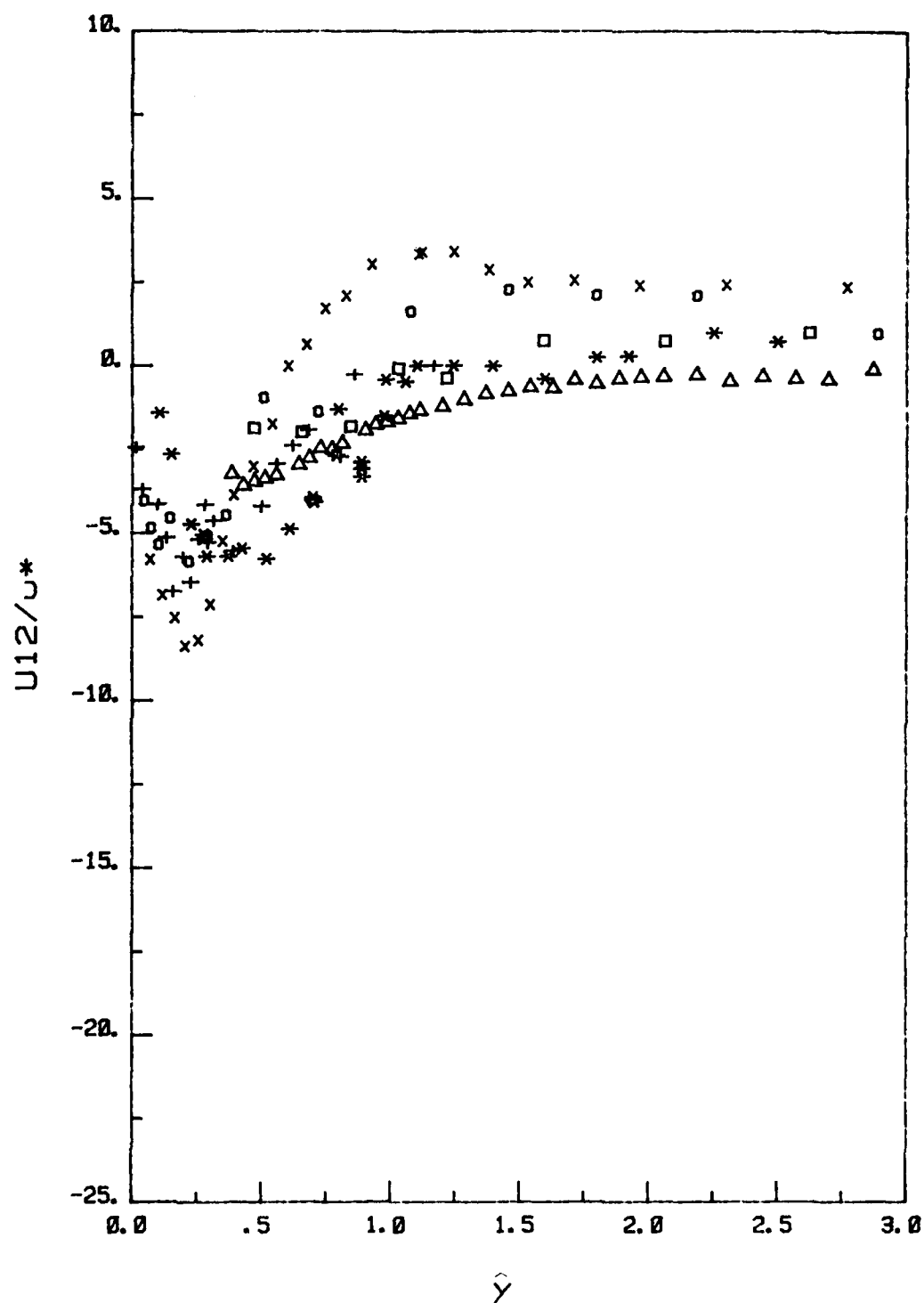
Figure 5.7. Out-of-phase velocity component in the unsteady layer coordinates for the intermediate frequency regime. Symbols as in Fig. 5.6.
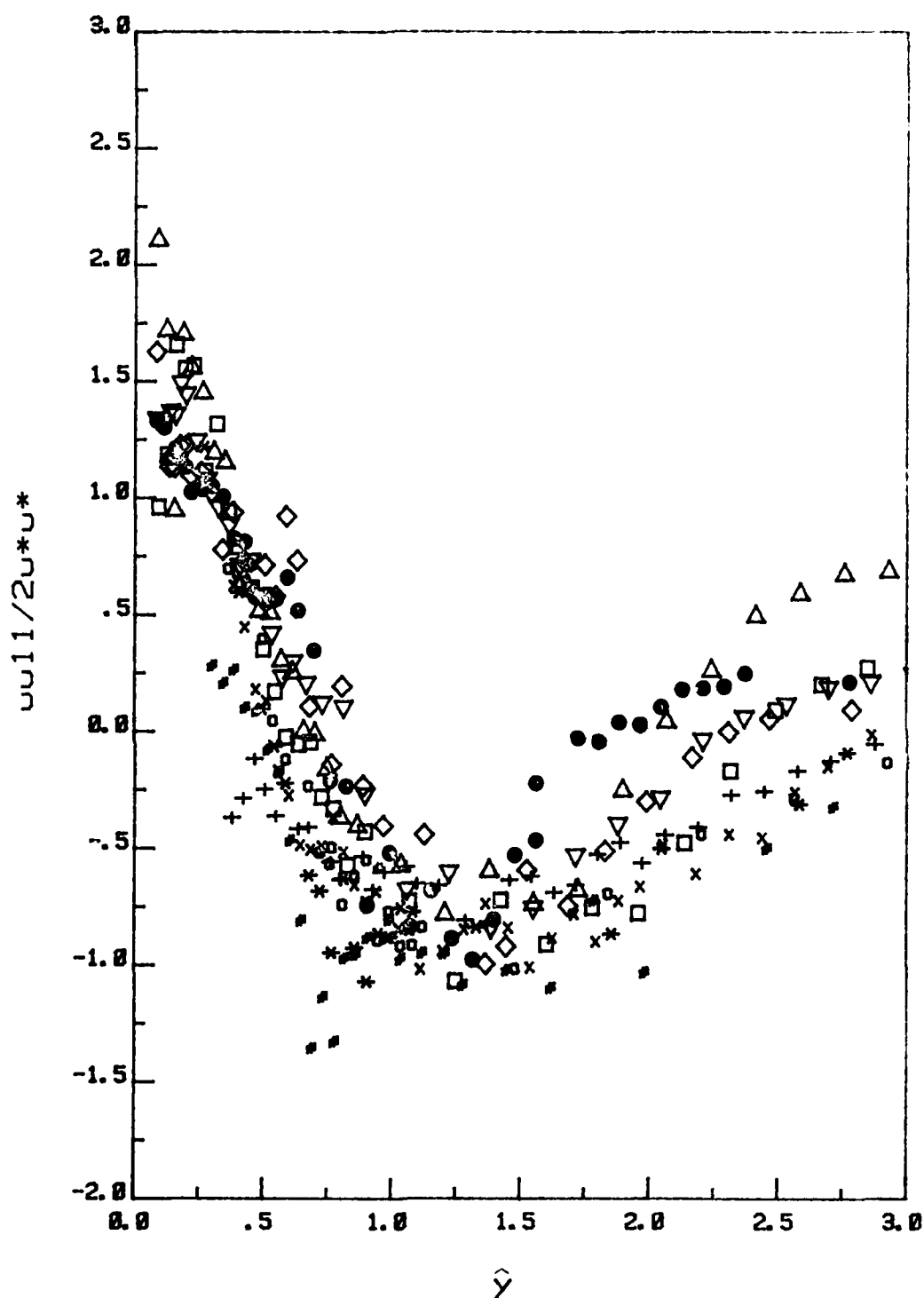
Figure 5.8. In-phase component for $\langle u^2 \rangle$ in unsteady layer
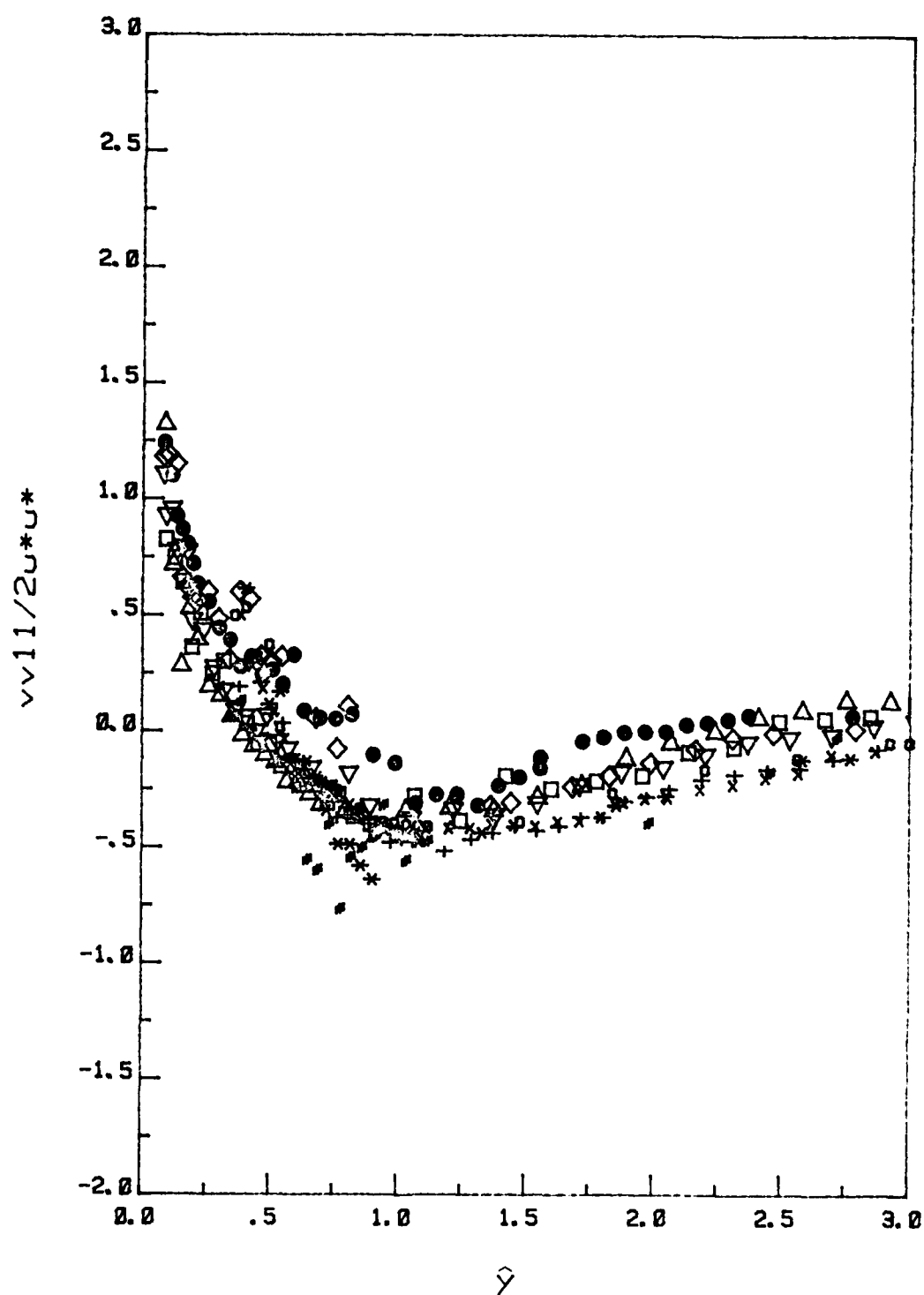coordinates. Symbols as in Fig. 5.4.

Figure 5.9. In-phase component for $<v^2>$ in unsteady layer coordinates. Symbols as in Fig. 5.4.

Figure 5.10.   In-phase component for <uv> in unsteady layer
coordinates.   Symbols as in Fig. 5.4.

Figure 5.11. Out-of-phase component for $\langle u^2 \rangle$ in unsteady layer coordinates. Symbols as in Fig. 5.4.
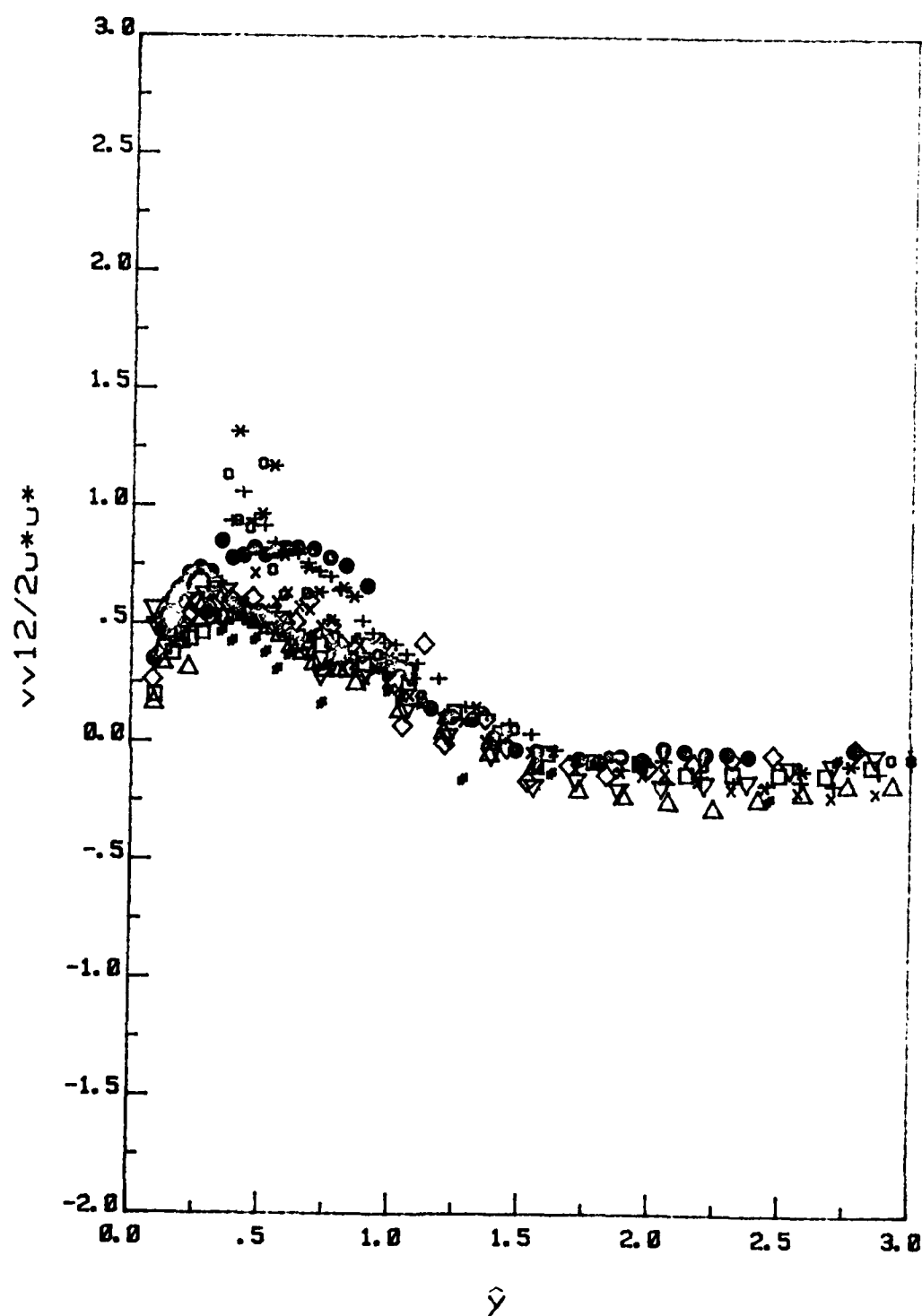
Figure 5.12. Out-of-phase component for $\langle v^2 \rangle$ in unsteady layer coordinates. Symbols as in Fig. 5.4.
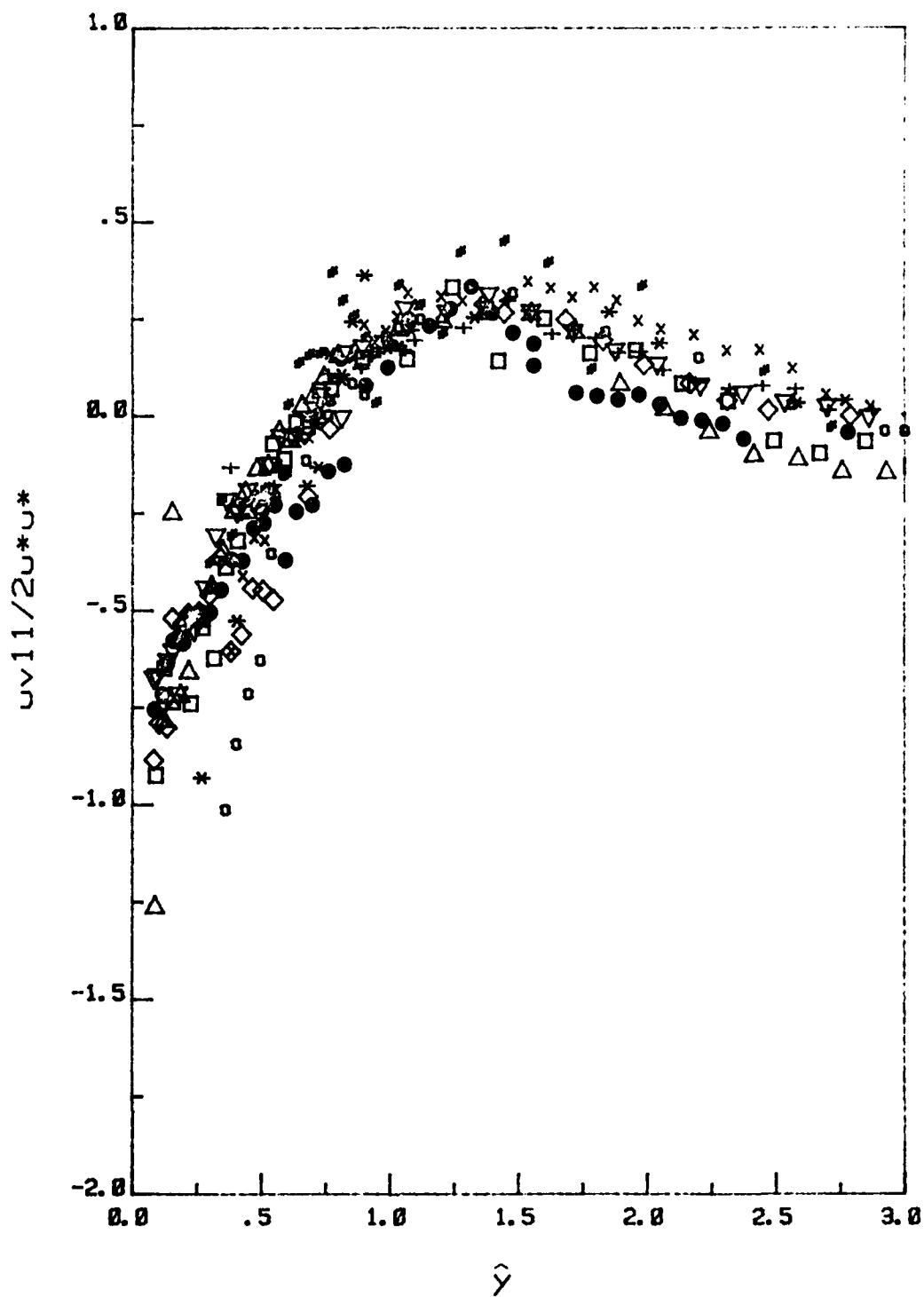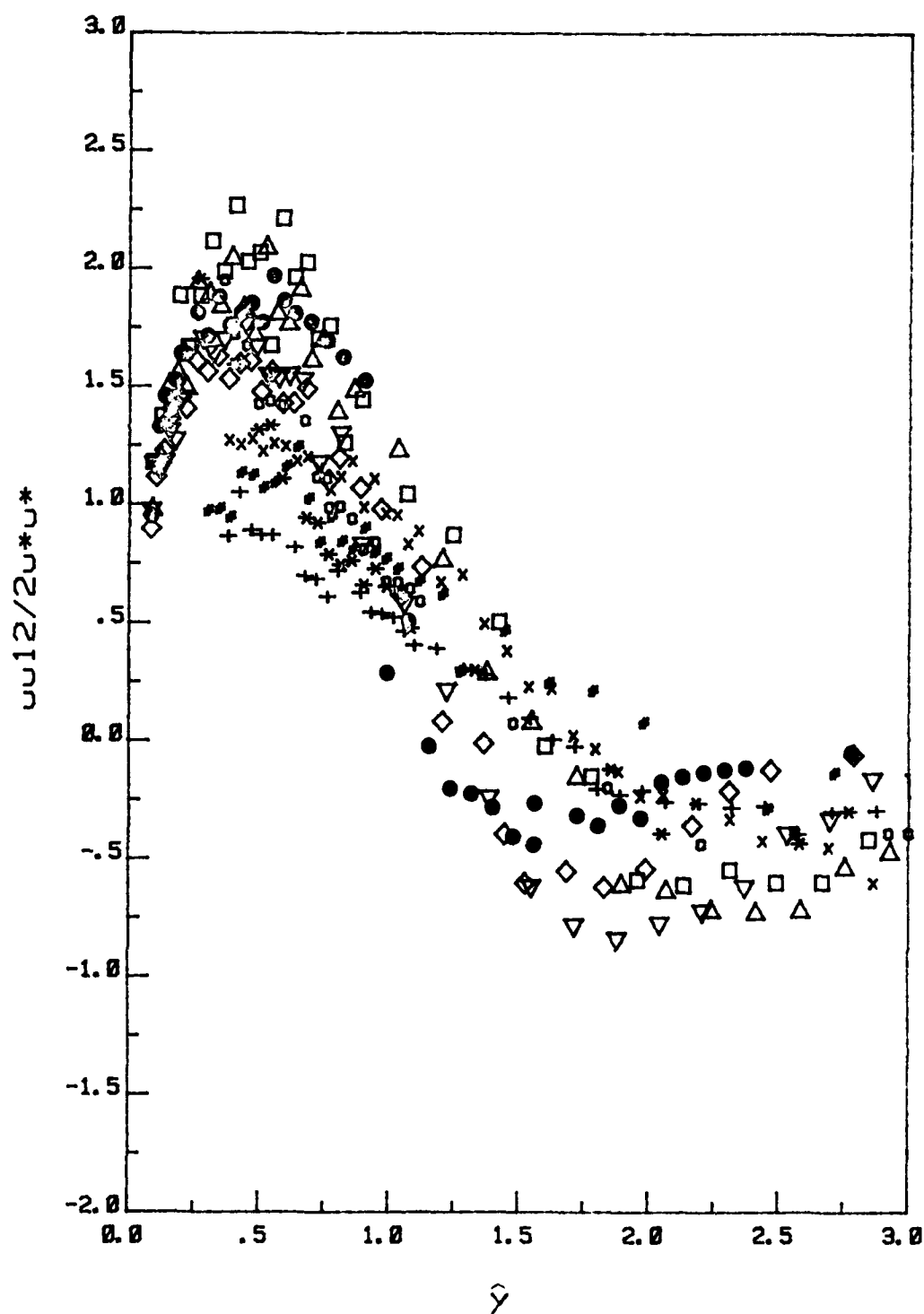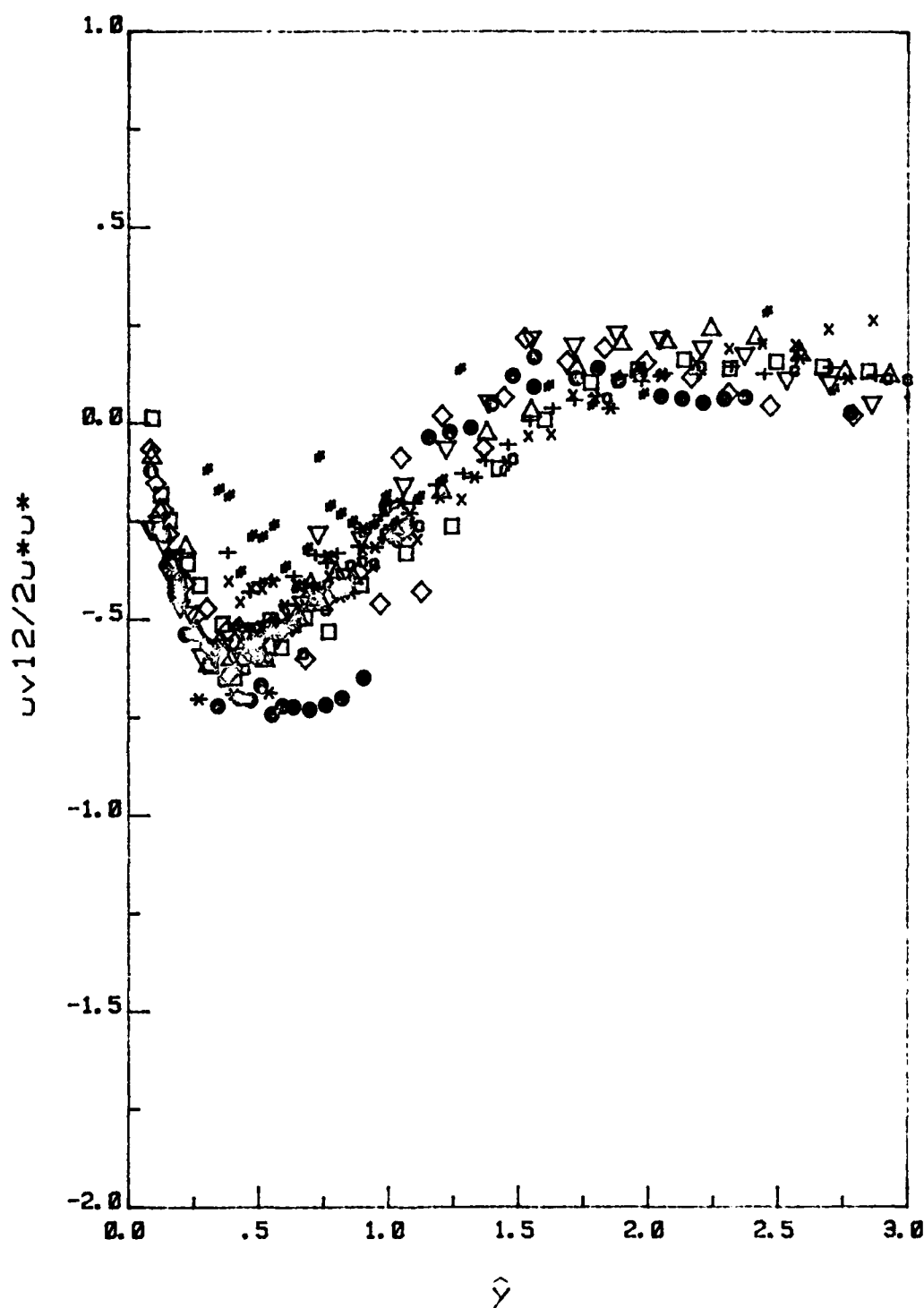
Figure 5.13.   Out-of-phase component for <uv> in unsteady
                layer coordinates.   Symbols as in Fig. 5.4.
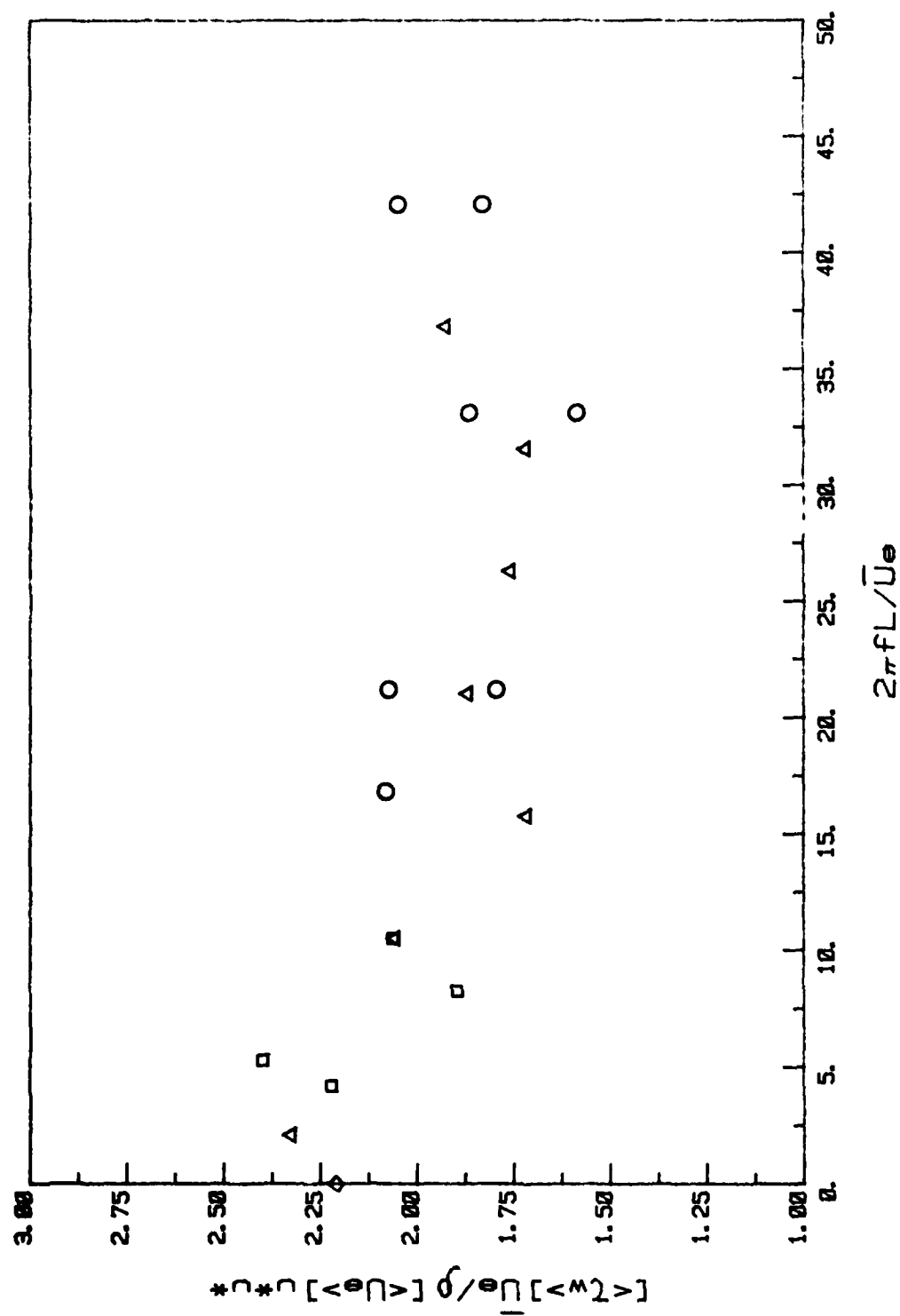
Figure 5.14. Correlation of the amplitude of the wall shear stress in terms of ..
□, f = 0.5 Hz; ○, f = 2 Hz; △, station 5, 0.5 Hz sleeve; , quasi-
steady.

Figure 5.15. Correlation of the phase of the wall shear stress in terms of $\tilde{\tau}$, station 5, 2 Hz sleeve. Other symbols as in Fig. 5.14.

Figure 5.16. In-phase component of $\langle \nu_t \rangle$ in unsteady layer coordinates. $\square$, experiment M5; 0, M10.

Figure 5.17. Out-of-phase component of $<\upsilon_t>$ in unsteady layer coordinates. Symbols as in Fig. 5.16.

CHAPTER 6

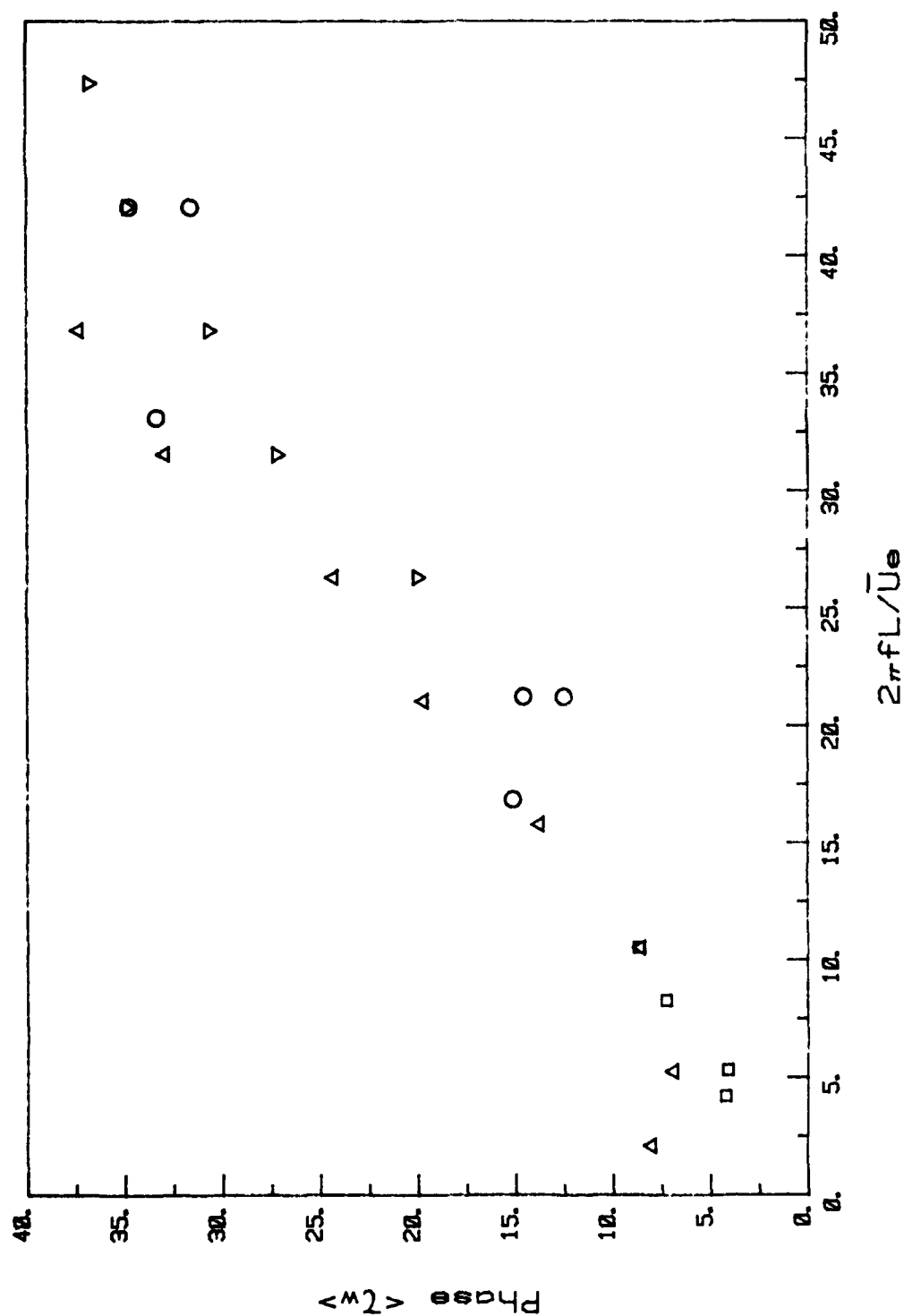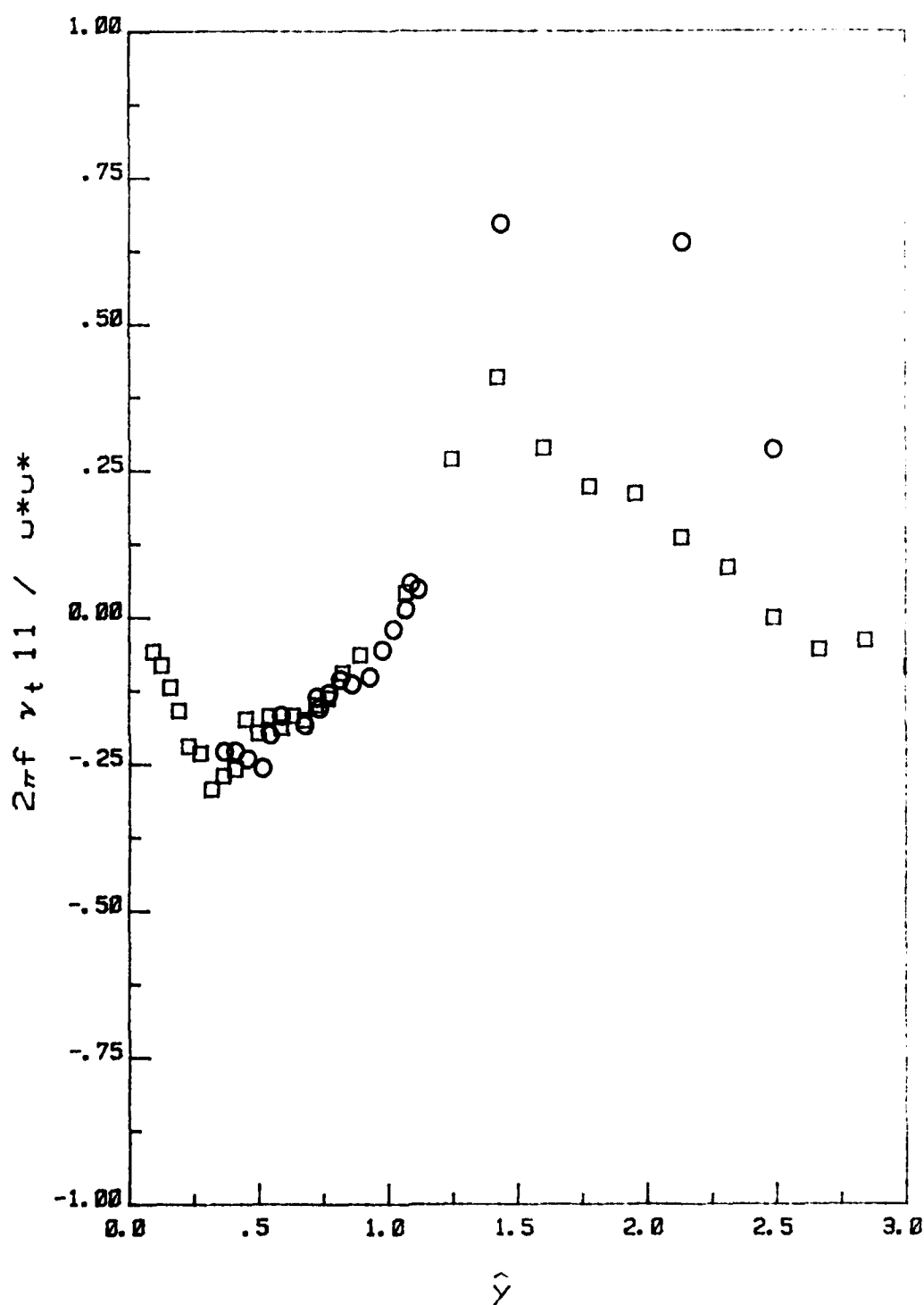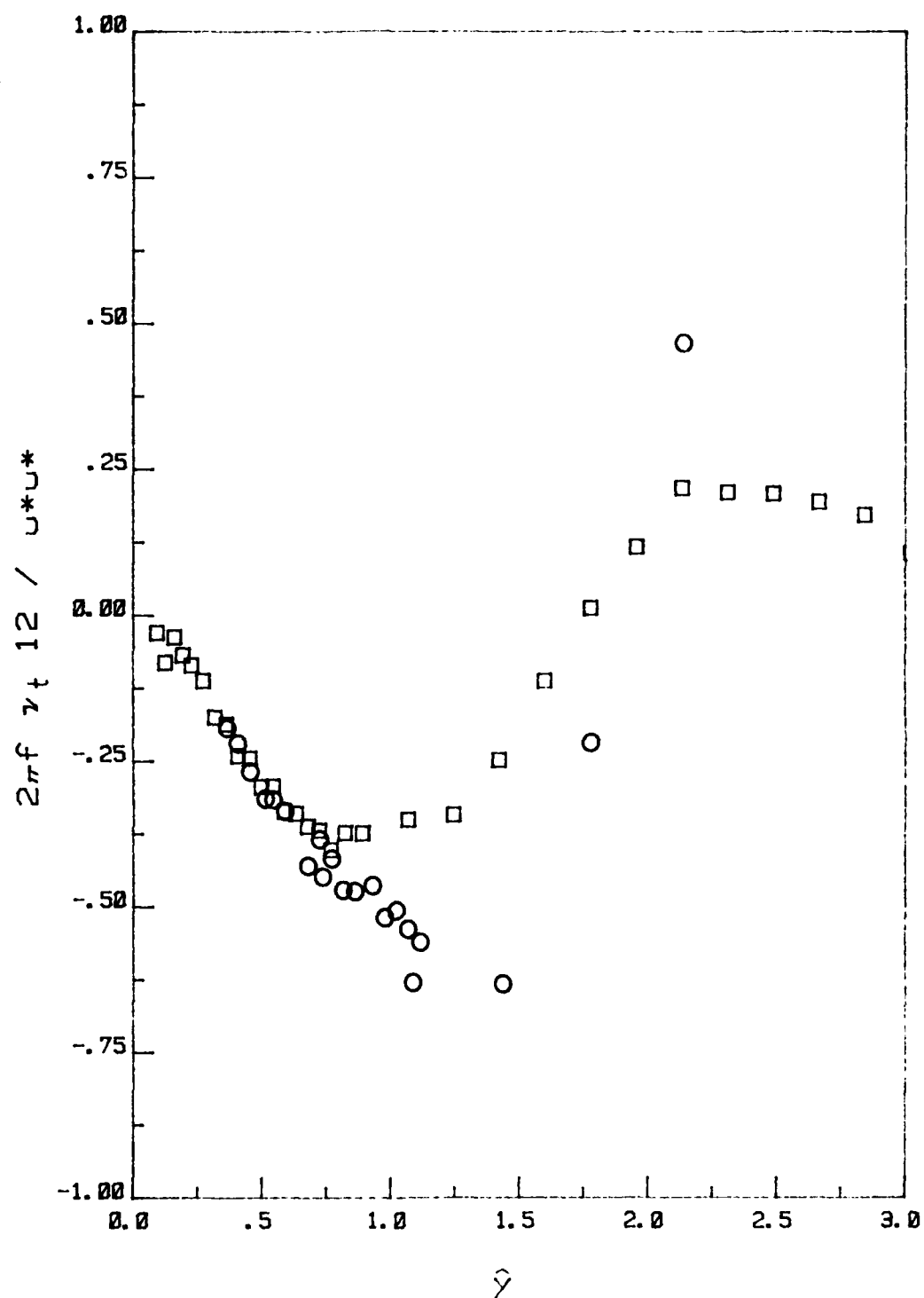## CONCLUSIONS

The following are the main findings of the present investigation:

(i) Spatial history effects on the time-mean properties have been identified and interpreted for a periodic, turbulent boundary layer developing in zero time-mean pressure gradient. It has been found that the oscillation accelerates the development of the outer flow, while it has little effect on the inner flow. The modification of the outer flow can be interpreted as a shift in the virtual origin of the turbulent boundary layer. For large Reynolds numbers, the time-mean properties tend to approach their steady distributions at the time-mean free-stream velocity. The small residual differences between the two can be considered to be 'frequency effects'.

(ii) Frequency effects on the time-mean properties have also been identified and correlated. They produce a small positive departure in the outer layer, relative to the steady-flow distribution at the same Reynolds number, for $8 \lesssim \tilde{\omega} \lesssim 20$.

(iii) The behavior of the oscillatory components of the motion has been seen to confirm what was previously known. In particular, many of the conclusions of Ramaprian and Tu (1982) on periodic pipe flows apply equally well to unsteady boundary layers. The thickness of the unsteady layer, i.e. the layer over which unsteady viscous

effects are significant, has been characterized by the quantity u_*/ω, in agreement with Ramaprian and Tu (1982). Phase differences of about 360 degrees in the oscillatory components of the turbulence properties, across the unsteady layer, have been measured. Eddy-viscosity calculations, obtained from the measurements, have shown that neither a quasi-steady nor a 'frozen' turbulence model is appropriate for unsteady boundary layers at the present frequencies.

(iv) Wall-shear-stress measurements have been made using a flush-mounted heat-flux gage. The time-mean wall shear stress has been found to decrease slightly with increasing frequency, a trend opposite to that observed in pipe flow [Ramaprian and Tu (1982)]. The amplitude of oscillation is close to the quasi-steady value at all the frequencies. Larger phase leads (of over 30 degrees) than those reported by Ramaprian and Tu (1982) have been observed in the boundary layer at the higher frequencies.

(v) An asymptotic theory, for large Reynolds numbers, has been developed for the oscillatory motion. It is valid for both boundary layers at zero and adverse time-mean pressure gradients and fully developed pipe and channel flow, and has been successfully applied to the present and previous available experimental information.

(vi) The theory identified the frequency parameters $\tilde{\omega} = \omega\Lambda/u_*$ and $\alpha = u_*^2/\omega\nu$, as the appropriate parameters to characterize the oscillatory motion at large Reynolds numbers. The first one is analogous to that introduced by Ramaprian and Tu (1982) based on eddy viscosity arguments.

(viii)   Four frequency regimes have been identified (excluding the quasi-steady regime):

* Low frequency regime: $\tilde{\omega} \lesssim 1$ $(\alpha \gtrsim R_\star)$

* Intermediate frequency regime: $1 \ll \tilde{\omega} \lesssim R_\star^{1/2}$ $(R_\star^{1/2} \lesssim \alpha \ll R_\star)$

* High frequency regime: $R_\star^{1/2} \ll \tilde{\omega} \ll R_\star$ $(1 \ll \alpha \ll R_\star^{1/2})$

* Very high frequency regime: $\tilde{\omega} \gtrsim R_\star$ $(\alpha \lesssim 1)$

Similarity laws have been identified for each one of these frequency regimes.   These laws are the extension to unsteady flows of the well known "law-of-the-wall", "velocity-defect law" and "logarithmic law" for steady flows, and are summarized in section 4.3.5.

REFERENCES

Acharya, M., Reynolds, W.C. (1975), "Measurements and Predictions of a Fully Developed Turbulent Channel Flow with Imposed Controlled Oscillations", Stanford University, Technical Report TF-8.

Ackerberg, R.C., Phillips, J.H. (1972), "The Unsteady Laminar Boundary Layer on a Semi-Infinite Plate Due to Small Fluctuations in the Magnitude of the Free-Stream Velocity", J. Fluid Mech., Vol. 51, Part 1, pp. 137-157.

Bradshaw, P. (1976), Turbulence, Springer-Verlag.

Bellhouse, B.J., Schultz, D.L. (1966), "Determination of Mean and Dynamic Skin Friction, Separation and Transition in Low-Speed Flow with a Thin-Film Heated Element", J. Fluid Mech., Vol. 24, pp. 379-400.

Binder, G., Kueny, J.L. (1981), "Measurements of the Periodic Velocity Oscillations near the Wall in Unsteady Turbulent Channel Flow", IUTAM Symposium on Unsteady Turbulent Shear Flows, Toulouse, France, 5-8 May.

Carr, L.W. (1981a), "A Review of Unsteady Turbulent Boundary Layer Experiments", IUTAM Symposium on Unsteady Turbulent Shear Flows, Toulouse, France, 5-8 May.

Carr, L.W. (1981b), "A Compilation of Unsteady Turbulent Boundary Layer Experimental Data", AGARDograph No. 265.

Coles, D.E. (1962), "The Turbulent Boundary Layer in a Compressible Fluid", Report R-403-PR, The RAND Corporation.

Cousteix, J., Houdeville, R., Desopper, A., (1977), "Resultats Experimentaux et Methodes de Calcul Relatifs Aux Couches Limites Turbulentes en Ecoulement Instationnaire", ONERA, T.P. No. 1977-134.

Cousteix, J., Houdeville, R., Javelle, J. (1981), "Response of a Turbulent Boundary Layer to a Pulsation of the External Flow with and Without Adverse Pressure Gradient", IUTAM Symposium on Unsteady Turbulent Shear Flows, Toulouse, France, 5-8 May.

Drain, L.E. (1980), The Laser Doppler Technique, Wiley-Interscience.

Hill, P.G., Stenning, A.H. (1960), "Laminar Boundary Layers in Oscillatory Flow", J. of Basic Engrg., Vol. 82, pp. 593-608.

Hussain, A.K.M.F., Reynolds, W.C. (1970), "The Mechanics of a Perturbation Wave in Turbulent Shear Flow", Report FM-6, Mech. Eng. Dept., Stanford University.

Jarayaman, R., Parikh, P., Reynolds, W.C. (1982), "An Experimental Study of the Dynamics of an Unsteady Turbulent Boundary Layer", Technical Report TF-18, Dept. of Mech. Eng., Stanford University.

Karlsson, S.K.F. (1959), "An Unsteady Turbulent Boundary Layer", Journal of Fluid Mechanics, Vol. 5, pp. 622-636.

Klebannoff, P.S., (1954), "Characteristics of Turbulence in a Boundary Layer with Zero Pressure Gradient", NACA Report No. 3178.

Kobashi, Y., Hayakawa, M., "Structure of Turbulent Boundary Layer on an Oscillating Flat Plate", IUTAM Symposium on Unsteady Turbulent Shear Flows, Toulouse, France, 5-8 May.

Landweber, L., Siao, T.T. (1958), "Comparison of Two Analyses of Boundary-Layer Data on a Flat Plate", Jour. of Ship Research, Vol. 1, No. 4, pp. 21-33.

Lighthill, M.J. (1954), "The Response of Laminar Skin Friction and Heat Transfer to Fluctuations in the Stream Velocity", Proc. Roy. Soc., 224A, pp. 1-23.

Lyrio, A.A., Ferziger, J.H. (1983), "A Method of Predicting Unsteady Turbulent Flows and Its Application to Diffusers with Unsteady Inlet Conditions", AIAA Journal, Vol. 21, No. 4, pp. 534-540.

McCroskey, W.J., Philippe, J.J. (1975), "Unsteady Viscous Flow on Oscillating Airfoils", AIAA Journal, Vol. 13, No. 1, pp. 71-79.

Menendez, A.N., Ramaprian, B.R. (1982), "Calculation of Unsteady Boundary Layers", IIHR Report No. 248.

Menendez, A.N., Ramaprian, B.R. (1983a), "Calculation of Unsteady Boundary Layers", III Int. Conf. on Numerical Methods in Laminar and Turbulent Flow, The University of Washington, Seattle, 8-11 August.

Menendez, A.N., Ramaprian, B.R. (1983b), "Prediction of Periodic Boundary Layers", to appear in Int. J. for Num. Meth. in Fluids.

Menendez, A.N., Ramaprian, B.R. (1983c), "On the Measurement of Skin Friction in Unsteady Flow Using a Flush Mounted Hot Film Gage", IIHR Report, under preparation.

Mizushina, T., Maruyama, T., Hirasawa, H. (1975), "Structure of the Turbulence in Pulsating Pipe Flows", J. of Chem. Eng. of Japan, Vol. 8, No. 3, pp. 210-216.

Nash, J.F., Patel, V.C. (1975), "Calculation of Unsteady Turbulent Boundary Layers with Flow Reversal", NASA Report CR-2546.

Orlandi, P. (1981), "Unsteady Adverse Pressure Gradient Turbulent Boundary Layers", Unsteady Turbulent Shear Flows, Ed. R. Michel, J. Cousteix, R. Houdeville, Springer-Verlag, Berlin, pp. 159-170.

Patel, M.H. (1977), "On Turbulent Boundary Layers in Oscillatory Flow", Proc. R. Soc. Lond. A. 353, 121-144.

Patel, V.C., Nash, J.F. (1971), "Some Solutions of the Unsteady Two-Dimensional Turbulent Boundary Layer Equations", IUTAM Symposium on Unsteady Boundary Layers, Quebec, Canada.

Pedley, T.J. (1972), "Two-Dimensional Boundary Layer in a Freestream which Oscillates without Reversing", J. Fluid Mech., Vol. 55, Part 2, pp. 359-383.

Ramaprian, B.R., Tu, S.W. (1982), "Study of Periodic Turbulent Pipe Flow", IIHR Report No. 238.

Ramaprian, B.R., Chandrasekhara, M.S. (1983), "Study of Vertical Plane Turbulent Jets and Plumes", IIHR Report No. 257.

Ramaprian, B.R., Tu, S.W., Menendez, A.N. (1983), "Periodic Turbulent Shear Flows", Fourth Int. Symp. on Turbulent Shear Flows, Universitat Karlsruhe, West Germany, 4-7 September.

Rao, K.N., Narasimha, R., Badri Narayanan, M.A. (1971), "The Bursting Phenomena in a Turbulent Boundary Layer", J. Fluid Mech., Vol. 48, pp. 339-352.

Schachenmann, A.A., Rockwell, D.A. (1976), "Oscillating Turbulent Flow in a Conical Diffuser", J. Fluids Eng. 98, 695-702.

Simpson, R.L., Shivaprasad, B.G., Chew, Y.-T. (1983a), "The Structure of a Separating Turbulent Boundary Layer, Part 4. Effects of Periodic Free-Stream Unsteadiness", J. Fluid Mech., Vol. 127, pp. 219-262.

Simpson, R.L., Shivaprasad, B.G. (1983b), "The Structure of a Separating Turbulent Boundary Layer. Part 5. Frequency Effects on Periodic Unsteady Free-Stream Flows", J. Fluid Mech., Vol. 131, pp. 319-340.

Telionis, D.P. (1981), Unsteady Viscous Flows, Springer-Verlag.

Tennekes, H., Lumley, J.L. (1980), A First Course in Turbulence, MIT Press.

Tsahalis, D. Th., Telionis, D.P. (1974), "Oscillating Boundary Layers with Large Amplitude", in Unsteady Flows in Jet Engines, F.O. Carta (Ed.).

Tu, S.W., Ramaprian, B.R. (1983a), "Fully Developed Periodic Turbulent Pipe Flow. Part 1. Main Experimental Results and Comparison with Predictions", J. Fluid Mech., Vol. 137, pp. 31-58.

Tu, S.W., Ramaprian, B.R. (1983b), "Fully Developed Periodic Turbulent Pipe Flow. Part 2. The Detailed Structure of the Flow", J. Fluid Mech., Vol. 137, pp. 59-81.

Van Dyke, M. (1975), Perturbation Methods in Fluid Mechanics, The Parabolic Press.

White, F.M. (1974), Viscous Fluid Flow, McGraw-Hill.

Yajnik, K.S. (1970), "Asymptotic Theory of Turbulent Shear Flows", J. Fluid Mech., Vol. 42, p p. 411-427.

END

FILMED

4-84

DTIC